Exotic phenomena in the new frustrated spin ladder Li2Cu2O(SO4)2

Ornella Vaccarelli

THÈSE DE DOCTORAT DE
SORBONNE UNIVERSITÉ

Spécialité : **Physique**

Présentée par :

Ornella VACCARELLI

Pour obtenir le grade de

DOCTEUR DE SORBONNE UNIVERSITÉ

Exotic phenomena in the new frustrated spin ladder $Li_2Cu_2O(SO_4)_2$

Dirigée par Guillaume RADTKE et Gwenaelle ROUSSE

Soutenue le 25 September 2018 devant le jury composé de :

M. Vincent ROBERT	Rapporteur
M. Roland HAYN	Rapporteur
Mme. Virginie SIMONET	Examinateur
M. Andreas HONECKER	Examinateur
M. Ricardo LOBO	Examinateur
M. Guillaume RADTKE	Directeur
Mme. Gwenaelle ROUSSE	Co-directeur
Mme. Paola GIURA	Invité

"*The universe is vast and men are but tiny specks on an insignificant planet. But the more we realize our minuteness and our impotence in the face of cosmic forces, the more astonishing becomes what human beings have achieved.*"

Bertrand Russell

Résumé

L'étude des systèmes d'échelles de spin-1/2 frustrés est une tâche fondamentale dans la physique de la matière condensée, car ils répondent à toutes les exigences favorisant l'émergence de phénomènes nouveaux et exotiques.

Cependant, malgré des décennies de travaux théoriques consacrés à l'étude de ces échelles de spin, les réalisations de tels systèmes restent encore limitées. Dans cette thèse, nous étudions les propriétés magnétiques d'un nouveau composé $Li_2Cu_2O(SO_4)_2$. Ce système apparaît comme une très rare réalisation d'échelle de spin-1/2 frustrée à deux jambes dans sa structure tétragonale à haute température, où la frustration géométrique provient des interactions concurrentes le long des jambes.

De plus, la diffraction de neutrons et de rayons X en fonction de la température révèlent la présence d'une transition de phase structurale se produisant vers 125 K, impliquant une très faible distorsion de la structure. En combinant les approches expérimentale et théorique, nous démontrons que cette distorsion faible et progressive, tout en maintenant la géométrie globale d'une échelle, induit la formation d'une structure de dimères alternés à travers un grand couplage magnétoélastique, éliminant la plupart des frustrations magnétiques. En outre, nous présentons la première étude détaillée des excitations magnétiques à basse température de $Li_2Cu_2O(SO_4)_2$ combinant la susceptibilité magnétique, la spectroscopie infrarouge et les mesures de diffusion inélastique de neutrons. Les observations expérimentales sont qualitativement expliquées par des calculs de diagonalisation exacte et perturbations d'ordre élevés effectués sur la base de la géométrie dimérisée dérivée des calculs de premiers principes.

Mots-clés

Frustration, échelle de spin, systèmes fortement corrélés, systèmes de faible dimension, excitations magnétiques

Abstract

The study of frustrated spin-1/2 ladder systems is a fundamental task in condensed-matter physics, as they fullfill all the requirements favouring the emergence of new and exotic phenomena.

However, despite decades of theoretical work devoted to the study of these spin ladders, real material realizations of such systems still remain limited. In this thesis, we investigate the magnetic properties of a new compound $Li_2Cu_2O(SO_4)_2$. This system appears as a very rare realization of a $S = 1/2$ frustrated two-leg spin ladder in its high-temperature tetragonal structure, where geometrical frustration arises from competing interactions along the legs.

Moreover, temperature dependent neutron and X-ray diffraction reveal the presence of a structural phase transition occurring at around 125 K. Combining the experimental and theoretical approaches, we demonstrate that this weak and progressive distortion, while maintaining the global geometry of a ladder, induces the formation of a staggered dimer structure through a large magnetoelastic coupling, removing most of the magnetic frustration. Furthermore, we present the first detailed investigation of the low-temperature magnetic excitations of $Li_2Cu_2O(SO_4)_2$ combining magnetic susceptibility, infrared spectroscopy and inelastic neutron scattering measurements. Experimental observations are qualitatively explained by exact diagonalization and higher-order perturbation calculations carried out on the basis of the dimerized geometry derived from first principle calculations.

Keywords

Frustration, spin-ladder, strongly-correlated systems, low-dimensional systems, magnetic excitations

Acknowledgements

Writing the acknowledgements is a formal but an important step to close the chapter of a PhD student. From the moment we started to the moment we left, we received a lot of knowledge, helps, advices and good moments shared with colleagues and friends. Here I would like to thank everyone who contributed to my personal and scientific growth.

First and foremost, I would like to express my endless gratitude to my supervisors Guillaume Radtke and Gwenaelle Rousse for their help, scientific advices and their patience during the supervision of my thesis. Their expertises and insights on many aspects of science have been invaluable towards the realization of this work.

I would like to thank all my collaborators. Paola Giura, an expert in the laboratory (IMPMC) in the infrared spectroscopy measurements, for her experimental knowledge and for psychological support in the few difficult moments. Andreas Honecker for establishing enormously helpful learning environments for the study of condensed matter physics and for his important contribution in advanced computational methods used in this work. Björn Fåk, for his help in the Inelastic Neutron Scattering experiments performed at the Institut Laue-Langevin (ILL) in Grenoble. Andrés Saúl, for his contribution in the understanding of the dimerization in our system, and Meiling Sun for providing the sample used in this study.

I would like to point out that this work was supported by French state funds managed by the ANR within the Investissements dAvenir programme under reference ANR-11-IDEX-0004-02, and more specifically within the framework of the Cluster of Excellence MATISSE led by Sorbonne Universités.

I also would like to express my gratitude to the members of the jury, which give me the opportunity to defend my PhD work, namely: Pr. Vincent Robert, Pr. Roland Hayn, Dr. Virginie Simonet and Dr. Ricardo Lobo.

My acknowledgements go now to the entire IMPMC laboratory. Thanks to Guillaume Fiquet for welcoming me in this laboratory. Thanks to Ali, Ouafa, Antonella, Danielle and Hortense for the management of my missions, fees and every administrative procedures not always easy to understand. Now, I would like to thanks all my colleagues with whom I shared so much good moments and who help to make the laboratory a pleasant and convivial place to work: Andreita, Silvia, Edo, Fra Pi, Fra Mi, Amrita, Lenny, Lucas, Maud, Johan, Yoann, Julie, Gabriele, Guillermux, the crazy Mourad, Gilbert, Marzena, Eric, Raffaello, Giovanna, Abdel, Betul, Guilia, il mago, Alexandre, Carlitos, Vinicius, Tommy, Nicolas, Mariolix, Devaux, and the forgotten (sorry).

I also would like to thank my friends of volley, especially Eva and Elena; my friends of Burraco, Sasi, Oscar and Matteo; and all of my "parisian" friends. Among them, a special thanks go to Fra Ri and Sara.

Finally, the most important ones. My wonderful family: my father, who transformed a post defence party to an amazing gastronomic buffet, my mother, who can listen complaining myself with an Olympic calm, my sister, who has always been here for me (even from a distance) and her future baby, Emma, that I do not know yet. At last, I have to thank my little David, who stayed with me every day (nobody know how he managed it) and saved my incredible life in Paris.

Contents

Chapter 1

Introduction

1.1 Motivation

Low-dimensional spin systems have attracted a lot of attention in recent decades. Two key physical ingredients, low dimensionality and low spin values, play a crucial role influencing the magnetic properties of novel materials. In such systems, quantum fluctuations are particularly strong, resulting in a variety of fascinating phenomena which can not be explained by any classical interpretation. Magnetic ions realizing these systems are quite often found in the first row of transition metals such as V^{4+} or Cu^{2+}. Hence, theoretical and experimental researches cooperate to provide better understanding to these systems.

The interest in such systems largely grew from the connection proposed by Anderson between high-T_C superconductivity and the so-called resonating-valence-bond (RVB) picture for the cuprates [1, 2]. The idea is that, in a RVB state, the electron spins from neighbouring atoms are coherently paired to form a valence bond in which the magnetic long-range order is absent. By doping, a "resonating" system is obtained, whereas the valence bonds are able to jump anywhere and to superconduct. Despite the elegance of this suggestion and decades of theoretical work, RVB scenario still remains unproven. Much attention has therefore been devoted to frustrated models, as they combine low spin, low dimensionality, and magnetic frustration, three ingredients favouring the emergence of a RVB state.

The concept of "frustration" has been introduced to describe the presence of competing interactions that cannot be simultaneously satisfied [3], leading to rich physics, high degeneracy of the ground-state and possibility of new phases of matter. These interesting systems are found to be at the cross over of few dimerized systems with exact solutions, such as the Majumdar-Ghosh point [4, 5] for the spin-half one-dimensional $J - J_2$ model at $J_2/J = 0.5$; the two-dimensional Shastry-Sutherland model [6] and linked-tetrahedral chain model proposed by Gelfand [7, 8] whose simple phase diagram presents two phases, the rung-singlet (RS) and the Haldane phase. Naturally, the introduction of an additional next-nearest-neighbor (NNN) interaction J_2 along the rungs in the two-leg spin ladder further increases frustration and gives rise to new quantum phases in the complicated phase diagram [9].

Nonetheless, after many years of continuous study, the field of low-dimensional spin systems still attracts an increasing interest. Several new unexplained problems and phenomena arise from the behavior of these systems and need further researches and investigations. Unfortunately, the development in the number and complexity of these theoretical toy models is not driven by a big amount of real magnetic materials studied experimentally. Some of the examples include the quasi-1D two-leg spin ladder systems $SrCu_2O_3$ [10], the compound $SrCu_2(BO_3)_2$, topologically equivalent to Shastry-Sutherland lattice [11], and the so-called *"phone number compound"*

$Sr_{14}Cu_{24}O_{41}$ which are prototypical realizations of non-frustrated ladders. Of particular interest is the recent discovered compound $BiCu_2PO_6$, which seems the only frustrated two-leg spin ladder found in the literature with frustrating NNN coupling along the legs [12].

In this thesis, we investigate the newly synthesized compound $Li_2Cu_2O(SO_4)_2$ [13], an interesting example for strongly correlated systems in which the electronic and magnetic properties are controlled by the Cu^{2+} magnetic ions. This cuprate displays a peculiar crystal structure in which the coppers are staggered together in order to form a geometry topologically equivalent to a two-leg spin ladder.

1.2 Layout of the Thesis

The main objective of the present study is to give an extensive analysis of the magnetic behavior of the compound $Li_2Cu_2O(SO_4)_2$, found to be an actual realization of a frustrated two-leg spin ladder. The high complexity of this frustrated system was challenging for both experimental and theoretical point of views. In this respect, the thesis is decomposed into the following chapters:

- Chapter 2 presents a general overview of the magnetism in low-dimensional spin ladder systems. Many of the topics addressed in this Chapter are often reused or devolved in the rest of the manuscript.
- Chapter 3 introduces theoretical background and tools used in this work for calculating the electronic and magnetic properties of our system.
- In chapter 4 the experimental methods used later in the thesis such as inelastic neutron scattering and infrared spectroscopy are explained. The development of the chapter is motivated mainly by the investigation of the magnetic excitations in low-dimensional spin systems.
- In Chapter 5 and 6 we present the main results obtained in this work. These chapters are heavily based on articles published during the course of the project [14, 15]. In particular, Chapter 5 is dedicated to the investigation of the magnetic properties of the $Li_2Cu_2O(SO_4)_2$. We will present its high-temperature tetragonal structure and its frustrated character. Furthermore, we will see the appearance of an intriguing phase transition at about 125 K. State-of-the-art density functional calculations reveal that this structural distortion is accompanied by a strong magnetic dimerization. In Chapter 6 we will investigate this dimerized phase, by focusing on its magnetic excitations.
- Finally, a summary and outlook in Chapter 7 close the thesis.

Chapter 2

Magnetism in 1D spin ladders

"Quantum mechanics is the key to understanding magnetism.
When one enters the first room with this key
there are unexpected rooms beyond,
but it is always the master key that unlocks each door."

J. H. Van Vleck

Strongly correlated spin systems have received considerable attention during the past decades from both theoretical and experimental points of views, creating a fascinating story of complex and exciting results. In particular, quantum fluctuations become significant in low-dimensional spin systems, especially for small spin values such as $S = 1/2$. The behaviour of these quantum many-body systems gives rise to new phenomena which are based on the breakdown of the classical picture.

Nonetheless, after many years of continuous study, the story of low-dimensional spin systems is not yet finished. Parameters like dimerization, frustration, anisotropies and spin-lattice coupling create several new unsolved problems that still attract a considerable interest for these intriguing systems, requiring further researches and investigations.

2.1 Magnetism and magnetic order

2.1.1 Atomic magnetism

Magnetism has its origin in the intrinsic spin and orbital magnetic moments of the electrons. In an atom the total angular momentum **J** is the sum of the individual spin **S** and orbital **L** contributions.

In first approximation the electronic configuration of an isolated atom is predicted by Hund's rules [16], which take into account the interactions in the many-electron problem. In this thesis, the most discussed ion is the copper Cu^{2+} in its $3d^9$ electronic configuration, which corresponds to the $^2D_{5/2}$ spectroscopic ground-state term. According to Hund's rules, this ion has total angular momentum $J = 5/2$, calculated from the sum of the spin $S = 1/2$ and the orbital momentum $L = 2$. However, this theoretical value does not agree with the magnetic properties of the copper in a solid crystal, for which $J \approx 1/2$. The reason of this disagreement lies in the environment that influences the magnetism in the ion. Indeed, in order to find the energetically favourable configuration we have to take into account the additional effect of the crystal field, which originates from the electrostatic interaction and hybridization of the d-orbital with the neighbouring ions. This means that the crystal structure itself has a strong effect on the energy levels.

As an example, Figure 2.1 shows a magnetic $3d$ ion in an octahedral environment (O_h in Schoenflies notation) of surrounding negative ions. There are 5 different $3d$ orbitals that are degenerate in the case of free ion.

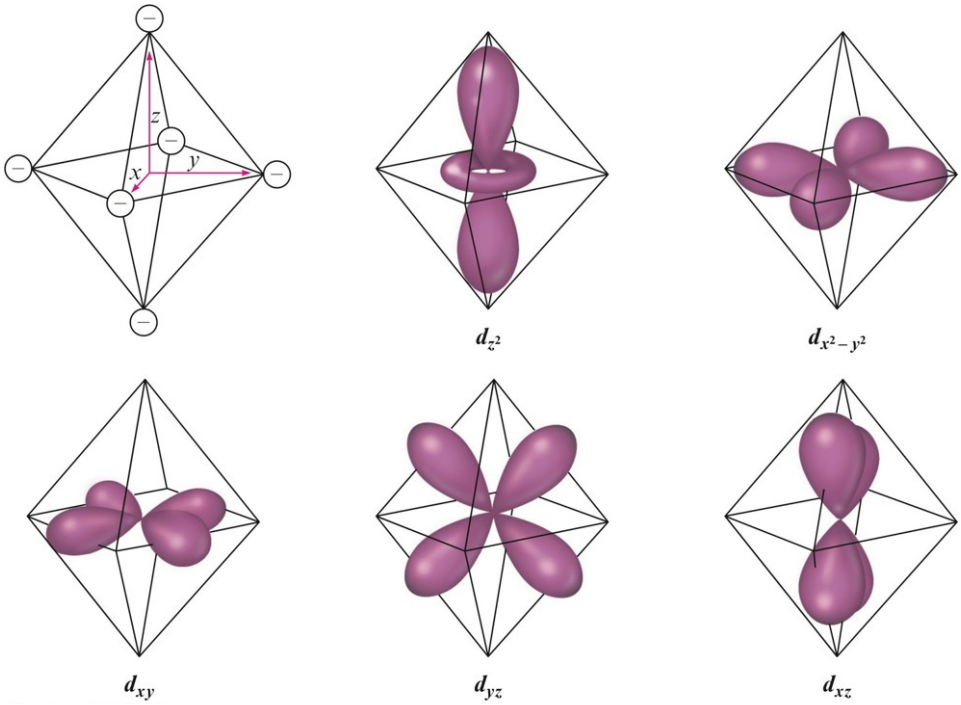

FIGURE 2.1: Illustration of an octahedral crystal field of negative point charges and relative orientation of the $3d$ orbitals. Figure taken from [17].

However, these orbitals interact with the negative oxygen ions in different manners and these different interactions lift the degeneracy. This leads to a splitting between the orbitals known as T_{2g} (which include d_{xy}, d_{xz} and d_{yz}), and the energetically higher levels E_g (d_{z^2} and $d_{x^2-y^2}$). The atomic ^{2}D term is branched in the ^2E_g crystal field term and the orbital momentum is totally or partially quenched. Thus $\mathbf{L} \sim 0$ and the corresponding total angular moment becomes equal to the spin, $J \sim 1/2$, in agreement with the experimental findings.

Sometimes high-symmetry states with orbitally degenerate ground-state are unstable with respect to a spontaneous distortion, this phenomenon is known as the Jahn-Teller effect. This distortion can further lift the degeneracy to lower the energy of the ground-state. In the case of the Cu^{2+} this leads to a distortion of the octahedron characterized by an elongation in the z axis and a compression in the xy plane. We obtain a tetragonal symmetry that belongs to the D_{4h} group, in which there are two different distances between the central metal ion Cu^{2+} and the negative oxygen ions, the distance along the z axis and the one in the xy plane. Therefore by stretching the octahedron and breaking the symmetry from cubic (three equal distances) to tetragonal, the orbital levels are further split, as illustrated in Fig. 2.2. Finally, filling up the levels, we arrive at the important result that only the $d_{x^2-y^2}$ orbital is partially occupied, being half-filled with a total angular momentum $\mathbf{J} \approx \mathbf{S}$.

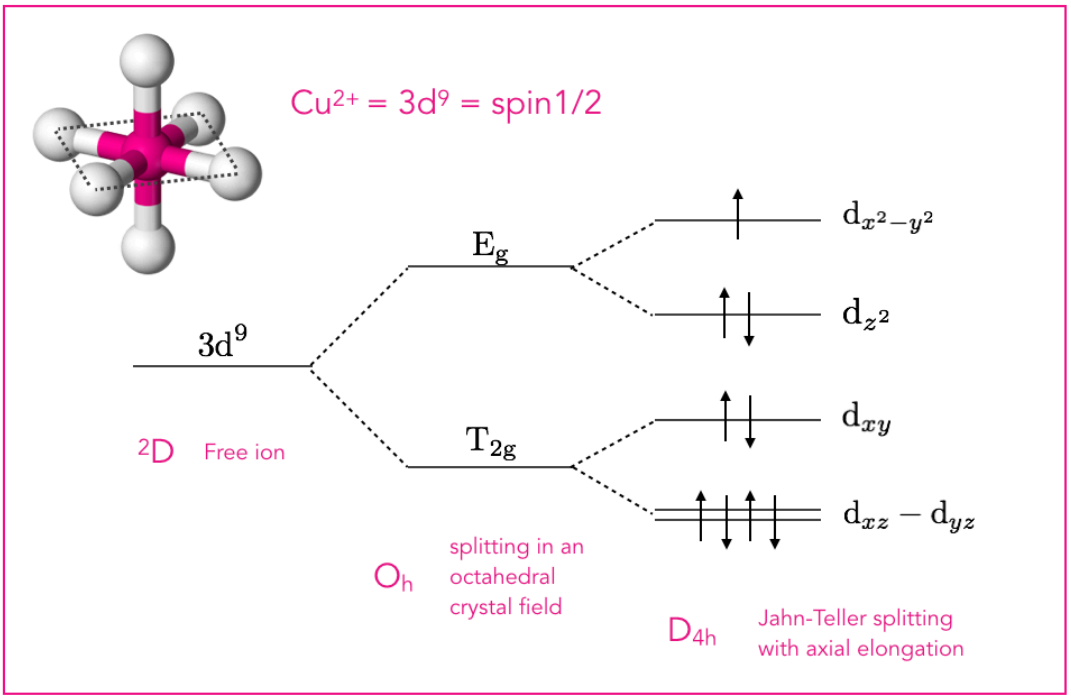

FIGURE 2.2: Illustration of the effect of an octahedral crystal field on the energy levels of a $3d^9$ transition metal Cu^{2+} surrounded by oxygen ions O^{2-}. The degeneracy of the orbitals is further lifted by a Jahn-Teller effect through an elongation of the axial bonds.

2.1.2 Magnetic interactions

Magnetic compounds allow for different interactions between magnetic ions, that depend on the distance between them as well as on the symmetry of the compound. Neighbouring magnetic ions in a solid can be coupled together via exchange interactions, which arise predominately as a consequence of the overlap of the electronic shells of the ions, the Pauli exclusion principle and the Coulomb interaction.

In a simple system of two electrons in the absence of spin-orbit coupling, the total wave function, composed of the product of the spatial and the spin wave functions, must be antisymmetric. Thus, there are two different possibilities for combining the spin and the spatial part: an antisymmetric (singlet) spin state ($S = 0$) with a symmetric spatial state, or a symmetric (triplet) spin state ($S = 1$) with an antisymmetric spatial state. The Coulomb interaction between the electrons lifts the degeneracy between the two possibilities resulting in an energy difference between the singlet E_S and the triplet state E_T, which defines the exchange constant $J = E_T - E_S$. The effective Hamiltonian can be expressed as:

$$H = J\,\mathbf{S}_1 \cdot \mathbf{S}_2, \tag{2.1}$$

where $\mathbf{S}_1$ and $\mathbf{S}_2$ are the spin operators, acting on the two electrons and J measures the interaction between the two spins. For $J < 0$, $E_T < E_S$ and the triplet state is favoured; otherwise, for $J > 0$, $E_T > E_S$ and the singlet state is favoured.

The generalization to a many-body system of interacting spins was derived by Heisenberg and Dirac simultaneously in 1926 [18, 19]. The result is know as the

Heisenberg Hamiltonian:

$$H = \sum_{ij} J_{ij}\, \mathbf{S}_i \cdot \mathbf{S}_j, \tag{2.2}$$

where the sum is over all pairs of spins on sites i and j which interact through the exchange constant J_{ij}. In this notation it is clear that $J_{ij} > 0$ favours antiparallel alignment (antiferromagnetic (AFM) exchange) and $J_{ij} < 0$ favours parallel alignment of moments (ferromagnetic (FM) exchange).

Despite its simplicity, the Heisenberg Hamiltonian provide excellent descriptions for many magnetic phenomena observed in spin-1/2 systems, where there is no single ion anisotropy.

Direct Exchange Direct exchange arises from the electrostatic Coulomb repulsion between two neighboring electrons which are close enough to directly interact via their electronic orbitals. This gives rise to a strong but short range coupling that is always ferromagnetic between orthogonal orbitals. However, in many materials, such as strongly correlated systems, the electrons orbitals are highly localized and, as the strength of the exchange interaction rapidly decreases with distance, a direct interaction between two localized orbitals is rare. In these cases, an indirect exchange interaction may dominate.

Superexchange Superexchange is an indirect exchange process where magnetic atoms interact via a non-magnetic intermediary. This process can be used to explain the predominance of antiferromagnetism in transition metal oxides, where magnetic ions are well separated by the non-magnetic oxygen atom.

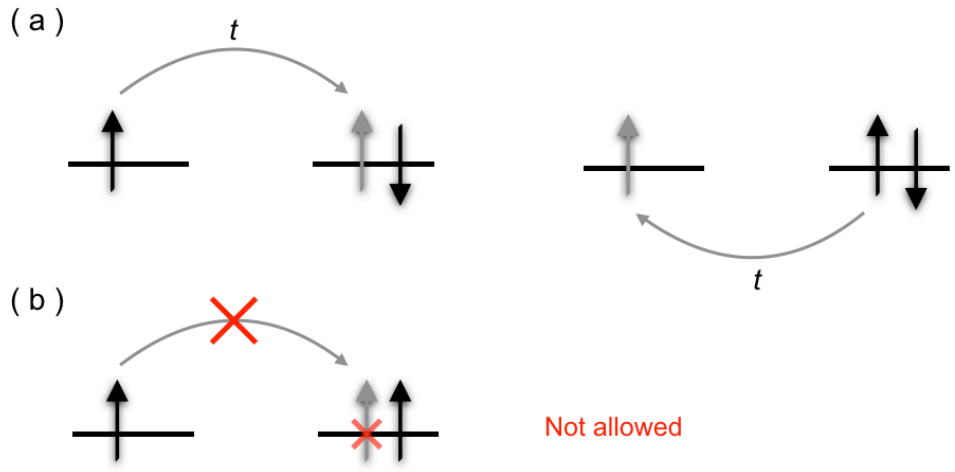

FIGURE 2.3: Representation of a simplified indirect exchange process. (a) 2-order antiferromagnetic direct exchange process. (b) Ferromagnetic hopping forbidden by the Pauli principle.

In order to discuss this interaction, we consider a simplified two-site Hubbard model, described by the Hamiltonian in Appendix A, with a on-site repulsion interaction U and a hopping term t_{eff} which implicitly includes the effect of the intermediate atom. In the strong coupling limit $U \gg t$, at half-filling, the hopping term is considered as a perturbation describing processes in which, for example, the electron at site 1 hops to the neighbour site 2 occupied by another electron and finally one of the two electrons returns to the original site 1 (Figure 2.3). It should be noted that only when

the spins are antiparallel to each other this type of process is possible; electrons with parallel spins are prohibited on the same site by the Pauli principle. Stabilization of the AFM configuration only is thus allowed through this configuration interaction mechanism. The resulting AFM coupling is often called "kinetic exchange".

As described in Appendix A, the perturbative treatment of the half-filled Hubbard model in the strong coupling limit results in an effective spin-1/2 Heisenberg Hamiltonian with an antifferromagnetic exchange coupling

$$J \simeq \frac{4t_{eff}^2}{U} > 0. \tag{2.3}$$

Therefore the indirect exchange described by this simplified model with two electrons favours antiferromagnetic alignment. However, the situation is not so simple when we take into account the presence of the oxygen atom.

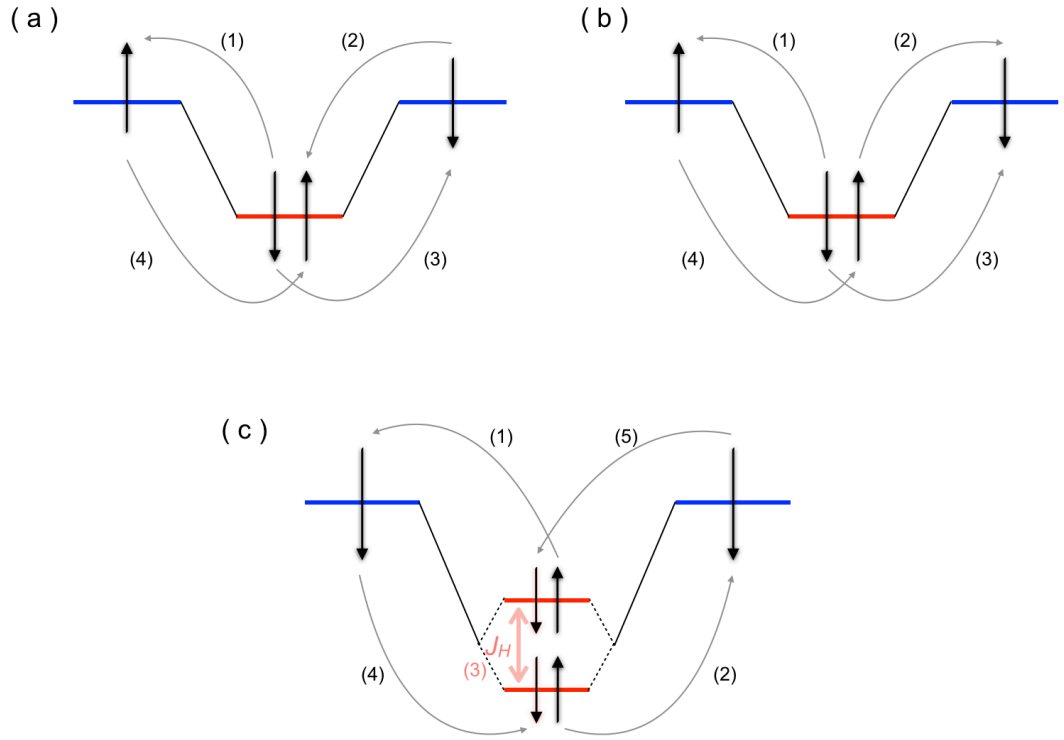

FIGURE 2.4: Simple picture of the fourth-order superexchange mechanism in the case of the AFM interaction between two Cu^{2+} ions at 180° (a) and (b); and in the FM case of two Cu^{2+} ions at 90° (c). The central orbital (red line) represents the p-orbital of an oxygen and the two orbitals on the sides (red lines) are the two Cu^{2+} d-orbital. (a) and (b) represent the two terms in the eq. 2.5. In (c) the additional effect of the interatomic exchange J_H is in red.

To understand the superexchange mechanism, we then need to consider a three-site Hubbard model composed by two $3d$-orbitals (copper Cu^{2+} in Fig. 2.5 (a)) and an oxygen p-orbital in between [20]. The electron dynamics in this model is described

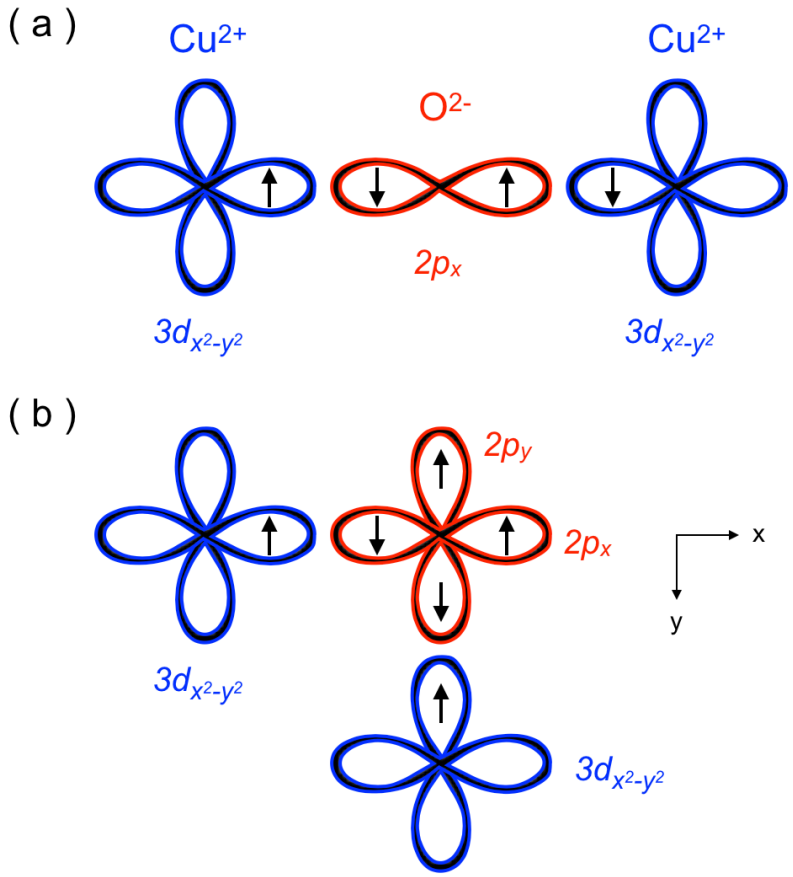

FIGURE 2.5: Schematic diagram of the atomic orbitals involved in AFM (a) and FM (b) ordering via superexchange for a Cu-O-Cu bond. The $d_{x^2-y^2}$ magnetic orbitals of the $3d^9$ transitional metal Cu^{2+} are shown. They overlap with the $2p$ bonding orbital of an oxygen atom forming a AFM interaction for a bond angle of 180° and a FM interaction for 90°.

by the Hamiltonian

$$\begin{aligned} H =& \epsilon_d \sum_{i,\sigma} d^\dagger_{i,\sigma} d_{i,\sigma} + (\epsilon_d + \Delta) \sum_{\sigma} p^\dagger_{\sigma} p_{\sigma} + U_{dd} \sum_{i} d^\dagger_{i,\uparrow} d_{i,\uparrow} d^\dagger_{i,\downarrow} d_{i,\downarrow} \\ &+ U_{pp} \sum_{i} p^\dagger_{i,\uparrow} p_{i,\uparrow} p^\dagger_{i,\downarrow} p_{i,\downarrow} + \sum_{\langle ij \rangle \sigma} t_{ij} (d^\dagger_{i,\sigma} p_{j,\sigma} + \text{h.c.}) \end{aligned} \tag{2.4}$$

where $d^\dagger_{i,\sigma}$ (and $d_{i,\sigma}$) and $p^\dagger_{i,\sigma}$ (and $p_{i,\sigma}$) create (and destroy) a hole in the copper $3d$ and in the oxygen $2p$, respectively. ϵ_d and ϵ_p are the on-site energies of Cu^{2+} and O^{2-} and $\Delta = \epsilon_p - \epsilon_d$. The Coulomb repulsion between two Cu holes, or two O holes is taken into account by U_{dd} and U_{pp}. t_{ij} describes the Cu-O hopping and is equal to $\pm t_{pd}$.

As before, we consider the hopping term as a perturbation. In this case we have to go up to the forth-order in the perturbation theory in order to describe the four hopping processes. The resulting exchange coupling is:

$$J \simeq \frac{4t_{pd}^4}{\Delta^2} \left[\frac{1}{U_{dd}} + \frac{2}{2\Delta + U_{pp}} \right], \tag{2.5}$$

where the effect of the two terms in eq. 2.5 is illustrated in Fig. 2.4 (a) and (b), respectively.

Therefore the superexchange coupling favours antiferromagnetic alignments of the spins. It should be noted that in the discussion we have assumed a 180° geometry, as illustrated in Fig. 2.5 (a). Note that if $t_{eff} = \frac{t_{pd}^2}{\Delta}$, then the first term in eq. (2.5) is the same as in the previous case (eq. (2.3)).

The situation is quite different when the oxygen orbitals and the two copper form a 90° configuration, represented in Fig 2.5 (b). In this case it is necessary to include an intra-atomic exchange $J_H > 0$ on the oxygen (Figure 2.4 (c)), which gives at the forth-order:

$$J \simeq \frac{4t_{pd}^4}{\Delta^2}\left[\frac{2}{2\Delta + U_{pp}} - \frac{1}{2\Delta + U_{pp} - J_H}\right]. \tag{2.6}$$

Therefore, the superexchange coupling is ferromagnetic and tends to be significantly weaker than the AFM 180° superexchange coupling.

This is the microscopic basis of the Goodenough-Kanamori-Anderson (GKA) rules [21, 22, 23] which provide a phenomenological model to predict the strength and sign of the superexchange interactions, dependent on the bond lengths and angles.

In summary, between half-filled orbitals (like Cu^{2+}) in the limit cases, strong AFM exchange is favoured for a bond angle of 180° and weak FM is found for an angle of 90° [24]. Unfortunately, GKA rules are not sufficient to predict the sign and strength of magnetic couplings in systems where bond angles are between the extremes of 180° and 90°. In these cases, we have to use a more sophisticate method to analyze the magnetic exchange interaction, as we describe in section 3.1.4.

Long-range exchange In the previous paragraphs we described the direct and indirect exchange, mediated by an intermediate atom. There also exist materials where magnetic interactions are mediated by more than one intermediate ion, represented with high-order processes. For example, in marinite compounds $Li_2M(SO_4)_2$ (M = Co, Fe, Mn) and $Li_1Fe(SO_4)_2$ the sulphate anion group SO_4 has been studied as intermediary between the copper ions which give rise to the Cu-O-S-O-Cu super-super-exchange interaction found to be antiferromagnetic [25].

Dzyaloshinskii-Moriya interactions Another type of magnetic interaction which can be met in Cu^{2+} systems is the antisymmetric Dzyaloshinsky-Moriya (DM) interaction, an anisotropic exchange interaction that arises between two neighboring spins, $\mathbf{S}_i$ and $\mathbf{S}_j$, in some low symmetry crystals. It is produced from the interplay of the spin-orbit and the superexchange interactions, causing a spin-canting in the system, a phenomenon through which spins are tilted by a small angle about their axis rather than being exactly co-parallel.

The DM interaction is described by the Hamiltonian,

$$H_{DM} = \mathbf{D}_{ij} \cdot (\mathbf{S}_i \times \mathbf{S}_j), \tag{2.7}$$

where $\mathbf{D}$ is the DM vector, whose direction is constrained by symmetry.

2.1.3 Magnetic ordering

The introduction of magnetic interactions in solid systems leads to various magnetic structures. In general, at high temperature, the magnetic state is a disordered paramagnetic state due to thermal excitations; while, at sufficiently low temperatures, it

is eventually energetically favourable for conventional magnetic materials to develop some sort of long-range order. The simplest ones are ferromagnetism which allows for a spontaneous magnetization with all magnetic moments aligned in the same direction, and the more common case of antiferromagnetism. It consists of two interpenetrating sub-lattices, where both are spontaneously magnetized but in opposite directions, leading to a net magnetization equal to zero.

The critical temperature T_C below which magnetic ordering occurs is know as the Curie temperature in ferromagnets and Néel temperature in antiferromagnets [26, 27]. As the temperature is increased, the thermal fluctuations will be strong enough to break the magnetic order, and at $T > T_C$ the spins have no longer a preferred orientation, but they are randomly oriented (paramagnetism).

Magnetic excitations Thermal fluctuations in long-range ordered magnetic systems allow for excitations away from the ground-state which propagate through the system, these excitations are the so-called spin waves. Spin waves are the analogue of lattice waves in crystal lattice, where the order can be disrupted by thermally excited lattice vibrations. As a quantized lattice wave is called a "phonon", a quantized spin wave is called a "magnon" that has a characteristic dispersion relation, depending on the type of magnetic order present in the system.

2.2 One-dimensional spin systems

In contrast to magnetic systems with classical long-range order below a critical temperature, quantum effects dominate the behavior of low-dimensional systems giving rise to new properties. In particular, in 1D spin systems quantum fluctuations are particularly strong and long-range order is often suppressed even at very-low temperatures [28].

Besides theoretical studies of these low-dimensional spin systems, real realizations of such systems are also discovered. The spin chains are realized when a spin-interaction in a certain direction is much stronger with respect to the others, and this direction represents the chain direction. In the end of the 90's different compounds were discovered for which the theoretical predictions for the physical properties of the Heisenberg antiferromagnetic chain have been confirmed [29] after which there were an explosion of experimental investigations [30]. Thus, the field of low-dimensional magnetism became one of the most active areas of contemporary condensed matter physics.

2.2.1 Antiferromagnetic Heisenberg Chain

The spin-1/2 antiferromagnetic Heisenberg chain is one of the best-studied examples of a low-dimensional system failing to develop long-range order and forming a gapless excitation spectrum.

The Hamiltonian of the Heisenberg spin chain can be written as

$$H = J \sum_i \mathbf{S}_i \cdot \mathbf{S}_{i+1}, \tag{2.8}$$

where J is the AFM exchange coupling. The model, represented in Fig. 2.7 (a), is exactly solvable. The first solution was given by Bethe in 1931 [31]. The ground-state is not the classical Néel state (a Néel state is not even an eigenstate of the Hamiltonian (2.8)), but a complicated spin-singlet state.

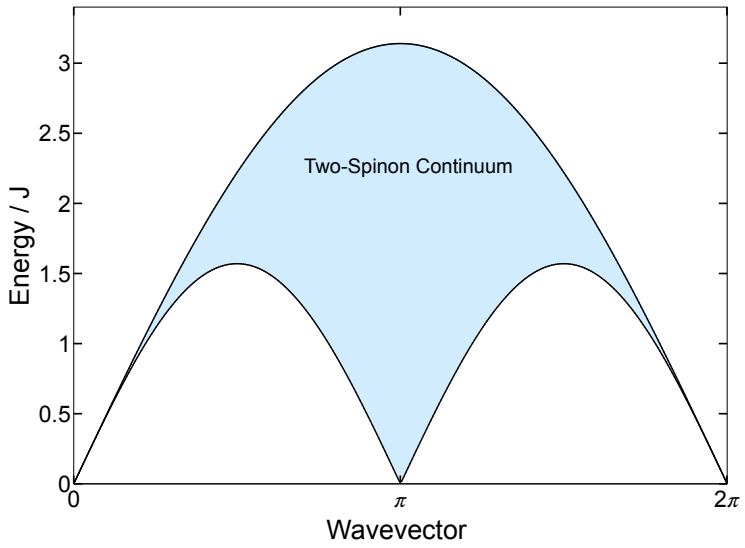

FIGURE 2.6: Dispersion relation for spinons in the 1D AFM Heisenberg chain and representation of the Two-Spinon Continuum as shaded area between the boundaries of equations (2.9) and (2.10).

After a plethora of theoretical studies, it was clearly established that long-range order in AFM spin chain is prevented due to the presence of strong quantum fluctuation and, as a consequence, the staggered spin-spin correlation as a function of the distance between spins decays slowly to zero as a power law.

By analogy to the classical antiferomagnetic system, the excitations were wrongly assumed to be $S = 1$ triplet spin-wave states [32] with dispersion relation

$$\frac{E_L(k)}{J} = \frac{\pi}{2}|\sin(k)|. \tag{2.9}$$

Only in 1981, Faddeev and Takhtajan introduced the massless $s = 1/2$ spinon as the true elementary excitation in the $S = 1/2$ AFM spin chain [33]. As the total spin of the chain must be either integer or half-integer (for even or odd number of spins), the excitation of a single spinon is not allowed, but requires a pair of spinons.

Indeed, dispersion relation in Eq. (2.9) represents the superposition of the two spinons and exactly the lower boundary of the continuum in which the spinons are deconfined. The upper boundary of this continuum corresponds to the two spinons with dispersion relation

$$\frac{E_U(k)}{J} = \pi|\sin(k/2)|. \tag{2.10}$$

Figure 2.6 shows the spinon dispersion and the two-spinon continuum.

In summary, the uniform spin-1/2 AFM Heisenberg chain is a gapless spin-singlet system with peculiar excitations (spinons). Moreover, no long-range order can develop, even at $T = 0$ K. However, the magnetic energy can be lowered by a Spin-Peierls transition.

2.2.2 Spin-Peierls transition and alternating AFM chain

Below a certain transition temperature T_{sp}, 1D systems may undergo a distortion where the distances between neighbouring spins are no longer uniform. Due to the magneto-elastic coupling this leads to an alternation of the exchange coupling leading

to a dimerized phase (Figure 2.7). This so-called dimerization opens a finite spin gap between the non-magnetic singlet ground-state and the first excited triplet state.

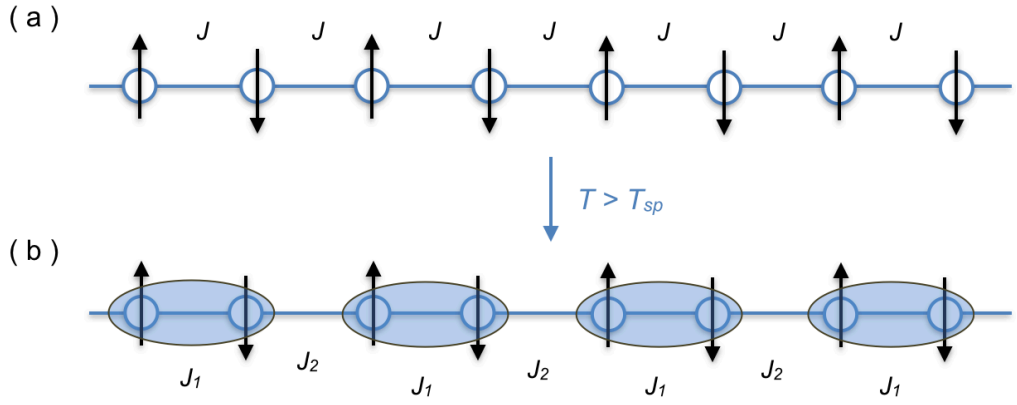

FIGURE 2.7: (a) An $S = 1/2$ spin chain with an uniform AFM interaction J. (b) The dimerized state below the spin Peierls transition temperature T_{sp} with alternatively enhances J_1 or reduces J_2 interactions and subsequent singlet pair formations on the enhanced exchange interactions.

From the experimental point of view there are several characteristic features which signal the spin-Peierls transition. Among them, the magnetic susceptibility usually shows a broad maximum caused by the existence of an AFM exchange interaction and a rapid drop below the transition temperature T_{sp}, due to the gap opening [34]. On the basis of magnetic susceptibility measurements, $CuGeO_3$ as well as TiOCl were recognized as potential candidates of spin-Peierls systems [35, 36].

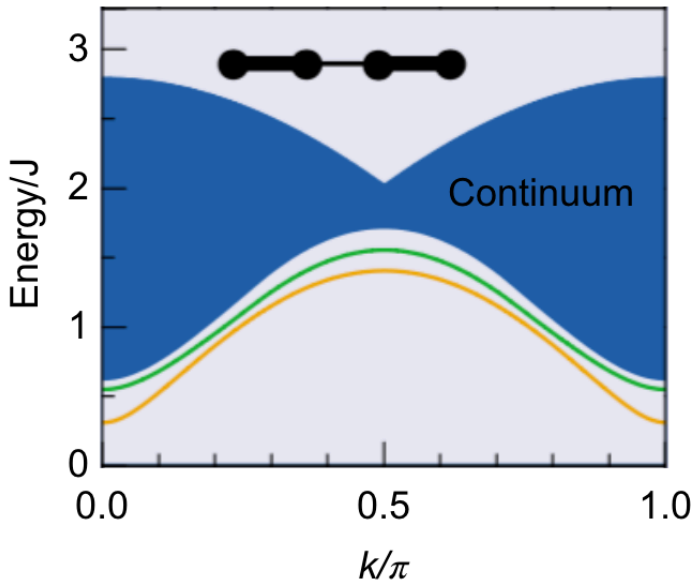

FIGURE 2.8: Excitation spectrum of the alternating chain. In yellow and green the first and second lowest excitations (that are, respectively, a triplet and a singlet state) and in blue the resulting continuum. Figure adapted from [37].

The generalized Hamiltonian for the alternating AFM chains is:

$$H = \sum_i J_1 \mathbf{S}_{2i-1} \cdot \mathbf{S}_{2i} + J_2 \mathbf{S}_{2i} \cdot \mathbf{S}_{2i+1}, \tag{2.11}$$

where J_1 and J_2 are the two alternating values of the exchange interactions. We can define a parameter $\lambda = J_2/J_1$, $0 \leq \lambda \leq 1$. For $\lambda = 1$ we obtain the uniform AFM chain with gapless excitation spectrum, and for $\lambda = 0$ the system becomes completely dimerized with a trivial ground-state described as a product of singlets on the dimers and opening a finite gap of energy equal to J_1 that creates a localized excited triplet state. For intermediate values the dimers interact with each other and a dispersive excitation above the singlet ground-state is found, corresponding to a one-triplon state.

Moreover, the two unbound excitations in the dimerized chain form a continuum, where the gap is twice the elementary triplet gap [38, 39]. Figure 2.8 reproduces the results of Uhrig and Schulz [37].

2.3 Quasi 1D systems: Spin Ladders

Previously, we showed the interest of 1D AFM spin-1/2 systems where quantum fluctuations prevent long-range order and create peculiar features. Structural alterations in this system could give rise to significant modifications in the magnetic properties. We already described how a spin-Peierls transition can open a gap between the ground-singlet state and the lowest triplet excitation. Now we consider different AFM spin-1/2 chains coupled together into a spin ladder. This quasi-1D spin system provides a bridge between one and two dimensional systems [40, 41]. Figure 2.9 (a) and (b) display, respectively, a two-leg and a three-leg ladder.

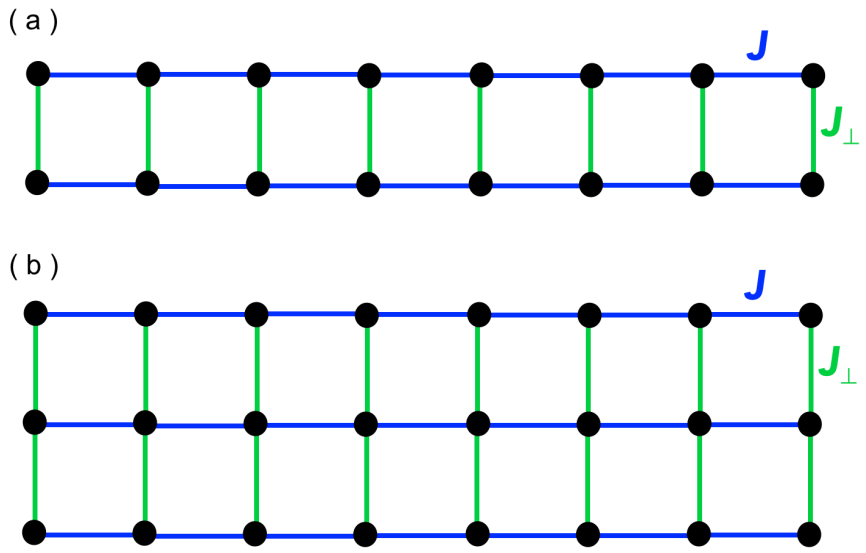

FIGURE 2.9: Representation of two spin ladders with $n = 2$ (a) and $n = 3$ (b) legs. The exchange coupling along the legs is J, whereas the rung coupling is $J_\perp$.

2.3.1 Two-leg spin ladder

The most common and interesting structure is the two-leg ladder (Figure 2.10 (a)). The Hamiltonian of this system is:

$$H = \sum_i J(\mathbf{S}_{1,i} \cdot \mathbf{S}_{1,i+1} + \mathbf{S}_{2,i} \cdot \mathbf{S}_{2,i+1}) + J_\perp \mathbf{S}_{1,i} \cdot \mathbf{S}_{2,i}, \tag{2.12}$$

where J and $J_\perp$ are the exchange couplings between the legs and the rungs, respectively. The first index denotes the leg number $\{1, 2\}$ and the second one, i, counts the rungs. An important parameter is the ratio $J_\perp/J$ between the exchange couplings that we suppose AFM. We study the properties of the model changing this ratio.

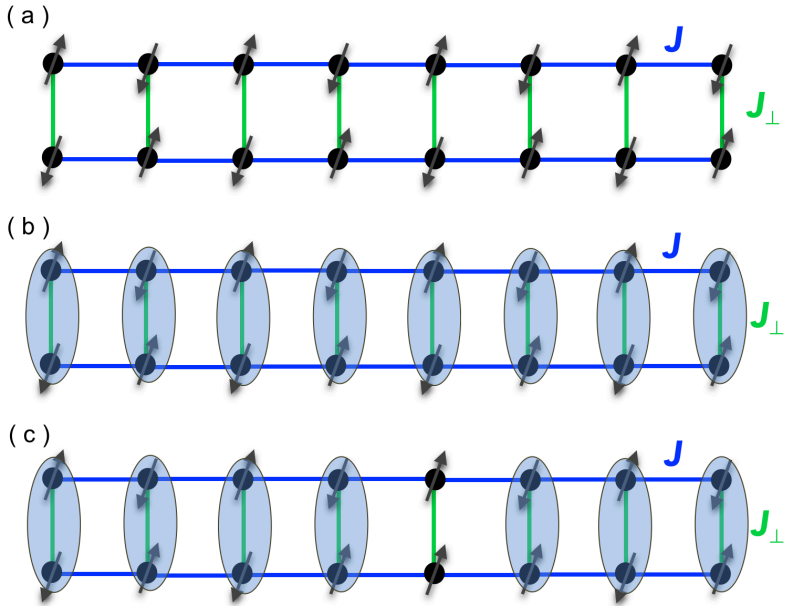

FIGURE 2.10: (a) Two-leg spin ladders with AFM couplings J and $J_\perp$ along the rungs and along the legs. (b) Ground-state of the two-leg ladder, where rungs form spin singlet states. (c) Elementary excitation with one rung-triplet state.

The general behavior of spin ladders is most easily understood in the limit of strong rung coupling $J_\perp/J \gg 0$ [42]. In this limit the rungs form dimer states that weakly interact with each other. Therefore, the ground-state is the direct product of rung-singlet states (one for every rung of the ladder) with total spin equal to zero (Figure 2.10 (b)) and the elementary excited state is created promoting a rung-singlet into a rung-triplet state with $S = 1$ (Figure 2.10 (c)).

For an isolated rung-singlet the value of the energy is $-\frac{3}{4}J_\perp$, whereas the energy of one rung-triplet is $\frac{1}{4}J_\perp$. Thus, the value of spin gap is simply $\Delta = J_\perp$. The introduction of a small coupling J along the chain is responsible of a weak interaction between the dimers and allows the hopping of the triplet state along the chain, i.e. the local triplet excitation can propagate along the ladder. As a consequence, the triplet excitation is dispersed with the following dispersion relation at $O(J_\perp^2/J)$ [42]:

$$E(k) = J_\perp + J\cos k + \frac{3}{4}\frac{J^2}{J}, \tag{2.13}$$

and a reduced spin gap energy:

$$\Delta = J_\perp - J + \frac{3}{4}\frac{J^2}{J}. \tag{2.14}$$

When the J becomes larger, the spin-gap energy decreases down to $\Delta = \frac{1}{2}J_\perp$ in the weak coupling limit $J_\perp/J = 1$ with dispersed triplet excitation. The value of the spin gap was first determined by Barnes and Dagotto in 1993 [42], and latter confirmed from other theoretical studies [43, 44, 45].

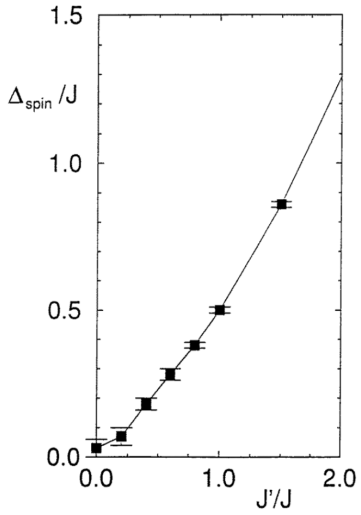

FIGURE 2.11: Figure taken from [46]. The spin gap is here indicated with Δ_{spin} and the exchange couplings J and J' are, respectively, the leg (that we also call J) and the rung couplings $J_\perp$. The plot represents the spin-gap energy of a $S = 1/2$ two-leg spin ladder in function of the ratio J'/J ($J_\perp/J$).

In Figure 2.11 the spin gap behaviour is plotted as a function of the ratio $J_\perp/J$. It should be noted that a spin gap exist for any value of $J_\perp > 0$. In the limit $J_\perp = 0$ we obtain two decoupled AFM spin-1/2 chains and, in this case, the excitation spectrum is gapless, as we saw previously.

2.3.2 Even and odd leg ladders

Increasing the number of legs in a n-leg spin ladder, the physical properties are qualitatively preserved, for any n even. In particular, the system continues to show rung-singlets ground-state and triplet excitation in the strong-coupling limit $J_\perp/J \gg 0$, with a non-zero spin gap for every finite n. The value of the spin gap decreases with n, in order to reach the limit of gapless 2D ($n \to \infty$) system [47].

In addition, the spin-spin correlation has been studied for $n = 2$ and 4 legs [44]. It turns out that its evolution as a function of the distance in the two cases has an exponential decay. The corresponding results are presented in Fig. 2.12 (a) and it clearly shows that the exponential decrease of the spin-spin correlation is slower for a higher value of n. As a consequence, a Resonant Valence Bond (RVB) picture is developed in these systems. The RVB model, introduced by Anderson [1, 2], assumes a ground-state of singlet pairs that interact with each other. This creates a more stable "resonant" spin-liquid state with singlets free to move in all the ladder. Despite the

elegance of this suggestion and decades of theoretical work, RVB scenario still remains unproven. In conclusion, even-leg ladders are found to be "quasi" spin liquids that exhibit short-range RVB ground-states with exponentially decaying correlations and gapped excitations.

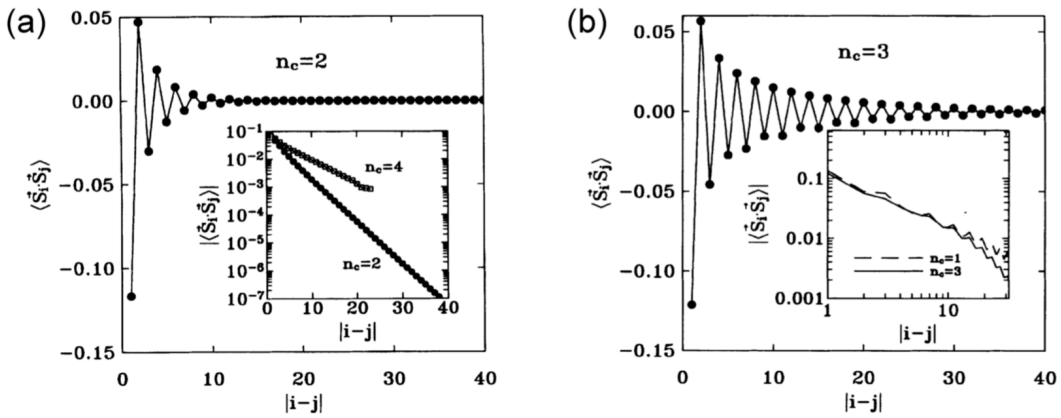

FIGURE 2.12: Figure taken from [44]. Spin-spin correlations $\langle \mathbf{S}_i \cdot \mathbf{S}_i \rangle$ in function of the distance $|i-j|$ for n-leg ladders. (a) n even. The inset shows the exponential behaviour for $n = 2$ and $n = 4$. (b) n odd. The inset shows the power-law behavior for $n = 1$ and 3.

The situation for odd-leg ladder is quite different [48, 43, 49]. In the strong limit case $J_\perp/J \gg 0$, one spin remains unpaired on each rung. Thus, a odd-leg ladder can be always mapped into a single AFM spin chain with an effective exchange interaction J_{eff} related to the weak coupling J along the legs. Therefore, the behavior of these models follows the typical properties of the AFM spin chain, with no spin gap and a spin-spin correlation which slowly decays as a power law. Figure 2.12 (b) shows the spin-spin correlation for a $n = 3$ leg ladder system as a function of the distance between the spins. Moreover, a long-range RVB ground-state has also been found [44].

2.3.3 Experimental investigations

The development in the number and complexity of these theoretical studies has been driven by the appearance of magnetic materials with ladder structures, which became available during the 90's. For instance, a new homologous series $Sr_nCu_{n+1}O_{2n+1}$ were discovered in 1991 by Hiroi et al. [50], containing ladder structures with $n + 1$ legs each [51].

We focus the attention on two important compounds $SrCu_2O_3$ and $Sr_2Cu_3O_5$ which have, respectively, a two-leg and a three-leg ladder structure. These compounds have been the subject of important experimental investigations by Azuma et al. [10]. The magnetic susceptibility measurements are shown in Fig. 2.13. The results reveal a dramatic difference in the magnetic ground-state in the two and three leg ladder materials.

In the two plots the susceptibility is obtained by subtracting the Curie component due to impurities from the raw data. The magnetic susceptibility of the two-leg ladder $SrCu_2O_3$ shows a continuous decrease toward zero lowering the temperature (Figure 2.13 (a)). The behavior follows the theoretical studies of two-leg ladder system

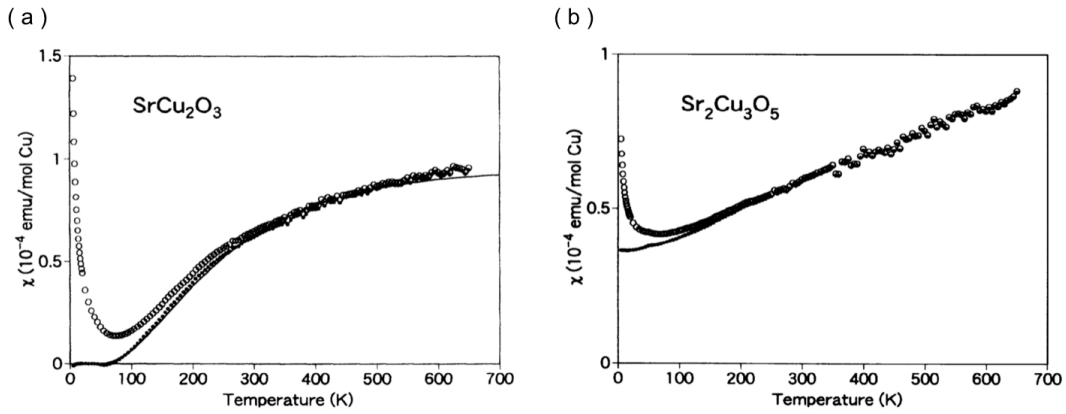

FIGURE 2.13: Figure taken from [10]. Temperature dependence of the magnetic susceptibility of $SrCu_2O_3$ (a) and $Sr_2Cu_3O_5$ (b). The open circles are the experimental raw data, while the data after subtraction of the Curie component are shown as closed circles. In (a) the solid line represents the calculated susceptibility assuming a spin gap of 420 K, using the equation 2.15 in the text.

[52], that gives the expression:

$$\chi(T) = \frac{\alpha}{\sqrt{T}} \exp(-\Delta/T), \tag{2.15}$$

where the parameter α depends on the dispersion of the excitation.

On the contrary, the magnetic susceptibility of the three-leg ladder $Sr_2Cu_3O_5$ (Figure 2.13 (b)) decreases continuously with decreasing temperature. In this case, this behavior is associated to a gapless spin excitation spectrum, as expected theoretically.

Muon spin relaxation (μSR) measurements also contributed to the analysis of the spin ladder cuprates $SrCu_2O_3$ and $Sr_2Cu_3O_5$ [53]. No magnetic order was observed in the two leg ladder, down to 20 mK and a magnetic order appear for the three leg ladder at T$\sim$ 52 K. These results are in agreement with theoretical expectation for the magnetic behaviour of even and odd ladder system.

Another interesting material is the "phone number" compound $Sr_{14}Cu_{24}O_{41}$ which appears as an excellent realization of a $S = 1/2$ two-leg ladder [54, 55]. Inelastic neutron scattering measurements revealed the presence of a spin gap and a dispersive triplet excitation, also confirmed by the magnetic susceptibility and further experimental investigations on the magnetic properties of this compound. In conclusion, $Sr_{14}Cu_{24}O_{41}$ has a "quasi" spin-liquid singlet ground-state separated by a spin-gap from the lowest triplet excitation, as theoretically predicted.

2.4 Frustrated systems

The concept of "frustration" in magnetic system has been introduced to describe the presence of competing interactions that cannot be simultaneously satisfied [3]. This competition gives rise to rich physics, high degeneracy of the ground-state and possibility of new phases of matter [56].

A simple example would be to consider a triangular Ising spin system, as illustrated in Fig. 2.14, with AFM interactions between the spins. The third spin can not be simultaneously anti-aligned to both of its nearest neighbours and the system is called

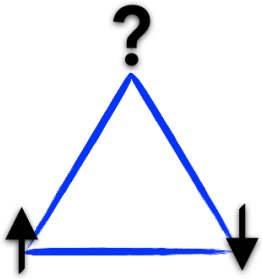

FIGURE 2.14: Illustration of frustrated triangular system. Geometric frustration may be observed in AFM interactions between the spins, where the third spin is unable to satisfy both AFM constraints in order to minimise the ground-state energy.

geometrically frustrated. In general, the frustrated spin system can not simultaneously minimizes all the interaction energies, finding a single state. As a consequence, there is no unique microscopic ground-state solution, but a degenerate ground-state manifold. Moreover, the long-range order is suppressed, even for low temperatures. This leads to the appearance of unusual and exotic properties in quantum magnetic systems.

Magnetic frustration is not only a theoretical phenomenon, but is actually present in different compounds. However, it should be noted that for real frustrated systems there may be small perturbations, such as anisotropy, magnetic dipolar interactions, structural distortion or quantum fluctuations, which could lift the degeneracy and stabilise the formation of a unique ground-state.

2.4.1 Frustrated spin chain

One of the early model studied is the frustrated AFM spin-1/2 chain, with nearest neighbour exchange interaction J and frustrating next-nearest neighbour interactions J_2. This model is shown schematically in Fig. 2.15 (a). It can equivalently be viewed as two chains with an intrachain coupling J_2 and a diagonal interchain coupling J (Figure 2.15 (b)) and is often called zigzag chain.

The Hamiltonian of this model is given by

$$H = J \sum_i \mathbf{S}_i \cdot \mathbf{S}_{i+1} + J_2 \sum_i \mathbf{S}_i \cdot \mathbf{S}_{i+2}. \tag{2.16}$$

Majumdar-Ghosh point The importance of this system lies in a particular point, $J_2/J = 1/2$, for which it was exaclty solved by Majumdar and Ghosh in 1969 [4, 5]. The Hamiltonian (2.16) in the Majumdar-Ghosh point takes a simple form:

$$H = J_{MG} \left(\sum_i \mathbf{S}_i \cdot \mathbf{S}_{i+1} + \frac{1}{2} \sum_i \mathbf{S}_i \cdot \mathbf{S}_{i+2} \right), \tag{2.17}$$

where $J_{MG} \equiv J_2 = J_1/2$. The ground-state is 2-fold degenerate, with neighboring pairs of spins in the diagonal interchain coupling forming singlet states, shown schematically in Figs. 2.15 (c) and (d). The two wavefunctions, direct product of

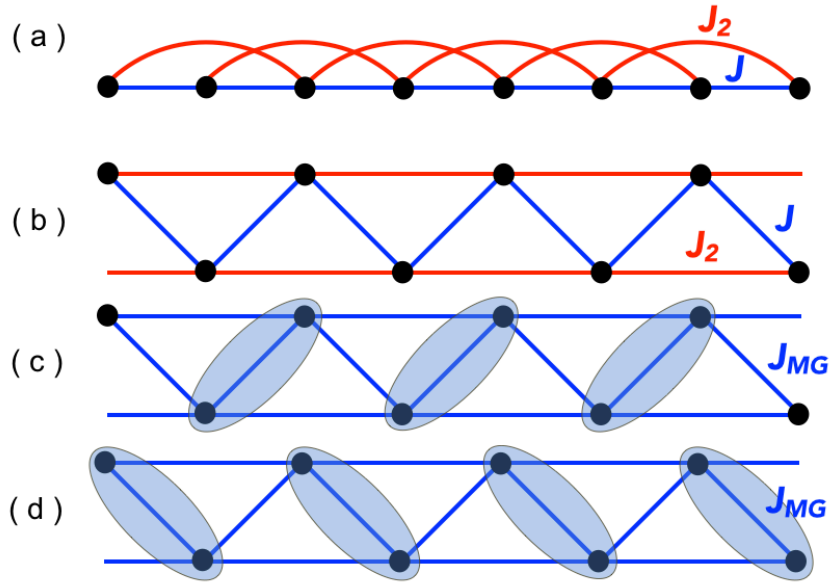

FIGURE 2.15: (a) Frustrated spin chain with NN interaction, in blue J, and NNN interaction, in red J_2. (b) Topological equivalent model, called zigzag chain, with intrachain interaction J_2 and diagonal interchain interaction J. (c) and (d) Representation of the two possible ground-states of the frustrated chain in the Majumdar-Ghosh point, from which $J_{MG} \equiv J_2 = J/2$. Ellipses represent the dimer singlet states.

these singlet states, are

$$\left|\psi_1^{MG}\right\rangle = \prod_i |S\rangle_{2i-1} |S\rangle_{2i} \tag{2.18}$$

$$\left|\psi_2^{MG}\right\rangle = \prod_i |S\rangle_{2i} |S\rangle_{2i+1} \tag{2.19}$$

where $|S\rangle_i = \frac{1}{\sqrt{2}} (|\uparrow_i\downarrow_{i+1}\rangle - |\downarrow_i\uparrow_{i+1}\rangle)$, with equal energy

$$E_{MG} = -J_{MG}\frac{N}{2}\frac{3}{4}, \tag{2.20}$$

because every dimer (of which there are $N/2$) contributes with an energy of $-J_{MG}3/4$ [57, 58].

Thus, the ground-state is constructed from uncorrelated spin dimers. Moreover, the lowest excitation is generated by promoting a dimer singlet into a triplet state with the emergence of a finite spin gap and an exponential decay of the spin-spin correlations with a minum at the MG point [6, 59].

Quantum phase transition The frustrated chain has been largely studied in function of the ratio J_2/J [57, 60, 61]. The system undergoes a quantum phase transition at the critical point $(J_2/J)_c = 0.2411$ between a gapless phase and a dimer phase.

For $J_2/J < 0.2411$, the system is described by a quasi AFM chain characterized by gapless excitation spectrum with a slow decay of the spin spin correlation function. On the other hand, in the dimer phase, $(J_2/J > 0.2411)$, there is doubly degenerate

gapped ground-state with an exponential decay of the spin spin correlation function and for all $J_2/J > r_I \approx 0.5$ this correlation function exhibits also an incommensurate behavior [62]. In this dimer phase we, obviously, find the exact MG point, $J_2/J = 1/2$.

2.4.2 The spin-1/2 linked-tetrahedra spin chain

Another interesting model is the spin-1/2 linked-tetrahedra spin chain, represented in Fig. 2.16. The Hamiltonian is given by:

$$H = J_\perp \sum_i \mathbf{S}_{1,i} \cdot \mathbf{S}_{2,i} + J \sum_{\{\alpha,\beta\}=\{1,2\}} \sum_i \mathbf{S}_{\alpha,i} \cdot \mathbf{S}_{\beta,i+1}, \tag{2.21}$$

where $J_\perp$ represents the vertical couplings along the rungs and J all the other couplings between the rungs. The spin operator is denoted by two indices. The first corresponds to the position of the site along the ladder i, whereas the second corresponds to the ladder leg $\{\alpha, \beta\} = \{1, 2\}$.

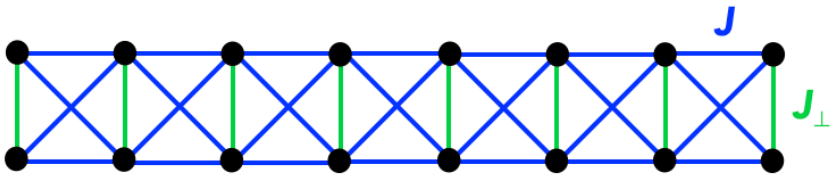

FIGURE 2.16: The spin-1/2 frustrated linked-tetrahedra spin chain with AFM interactions J and $J_\perp$.

The model has an exact solution (a direct product of singlets), as shown for the first time by Gelfand in 1991 [8]. In particular, he found two phases separated by a quantum phase transition at $r_c = J/J_\perp = 0.71$ [63]. The phase diagram is represented in Fig. 2.17. In the region $J/J_\perp < r_c$ the ground-state is exact and consists in a

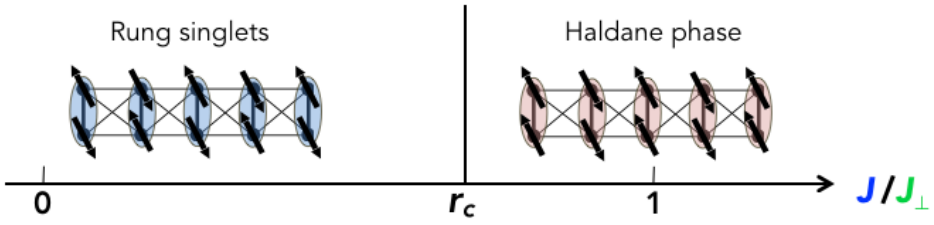

FIGURE 2.17: Ground-state phase diagram of the spin-1/2 linked-tetrahedra spin chain. The system has two phase, a rung singlet and a rung triplet, i.e. Haldane phase. The singlet state are illustrated by blue ellipsoids, the triplets with red ones.

product of singlets on each rungs:

$$|\psi_{GS}\rangle = \prod_i \frac{1}{\sqrt{2}} \left(|\uparrow_{i,1}\downarrow_{i,2}\rangle - |\downarrow_{i,1}\uparrow_{i,2}\rangle \right), \tag{2.22}$$

with energy per site $E_{GS} = -3J_\perp/8$. The elementary excitations consist of a single triplet pair with energy $J_\perp$ above the ground-state. These triplets are strictly localized

in the sense that the action of inter-rungs interactions on an isolated triplet gives zero, so that hopping is completely blocked on this particular geometry. Increasing the value of the ratio $r = J/J_\perp$, the lowest excited states change from isolated triplets to sets of four consecutive triplets.

The situation is completely different in the limit $r > r_c$, where the two spins on the rungs are coupled magnetically to form a spin-1 state. The model can be represented by a spin-1AFM chain that, in contrast to the case of half-integer value of the spin, has a disordered ground-state with a finite excitation gap. These results were first shown by Haldane in 1983 [64], and its ground-state is therefore know as Haldane state.

Generalization: Cross-coupled ladder We analyse the generalized spin-1/2 linked-tetrahedra spin chain in the case where the diagonal couplings between the rungs are different from the couplings along the legs, $J \neq J_\times$ [65, 66]. The system is represented in Fig. 2.18. The Hamiltonian of this system is given by:

$$H = J_\perp \sum_i \mathbf{S}_{1,i} \cdot \mathbf{S}_{2,i} + J \sum_{\alpha=1,2} \sum_i \mathbf{S}_{\alpha,i} \cdot \mathbf{S}_{\alpha,i+1} + J_\times \sum_{\alpha=1,2} \sum_i \mathbf{S}_{\alpha,i} \cdot \mathbf{S}_{\bar{\alpha},i+1}, \quad (2.23)$$

where the index $\bar{\alpha}$ represents the leg opposite to α and the three couplings are considered AFM, i.e. $J, J_\times, J_\perp > 0$.

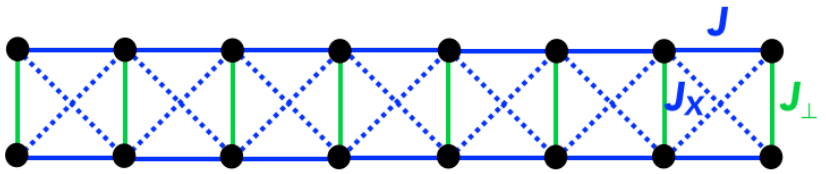

FIGURE 2.18: The cross-coupled ladder with three AFM interactions J (blue solid line), $J_\times$ (blue dashed line) and $J_\perp$ (green solid line).

Introducing the total-spin and spin-difference operators on rung i,

$$T_i = \mathbf{S}_{1,i} + \mathbf{S}_{2,i}, \qquad D_i = \mathbf{S}_{1,i} - \mathbf{S}_{2,i}, \quad (2.24)$$

the Hamiltonian (2.23) can be rewritten as

$$H = \sum_i \left(J_\perp \left(\frac{1}{2} T_i^2 - S(S+1) \right) + \frac{J + J_\times}{2} T_i \cdot T_{i+1} + \frac{J - J_\times}{2} D_i \cdot D_{i+1} \right). \quad (2.25)$$

For $J_\times = 0$, we obtain the unfrustrated spin ladder, that has a gapless phase obtained for two decoupled spin-1/2 AFM chain in the limit $J_\perp = 0$ and a gapped rung-singlet phase for all $J_\perp > 0$.

Another important case is the already studied spin-1/2 linked-tetrahedra spin chain in the fully frustrated case, $J_\times = J$. The third term in the Hamiltonian in eq. (2.25) is zero and the total rung spin operator becomes a good quantum number. As $S = 1/2$, T_i^2 can be 0 (rung singlet phase) or 1 (rung triplet phase). The transition between these two phase is a first order transition that takes place for the critical value $r_c = J/J_\perp = 0.71$.

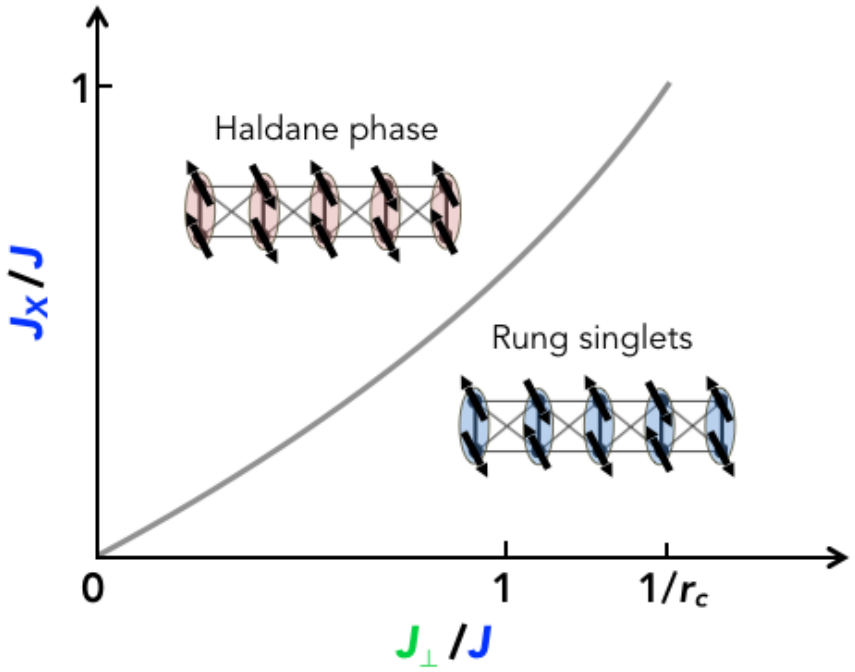

FIGURE 2.19: Ground-state phase diagram of the cross-coupled ladder. The system has two phase, a rung singlet and a Haldane phase, separeted by a first order phase transition (solid grey line). It should be noted that in the fully frustrated case, $J_\times/J = 1$, the first order phase transition takes place at $J_\perp/J = 1/r_c = 1.408$. Figure adapted from [67].

The transition from the rung singlet to the Haldane phase is still present for $J_\times \neq J$, and in the weakly coupled limit $J_\perp, J_\times \ll J$ the critical value was found at $J_\perp = 2J_\times$. The resulting ground-state phase diagram is shown in Fig. 2.19.

2.4.3 Frustrated two-leg spin ladder

The cross-coupled ladder phase diagram displays two different phases, a rung singlet and a Haldane phase, separated by a first order transition. However, it was later suggested that this picture might be incomplete and that an additional, intermediate dimerized phase could also occur [68, 69]. On the other hand, Vekua and Honecker [9] argued that this intermediate phase may be weak and unstable and, thus, difficult to be observed. In order to stabilize it, an additional next-nearest-neighbor exchange interaction, J_2, along the legs was taken into consideration. The geometry of the model is depicted in Fig. 2.20.
The Hamiltonian reads:

$$\begin{aligned} H =& J_\perp \sum_i \mathbf{S}_{1,i} \cdot \mathbf{S}_{2,i} + J \sum_{\alpha=1,2} \sum_i \mathbf{S}_{\alpha,i} \cdot \mathbf{S}_{\alpha,i+1} + J_\times \sum_{\alpha=1,2} \sum_i \mathbf{S}_{\alpha,i} \cdot \mathbf{S}_{\bar{\alpha},i+1} \\ &+ J_2 \sum_{\alpha=1,2} \sum_i \mathbf{S}_{\alpha,i} \cdot \mathbf{S}_{\alpha,i+2}. \end{aligned} \tag{2.26}$$

For $J_2 = 0$ we reobtain the Hamiltonian in eq. (2.23). The additional AFM coupling J_2 causes further frustration along the ladder, and hence, may give rise to some new phases.

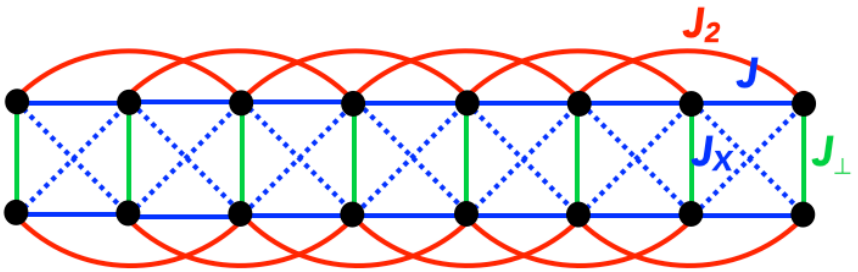

FIGURE 2.20: Structure of the frustrated spin ladder with next-nearest-neighbor interactions with the AFM couplings J (blue solid line), $J_\times$ (blue dashed line), $J_\perp$ (green solid line) and the added NNN coupling along the legs J_2.

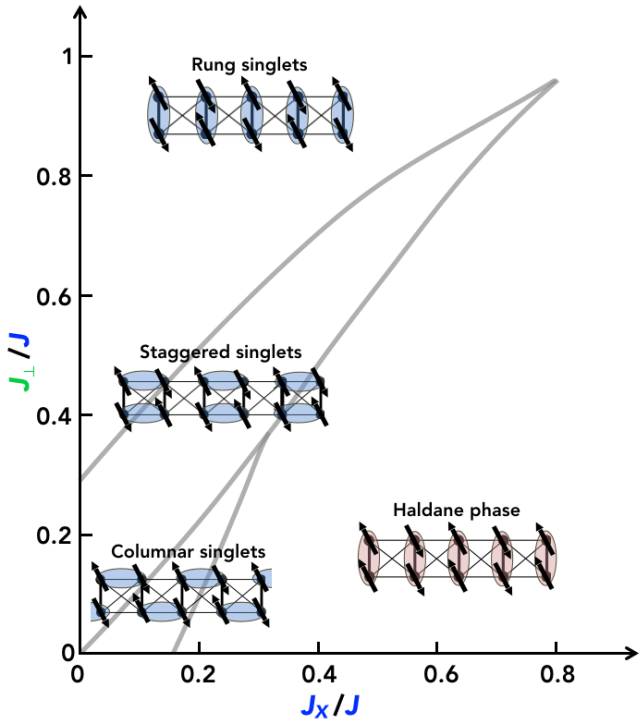

FIGURE 2.21: Ground-state phase diagram of the frustrated two-leg spin ladder in the $J_2 = J/2$ plane. Haldane, columnar dimer, and staggered dimer phases can be distinguished. Figure adapted from [9].

Between the rung singlet and the Haldane phase, already present for $J_2 = 0$, Vekua and Honecker predicted the appearance of two dimerized phases, a columnar and a staggered dimer phases. The complicated ground-state phase diagram for a sufficiently large $J_2 = J/2$ is illustrated in Fig. 2.21.

These results have been confirmed by subsequent theoretical works [70, 71, 72]. However, only a very limited number of material systems can be considered as true realizations of frustrated $S = 1/2$ two-leg spin ladders and thus, provide experimental evidence to be confronted to these theoretical predictions.

2.5 Real realizations

In this chapter we have reviewed some results obtained on the frustrated spin-1/2 two-leg ladders which has been the subject of intense theoretical interest during the last decades. Thanks to their low dimensionality, low spin and, furthermore, their frustrated character, they indeed fullfill all the requirements favouring the emergence of new and exotic phenomena.

Unfortunately, true material realizations of these models are very rare. A noticeable exception is the recent discovered $BiCu_2PO_6$, which appears as one of the very rare examples of $S = 1/2$ two-leg spin ladders where frustration arises from competing antiferromagnetic nearest and next-nearest neighbor interactions along the legs [12]. However, due to the presence of two crystallographically inequivalent copper sites, band structure calculations reveal that the NNN exchange interactions are alternated. The schematic structure of the compound is illustrated in Fig. 2.22, with NN exchange couplings along the legs J (solid blue line), couplings along the rungs $J_\perp$ (solid green line) and the alternated NNN exchange couplings along the legs J_2 (solid red line) and J_2' (dashed red line).

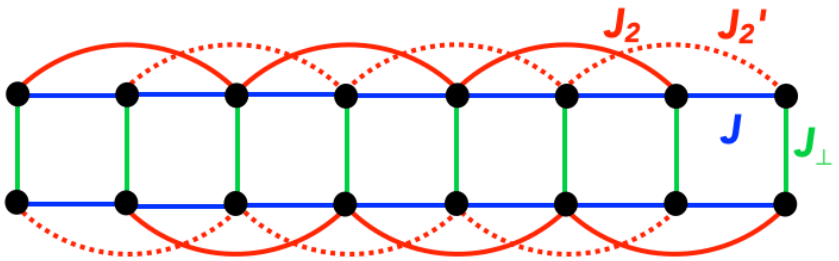

FIGURE 2.22: Schematic representation of the $S = 1/2$ two-leg spin ladder $BiCu_2PO_6$.

The rich physics emerging from this particular geometry has triggered many experimental investigations of the magnetic properties of this compound over the past decade. Notably, the magnetic susceptibility, heat capacity and magnetization measurements indicate the presence of a spin-gap behavior [12, 73], with an energy value around 30K. The frustration increases the spin gap and induce an incommensurate minimum in the dispersion of triplet quasiparticle excitations [74, 75], with a multi-quasiparticle continuum [76]. Moreover, a significant signature of the frustration is the presence of incommensurability also in the spin-spin correlation function, emphasised by neutron diffraction measurements [74].

However, the frustrated spin-1/2 two-leg ladder $BiCu_2PO_6$ is not a complete example of the spin ladder system illustrated in Fig. 2.20 as the diagonal exchange coupling $J_\times$ is not present.

2.5.1 The new spin ladder $Li_2Cu_2O(SO_4)_2$

In this thesis we will analyse the newly discovered compound $Li_2Cu_2O(SO_4)_2$, which appears as another partial realization of the frustrated spin-1/2 two-leg ladder system [13].

At high-temperature, this compound crystallizes in a tetragonal structure where $[Cu_2O(SO_4)_2]^{2-}$ chains running along the c axis are well separated by Li^+ ions, thus forming quasi-1D structural units (see Fig. 2.23 (a) and (b)). From magneto-structural

considerations, we can anticipate the presence of three principle interactions between the copper atoms, that are the NN interaction $J_\perp$ in green, the interaction between the copper in two different $[Cu_2O_6]$ platelets J in blue and the interaction mediated by the sulphate group SO_4 which creates a bridge from one copper to another in two different platelets pointing in the same direction (Fig. 2.23 (c)). This structure is topologically equivalent to a two-leg frustrated spin ladder, represented in Fig. 2.23 (d).

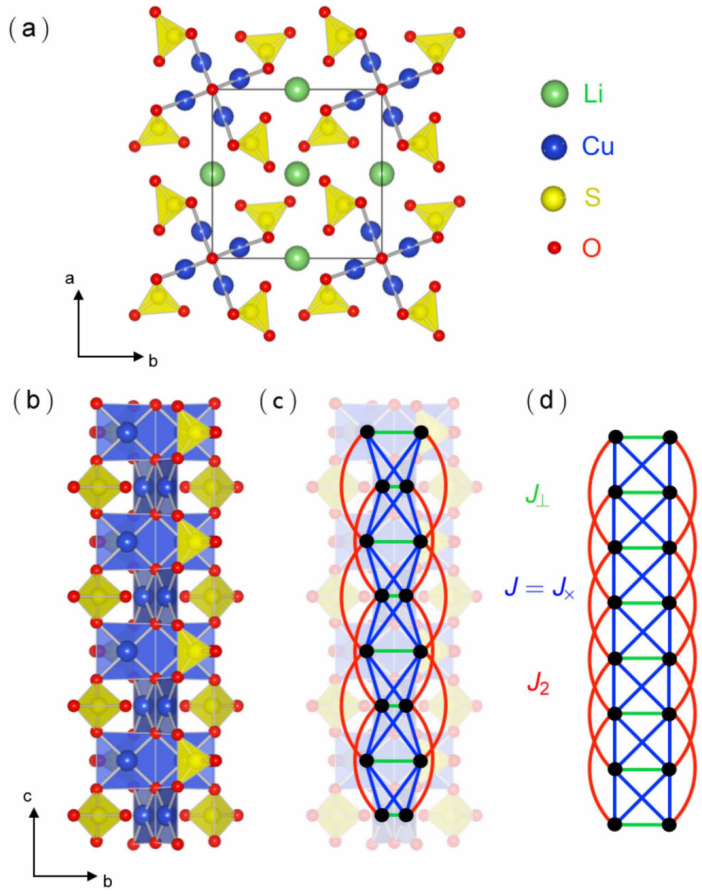

FIGURE 2.23: (a) Tetragonal crystal structure of $Li_2Cu_2O(SO_4)_2$ at room temperature. Cu are in blue, O in red, S in yellow, and Li in green. (b) Detail of the atomic structure of the chains running along the c axis. (c) Magnetic model deduced from the atomic structure, with the three dominant interactions along the chain: $J_\perp$ in green, $J = J_\times$ in blue, and J_2 in red. (d) Topologically equivalent frustrated two-leg spin ladder.

Therefore this compound appeared in 2015, at the beginning of this work, as a potential realization of the frustrated spin-1/2 two-leg ladder, with the presence of the additional diagonal exchange interaction $J_\times = J$. In the remainder of this thesis, we will investigate this interesting new material combining experimental and theoretical investigations.

Chapter 3

Theoretical Background

"Give me a place to stand,
a lever long enough and a fulcrum.
and I can move the Earth."

Archimedes

The electronic and magnetic properties of condensed matter systems are investigated in this thesis using first-principles calculations on electronic structures, based on density functional theory (DFT). In the first section of the present chapter, we briefly introduce and discuss the electronic structure calculation in the framework of DFT.

The atomic-level properties of solid materials are determined by first principle calculations and can then be employed in spin models which, in turn, can be studied by various rigorous numerical approaches like Quantum Monte Carlo (QMC) and Exact Diagonalization (ED) or by approximated schemes such as Perturbation Theory (PT) or Density Matrix Renormalization Group (DMRG). In the second section we will focus on the methods utilized in this work, which are respectively the Exact Diagonalization and the Perturbation Theory.

3.1 Electronic structure calculations

3.1.1 Density Functional Theory (DFT)

DFT is a theory of many-body quantum systems whose purpose is to evaluate electronic structure properties of atoms, molecules and solids by first principles. In the present section, we briefly introduce and discuss the relevant aspects underlying DFT. To have a thorough description of the theoretical and computational principles of this method, the reader is referred to any of the standard textbooks [77, 78, 79, 80, 81] and review articles [82, 83, 84].

The standard model of solid state physics is composed of electrons, nuclei, and the Coulomb interaction between them. In this thesis we will always assume the Born-Oppenheimer approximation to hold, hence the Hamiltonian operator H of a system containing N electrons and N_{at} atoms in its non-relativistic form reads:

$$\begin{aligned} H &= T + W + V_{\text{ext}} \\ &= -\frac{\hbar^2}{2m}\sum_{i=1}^{N}\nabla_i^2 + \frac{1}{2}\sum_{i=1}^{N}\sum_{i\neq j}\frac{e^2}{|\mathbf{r}_i-\mathbf{r}_j|} - \sum_{i=1}^{N}\sum_{n=1}^{N_{at}}\frac{Z_n e^2}{|\mathbf{r}_i-\mathbf{R}_n|}, \end{aligned} \tag{3.1}$$

where we denote as $\mathbf{r}_i$ and $\mathbf{R}_n$ the electronic and the nuclei positions respectively, $\hbar$ the Planck's constant, Z_n the atomic charges, m the electron mass and e its charge. T is the kinetic energy, W the electron-electron Coulomb interaction and V_{ext} the

interaction between electrons and nuclei, treated as a static external potential caused by the charges of the nuclei at fixed positions. The corresponding N-electron time-independent Schrödinguer equation is:

$$H\left|\Psi(\{\mathbf{x}_i\})\right\rangle = E\left|\Psi(\{\mathbf{x}_i\})\right\rangle, \quad i = 1, .., N \tag{3.2}$$

where E is the total electronic energy and $\Psi(\{\mathbf{x}_i\})$ is the many-body wavefunction, which depends on $\mathbf{x}_i = (\mathbf{r}_i, \sigma_i)$, with $\mathbf{r}_i$ the $3N$ spatial variables and σ_i the spins.

In practice, the Schrödinger equation cannot be solved exactly due to the huge number of degrees of freedom. In addition, the many-body wavefunction describes a fermionic system and, for the Pauli principle, it must be antisymmetric with respect to particle exchange. A powerful method to solve this problem is DFT, a method based on a completely different approach than the wavefunction based, used in condensed matter physics, such as Hartree-Fock or Quantum Monte Carlo methods. In DFT, the main physical object is the electron density $n(\mathbf{r})$, defined as:

$$n(\mathbf{r}) = N \int d\mathbf{r}_2 ... d\mathbf{r}_N \Psi^*(\mathbf{r}, \mathbf{r}_2, ..., \mathbf{r}_N)\Psi(\mathbf{r}, \mathbf{r}_2, ..., \mathbf{r}_N). \tag{3.3}$$

The basic idea of DFT is to describe the system in terms of the electronic density $n(\mathbf{r})$, instead of the many-body wavefunction, hence depending on just 3 variables (the three coordinates in the space) plus, in spin-polarized systems, the spin, and thus tractable numerically. This reformulation of the many-body problem was proven by Hohenberg and Kohn in 1964 [85] with two cardinal theorems, which establish the theoretical foundations of modern electronic structure calculations.

Hohenberg and Kohn (HK) theorems

- **Theorem 1**: The electron density $n(\mathbf{r})$ of a system of interacting particles in an external potential $V_{\text{ext}}(\mathbf{r})$ uniquely determines the external potential $V_{\text{ext}}(\mathbf{r})$, apart from a trivial additive constant.
  Corollary 1: The ground-state wavefunction is uniquely determined by the ground-state electron density $n(\mathbf{r})$, *i. e.* the wave function is a *functional* of the density, $\Psi_0 = \Psi_0(n_0(\mathbf{r}))$. Consequently, the expectation values of any ground-state observable O for the given system can be expressed as a unique functional of the ground-state density $n_0(\mathbf{r})$, $O[n_0] = \langle\Psi[n_0]|O|\Psi[n_0]\rangle$. The Hamiltonian and the ground-state energy are also determined uniquely in terms of the ground-state electron density. Thus, all the internal properties of the system are fully determined.

- **Theorem 2**: For any particular V_{ext}, there exists a universal functional of the electron density, $F[n(\mathbf{r})]$ such that the global minimum value of the functional of the total energy $E[n(\mathbf{r})]$ is the exact ground-state energy of the system, and the density that minimizes the functional is the exact ground-state density $n_0(\mathbf{r})$.
  The ground-state energy can be determined by minimizing the energy as a functional of the density, in the same way as, in standard quantum mechanics, one can determine the energy by minimizing the expectation value of the Hamiltonian with respect to the wavefunction (*variational principle*).
  Corollary 2: The exact ground-state energy and density are fully determined by the functional $E[n(\mathbf{r})]$, defined as:

$$E[n(\mathbf{r})] = F[n(\mathbf{r})] + V[n(\mathbf{r})], \tag{3.4}$$

where

$$\begin{aligned} F[n(\mathbf{r})] &= \min_{\Psi \to n} \langle \Psi | T + W | \Psi \rangle \,, \\ V[n(\mathbf{r})] &= \int V_{\text{ext}}(\mathbf{r}) n(\mathbf{r}) d\mathbf{r}. \end{aligned} \tag{3.5}$$

It should be noted that these theorems can be applied not only to condensed-matter systems of electrons with fixed nuclei, but also more generally to any system of interacting particles in an external potential. The main problem is that the expression of this functional remains unknown up to now and that DFT under this form is impossible to use. Note, however, that these theorems can also be generalized to magnetic systems, such as spin polarized system (spin density functional theory), or include temperature and time dependence known as time-dependent density functional theory (TD-DFT).

Kohn-Sham (KS) ansatz

The practical implementation of the HK theorems has been realized by Kohn and Sham in 1965 [86] and makes DFT calculations possible.

The main idea is to replace the original many-body system of interacting electrons in a static external potential V_{ext} by an auxiliary independent-particle system, which still has the same ground-state density $n_0(\mathbf{r})$, whereby the electrons move within an effective Kohn-Sham single-particle potential $V_{\text{KS}}(\mathbf{r})$ generated by the nuclei and the other electrons.

The major advantage of this picture is related to its non-interacting nature, that simplifies the many-body wavefunction into a single Slater determinant defined by single-particle occupied orbitals $\phi_i(\mathbf{r})$, $i = 1, .., N$:

$$\Psi(\mathbf{r}_1, \mathbf{r}_2, \ldots, \mathbf{r}_N) = \frac{1}{\sqrt{N!}} \begin{vmatrix} \phi_1(\mathbf{r}_1) & \phi_2(\mathbf{r}_1) & \cdots & \phi_N(\mathbf{r}_1) \\ \phi_1(\mathbf{r}_2) & \phi_2(\mathbf{r}_2) & \cdots & \phi_N(\mathbf{r}_2) \\ \vdots & \vdots & \ddots & \vdots \\ \phi_1(\mathbf{r}_N) & \phi_2(\mathbf{r}_N) & \cdots & \phi_N(\mathbf{r}_N) \end{vmatrix}, \tag{3.6}$$

and the ground-state electron density of the auxiliary system is equal to the density of the real system,

$$n(\mathbf{r}) \equiv n_{\text{KS}}(\mathbf{r}) = \sum_{i=1}^{N} |\phi_i(\mathbf{r})|^2, \tag{3.7}$$

and, for the conservation condition,

$$\int n(\mathbf{r}) d\mathbf{r} = N. \tag{3.8}$$

Following the HK theorems, the energy functional takes the form:

$$E_{\text{KS}}[n(\mathbf{r})] = F_{\text{KS}}[n(\mathbf{r})] + \int V_{\text{ext}}(\mathbf{r}) n(\mathbf{r}) d\mathbf{r}. \tag{3.9}$$

The universal functional $F_{\text{KS}}[n(\mathbf{r})]$:

$$F_{\text{KS}}[n(\mathbf{r})] = T_{\text{KS}}[n(\mathbf{r})] + E_{\text{Har}}[n(\mathbf{r})] + E_{\text{XC}}[n(\mathbf{r})], \tag{3.10}$$

where $T_{\mathrm{KS}}[n(\mathbf{r})]$ is the non-interacting particle kinetic energy, $E_{\mathrm{Har}}[n(\mathbf{r})]$ the classic electrostatic Hartree energy and $E_{\mathrm{XC}}[n(\mathbf{r})]$ is the exchange-correlation energy,

$$\begin{aligned} T_{\mathrm{KS}}[n(\mathbf{r})] &= -\frac{\hbar}{2m}\sum_{i=1}^{N}\langle\phi_i|\nabla^2|\phi_i\rangle = -\frac{\hbar}{2m}\sum_{i=1}^{N}\int\phi_i^*(\mathbf{r})\nabla^2\phi_i(\mathbf{r})d\mathbf{r}, \\ E_{\mathrm{Har}}[n(\mathbf{r})] &= \frac{e^2}{2}\int\int\frac{n(\mathbf{r})n(\mathbf{r}')}{|\mathbf{r}-\mathbf{r}'|}d\mathbf{r}d\mathbf{r}', \\ E_{\mathrm{XC}}[n(\mathbf{r})] &= T[n(\mathbf{r})] - T_{\mathrm{KS}}[n(\mathbf{r})] + W[n(\mathbf{r})] - E_{\mathrm{Har}}[n(\mathbf{r})], \end{aligned} \tag{3.11}$$

where $T[n(\mathbf{r})]$ and $W[n(\mathbf{r})]$ are the exact kinetic and electron-electron interaction energies respectively. Physically, $E_{\mathrm{XC}}[n(\mathbf{r})]$ can be interpreted as containing the contributions of detailed correlation and exchange to the system energy. However, the exact form of this term is still unknown, and different approximate expressions are usually employed, as we will discuss below.

The Kohn-Sham auxiliary system can be solved by minimizing the energy functional (3.9) with respect to the single-particle wavefunctions $\phi_i(\mathbf{r})$. Taking into account the normalization condition (3.8) and, consequently, the constraint $\int\delta n(\mathbf{r})d\mathbf{r} = 0$, the minimization of E_{KS} yields

$$\delta\left[F_{\mathrm{KS}}[n(\mathbf{r})] + \int V_{\mathrm{ext}}(\mathbf{r})n(\mathbf{r})d\mathbf{r} - \mu\left(\int n(\mathbf{r})d\mathbf{r} - N\right)\right] = 0, \tag{3.12}$$

where μ is the Lagrange multiplier associated with the normalization condition. The Euler-Lagrange equation associated with the minimization of this functional is then

$$\frac{\delta E_{\mathrm{KS}}[n(\mathbf{r})]}{\delta n(\mathbf{r})} = \frac{\delta F_{\mathrm{KS}}[n(\mathbf{r})]}{\delta n(\mathbf{r})} + V_{\mathrm{ext}}(\mathbf{r}) = \mu. \tag{3.13}$$

Solving this equation is strictly equivalent to solve the following set of single-particle equations usually called KS equations:

$$H_{\mathrm{KS}}\phi_i(\mathbf{r}) = \epsilon_i\phi_i(\mathbf{r}), \tag{3.14}$$

where the KS Hamiltonian H_{KS} is given by

$$\begin{aligned} H_{\mathrm{KS}} &= \frac{\delta F_{\mathrm{KS}}[n(\mathbf{r})]}{\delta n(\mathbf{r})} + V_{\mathrm{ext}}(\mathbf{r}) \\ &= -\frac{\hbar^2}{2m}\nabla_i^2 + V_{\mathrm{eff}}(\mathbf{r}) \end{aligned} \tag{3.15}$$

with the effective potential $V_{\mathrm{eff}}(\mathbf{r})$ equal to

$$V_{\mathrm{eff}}(\mathbf{r}) = V_{\mathrm{ext}}(\mathbf{r}) + V_{\mathrm{Har}}(\mathbf{r}) + V_{\mathrm{XC}}(\mathbf{r}). \tag{3.16}$$

$V_{\mathrm{Har}}(\mathbf{r})$ is the Hartree potential:

$$V_{\mathrm{Har}}(\mathbf{r}) = \frac{\delta E_{\mathrm{Har}}[n(\mathbf{r})]}{\delta n(\mathbf{r})} = e^2\int\frac{n(\mathbf{r}')}{|\mathbf{r}-\mathbf{r}'|}d\mathbf{r}', \tag{3.17}$$

$V_{\mathrm{XC}}(\mathbf{r})$ is the exchange-correlation potential:

$$V_{\mathrm{XC}}(\mathbf{r}) = \frac{\delta E_{\mathrm{XC}}[n(\mathbf{r})]}{\delta n(\mathbf{r})}. \tag{3.18}$$

As in the Hartree-Fock method, the KS equations (3.14) have to be solved self-consistently. We have to choose a set of initial orbitals, the initial guess, which determine the initial electron density. At each step the diagonalization of the KS Hamitonian yields to new set of orbitals which, in turn, define a new density. The DFT iterative procedure is repeated until convergence, i.e. when the difference in total density $\left|n^{in}(\mathbf{r}) - n^{out}(\mathbf{r})\right|$ is below a certain threshold.

The KS ansatz successfully maps the original interacting many-body system onto a fictitious independent single-particle system, described by the KS Hamiltonian (3.15). However, without an analytical expression for the exact exchange-correlation energy functional $E_{\mathrm{XC}}[n(\mathbf{r})]$, the KS equations still remain unsolvable. Therefore, several approximations to the exchange-correlation functional have been developed during the last decades. The simplest one is the Local Density Approximation (LDA), already introduced by Kohn and Sham [86].

Local Density Approximation (LDA) In LDA, the electron density around a particular point in space is the same as that for an homogeneous electron gas (HEG) of interacting electrons with the same *local* density. The total exchange-correlation functional $E_{\mathrm{XC}}^{\mathrm{LDA}}[n(\mathbf{r})]$ can than be written as

$$E_{\mathrm{XC}}^{\mathrm{LDA}}[n(\mathbf{r})] = \int n(\mathbf{r})\epsilon_{\mathrm{XC}}(n(\mathbf{r}))d\mathbf{r}, \tag{3.19}$$

where $\epsilon_{\mathrm{XC}}(n(\mathbf{r}))$ is the exchange-correlation energy density per particle, which can be decomposed into a sum of an exchange part $\epsilon_{\mathrm{X}}^{\mathrm{LDA}}$ and a correlation part $\epsilon_{\mathrm{C}}^{\mathrm{LDA}}$,

$$\epsilon_{\mathrm{XC}}^{\mathrm{LDA}} = \epsilon_{\mathrm{X}}^{\mathrm{LDA}} + \epsilon_{\mathrm{C}}^{\mathrm{LDA}}. \tag{3.20}$$

The exchange energy density is known exactly [87, 88], $\epsilon_{\mathrm{X}}^{\mathrm{LDA}} = -\frac{3}{4}\left(\frac{3}{\pi}\right)^{\frac{1}{3}} n^{\frac{1}{3}}(\mathbf{r})$. For $\epsilon_{\mathrm{C}}^{\mathrm{LDA}}$ there exist analytic expressions only in the high [89] and low density limits and QMC simulations have been performed in order to obtain accurate values for intermediate density values [90, 91, 92].

LDA could also be extended to spin polarized system (LSDA - Local Spin Density Approximation). In this case, we have

$$E_{\mathrm{XC}}^{\mathrm{LSDA}}[n_\uparrow(\mathbf{r}), n_\downarrow(\mathbf{r})] = \int n(\mathbf{r})\epsilon_{\mathrm{XC}}(n_\uparrow(\mathbf{r}), n_\downarrow(\mathbf{r}))d\mathbf{r}. \tag{3.21}$$

where $n_\uparrow(\mathbf{r})$ and $n_\downarrow(\mathbf{r})$ represent the density of electrons with spin up and spin down, respectively.

Despite its simplicity, the solutions of KS equations within LDA are surprisingly successful in systems where the electron density varies slowly [93]. The LDA reproduces the ground properties of many systems with high accuracy, such as ionization energy of atoms, bond lengths for molecules and the cohesive energy in realistic materials.

Generalized Gradient Approximation (GGA) LDA assumes local homogeneity of real electron densities. This led to the development of more sophisticated functionals. The most straightforward model is the Generalized Gradient Approximation (GGA) [94, 95]. It assumes that the exchange-correlation energy depends not only on

$n(\mathbf{r})$ but also on its gradient $\nabla n(\mathbf{r})$,

$$E_{\mathrm{XC}}^{\mathrm{GGA}}[n(\mathbf{r})] = \int n(\mathbf{r})\epsilon_{\mathrm{XC}}^{\mathrm{GGA}}\left[n(\mathbf{r}), \nabla n(\mathbf{r})\right] d\mathbf{r}. \tag{3.22}$$

Different GGA functionals can reproduce accurately physical properties of real materials. The most widely used for solid materials are Perdew-Wang functional (PW91) [96] and the Perdew-Burke-Ernzerhof functional (PBE) [97], employed throughout this thesis.

GGA generally gives better results than LDA in systems where the charge density varies rapidly. Nevertheless, both LDA and GGA functionals tend to over-delocalize electrons and thus do not work well for materials where the electrons are localized and strongly correlated. This leads to further approximations beyond LDA and GGA. A way to improve the accuracy of DFT within LDA or GGA is by including a parameter derived from the Hubbard model.

LDA (GGA) + U The basic idea behind DFT+U consists in implementing the DFT functionals (with LDA or GGA approximations) to describe strongly correlated electronic systems by adding the on-site Coulomb interaction between localized electrons (typically, localized d or f orbitals) through the introduction of an Hubbard-like term U [98, 99, 100, 101]. The parameter U can be extracted from *ab-initio* calculations, but is usually obtained semi-empirically.

The DFT+U total energy of a system can be written as follows:

$$E^{\mathrm{DFT\,+\,U}}[n(\mathbf{r})] = E^{\mathrm{DFT}}[n(\mathbf{r})] + E^{Hub}[\{n_m^{I,\sigma}\}] - E^{\mathrm{dc}}[\{n^{I,\sigma}\}], \tag{3.23}$$

where $n_m^{I,\sigma}$ are the set of orbital occupancies for the localized states, identified by the atomic index I, spin σ and state index m related to an angular moment L_z; $n^{I,\sigma} = \sum_m n_m^{I,\sigma}$. E^{DFT} represents the approximate DFT total energy functional, E^{Hub} is the penality term that contains the Coulomb electron-electron interactions as described in the Hubbard model [102, 103, 104]. E^{dc} is the so called the "double counting" term. Because we add explicitly the Hubbard term for the localized orbitals, it is necessary to the energy contribution of these orbitals already included in the DFT functional through the subtraction of the E^{dc} term.

Computing the Hubbard U from linear-response The Hubbard correction to the total energy can be written as

$$\begin{aligned} E^{U}[\{n_m^{I,\sigma}\}] &= E^{Hub}[\{n_m^{I,\sigma}\}] - E^{\mathrm{dc}}[\{n^{I,\sigma}\}] \\ &= \sum_{I,\sigma} \frac{U_I}{2} \mathrm{Tr}\left[\mathbf{n}^{I\sigma}(1-\mathbf{n}^{I,\sigma})\right] \\ &= \sum_{I,\sigma} \frac{U_I}{2} \sum_i \lambda_i^{I\sigma}(1-\lambda_i^{I,\sigma}) \end{aligned} \tag{3.24}$$

where $\mathbf{n}^{I,\sigma}$ are the occupation matrices of the relevant localized manifold. Using a representation where $\mathbf{n}^{I,\sigma}$ are diagonal (i.e. linear combination of atomic orbitals):

$$\mathbf{n}^{I,\sigma}\mathbf{v}_m^{I,\sigma} = \lambda_m^{I,\sigma}\mathbf{v}_m^{I,\sigma}, \tag{3.25}$$

with the localized orbitals $\mathbf{v}_m^{I,\sigma}$ and $0 \leq \lambda_m^{I,\sigma} \leq 1$ ($\lambda_m^{I,\sigma} = 0$ completely empty orbital and $\lambda_m^{I,\sigma} = 1$ fully occupied).

The Hubbard parameter U can be calculated by the linear-response approach proposed by Cococcioni et al. [105, 106]. This method is based on the difference between the exact total energy of localized states, able to exchange electrons with a reservoir (the rest of the crystal) and the DFT energy. The exact total energy has to be represented as a series of straight segments joining the energies corresponding to integer occupations. Instead, DFT total energy is quadratic on on-site occupations and it could be represented with a parabola (Figure 3.1). Therefore, the correction U has to correspond to the spurious curvature of the DFT-functional and it can be calculated taking the second derivative of the total energy with respect to the occupation number of the localized states.

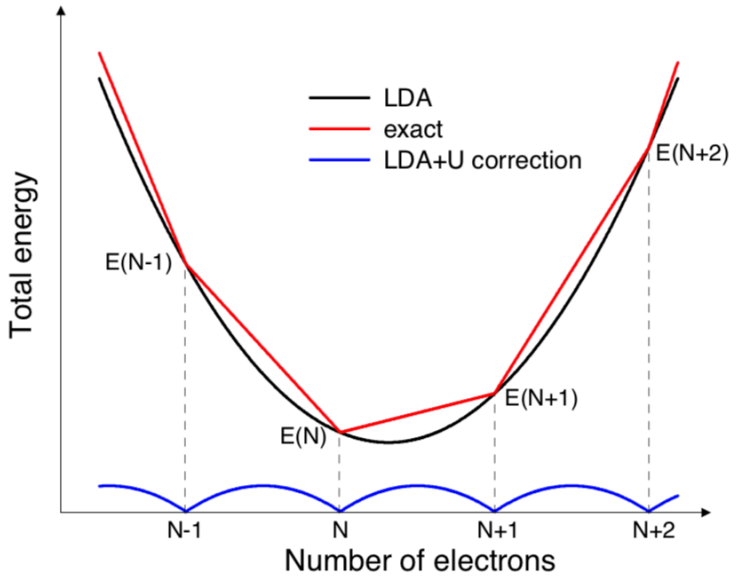

FIGURE 3.1: (From [105]) Total energy of a generic atomic system in contact with a reservoir in function of the number of electrons in its localized atomic orbitals. The black line represents the DFT energy, the red the exact limit, the blue the difference between the two.

The second derivative can not be directly obtained from DFT calculations based on plane-waves method (we have not localized basis set). In order to solve this problem, Cococcioni et al. used a Legendre transform:

$$E[\{n^I\}] = E(\alpha_I) - \alpha_I n_I, \tag{3.26}$$

where α^I is a perturbation which shifts the external potential that only acts on the localized orbitals of a Hubbard atom I. The second derivative of the energy can be calculated from the response matrix:

$$\chi_{IJ} = \frac{\partial^2 E^{\mathrm{DFT}}}{\partial\alpha_I\alpha_J} = \frac{\partial n_I}{\partial\alpha_J}. \tag{3.27}$$

The Hubbard U is thus the inverse of the response matrix $\dfrac{\partial^2 E}{\partial(n^I)^2} = -(\chi^{-1})_{II}$ where we have also to subtract a non-interacting contribution (due to re-hybridization of the electronic wave functions). In fact, during a DFT calculation a starting wavefunction is changed such that the energy is minimized and the subsequent electronic wave

functions are allowed to interact and hybridize (screening process). The parameter U is thus given by:

$$U = (\chi_0^{-1} - \chi_1^{-1})_{II}, \tag{3.28}$$

where χ_0 is the non-interacting response function calculated at first iteration and χ is the interacting one, evaluated after self-consistency.

3.1.2 DFT calculations on solids

DFT can be applied to extended systems, such as crystalline solids, where the number of atoms that has to be taken into account tend to infinite. A solution to this computationally "impossible" problem is to perform the DFT calculations by exploiting the periodicity of the crystal.

Bloch Theorem

The time independent Schrödinger equation for an electron in an infinite crystal structure is:

$$H\psi_i(\mathbf{r}) = \left[-\frac{\hbar^2}{2m}\nabla^2 + V(\mathbf{r})\right]\psi_i(\mathbf{r}) = E_i\psi_i(\mathbf{r}). \tag{3.29}$$

The potential $V(\mathbf{r})$ has the periodicity of the crystal, $V(\mathbf{r}+\mathbf{R}) = V(\mathbf{r})$, where $\mathbf{R} = n_1\mathbf{a}_1 + n_2\mathbf{a}_2 + n_3\mathbf{a}_3$ is a vector of the Bravais lattice $\mathcal{B}$, with $\{n_1, n_2, n_3\} \in \mathbb{Z}$ and $\{\mathbf{a}_1, \mathbf{a}_2, \mathbf{a}_3\}$ basis vectors of the unit cell. Therefore, the Hamiltonian is invariant under translation, $[H, \mathbf{T}_\mathbf{R}] = 0$, and the wavefunctions, solutions of the Schrödinger equation, are given by the Bloch Theorem [107]:

$$\psi_{n\mathbf{k}}(\mathbf{r}) = e^{i\mathbf{k}\cdot\mathbf{r}}u_{n\mathbf{k}}(\mathbf{r}). \tag{3.30}$$

These Bloch waves are plane waves enveloped with a function, $u_{n\mathbf{k}}$, where n is the band index and $\mathbf{k}$ is a wavevector in the first Brillouin zone (BZ). This function shares the periodicity of the crystal lattice, i.e. $u_{n\mathbf{k}}(\mathbf{r}+\mathbf{R}) = u_{n\mathbf{k}}(\mathbf{r})$. Within a band (i.e. for fixed n), $\psi_{n\mathbf{k}}$ varies continuously with $\mathbf{k}$, as does its energy, $E_n(\mathbf{k})$. The family of continuous function $E_n(\mathbf{k})$ represents the electronic band structure of the crystal as a graph of E vs $\mathbf{k}$ along one dimensional sections of $\mathbf{k}$-space (the $\mathbf{k}$-path).

Basis function : The Plane Wave formalism

The KS equations (3.14) have to be solved expanding the single-particle eigenstates $\psi_i(\mathbf{r})$ in an orthogonal basis set. A simple and very popular choice for this basis is to use orthogonal plane wave functions [108, 109]. The plane wave representation uses the Bloch waves $\psi_{n\mathbf{k}}(\mathbf{r})$ with the Fourier expansion of $u_{n\mathbf{k}}(\mathbf{r})$ over the reciprocal $\mathbf{G}$-vector, $\mathbf{G} = m_1\mathbf{b}_1 + m_2\mathbf{b}_2 + m_3\mathbf{b}_3$ ($m_i \in \mathbb{Z}$ and $\mathbf{b}_i$ basis vectors of the reciprocal unit cell). These Bloch waves can be expressed as:

$$\psi_{n\mathbf{k}}(\mathbf{r}) = \sum_{\mathbf{G}} c_{n\mathbf{k}}(\mathbf{G})e^{i(\mathbf{k}+\mathbf{G})\cdot\mathbf{r}}. \tag{3.31}$$

The Bloch waves basis set should in principle be infinite in size. In practice, these functions can be interpreted as having a kinetic energy equal to:

$$\frac{\hbar^2}{2m}\left|\mathbf{k}^2 + \mathbf{G}^2\right|. \tag{3.32}$$

It is common to truncate the sum over $\mathbf{G}$ in Eq. (3.31) to include only solutions with a kinetic energy lower than a predefined energy cutoff

$$\frac{\hbar^2}{2m}\left|\mathbf{k}^2+\mathbf{G}^2\right| \leq E_{cut} = \frac{\hbar^2}{2m}\mathbf{G}_{cut}^2. \tag{3.33}$$

The Bloch wave expression thus becomes:

$$\psi_{n\mathbf{k}}(\mathbf{r}) = \sum_{|\mathbf{k}+\mathbf{G}|<\mathbf{G}_{cut}} c_{n\mathbf{k}}(\mathbf{G}) e^{i(\mathbf{k}+\mathbf{G})\cdot\mathbf{r}}. \tag{3.34}$$

This means that the finite number of the basis set confined on the sphere of radius $\mathbf{G}_{cut}$ in the reciprocal space is normally sufficient to ensure the convergence towards numerically accurate results.

Pseudopotential The KS equations have been shown to be solvable within a plane waves basis set. Unfortunately the total electronic wavefunction, including both core and valence electrons, still remains prohibitively expensive. Indeed, the valence states rapidly oscillate in the core region to maintain their orthogonality with the core electrons, which are localised in the vicinity of the nucleus because of the strong Coulomb potential. The highly oscillatory nature of the valence electrons results in a large kinetic energy and consequently a high value of E_{cut} (defined in Eq. (3.33)) that corresponds to a large number of plane waves.

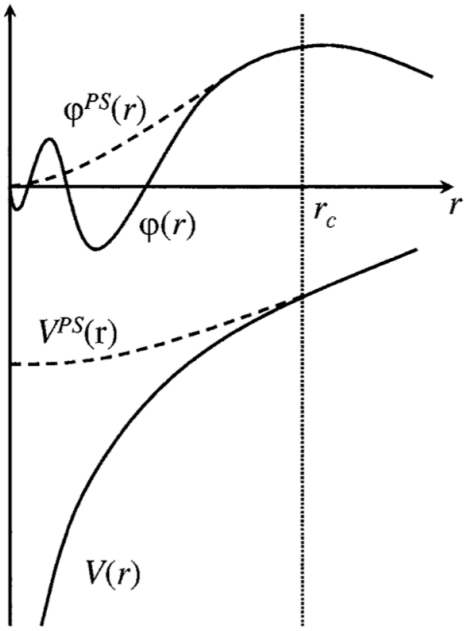

FIGURE 3.2: Schematic illustration of a pseudopotential taken from [110]. The full all-electronic wavefunction $\varphi(r)$ and the electronic potential $V(r)$ (dashed lines) are plotted against distance from the atomic nucleus r. The solid lines correspond to the pseudo wavefunction $\varphi^{PS}(r)$ and the respective pseudopotential $V^{PS}(r)$.

However, it is well known that core electrons do not contribute significantly to

the interatomic interactions in solids, and thus it would be desirable from a computational efficiency perspective not to treat them explicitly (*frozen core* approximation). The solution consists in introducing the pseudopotential approximation [111]. In this approximation, one removes the core electrons and the strong Coulomb potential and replaces them with an effective pseudopotential $V^{PS}(r)$, much weaker in the core region, which acts on a set of smooth pseudo wavefunctions $\varphi^{PS}(r)$ rather than on the true oscillating valence wavefunctions. The pseudopotential is constructed in such a way that in the core region there are no radial nodes for the pseudo wavefunction and outside a radius cutoff r_c the pseudo wavefunctions and pseudopotential are identical to the all electron wavefunction and potential (Figure 3.2).

3.1.3 Tight Binding Method and Wannier Functions

One of the standard methods for calculating band structure and single-particle Bloch states of a material is the tight binding (TB) method. This was originally proposed by Bloch in 1928 [107] and developed in the years thereafter [112]. It consists of expanding the Bloch waves in a linear combination of atomic orbitals located on the various atoms of the crystal. This approach is valid in systems where the electrons are localized, i.e. tightly-bound to the atom. Therefore, it is well adapted to the description of highly localized $3d$ and $4f$ electrons.

In this section, we describe the TB method using real, orthogonal wavefunctions (the Wannier functions) instead of atomic orbitals. We start by introducing these functions and then we derive simple analytical models in the "spirit" of the TB method.

Wannier Analysis

Wannier functions (WFs), first proposed by G. Wannier [113], provide an alternative representation of the electronic band structure, where electronic functions are expanded with orbitals localized in real space instead of Bloch states, defined in the reciprocal space. These localized Wannier functions are particularly useful for describing systems with isolated sets of narrow bands, such as strongly correlated systems.

Technically, Wannier functions form a complete set of orthogonal wavefunctions, constructed from the Fourier transform of the Bloch waves, providing a fully equivalent description of the electronic structure.

The Wannier functions localized at site $\mathbf{R}$ of the crystal are defined by the Fourier transform of the Bloch states $\psi_{n\mathbf{k}}(\mathbf{r})$:

$$\omega_{n\mathbf{R}}(\mathbf{r}) = \frac{V}{(2\pi)^3} \int_{\mathrm{BZ}} d\mathbf{k}\, e^{-i\mathbf{k}\cdot\mathbf{R}}\, \psi_{n\mathbf{k}}(\mathbf{r}) \tag{3.35}$$

or, switching to the Dirac notation

$$|\mathbf{R}n\rangle = \frac{V}{(2\pi)^3} \int_{\mathrm{BZ}} d\mathbf{k} e^{-i\mathbf{k}\cdot\mathbf{R}}\, |\psi_{n\mathbf{k}}\rangle\,. \tag{3.36}$$

It is easily shown that $|\mathbf{R}n\rangle$ are normalized and form an orthogonal set, $\langle \mathbf{R}'m | \mathbf{R}n \rangle = \delta_{\mathbf{R},\mathbf{R}'}\delta_{m,n}$.

The Bloch functions and the Wannier functions are related by Fourier transform:

$$|\psi_{n\mathbf{k}}\rangle = \sum_{\mathbf{R}} e^{i\mathbf{k}\mathbf{R}}\, |\mathbf{R}n\rangle\,. \tag{3.37}$$

These two orthogonal sets could thus give an equivalent description of the electronic structure. However, the WFs are not unique because of the "gauge invariance" related to the Bloch functions:

$$|\psi_{n\mathbf{k}}\rangle \quad \rightarrow \quad \left|\widetilde{\psi}_{n\mathbf{k}}\right\rangle = e^{i\varphi_n(\mathbf{k})}\,|\psi_{n\mathbf{k}}\rangle\,. \tag{3.38}$$

The arbitrariness of the phase factor $\varphi_n(\mathbf{k})$ makes the Wannier functions non-unique, without changing the physical description of the system. Moreover, we are implicitly working with the condition that a single isolated Bloch band n corresponds to one Wannier orbital. In the more general case, we have to consider a manifold of L bands, which includes degeneracies and crossing among the bands. Therefore, the "gauge invariance" has to be generalized by

$$\left|\widetilde{\psi}_{n\mathbf{k}}\right\rangle = \sum_{m=1}^{L} U_{mn}^{(\mathbf{k})}\,|\psi_{n\mathbf{k}}\rangle\,, \tag{3.39}$$

where $U_{mn}^{(\mathbf{k})}$ is an unitary matrix. The subsequent expression for the WFs becomes

$$|\mathbf{R}n\rangle = \frac{V}{(2\pi)^3}\int_{\mathrm{BZ}} d\mathbf{k} e^{-i\mathbf{k}\cdot\mathbf{R}} U_{mn}^{(\mathbf{k})}\,|\psi_{n\mathbf{k}}\rangle\,. \tag{3.40}$$

Again, in the procedure, the choice of $U_{mn}^{(\mathbf{k})}$ is not unique. Many localization procedures were introduced to remove this ambiguity in the gauge choice. A widely used approach has been proposed by Marzari and Vanderbilt [114] and the resulting WFs are the "Maximally Localized Wannier Functions" (MLWFs).

Maximally Localized Wannier Functions Marzari and Vanderbilt solved the problem of constructing maximally localized WFs by introducing a well-defined *localization criterion*. They constructed the localization functional

$$\begin{aligned}\Omega &= \sum_n \left[\,\langle \mathbf{0}n|r^2|\mathbf{0}n\rangle - \langle \mathbf{0}n|r|\mathbf{0}n\rangle^2\right] \\ &= \sum_n \left[\left\langle \mathbf{r}^2\right\rangle_n - \langle \mathbf{r}\rangle_n^2\right].\end{aligned} \tag{3.41}$$

It measures the spread, i.e. the delocalization of the Wannier functions. The goal is to find an unitary transformation $U_{mn}^{(\mathbf{k})}$ that minimizes the functional Ω in order to produce a set of MLWFs. This is a post-processing step which was carried out with the code WANNIER90 [115]. First we have to determine the Bloch states $|\psi_{n\mathbf{k}}\rangle$ within a conventional self-consistent DFT electronic-structure calculation. The unitary matrix is then iteratively refined by minimizating the localization functional and the resulting $U_{mn}^{(\mathbf{k})}$ is used to construct explicitly the MLWFs.

"Tight-binding" method

In this work, we also carried out simple analytical calculations to describe the electronic structure of $LiCu_2O(SO_4)_2$ in the spirit of the tight-binding method. We therefore assumed that a set of real, orthogonal orbitals localized on the magnetic ions exist, which could, for example, be considered as similar to the MLWF functions just described above. These localized functions give us a complete set of orthonormal

wavefunctions, $|\mathbf{R}_{i,n}\rangle$, localized in real space on the lattice site i of the unit cell of the Bravais lattice located at $\mathbf{R}$.

Let us now define the basis functions with which we are going to work. These functions, $\varphi^{\mathbf{k}}_{i,n}(\mathbf{r})$, are called "Bloch sums" and are related to the localized functions $|\mathbf{R}_{i,n}\rangle$ by the Fourier transform:

$$|\mathbf{R}_{i,n}\rangle = \sum_{\mathbf{k}} e^{-i\mathbf{k}\cdot\mathbf{R}} \left|\varphi^{\mathbf{k}}_{i,n}\right\rangle . \tag{3.42}$$

Now, we can express the Bloch wave as a linear combination of these Bloch sums

$$|\psi_{\mathbf{k}}\rangle = \sum_{i,n} b_{i,n}(\mathbf{k}) \left|\varphi^{\mathbf{k}}_{i,n}\right\rangle , \tag{3.43}$$

where $b_{i,n}(\mathbf{k})$ are coefficients depending on $\mathbf{k}$. We can find the dispersion relation by solving the Schrödinger equation

$$H\,|\psi_{\mathbf{k}}\rangle = E(\mathbf{k})\,|\psi_{\mathbf{k}}\rangle . \tag{3.44}$$

Expanding $|\psi_{\mathbf{k}}\rangle$ in the basis $\left|\varphi^{\mathbf{k}}_{i,n}\right\rangle$ and multiplying by $\left\langle\varphi^{\mathbf{k}'}_{j,m}\right|$, we obtain

$$\sum_{i,n} H^{\mathbf{k},\mathbf{k}'}_{(i,n),(j,m)} b_{i,n}(\mathbf{k}) = E(\mathbf{k}) \sum_{i,n} S^{\mathbf{k},\mathbf{k}'}_{(i,n),(j,m)} b_{i,n}(\mathbf{k}), \tag{3.45}$$

where $H^{\mathbf{k},\mathbf{k}'}_{(i,n),(j,m)} = \left\langle\varphi^{\mathbf{k}}_{i,n}\right|H\left|\varphi^{\mathbf{k}'}_{j,m}\right\rangle$ and $S^{\mathbf{k},\mathbf{k}'}_{(i,n),(j,m)} = \left\langle\varphi^{\mathbf{k}}_{i,n}\middle|\varphi^{\mathbf{k}'}_{j,m}\right\rangle$ are the Hamiltonian and the overlap matrix. Because of the orthogonality of the localized states, the overlap matrix becomes:

$$S^{\mathbf{k},\mathbf{k}'}_{(i,n),(j,m)} = \delta_{kk'}\delta_{ij}\delta_{nm}. \tag{3.46}$$

Therefore, the calculation of the the expectation values of the energies becomes strictly equivalent to solve a matrix eigenvalue problem when the matrix elements of the Hamiltonian in the basis of the Bloch functions are defined as:

$$H^{\mathbf{k},\mathbf{k}'}_{(i,n),(j,m)} = \sum_{\mathbf{R},\mathbf{R}'} e^{i(\mathbf{k}'\cdot\mathbf{R}'-\mathbf{k}\cdot\mathbf{R})} \left\langle\mathbf{R}_{n,i}\middle|H\middle|\mathbf{R}'_{m,j}\right\rangle . \tag{3.47}$$

$\left\langle\mathbf{R}_{n,i}\middle|H\middle|\mathbf{R}'_{m,j}\right\rangle$ is the amplitude that an electron in the localized orbital $|\mathbf{R}_{n,i}\rangle$ at site $(\mathbf{R}+\mathbf{r}_i)$ will hop to the localized orbital $\left|\mathbf{R}'_{m,j}\right\rangle$ at $(\mathbf{R}'+\mathbf{r}_j)$ under the action of the Hamiltonian H, and is usually denoted as a hopping parameter

$$\left\langle\mathbf{R}_{n,i}\middle|H\middle|\mathbf{R}'_{m,j}\right\rangle = t^{(n,m)}_{i\mathbf{R},j\mathbf{R}'} \quad \text{if} \quad \{i\mathbf{R}\} \neq \{j\mathbf{R}'\} \tag{3.48}$$

and for $\{i\mathbf{R}\} = \{j\mathbf{R}'\}$ we have the one-site term

$$\langle\mathbf{R}_{n,i}|H|\mathbf{R}_{m,i}\rangle = \delta_{m,n}\epsilon_{i,n}. \tag{3.49}$$

The matrix Hamiltonian $H^{\mathbf{k},\mathbf{k}'}_{(i,n),(j,m)}$ becomes

$$H^{\mathbf{k},\mathbf{k}'}_{(i,n),(j,m)} = \delta(\mathbf{k}'-\mathbf{k}) \left(\delta_{ij}\delta_{mn}\epsilon_{i,n} + \sum_{\boldsymbol{\delta}\neq 0} e^{i\mathbf{k}\boldsymbol{\delta}} t^{(m,n)}_{ij\boldsymbol{\delta}} \right) , \tag{3.50}$$

where $\boldsymbol{\delta} = \mathbf{R}-\mathbf{R}'$. We have obtained the general expression of a matrix Hamiltonian

in the tight-binding approximation. The advantage of this "tight binding" method is the extraction of the parameters $\epsilon_{i,n}$ and t_{ij} which can be used to "fit" the electronic band structures, obtained form DFT calculations, using minimal analytical models.

3.1.4 Estimation of magnetic couplings in DFT

The magnetic exchange interaction arises nonclassically when one takes into account the spins ($\uparrow$ or $\downarrow$) of two interacting electrons. We analyze the simplest model describing the magnetism of a spin-1/2 system, given by the Heisenberg Hamiltonian

$$H = H_0 + \sum_{ij} J_{ij} \mathbf{S}_i \cdot \mathbf{S}_j, \tag{3.51}$$

where H_0 is the spin-independent part of the Hamiltonian, $\mathbf{S}_i$ and $\mathbf{S}_j$ represent the spin-1/2 operators localized on site i and j respectively and J_{ij} are the isotopic magnetic couplings between the spins. J_{ij} result in the solid state from different mechanisms (direct exchange, superexchange, ..), and can be written generally as the sum of a ferromagnetic (FM) and antiferromagnetic (AFM) components,

$$J_{ij} = J_{ij}^{\mathrm{AFM}} + J_{ij}^{\mathrm{FM}}. \tag{3.52}$$

As soon as the coupling constants are known, the magnetic properties of the system can be determined. The objective of this section is to describe how to evaluate these couplings starting from DFT calculations.

Mapping the Hubbard model onto the Heisenberg Hamiltonian

To determine the values of the exchange couplings, J_{ij}, a first approach exploits the fact that in the strong coupling limit at half-filling a Hubbard model can be mapped onto a Heisenberg Hamiltonian.

Let us assume a system of interacting electrons described in terms of the so-called Hubbard model, with Hamiltonian

$$\widehat{H} = {\sum_{ij\sigma}}' t_{ij} \hat{c}_{i\sigma}^{\dagger} \hat{c}_{j\sigma} + U \sum_i \hat{\mathbf{n}}_{i\uparrow} \hat{\mathbf{n}}_{i\downarrow}, \tag{3.53}$$

where the prime over the first sum excludes the terms $i = j$. The operators $\hat{c}_{i\sigma}^{\dagger}$ and $\hat{c}_{i\sigma}$ create and destroy electrons with spin σ (up or down) at lattice sites $i \in \Lambda$. The number operator $\hat{\mathbf{n}}_{i\sigma} = \hat{c}_{i\sigma}^{\dagger} \hat{c}_{i\sigma}$ counts the number of electrons of spin σ on site i. The Hubbard model describes the competition between the kinetic energy, represented by the hopping term t_{ij}, and the interaction energy of electrons on a lattice, represented by on-site Coulomb repulsion U. In the strong coupling limit $U \gg t$ at half-filling, with exactly one electron on each site, the kinetic energy term ($\propto t$) is treated as a perturbation. If two electrons at site i and j have opposite spins, an electron can hop from the site i to the site j (Figure 3.3 (a)). Otherwise, if the two spins are parallel such hopping is forbidden, as the state with two electrons on the same site with the same spin would violate the Pauli principle (Figure 3.3 (b)). Therefore in this situation an effective interaction is generated which favors neighboring electrons to have opposite spin, i.e. antiparallel orientation.

It can be shown (see Appendix A)) that the resulting effective model can be described by an antiferromagnetic ($J > 0$) Heisenberg Hamiltonian (3.51). In particular, this mapping provides a direct link between the hopping parameters t_{ij} and the AFM

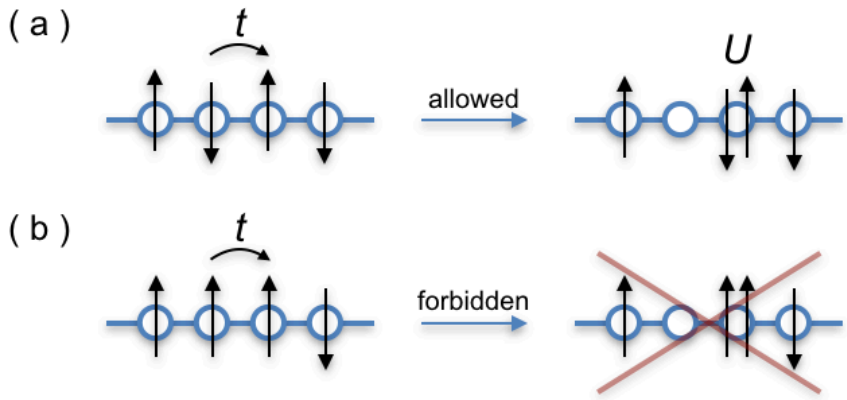

FIGURE 3.3: Schematic illustration of the hopping process in an Hubbard model in the strong coupling limit at half-filling. In (a) and (b) it is shown the allowed (and forbidden) transition between two antiparallel (and parallel) spins.

component of the magnetic couplings:

$$J_{ij}^{\mathrm{AFM}} = \frac{4t_{ij}^2}{U}. \tag{3.54}$$

In this work, we used the hopping parameters t_{ij} extracted from a MLWF analysis or a straightforward tight-binding fit described earlier.

The ratios of t^2/U thus give us directly the ratios of the antiferromagnetic components of the magnetic couplings. A more sophisticated approach is thus necessary to determine numerical values of the exchange constants J_{ij}, the Broken Symmetry formalism.

Broken Symmetry Formalism

The Broken Symmetry formalism is a method first developed by Noodleman in 1981 [116, 117]. In our work, we slightly modified the original method, in order to estimated the numerical values of the exchange couplings, starting from the mapping of total energies differences corresponding to various collinear spin arrangement within a supercell onto a Heisenberg Hamiltonian (3.51).

We start introducing the model for a simple dimer system, composed by a single spin-1/2 pair with spin momenta $\mathbf{S}_1$ and $\mathbf{S}_2$. The Heisenberg Hamiltonian becomes:

$$H_d = J\mathbf{S}_1 \cdot \mathbf{S}_2. \tag{3.55}$$

The eigenfunctions of the Heisenberg Hamiltonian (3.55) are the singlet state

$$|s\rangle = |0,0\rangle = \frac{1}{\sqrt{2}}\left(|\uparrow\downarrow\rangle - |\downarrow\uparrow\rangle\right), \tag{3.56}$$

and the triplet

$$|t\rangle = \begin{cases} |1,1\rangle & = |\uparrow\uparrow\rangle \\ |1,0\rangle & = \frac{1}{\sqrt{2}}\left(|\uparrow\downarrow\rangle + |\downarrow\uparrow\rangle\right) \\ |1,-1\rangle & = |\downarrow\downarrow\rangle \end{cases} \tag{3.57}$$

The corresponding expectation values of these two states are directly related to the exchange coupling J:

$$\begin{aligned} E_s &= \langle s|H_d|s\rangle = -\frac{3J}{4}, \\ E_t &= \langle t|H_d|t\rangle = \frac{J}{4}. \end{aligned} \tag{3.58}$$

The value of J turns out to be equal to the difference in energies between these two states:

$$J = E_T - E_S. \tag{3.59}$$

However, in the Broken Symmetry approach, we use states that can be written as a single Slater determinant and are in general not eigenstates of the Heisenberg Hamiltonian. In order to evaluate the coupling from the difference in energies, we choose the spin states corresponding to the high symmetry wave function, which corresponds to the triplet state $|HS\rangle \equiv |\uparrow\uparrow\rangle$ (energy $E_{HS} = J/4$), and the broken (lower) symmetry one, i.e. the Néel like antiferromagnetic state $|BS\rangle \equiv |\uparrow\downarrow\rangle$. The $|HS\rangle$ state is the only pure state that can be described by a single determinant wave function. The $|BS\rangle$ state is an eigenfunction of S_z, but not of the total spin operator S^2, i.e. it is not an eigenstate of the Hamiltonian (3.55). However, it can be written as a linear combination of its eigenstates. Accordingly, we have

$$|BS\rangle \equiv |\uparrow\downarrow\rangle = \frac{1}{2}\Big(|1,0\rangle + |0,0\rangle\Big). \tag{3.60}$$

Consequently, we can calculate the expectation value of the contaminated antiferromagnetic state $|BS\rangle$ in terms of the corresponding quantities of the eigenstates, obtaining $E_{BS} = -J/4$. Now we can calculate the value of exchange constant as:

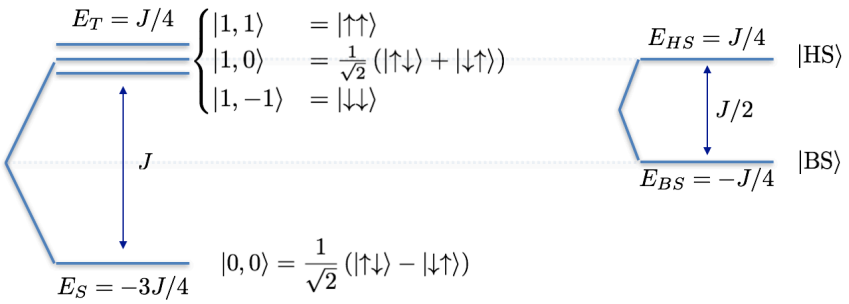

FIGURE 3.4: Schematic illustration of the energies differences between the singlet and the triplet states and the BS and HS states.

$$J = 2(E_{HS} - E_{BS}). \tag{3.61}$$

The Broken Symmetry formalism is easily generalized for a spin-system described by the Heisenberg Hamiltonian in Eq. (3.51). The calculation of the magnetic couplings is carried out by mapping total energies corresponding to various collinear spin arrangements within a supercell onto an Heisenberg Hamiltonian[118, 119, 120].

We take a state $|\alpha\rangle$ obtained by preparing an initial state with a particular collinear spin arrangement in the supercell and performing a self-consistent DFT calculation until convergence. The expectation value of the Hamiltonian (3.51) can be simply

written under the form of an Ising Hamiltonian [121]:

$$\epsilon_\alpha^{\mathrm{DFT}} = \langle\alpha|H|\alpha\rangle = \epsilon_0 + \sum_{ij} \frac{J_{ij}}{4}\sigma_i\sigma_j, \tag{3.62}$$

where $\sigma_i = \pm 1$ and $\epsilon_0 = \langle\alpha|H_0|\alpha\rangle$. Numerical total energies obtained from density functional theory calculations for a set of distinct spin configurations can thus be analyzed in terms of these Ising expressions involving the unknown magnetic couplings. The total energies can thus be expressed in terms of these couplings:

$$\epsilon_\alpha^{\mathrm{DFT}} = \epsilon_0 + \sum_k a_{\alpha k} J_k, \tag{3.63}$$

where $a_{\alpha k}$ are coefficients dependent on the configuration. In order to calculate the magnetic couplings J_k, we analyze all the "inequivalent" spin configuration (with respective degeneracies g_α) out of the 2^N, if N is the number of spins-1/2 in the supercell. By inequivalent, we mean with a different Ising expression and different total magnetization.

Finally, a numerical evaluation of the magnetic couplings can be obtained from a least-squares minimization of the difference between the DFT and Ising relative energies in a sum over all the inequivalent spin configurations, i.e. by minimization of

$$F = \sum_\alpha g_\alpha \left(\epsilon_\alpha^{\mathrm{DFT}} - \epsilon_0 - \sum_k a_{\alpha k} J_k\right)^2. \tag{3.64}$$

3.2 Methods to solve the spin Hamiltonian

3.2.1 Exact Diagonalization of quantum spin model

Exact Diagonalization (ED) plays a very important role in understanding the ground and excited states properties of quantum spin systems. In numerically exact diagonalization method we extract the eigenenergies and the eigenstates of the Hamiltonian that describes the physics of the system of interest, and, starting form that, any static or dynamic quantity con be computed. Thus the ED could, in principle, provide a complete knowledge of the system. In practice, however, such method is limited to finite quantum systems. The idea is to construct the $N \times N$ matrix Hamiltonian in a finite Hilbert space of dimension N and to calculate the eigenpairs (eigenvalues and eigenvectors) by diagonalizing the matrix. Since the Hilbert space of quantum system grows exponentially with the system size, a computational job is numerically impractical for large N.

In the following, we will mainly focus on 1D quantum spin-1/2 systems, objects of this thesis. In particular, in this section we will deal with the exact diagonalization of the 1D Heisenberg model, which describes the dynamic of a quantum spin-1/2 lattices (chains or ladders). The Hamiltonian is:

$$H = \sum_{\langle ij\rangle} J_{ij}\mathbf{S}_i\mathbf{S}_j, \tag{3.65}$$

where J_{ij} represent the magnetic couplings. For a finite system of N spins we see that this Hamiltonian becomes a matrix of dimension $2^N \times 2^N$. Thus for a spin chain with a small number of N, for example $N = 20$, we obtain a 1048576×1048576 matrix

that have to be diagonalized. In order to solve this problem, we will use the block diagonalization method, which exploits certain symmetries of the Hamiltonian.

Hilbert space and orthonormal basis for spin systems

The spin operators $\mathbf{S}_i$ obey the Lie algebra of the $SU(2)$ group

$$[S_i^\alpha, S_j^\beta] = \delta_{ij}\epsilon^{\alpha\beta\gamma}S_i^\gamma, \qquad \text{per} \quad i \neq j, \tag{3.66}$$

where $\alpha, \beta, \gamma = x, y, z$ and $\epsilon^{\alpha\beta\gamma}$ is the completely antisymmetric tensor.

In general, the irreducible representation of the $SU(2)$ group is given by $n \times n$ square matrix S^α, with $n = 2s + 1$. Consequently, a particle with spin s lives in an Hilbert space isomorphic to $\mathbb{C}^{2s+1}$ and its orthonormal basis is given by the eigenstate of the matrix S^α.

In our case, $s = \frac{1}{2}$. We define the spin states $|\uparrow\rangle = \binom{1}{0}$ and $|\downarrow\rangle = \binom{0}{1}$. We choose the 2×2 irreducible representation defined by the Pauli matrices

$$\mathbf{S}_j = \frac{1}{2}\boldsymbol{\sigma}_j, \tag{3.67}$$

where

$$\sigma_j^x = \begin{pmatrix} 0 & 1 \\ 1 & 0 \end{pmatrix}, \qquad \sigma_j^y = \begin{pmatrix} 0 & -i \\ i & 0 \end{pmatrix}, \qquad \sigma_j^z = \begin{pmatrix} 1 & 0 \\ 0 & -1 \end{pmatrix}.$$

We introduce the ladder operators

$$S_j^\pm = S_j^x \pm iS_j^y. \tag{3.68}$$

In this representation we have

$$S_j^z |\uparrow_j\rangle = \frac{1}{2}|\uparrow_j\rangle, \qquad S_j^z |\downarrow_j\rangle = -\frac{1}{2}|\downarrow_j\rangle, \tag{3.69}$$

$$S_j^- |\uparrow_j\rangle = |\downarrow_j\rangle, \qquad S_j^- |\downarrow_j\rangle = 0, \tag{3.70}$$

$$S_j^+ |\uparrow_j\rangle = 0, \qquad S_j^+ |\downarrow_j\rangle = |\uparrow_j\rangle. \tag{3.71}$$

The orthonormal basis set is thus defined by the spin state $|\uparrow\rangle$ and $|\downarrow\rangle$, eigenstates of the operator S_i^z. This can be represented in a spin-1/2 system where each spin state is localized on a site of a lattice $\Lambda \subset \mathbb{Z}^d$, where d represents the dimension of the lattice (Figure 3.5). For every site, we have two possible states: spin up $|\uparrow\rangle$ and spin down $|\downarrow\rangle$. Therefore, the generated local Hilbert space $\mathcal{H}_i$ is bidimensional, isomorphic to $\mathbb{C}^2$.

For N spins, we have 2^N possible states and the total Hilber space $\mathcal{H}$, isomorphic to $\mathbb{C}^{2N}$ is

$$\mathcal{H} = \bigotimes_{i=1}^{N} \mathcal{H}_i. \tag{3.72}$$

The basis state, representative of the spin chain with N spin states, is a vector in a space of dimension 2^N. We use the notation $|\psi\rangle = |A_0, ..., A_{N-1}\rangle$ for the basis states, where A_i corresponds to the spin state ($|\uparrow\rangle$ or $|\downarrow\rangle$) on the i-lattice site. In order to build this basis set in computational programs, we have to choose a numerical representation that could be easily generated. The answer is in the bit values $\{1, 0\}$ which correspond directly to the spin states $\{|\uparrow\rangle, |\downarrow\rangle\}$ respectively. The basis state becomes a binary string in which each bit has a definite value, either 0 or 1. A general

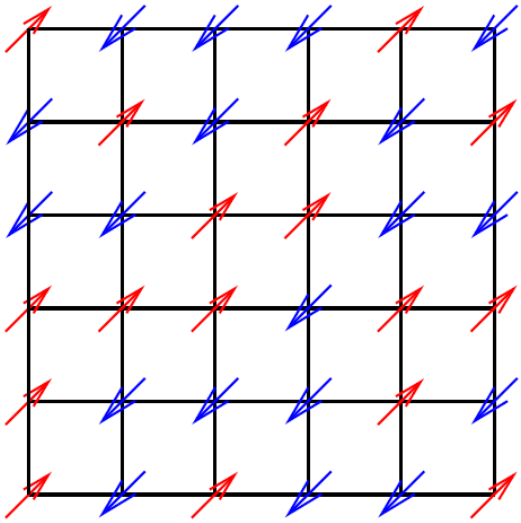

FIGURE 3.5: Schematic illustration of a finite lattice $\Lambda \subset \mathbb{Z}^2 d$ for a spin-1/2 system, with $N = 36$ spins.

vector can be expanded in this basis as $\sum_{x=0}^{2^N-1} |x\rangle$, where we have associated with each string the integer it represents in binary notation. For example, the basis set for $N = 4$ spin-1/2 $|\psi\rangle = |\uparrow, \uparrow, \downarrow, \uparrow\rangle$ will be written as $\{1, 0, 1, 1\} = 2^3 + 2^1 + 2^0 = 11$.

Heisenberg chain

In the following we reduce our analysis on the spin-1/2 chain ($\Lambda \subset \mathbb{Z}^1$) described by the Heisenber Hamiltonian

$$\begin{aligned} H &= \sum_{ij} J_{ij} \mathbf{S}_i \mathbf{S}_j \\ &= \sum_{ij} J_{ij} \left[S_i^x S_j^x + S_i^y S_j^y + S_i^z S_j^z \right] \\ &= \sum_{ij} J_{ij} \left[S_i^z S_j^z + \frac{1}{2} \left(S_i^+ S_j^- + S_i^- S_j^+ \right) \right]. \end{aligned} \tag{3.73}$$

where we impose the periodic boundary conditions for which $\mathbf{S}_{N+i} = \mathbf{S}_i$, with N number of spins in the chain.

We construct the Hamiltonian ($2^N \times 2^N$) starting from a list "topology", which defines all the (relevant) interactions $J_{i0,i1}$ present in the system between two spins localized on two sites of the chain $i0$ and $i1$, where $0 < i0, i1 < N - 1$.

```
topology = [i0, i1, J_{i0, i1}
 i2, i3, J_{i2 i3}
...]
```

We take the numbers (`int_type`) from 0 to 2^{N-1} to label the basis states and we examine the bit pairs corresponding to the previous two lattice sites (for example $i0$ and $i1$ in the first line of `topology`) within the function `testBit(int_type, offset)`, which returns 1 if the bit at `offset` & `int_type` is different from 0, 0 otherwise.

Now we can construct the Hamiltonian. If the two bit pairs are equal (corresponding to two spin up or two spin down) we have only the diagonal contribution

$$H[i,i] = \langle\uparrow_{i0}|S^z_{i0}S^z_{i1}|\uparrow_{i1}\rangle = \frac{J_{i0,i1}}{4}, \tag{3.74}$$

if not we have diagonal and off-diagonal contributions:

$$\begin{aligned} H[i,i] &= \langle\uparrow_{i0}|S^z_{i0}S^z_{i1}|\downarrow_{i1}\rangle = -\frac{J_{i0,i1}}{4}, \\ H[i,j] &= \langle\uparrow_{i0}|\frac{1}{2}\left(S^+_{i0}S^-_{i1} + S^-_{i0}S^+_{i1}\right)|\downarrow_{i0}\rangle = \frac{J_{i0,i1}}{2}. \end{aligned} \tag{3.75}$$

The python code used to generate the Hamiltonian is:

```
for i in range(0, pow(2,N), 1):
    for interaction in topology:
        i0 = interaction[0]-1
        i1 = interaction[1]-1
        test0 = testBit(i,i0)
        test1 = testBit(i,i1)
        if test0 == test1:
            H[i,i] = H[i,i] + float(interaction[2])/4
        else:
            H[i,i] = H[i,i] - float(interaction[2])/4
        # j is the index with flipped i0 and i1 bits
            j = i ^ (pow(2,i0)+pow(2,i1))
            H[i,j] = H[i,j] + float(interaction[2])/2
```

Block diagonalization

In a spin-1/2 system formed by N spin states, the dimension of the Hilbert space increases as 2^N and the matrix Hamiltonian that has to be diagonalized has dimension $2^N \times 2^N$. This exponential growth makes even small lattices difficult to handle with standard diagonalization techniques. In order to make the problem accessible to available computing power, it is possible to divide the Hamiltonian in different blocks, exploiting the symmetries of the Hamiltonian. In particular, using the pos-

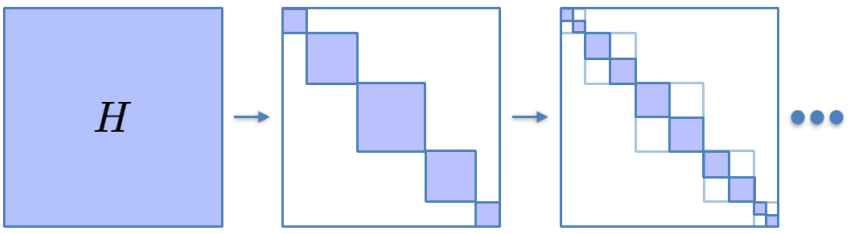

FIGURE 3.6: Schematic illustration of block diagonalization.

sible conservation laws for the Hamiltonian allows us to choose an appropriate basis set in such a way that the Hamiltonian will be reduced in a block-diagonal form (Figure 3.6). The advantage in the matrix-block diagonal structure is that every block can be diagonalized independently, thus reducing the total computational cost.

Rotational symmetry An important set of operators is represented by the total magnetization, defined by

$$S^{\alpha} = \sum_{j=1}^{N} S_j^{\alpha}, \qquad \text{with} \quad \alpha = x, y, z. \tag{3.76}$$

If the Hamiltonian commutes with these operators, $[H, S^{\alpha}] = 0$, we will say that it is invariant under rotation. The total spin in the α direction, S^{α}, is thus conserved.

The Hamiltonian defined by Eq. (3.73) conserves the total spin in the direction of the quantization axis z, i.e. the operator $S^z = \sum_{k=1}^{N} S_k^z$ commutes with the Hamiltonian, $[H, S^z] = [H, \sum_{k=1}^{N} S_k^z] = 0$. The Hamiltonian is thus block diagonal in the sector with fixed S^z values, i.e. fixed numbers N^{σ} of σ ($\uparrow$ or $\downarrow$) spins. The total Hilbert space can be separated into disjoint subspaces characterized by fixed magnetization S^z. For every values of S^z, we have two subspaces of dimensions:

$$L_{\uparrow} = \binom{N}{N^{\uparrow}}, \qquad L_{\downarrow} = \binom{N}{N^{\downarrow}}, \tag{3.77}$$

where $N^{\uparrow} = \frac{1}{2}N + S^z$ and $N^{\downarrow} = N - N^{\uparrow} = \frac{1}{2}N - S^z$. The total number of basis states in the sector of fixed S^z is therefore

$$M = L_{\uparrow} L_{\downarrow}. \tag{3.78}$$

In the case in which $S^z = 0$, we obtain $N^{\uparrow} = N^{\downarrow} = \frac{1}{2}N$ and the dimension of the subspaces becomes:

$$L_1 \equiv L_2 = \binom{N}{\frac{1}{2}N}. \tag{3.79}$$

This represents the largest block and the corresponding number of basis states becomes:

$$M_{S^z=0} = \frac{N!}{(N/2)!(N/2)!}. \tag{3.80}$$

To implement the rotational symmetry we have to start with a even number of total spin N. We construct the fixed block $S^z = \frac{1}{2}(2N^{\uparrow} - N)$, looping on $N^{\uparrow} = 0, ..., N/2$. To generate the basis set, we loop over all the states of the system $i = 0, ..., 2^N$ and we check when the total number of spin up in the state (number of set bits) corresponds to $N^{\uparrow}$. The python code is:

```
for s in xrange(0,N/2+1):
 Sz = (-N+2*s)/2.
 BaseSz = []
 for i in range(0, pow(2,N), 1):
 if bitCount(i) == s:
 BaseSz.append(i)
```

The construction of the Hamiltonian follows from equations (3.74) and (3.75), with the exception that now we are in fixed S^z blocks and the advantage is that, for each independent block, we can directly extract the quantum number S^z. In every S^z block, we can also implement additional symmetries to further block-diagonalize the Hamiltonian.

Translational invariance In the Hamiltonian (3.73) we impose periodic boundary conditions, $\mathbf{S}_{N+i} = \mathbf{S}_i$. H is thus invariant under translations. The translation

operator (that shifts the spins to the right) can be written as:

$$T\,|A_0, A_1, ..., A_{N-1}\rangle = |A_{N-1}, A_0, ..., A_{N-2}\rangle\,. \tag{3.81}$$

The momentum states, eigenstates of T, are defined by:

$$T\,|\psi(k)\rangle = e^{ik}\,|\psi(k)\rangle\,, \tag{3.82}$$

where $k = m2\pi/N$, with $m = 0, ..., N/2$. The Hamiltonian commutes with T, $[H, T] = 0$. Since $[H, S^z] = 0$ and $[T, S^z] = 0$, we can start from the S^z block-diagonal Hamiltonian and introduce translational invariance. We construct the corresponding basis set using the "representative" states

$$|a(k)\rangle = \frac{1}{\sqrt{N_a}} \sum_{r=0}^{N-1} e^{-ikr} T^r\,|a\rangle\,, \tag{3.83}$$

where $|a\rangle$ basis states of S^z and $N_a \equiv N$ if all the states $T^r\,|a\rangle$ are distinct; otherwise, if $T^{R_a}\,|a\rangle = |a\rangle$ for some R_a, $N_a = N^2/R_a$.

We can demonstrate that the matrix elements of the Hamiltonian are:

$$\begin{cases} \langle a(k)|H|a(k)\rangle = \sum_{ij} J_{ij} S_i^z S_j^z, \\ \langle b_j(k)|H|a_l(k)\rangle = e^{-ikg_j} \dfrac{J_{lj}}{2} \dfrac{R_{a_l}}{R_{b_j}}, \quad |b_j\rangle \propto T^{-g_j} H\,|a\rangle \quad \text{for } j > 0. \end{cases} \tag{3.84}$$

Reflection symmetry The Heisenberg Hamiltonian may also commute with the parity operator,

$$P\,|A_0, A_1, ..., A_{N-1}\rangle = |A_{N-1}, ..., A_1, A_0\rangle\,. \tag{3.85}$$

For an eigenstate of P, $T\,|\psi(k)\rangle = p\,|\psi(p)\rangle$, where $p = \pm 1$ since $P^2 = 1$. However, while $[H, T] = 0$ and $[H, P] = 0$, in general $[T, P] \neq 0$.

We consider an extension of the momentum state,

$$|a(k,p)\rangle = \frac{1}{\sqrt{N_a}} \sum_{r=0}^{N-1} e^{-ikr} T^r (1 + pP)\,|a\rangle\,, \quad k = m\frac{2\pi}{N},\ m = 0, ..., N/2, \tag{3.86}$$

which is eigenstate of T, but for the parity operator P we have

$$P\,|a(k,p)\rangle = p\frac{1}{\sqrt{N_a}} \sum_{r=0}^{N-1} e^{ikr} T^r (1 + pP)\,|a\rangle\,. \tag{3.87}$$

The state $|a(k,p)\rangle$ is thus eigenstate of T and P, i.e. $[T, P] = 0$, in the subspaces with momenta $k = 0$ and $k = \pi$.

In order to implement the reflection symmetry for all the possible k values, we have to introduce the semi momentum states. We let the reader follow the lecture notes [122].

Thermodynamics

The exact diagonalization method provides a complete solution to the secular equation:

$$\det[H - E_n \mathbb{1}] = 0 \tag{3.88}$$

and, from the eigenvalues E_n, we can extract the corresponding eigenvectors $|\psi_n\rangle$ by solving the linear system of equations:

$$H\,|\psi_n\rangle = E_n\,|\psi_n\rangle\,. \tag{3.89}$$

We are now able to extract all the thermodynamic properties of the system. In the context of this work, we calculated the magnetic susceptibility, defined by:

$$\chi = \left(\frac{\partial M}{\partial H}\right)_T = \frac{1}{T}(\langle M^2\rangle - \langle M\rangle^2), \tag{3.90}$$

where M is the magnetization and corresponds to the values of S^z, which can be directly extracted from the S^z-block. Another important quantity is the spin-spin correlation function

$$C(i,j) = \langle \mathbf{S}_i \cdot \mathbf{S}_j\rangle\,. \tag{3.91}$$

The exact diagonalization method will be used to analyze the compound $Li_2Cu_2O(SO_4)_2$ in chapter 6 and 7.

3.2.2 Perturbation Expansions for Quantum Many-Body Systems

The perturbation theory provides a solution to study quantum systems which are not exactly diagonalizable. The main assumption on which the present theory is based is that the Hamiltonian describing the system can be written as a sum of an unperturbed part H_0 and a perturbation V:

$$H = H_0 + \lambda V. \tag{3.92}$$

Here we have introduced the parameter λ, which is assumed to be real with a value between 0 and 1.

Degenerate case

Here we revisit the derivation of the series expansions to in principle arbitrary order for the degenerate case. We assume that there is a n-fold degeneracy of the eigenvalue of the unperturbed Hamiltonian, with the unperturbed eigenstate forming a eigenspace $\mathbb{H}_n$. The Schrödinger equation for H_0 is:

$$H_0\,|k_i\rangle = \epsilon^{(0)}\,|k_i\rangle\,, \quad i = 1,..,n. \tag{3.93}$$

We chose the normalization condition

$$\langle k_i|k_j\rangle = \delta_{ij}. \tag{3.94}$$

Thus, we can define the projector operator P, which projects onto the eigenspace $\mathbb{H}_n$,

$$P = \sum_{i=1}^{n} |k_i\rangle\,\langle k_i|\,, \tag{3.95}$$

and the resolvent $g(z)$, for $z \in \mathbb{C}$,

$$g(z) = \frac{\mathbb{1} - P}{z - H_0}, \tag{3.96}$$

where the projector $(\mathbb{1} - P)$ eliminates the singularity in $g(z)$ at $z = E^(0)$.

We analyse the degenerate problem introducing an effective Hamiltonian such that

$$HS = SH^{\text{eff}}, \tag{3.97}$$

where S is a similarity transformation, which in this case could be written as a set of vectors $|\psi_i\rangle$, with $i = 1, .., n$. The stationary Schrödinger equation can be written as

$$H\,|\psi_i\rangle = \sum_{j=1}^{n} H_{ij}^{\text{eff}}\,|\psi_j\rangle\,. \tag{3.98}$$

We expand as a power series in the coupling constant λ

$$|\psi_i\rangle = \sum_{\nu=0}^{\infty} \lambda^{\nu}\,|\nu, i\rangle\,, \tag{3.99}$$

such that

$$|0, i\rangle = |k_i\rangle\,. \tag{3.100}$$

The effective Hamiltonian expanding in power series has the form

$$H^{\text{eff}} = \sum_{\mu=0}^{\infty} \lambda^{\mu} H^{\text{eff}(\mu)}, \tag{3.101}$$

such that

$$H_{ij}^{\text{eff}(0)} = E^{(0)}\delta_{ij}. \tag{3.102}$$

We choose the higher-order corrections of the wave function $|\nu, i\rangle$ orthogonal to the unperturbed eigenvectors k_i, i.e.

$$\langle k_i|\nu, j\rangle = 0 \quad \text{for } \nu \geq 1. \tag{3.103}$$

We obtain

$$\begin{aligned}\langle k_i|H|\psi_j\rangle &= \sum_{l=1}^{n}\langle k_i|H_{j,l}^{\text{eff.}}|\psi_l\rangle = \sum_{l=1}^{n}\sum_{\nu=0}^{\infty} H_{j,l}^{\text{eff}}\,\lambda^{\nu}\,\langle k_i|\nu, l\rangle \\ &= \sum_{l=1}^{n} H_{j,l}^{\text{eff}}\,\langle k_i|0, l\rangle = \sum_{l=1}^{n} H_{j,l}^{\text{eff}}\,\langle a_i|a_l\rangle = H_{j,i}^{\text{eff}},\end{aligned} \tag{3.104}$$

thus, we have

$$H_{j,i}^{\text{eff}} = \langle a_i|H|\psi_j\rangle = E^{(0)}\,\langle a_i|\psi_j\rangle + \lambda\langle a_i|V|\psi_j\rangle \tag{3.105}$$

consequently

$$H_{i,j}^{\text{eff},(0)} = E^{(0)}\delta_{i,j} \tag{3.106}$$

$$H_{i,j}^{\text{eff},(\mu+1)} = \langle a_j|V|\mu, i\rangle \quad \text{for } \mu \geq 0. \tag{3.107}$$

We note that we re-obtain the same formulation for $H_{i,j}^{\text{eff.},(0)}$, expressed in Eq. (3.102).

The Eq. (3.98) became

$$\begin{aligned}(H_0+\lambda V)\sum_{\nu=0}^{\infty}\lambda^\nu\,|\nu,i\rangle &= \sum_{j=1}^{n}\sum_{\mu=0}^{\infty}\lambda^\mu H_{ij}^{\mathrm{eff}(\mu)}\sum_{\nu=0}^{\infty}\lambda^\nu\,|\nu,i\rangle \\ &= E^{(0)}\lambda^\nu\,|\nu,i\rangle+\sum_{j=1}^{n}\sum_{\mu=1}^{\infty}\sum_{\nu=0}^{\infty}\lambda^{\mu+\nu}H_{ij}^{\mathrm{eff}(\mu)}\,|\nu,j\rangle\,.\end{aligned} \tag{3.108}$$

Collecting the terms λ^ν, we have

$$(E^{(0)}-H_0)\,|\nu,i\rangle = V\,|\nu-1,i\rangle-\sum_{j=1}^{n}\sum_{\mu=1}^{\nu}H_{ij}^{\mathrm{eff}(\mu)}\,|\nu-\mu,j\rangle\,. \tag{3.109}$$

We apply the projector operator $(\mathbb{1}-P)$

$$(\mathbb{1}-P)(E^{(0)}-H_0)\,|\nu,i\rangle = (\mathbb{1}-P)\left\{V\,|\nu-1,i\rangle-\sum_{j=1}^{n}\sum_{\mu=1}^{\nu-1}H_{ij}^{\mathrm{eff}(\mu)}\,|\nu-\mu,j\rangle\right\}, \tag{3.110}$$

where in the sum over ν the projector operator have eliminate the term $\mu=\nu$.
Finally, we can invert $(E^{(0)}-H_0)$ and, using the definition (3.96) of the resolvent, we obtain

$$|\nu,i\rangle = g(z)\left\{V\,|\nu-1,i\rangle-\sum_{j=1}^{n}\sum_{\mu=1}^{\nu-1}H_{ij}^{\mathrm{eff}(\mu)}\,|\nu-\mu,j\rangle\right\}. \tag{3.111}$$

The two main results are Eqs. (3.107) and (3.111) that can be seen essentially as Eq. (11–18) of [123], apart from the issue of degeneracy. These equations permit an iterative computation of degenerate perturbation theory to (at least in principle) arbitrary order.

Chapter 4

Experimental techniques for magnetic excitations

"It doesn't matter how beautiful your theory is,
it doesn't matter how smart you are.
If it doesn't agree with experiment, it's wrong."

Richard P. Feynman

In Chapter 2 we have focussed our attention on the theory of magnetic excitations in spin ladder systems. In this chapter, we will discuss the possible experimental approaches to probe the physics they exhibit, with emphasis on the methods used in this work.

One of the basic possibilities for having direct information on the magnetic properties of a system is the SQUID magnometer, which can measure extremely weak magnetizations under an applied magnetic field (and/or temperature), and hence be able to provide accurate measurements of magnetic systems. This first measurement will be described in section 4.1.

Then, we will examine inelastic neutron scattering, one of the most powerful experimental techniques to investigate the dispersion properties of magnetic excitations. The theoretical details of this method and the experimental instrumentation are described in section 4.2.

Other approaches take advantage of the interaction of the sample with light, and can therefore be called optical methods. Section 4.3 is dedicated to infrared (IR) spectroscopy, a remarkable technique for the identification of the phonon modes in the analysed systems, but in general not sensitive to magnetic excitations. However, we will see how a magnetic excitation could be IR active. In particular, in the context of low-dimensional spin-systems, we will describe the Lorenzana and Sawatzky process and the Dzyaloshinskii-Moriya (DM) mechanism, which allow electric dynamic transitions between singlet and triplet states.

4.1 Magnetic Properties Measurement System (MPMS)

The MPMS with a SQUID (Superconducting Quantum Interference Device) detection is one of the most effective and sensitive magnetometers used to characterize magnetic materials. The system is configured to measure extremely weak changes in the magnetic flux produced by a sample, from which related physical quantities can be obtained (current, voltage, magnetization, magnetic susceptibility etc.).

The basic working principle of a SQUID magnetometer is governed by the Josephson tunneling effect (1962) [124]. Josephson predicted that copper-pairs can tunnel

through a thin insulator layer between two superconductors (Josephson junction) and the related electrical current depends on the phase difference $\theta(t)$ of the two superconducting wave functions:

$$I(t) = I_c \sin\theta(t), \tag{4.1}$$

where I_c is the critical current. Moreover, the time derivative of the phase difference $\theta(t)$ is correlated with the voltage $V(t)$ across this weak contact:

$$\frac{d}{dt}\theta(t) = \frac{2\pi V(t)}{\phi_0}, \tag{4.2}$$

where $\phi_0 = 2\pi\hbar\ 2e$ is the quantized magnetic flux.

The SQUID magnetometer can be represented by one ring composed by two superconductors separated by thin insulating layers to form two parallel Josephson junctions. In such a system the incoming current I_0 can be influenced by an induced magnetic flux ϕ_{ext} flowing through the ring generated by an external magnetic field. The critical current through the SQUID is then given by:

$$I_c = I_0 \left| \cos\frac{\pi\phi_{ext}}{\phi_0} \right|. \tag{4.3}$$

Thanks to the two Josephson junctions, the SQUID is able to measure the magnetic flux by its conversion into an electrical voltage.

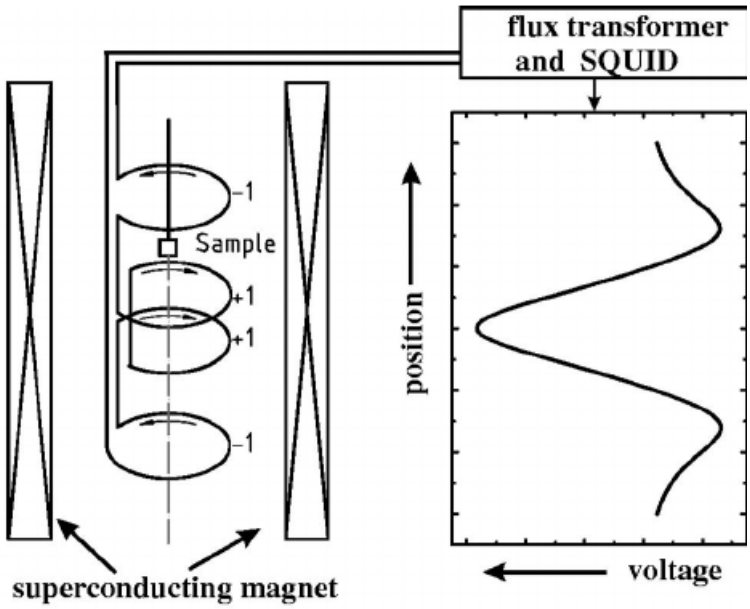

FIGURE 4.1: Schematic diagram of a MPMS SQUID magnetometer and the theoretical voltage response of an ideal dipole as a function of the position [125].

In a MPMS the sample is located at the center of a superconducting detection coil (pick-up coil) which forms, together with the SQUID, a closed superconducting loop (Figure 4.1). A measurement is performed by moving the sample through the pick-up coil. The magnetic moment of the sample induces an electric current in the detection circuit which is proportional to the change in the magnetic flux. The SQUID measures

a variation in the voltage as a function of the sample position directly correlated to the magnetic moment of the sample.

Thanks to this very sensitive electronic device, a small variation of the magnetic flux produced by a displacement of the sample can be detected and, starting from it, it is possible to go back to the magnetic properties of the sample.

4.2 Neutron Scattering

Neutron scattering measurement is a powerful technique for probing the structural and magnetic properties of materials. In this section the bases of the technique are described, emphasizing the relevance of the elastic and inelastic neutron scattering for the determination of nuclear structures and magnetic excitation spectra. To have a more detailed description, there are different textbooks on the subject, see for example [126, 127, 56, 128].

4.2.1 Neutron Scattering Theory

Neutron scattering is a powerful tool particularly well suited to study structure and dynamics of condensed matter systems, that also provides detailed and direct access to magnetic properties.

The advantage of neutron scattering comes mainly from the important properties of the neutron itself. The neutron is a massive particle ($m = 1.675 \times 10^{-27}$ kg) that gives rise to a de Broglie wavelength of the order of the interatomic distances, making interference patterns performed to study the structure of solids. It has no electric charge, therefore it is not scattered from the electron clouds but it can deeply penetrate into the sample to directly interact with atomic nuclei via the strong short range nuclear force. Although charge-less, the neutron has spin $s = 1/2$ and a magnetic moment that is able to interact with magnetic dipole moments, allowing neutron scattering to directly probe magnetic order and excitations in condensed matter systems. Finally, neutrons scatter weakly, so they can travel large distances through most materials without being scattered or absorbed and do not destroy samples.

Neutrons are indispensable as an investigative tool for understanding a broad array of material phenomena depending on their energy $E = \hbar^2 k^2/2m$. An overview of the kinematic range accessible to neutron scattering experiments is given in Figure 4.2. In particular, for thermal neutrons, the energy spectrum is of the same order of magnitude as elementary excitations in matter, which means that neutron scattering, by creating or annihilating an excitation, causes a large change in the neutron's energy. Thus, neutron scattering is an efficient tool to study the dynamics and the excitations in a system.

The Cross-Section

In a neutron scattering experiment, a collimated (usually monochromatic) beam with well defined momentum $\mathbf{k}_i$ and energy E_i is scattered through its interaction with a sample at an angle 2θ with a wave vector $\mathbf{k}_f$ and a final energy E_f measured by a detector as a function of scattering angle. Since the total energy and momentum are conserved quantities, the momentum and the energy transfer are given by

$$\mathbf{Q} = \mathbf{k}_i - \mathbf{k}_f, \quad Q^2 = k_i^2 + k_f^2 - 2k_i k_f \cos(2\theta); \tag{4.4}$$

$$E_i - E_f = \frac{\hbar^2}{2m}\left(k_i^2 - k_f^2\right) = \hbar\omega. \tag{4.5}$$

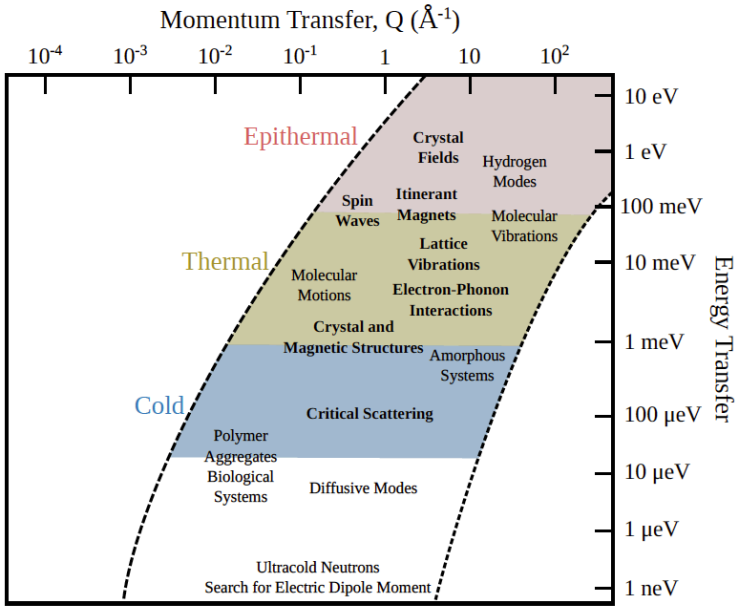

FIGURE 4.2: Various applications of neutron scattering in terms of energy and accessible momentum transfer. Figure adapted from [128].

For elastic scattering no energy is transferred from the neutron to the sample, therefore $\hbar\omega = 0$, $|\mathbf{k}_i| = |\mathbf{k}_f|$ and the wave vector transfer is $|\mathbf{Q}| = 2|\mathbf{k}_i| \sin\theta$. In an inelastic scattering, instead, both energy and momentum are transferred and $\mathbf{Q}$ is equal to:

$$\left|\frac{\mathbf{Q}}{\mathbf{k}_i}\right| = \sqrt{1 + \left(1 - \frac{\hbar\omega}{E_i}\right) - 2\cos(2\theta)\sqrt{1 - \frac{\hbar\omega}{E_i}}}. \tag{4.6}$$

The quantity detected in a scattering experiment, represented in Figure 4.3, is the *double differential cross-section*, i.e. the flux of scattered neutrons into a solid angle $d\Omega$ within a particular range of energies $[E_f, E_f + dE_f]$. To obtain an expression, we have to calculate the probability of a transition from an initial state $|k_i, s_i, \lambda_i\rangle$ to a final one $|k_f, s_f, \lambda_f\rangle$, where k_i is the wavevector of the incident neutron and k_f of the scattered one, s_i and s_f represent the spin-state of the neutron before and after the interaction and λ_i is the initial state of the sample, λ_f the final one.

Since neutron scattering is a a relatively weak interaction, *Fermi's golden rule* for first-order perturbation can be applied to calculate the probability of transitions. In a scattering process this is equivalent to the Born approximation which assumes that both the incoming and scattered beam are plane waves.

The *double differential cross-section* can be written as

$$\frac{d^2\sigma}{d\Omega dE_f} = \frac{k_f}{k_i}\left(\frac{m}{2\pi\hbar^2}\right)^2 \sum_{\lambda_i, s_i} p_{\lambda_i} p_{s_i} \sum_{\lambda_f, s_f} \left|\langle k_f, s_f, \lambda_f | \widehat{V} | k_i, s_i, \lambda_i \rangle\right|^2 \delta\left(E_i - E_f + \hbar\omega\right), \tag{4.7}$$

where we sum over all possible initial and final states of the system, and over all possible initial and final spin-states of the neutron, with p_{λ_i}, p_{s_i} that represent the statistical weight factors (assuming Boltzmann distribution) for the initial states. $\widehat{V}$ is the operator corresponding to the scattering potential V, therefore the scattering cross-section is dependent on the type of interaction between the neutron and the matter it scatters from.

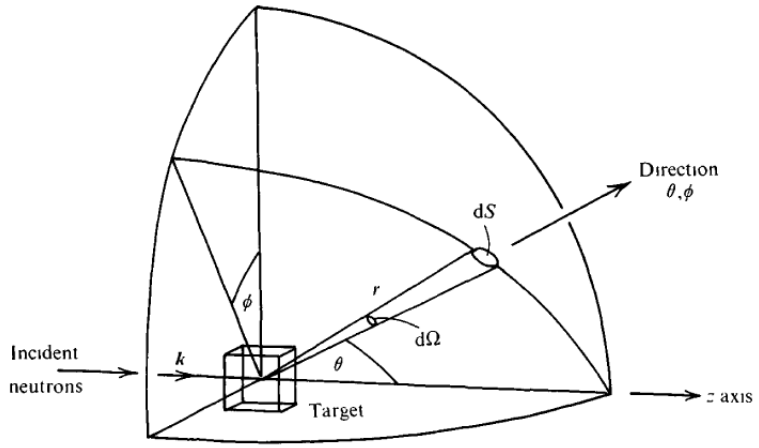

FIGURE 4.3: Geometry for scattering experiment [127].

The Nuclear Interaction

The interaction between an incident neutron at position $\mathbf{r}$ and the l-th atomic nucleus positioned at $\mathbf{R}_l$ can be described by the Fermi pseudo-potential

$$V_l(\mathbf{r}) = \frac{2\pi\hbar^2}{m} b_l \delta\left(\mathbf{r} - \mathbf{R}_l\right), \tag{4.8}$$

where b_l is the scattering length of the atomic nucleus l and depends on the type of nucleus, the isotope and the relative orientation of the nuclear and neutron spins. The δ-function arises from the fact that the strong nuclear force has a very short range and it is approximately spherically symmetrical.

Substituting the potential in (4.7), the scattering cross section becomes

$$\frac{d^2\sigma}{d\Omega dE_f} = \frac{k_f}{k_i}\frac{1}{2\pi\hbar}\int_{-\infty}^{\infty}\sum_{ij}\left\langle b_i^\dagger b_j e^{-i\mathbf{Q}\mathbf{R}_i(t)} e^{-i\mathbf{Q}\mathbf{R}_i(0)} e^{-i\omega t}\right\rangle dt, \tag{4.9}$$

where the integral are substituting to the sum. In this formula we take the δ with his integral representation and the Heisenberg operator in the time-dependent representation. When the atomic nuclei in the sample are randomly distributed, with a different value of b_i, we can dissociate b_i from R_i

$$\frac{d^2\sigma}{d\Omega dE_f} = \frac{k_f}{k_i}\frac{1}{2\pi\hbar}\int_{-\infty}^{\infty}\sum_{ij}\overline{b_i b_j}\left\langle e^{-i\mathbf{Q}\mathbf{R}_i(t)} e^{-i\mathbf{Q}\mathbf{R}_i(0)} e^{-i\omega t}\right\rangle dt. \tag{4.10}$$

On the assumption of no correlation between the b values of different nuclei

$$\overline{b_i b_j} = \overline{b}^2 + \left(\overline{b^2} - \overline{b}^2\right)\delta_{i,j}, \tag{4.11}$$

where $\bar{b}$ is the average scattering length. The partial differential cross-section can be expressed as a sum of two independent terms, a coherent and an incoherent part:

$$\begin{aligned}\frac{d^2\sigma}{d\Omega dE_f} &= \left(\frac{d^2\sigma}{d\Omega dE_f}\right)_{coh} + \left(\frac{d^2\sigma}{d\Omega dE_f}\right)_{inc} \\ &= \frac{\sigma_{coh}}{4\pi}\frac{k_i}{k_f}S_{coh}(\mathbf{Q},\omega) + \frac{\sigma_{inc}}{4\pi}\frac{k_i}{k_f}S_{inc}(\mathbf{Q},\omega),\end{aligned} \tag{4.12}$$

where $S_{coh}(\mathbf{Q},\omega)$ and $S_{inc}(\mathbf{Q},\omega)$ are the *dynamic structure factors.*

The coherent scattering results from the coherent interference between the same nucleus at different times, as well as from interference between different nuclei. Therefore, the coherent part in a neutron scattering experiment provides information about the crystal structure and lattice excitations. In contrast, incoherent scattering arises only from interference effects of the same nucleus at different times and is observed as an isotropic background.

In crystalline samples, the major contribution is in the coherent elastic scattering and this is caused by the periodic atomic planes, which produce peaks in the scattering pattern. These peaks, Bragg peaks, are seen when the scattering vectors $\mathbf{Q}$ is equal to a reciprocal lattice vector $\boldsymbol{\tau}$ perpendicular to the crystal planes. The partial differential cross-section under this condition is:

$$\left(\frac{d^2\sigma}{d\Omega dE_f}\right)_{coh,elast} = \frac{N(2\pi)^3}{V_0}|F_N(\mathbf{Q})|^2\delta(\mathbf{Q}-\boldsymbol{\tau})\delta(\hbar\omega), \tag{4.13}$$

here $\delta(\mathbf{Q}-\boldsymbol{\tau})$ reflects the periodicity of the crystal lattice and N is the number of unit cells included in the volume V_0. $F_N(\mathbf{Q})$ is the *nuclear structure factor*

$$F_N(\mathbf{Q}) = \sum_l \bar{b}_l e^{i\mathbf{Q}\cdot\mathbf{R}_l}e^{-W_l(\mathbf{Q},T)}, \tag{4.14}$$

where the sum over l extends over all nuclei at positions $\mathbf{R}_l$ in the unit cell and $\bar{b}_l$ are the scattering lengths of each atom. The factor $e^{-W_l(\mathbf{Q},T)}$ is the (temperature dependent) Debye-Waller factor which indicates the probability that an atom is at position $\mathbf{R}_l$ at temperature T. This factor describes the thermal fluctuations of the atoms around their equilibrium positions.

The Magnetic Interaction

Magnetic scattering of neutrons results from interaction between the magnetic dipole moment of the incident neutron $\boldsymbol{\mu}_n$ and the electromagnetic field $\mathbf{B}(\mathbf{r})$ created by the atoms of the sample. In this case the magnetic potential is

$$V_M = -\boldsymbol{\mu}_n \cdot \mathbf{B}(\mathbf{r}). \tag{4.15}$$

In general, the $\mathbf{B}(\mathbf{r})$ is generated by the contributions of the spin and the orbital momentum of the unpaired electrons. For crystals in which the orbital component of the angular moment is quenched, the time average is $\langle\mathbf{L}\rangle = 0$ and $\mathbf{L}$ will not contribute to the total magnetic moment. The cross section becomes:

$$\frac{d^2\sigma}{d\Omega dE_f} = \frac{k_f}{k_i}\left(\frac{r_0}{2}\right)^2 f^2(\mathbf{Q})e^{-2W(\mathbf{Q},T)}S(\mathbf{Q},\omega), \tag{4.16}$$

where $r_0 = \gamma_n e^2/m_e c^2 = -0.5391 \times 10^{-14}$ m is the magnetic scattering length (γ_n is the neutron gyromagnetic ratio), g is the Landé splitting factor and $f(\mathbf{Q})$ is the magnetic form-factor, given by the Fourier transform of the normalized unpaired spin density ρ_a localized in the site a:

$$f(\mathbf{Q}) = \int \rho_a(\mathbf{r}) e^{i\mathbf{Q}\cdot\mathbf{r}} d\mathbf{r}. \tag{4.17}$$

As ρ_a has a finite spatial extent associated to a characteristic length λ, the form factor decreases rapidly for $Q > 1/\lambda$, limiting the range in which magnetic scattering could be observed. On the contrary, in nuclear scattering, the interaction is much more localized and it does not depend on $\mathbf{Q}$. $S(\mathbf{Q},\omega)$ is the response function, and is written as

$$S(\mathbf{Q},\omega) = \sum_{\alpha\beta} \left\langle \left(\delta_{\alpha\beta} - \frac{Q_\alpha Q_\beta}{Q^2}\right) S^{\alpha\beta}(\mathbf{Q},\omega) \right\rangle \tag{4.18}$$

where $\alpha,\beta = x,y,z$ are the cartesian components. The term $\left(\delta_{\alpha\beta} - \frac{Q_\alpha Q_\beta}{Q^2}\right)$ derives from the dipole nature of the magnetic interaction and implies that the cross section depends only on the components of the magnetization perpendicular to the momentum transfer $\mathbf{Q}$. $S^{\alpha\beta}(\mathbf{Q},\omega)$ is the dynamical structure factor, which is equal to the Fourier transform, in space and time, of the time-dependent spin-spin correlation function:

$$S^{\alpha\beta}(\mathbf{Q},\omega) = \frac{1}{2\pi\hbar} \int \frac{1}{N} \sum_{j,j'} e^{i\mathbf{Q}\ (\mathbf{r}_j - \mathbf{r}_{j'})} e^{-i\omega t} \left\langle S^\alpha_{j'}(0) S^\beta_j(t) \right\rangle dt, \tag{4.19}$$

where $S^\beta_j(t)$ is the time dependent operator for the β component of the spin on the site j. We can rewrite equation (4.19) as the sum of a static (elastic) and a dynamic (inelastic) contributions:

$$S^{\alpha\beta}(\mathbf{Q},\omega) = S^{\alpha\beta}_s(\mathbf{Q},\omega) + S^{\alpha\beta}_d(\mathbf{Q},\omega), \tag{4.20}$$

where the static (elastic) component is

$$S^{\alpha\beta}_s(\mathbf{Q},\omega) = \frac{1}{N}\delta(\hbar\omega) \sum_{jj'} \left\langle S^\alpha_j \right\rangle \left\langle S^\beta_{j'} \right\rangle e^{-i\mathbf{Q}(\mathbf{r}_j - \mathbf{r}_{j'})} \tag{4.21}$$

and the dynamic (inelastic) component is related to the imaginary part of the dynamical magnetic susceptibility (which does not depend on temperature) through the fluctuation dissipation theorem [129]:

$$S^{\alpha\beta}_d(\mathbf{Q},\omega) = \frac{1}{\pi} \frac{1}{1 - e^{-\hbar\omega/k_B T}} \chi''_{\alpha\beta}(\mathbf{Q},\omega). \tag{4.22}$$

The observation of an inelastic peak with an energy ω_d and momentum $\mathbf{Q}_d$ corresponds to a process where a quantum of energy has been absorbed or emitted by the magnetic system, with the consequent creation or annihilation of a quasi particle, for example a magnon, with the same energy ω_d and momentum $\mathbf{Q}_d$. The dynamic magnetic susceptibility is the linear response function of the magnetic system and the imaginary component is related to the energy dissipation rate in the perturbed system. This relation is very useful because the dynamical susceptibility can be compared to the theoretically predicted one, a quantity often calculated in theoretical treatments. In

this context, the detailed balance principle can be written as

$$S_d^{\alpha\beta}(\mathbf{Q},\omega) = e^{\hbar\omega/k_BT} S_d^{\beta\alpha}(-\mathbf{Q},-\omega), \tag{4.23}$$

and it could be derived from (4.22) and from the causality principle, which implies that $\chi''_{\alpha\beta}(\mathbf{Q},\omega)$ is properly antisymmetric. The detailed balance principle expresses the fact that the probability of a transition in a sample depends on the statistical weight factor of the initial state, which is always lower for annihiling an excitation than creating one.

Magnetic excitations on dimers We analyse a simple dimer model, elaborated several times throughout this thesis. This model, composed by two coupled spins $\mathbf{S}_1$ and $\mathbf{S}_2$, is described by the Hamiltonian:

$$H = J\mathbf{S}_1 \cdot \mathbf{S}_2 \tag{4.24}$$

where J is the exchange coupling between the two spins 1/2. This system has a singlet ground-state with $E_S = -3J/4$ and a triplet excited state $E_T = +J/4$. In an inelastic neutron scattering experiment, we can excite the triplet state resulting in a peculiar measured signal.

In this simple case we can derive the expression for the dynamic form factor $S(\mathbf{Q},\omega)$ and the corresponding magnetic cross-section. Following [130], we obtain

$$\frac{d^2\sigma}{d\Omega dE_f} = N p_s \frac{k_f}{k_i} \left(\frac{r_0}{2}\right)^2 f^2(\mathbf{Q}) e^{-2W(\mathbf{Q},T)} \left(1 - \frac{\sin(QR)}{QR}\right) \delta(\hbar\omega - (E_T - E_S)) \tag{4.25}$$

where N is the total number of dimers, p_s is the Boltzmann population factor, R the intradimer separation and $(E_T - E_S)$ is the energy of the magnetic excitation gap.

The particular aspect of this expression is given by the combination of the square of the form factor, that decreases with increasing $|Q|$, and the structure factor $\left(1 - \frac{\sin(QR)}{QR}\right)$ causing a particular oscillating behavior.

4.2.2 Instrumentation

Nowadays the two most common sources for modern neutron scattering measurements are nuclear reactors and spallation or pulsed sources. The first one is characterized by a continuous flux of neutrons produced by the spontaneous fission of ^{235}U. In a spallation source pulses of neutrons are produced by bombarding heavy targets (W, Ta, Pb, or Hg) with high-energy protons provided by an accelerator. There are two different advanced research facilities currently operating in France, the High Flux Reactor at the Institute Laue–Langevin (ILL) in Grenoble and Orphée at the Laboratoire Léon Brillouin in Saclay.

In particular, several instrumentations have been developed for inelastic neutron scattering studies. The most common used techniques are the three-axis spectroscopy and the time-of-flight spectroscopy. While the triple-axis spectrometer can only probe one specific position at a time in the momentum and energy $(\mathbf{Q},\omega)$ space, the time-of-flight spectrometer can explore a large region in the $(\mathbf{Q},\omega)$ phase space.

In this work, neutron scattering measurements were performed at the ILL in Grenoble on the Time-of-Flight spectrometer IN4 (Figure 4.4).

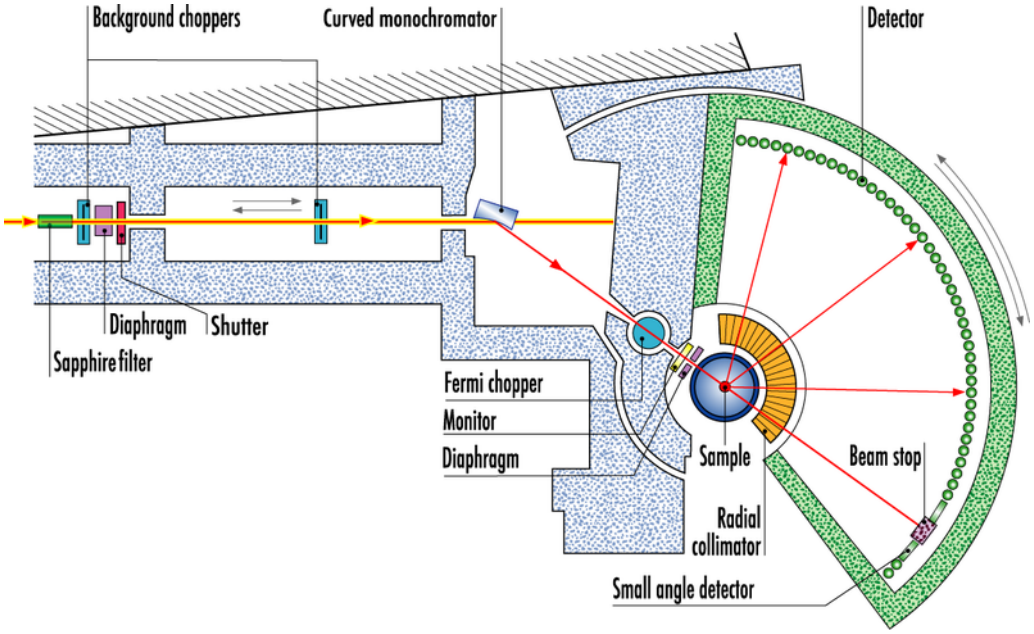

FIGURE 4.4: Schematic diagram of the IN4 time-of-flight spectrometer at the Institute Laue–Langevin (ILL) in Grenoble [131].

Time-of-Flight spectrometer

Time-of-Flight spectrometer is one of the most versatile instruments for inelastic studies, particularly well suited for investigating magnetic excitations and phonons. This technique was originally employed for pulsed neutrons in spallation sources but it has been implemented also in nuclear reactors with the introduction of additional choppers to create a pseudo pulsed source. There are two possible setups, the direct and the indirect geometry. Although both classes of spectrometers are in service at many neutron sources, the inelastic neutron experiment performed in this work was in a direct geometry configuration, and we restrict the discussion to this class.

In the direct geometry instrument, the incident neutrons wavevector $\mathbf{k}_i$ is fixed by a chopper, phased appropriately with respect to the initial pulse. A specified energy and momentum is transferred to the sample that scatters neutrons which are finally detected by an array of position sensitive detectors that cover a large range of scattering angles. The final energy E_f is calculated taking into account the time of flight t of the neutron and the distance D between the sample and the detector:

$$E_f = \frac{m_n v^2}{2} \quad \text{and} \quad v = \frac{D}{t}, \tag{4.26}$$

where m_n is the mass of the neutron and v is its velocity. The scattered wavevector $\mathbf{k}_f$ is now fully defined by E_f and the angular position of the scattered neutron detected by the detector. The wavevector transfer $\mathbf{Q}$ can be calculated from $\mathbf{k}_i$ and $\mathbf{k}_f$ using the standard scattering triangle.

4.3 Infrared Spectroscopy

Infrared spectroscopy is a powerful tool to investigate the microscopic vibrational properties of materials. The dominant contribution to the excitation processes observable by IR spectroscopy are transitions which are electric dipole allowed and, among them, one can observe those associated with atomic vibrations (IR active phonons). In the specific case of the present work, we are also interested in magnetic transitions between singlet and triplet states (magnons), which could be IR optically accessible in the presence of an antisymmetric interaction.

4.3.1 Vibrational excitations

In this section we describe the problem of infrared spectroscopy associated with the interaction of an infrared electromagnetic field (the IR light) with the vibrational states of the analysed system. The process involves the annihilation of a photon with energy equal to the energy of the transition between vibrational states with the concomitant creation of a phonon. The conservation of the momentum and of the energy implies that the first-order infrared absorption process (one-phonon process) is possible when a $\mathbf{k} \cong 0$ photon is annihilated and a phonon at $\mathbf{Q} \cong 0$ is created.

The frequencies of the vibrational states are obtained by diagonalizing the dynamical matrix $\mathcal{D}(\mathbf{Q})$, which depends on the phonons wavevector $\mathbf{Q}$. In particular, in a 3D crystal with N atoms per cell we have $3N$ branches from which 3 acoustic modes and $(3N-3)$ optical modes. These modes have a higher energy vibration (the frequency is higher), thus they need a certain amount of energy to be excited. This energy could be given by the IR radiation. Moreover, the optical modes are distinguished in two further categories, the longitudinal modes that have a polarization wavevector $\mathbf{u}$ parallel to the propagation wave $\mathbf{k}$ and the transverse ones, with $\mathbf{u} \perp \mathbf{k}$. The infrared radiation is able to excite the optical transversal modes, with frequencies ω^{TO}.

Following [132], we recall that, for polar systems at $\mathbf{Q} = \mathbf{0}$, $\mathcal{D}(\mathbf{0})$ is not well defined. However in the limit:

$$\lim_{\mathbf{Q}\to\mathbf{0}} \mathcal{D}(\mathbf{Q}) = \mathcal{D}_{an}(\mathbf{0}) + \mathcal{D}_{na}(\hat{\mathbf{Q}}) \tag{4.27}$$

the matrix can be decomposed in an analytical part $\mathcal{D}_{an}$, which does not depend on $\mathbf{Q}$, and a non analytical contribution $\mathcal{D}_{na}$, which depends on the direction $\hat{\mathbf{Q}}$ used to make the limit. Note that here we are assuming that the light is propagating as a wave within the sample, that is $\mathbf{Q} \times \mathbf{E} = \mathbf{0}$ and $\mathbf{Q} \cdot \mathbf{D} = 0$, where $\mathbf{E}$ is the electric field and $\mathbf{D}$ the electric displacement field.

In the IR absorption process the created phonon at $\mathbf{Q} \cong 0$ has the so-called TO frequency ω^{TO}, obtained by the diagonalization of the analytical part of the dynamical matrix $\mathcal{D}_{an}(\mathbf{0})$.

The Hamiltonian describing the IR absorption can be written:

$$H = H_0 + H'. \tag{4.28}$$

H_0 represents the Hamiltonian of the vibrational atoms in the crystal (phonons) at $\mathbf{Q} \cong 0$:

$$H_0 = \sum_{\nu} \hbar\omega_{\nu}^{\mathrm{TO}} \left(a_{\nu}^{\dagger} a_{\nu} + \frac{1}{2}\right), \tag{4.29}$$

where the TO phonon frequencies $\omega_{\nu}^{\mathrm{TO}}$ are characterized by the branch index ν and $a_{\nu}^{\dagger}$ (a_{ν}) are the corresponding creation (annihilation) operators.

H' couples the electromagnetic field of the IR radiation with the total dipole moment of the system $\mathbf{M}$

$$H' = -\mathbf{E} \cdot \mathbf{M}. \tag{4.30}$$

The dipole moment $\mathbf{M}$ is to be considered as a function of the displacement of the ions from their equilibrium position and thanks to this dependence it acts as an operator on the Hilbert space of the Hamiltonian H_0. $\mathbf{E} = \mathbf{E}_0 e^{i(\mathbf{k}\cdot\mathbf{r}-\omega t)}$ is the oscillating electric field of the IR light propagating in space and time ($\mathbf{r}$,$\mathbf{t}$). Here, ω is the angular frequency, $\mathbf{E}_0$ the amplitude of the electric field and $\mathbf{k}$ the wave vector.

The transition probability from the ground-state $|0\rangle$ where no phonons are excited to an excited state with only one phonon $|\nu\rangle = a_\nu^\dagger |0\rangle$ is given by the Fermi Golden rule

$$P_{0\to\nu} = \frac{2\pi}{\hbar^2} \left| \langle \nu | H' | 0 \rangle \right|^2 \delta(\omega - \omega_\nu^{\mathrm{TO}}). \tag{4.31}$$

Substituting the perturbed Hamiltonian defined in (4.30)

$$P_{0\to\nu} = \frac{2\pi}{\hbar^2} |\mathbf{E}_0 \langle \nu | \mathbf{M} | 0 \rangle|^2 \delta(\omega - \omega_\nu^{\mathrm{TO}}). \tag{4.32}$$

This means that an incident IR electric field can induce a transition from the initial state $|0\rangle$ to a final state $|\nu\rangle$ if the expectation value $\langle \nu | \mathbf{M} | 0 \rangle$ of the total dipole operator is non-vanishing. In particular, the operator $\mathbf{M} \equiv \mathbf{M}(\{u_{s\alpha l}\})$ can be expressed as a Taylor series expansion with respect to the ionic displacements $u_{s\alpha l}$ of the s-th ion in the l-th cell of the crystal along the $\alpha = \{x, y, z\}$ cartesian coordinate around the equilibrium position $u = 0$

$$\mathbf{M} = \mathbf{M}^{(0)} + \mathbf{M}^{(1)} + ... = \mathbf{M}^{(0)}(\{u_{s\alpha l}\}) + \sum_{s'\alpha' l'} \frac{\partial\ \mathbf{M}(\{u_{s\alpha l}\})}{\partial u_{s'\alpha' l'}}\bigg|_{u=0} u_{s'\alpha' l'} + ... \tag{4.33}$$

$\mathbf{M}^{(0)}$ is usually zero, and if not, is a static moment of no consequence for IR transition (because of the orthogonality of $|0\rangle$ and $|\nu\rangle$, eigenvectors of the Hamiltonian H_0). We are concerned, therefore, only with the part of $\mathbf{M}$ that depends on the ionic displacement. In the one phonon process the term that has to be considered to the expectation value of $\mathbf{M}$ is the first order dipole moment $\mathbf{M}^{(1)}$, which is linear in the ionic displacement and makes the largest contribution to the intensity of fundamental vibrational transitions. We have determined one of the principal selection rules for IR vibrational transition $\mathbf{M}^{(1)} \neq 0$.

We can now introduce the ionic effective charge [132]:

$$e\mathbf{Z}^*_{s\alpha} = \frac{\partial\ \mathbf{M}}{\partial u_{s\alpha l}}\bigg|_{u=0}, \tag{4.34}$$

which does not depends on l. $e = |e|$ is the electron charge. The ionic effective charge is the coefficient of proportionality between a change in macroscopic dipole momentum caused by a ionic displacement under conditions of zero external field. Since the interaction of the external field with the crystal is coupled to the total dipole moment $\mathbf{M}$, the magnitude of the effective charge determines the strength of this interaction.

Representing $u_{s\alpha}$ in terms of creation and annihilation operators we obtain:

$$\langle \nu | \mathbf{M}^{(1)} | 0 \rangle = \sqrt{\frac{\hbar}{2\omega_\nu^{\mathrm{TO}}}} \sum_{s\alpha} e\mathbf{Z}^*_{s\alpha} \frac{e\,(s\alpha|\mathbf{0}\nu)}{\sqrt{m_s}} \tag{4.35}$$

where $\frac{e\,(s\alpha|\mathbf{0}\nu)}{\sqrt{m_s}}$ represents the time independent normalized displacement of the s-th ion (with mass m_s) in the TO phonon mode ($\mathbf{Q} = \mathbf{0}$).

The transition probability (4.32) thus becomes:

$$P_{0\to\nu} = \frac{\pi}{\hbar\omega_\nu^{TO}}\left|\mathbf{E}_0 \sum_{s\alpha} e\mathbf{Z}^*_{s\alpha}\frac{e\,(s\alpha|\mathbf{0}\nu)}{\sqrt{m_s}}\right|^2 \delta(\omega-\omega_\nu^{\mathrm{TO}}). \tag{4.36}$$

Following [133], we can calculate the (static) dielectric constant $\epsilon(\omega)$. In our notations, we obtain:

$$\epsilon^{\alpha,\beta}(\omega) = \epsilon_\infty^{\alpha,\beta} + \frac{4\pi}{\Omega}\sum_\nu \frac{S_\nu^\alpha S_\nu^\beta}{(\omega_\nu^{\mathrm{TO}})^2-\omega^2-i\gamma_\nu\omega} \tag{4.37}$$

which is a sum of oscillator modes of characteristic frequencies ω_ν^{TO} where S_ν^α is the α Cartesian component of $\mathbf{S}_\nu = \sum_{s\alpha} e\mathbf{Z}^*_{s\alpha}\frac{e\,(s\alpha|\mathbf{0}\nu)}{\sqrt{m_s}}$, which represents the mode-oscillator strength vector, Ω is the volume of the unit cell, γ_ν are the damping constants and ϵ_∞ is a constant limiting value as $\omega\to\infty$, *i.e.* for frequencies large compared with the lattice vibration frequencies but small compared with the electronic transition frequencies. Equation (4.37) gives the standard expression of the dielectric function associated to the one-phonon processes and it has the same form as the Lorentz-Drude model.

The dielectric function

The dielectric function is the fundamental linear-response function which relates the displacement field $\mathbf{D}$ to the incident electric field

$$\mathbf{D}(\omega) = \epsilon(\omega)\mathbf{E}(\omega). \tag{4.38}$$

The dielectric function is a second-rank tensor but, for simplicity, in the following we will consider it as a scalar. It is a complex quantity $\epsilon(\omega) = \epsilon_1(\omega) + i\epsilon_2(\omega)$. Let $n(\omega) = \sqrt{\epsilon(\omega)} = n_1(\omega) + in_2(\omega)$ be the complex index of refraction , where $n_1(\omega)$ is the refractive index and $n_2(\omega)$ the extinction coefficient. The relations to the dielectric function are

$$\epsilon_1(\omega) = n_1^2(\omega) - n_2^2(\omega) \quad \text{and} \quad \epsilon_2(\omega) = 2n_1(\omega)n_2(\omega) \tag{4.39}$$

It should be noted, however, that $\epsilon(\omega)$ cannot be observed directly; what is seen is the absorbance $A(\omega)$

$$A(\omega) = -\log_{10}\frac{I_t}{I_0} \tag{4.40}$$

where I_0 is the intensity of the radiation and I_t is the intensity transmitted through the sample [134]. When the IR radiation is reflected at near-normal incidence at the surface of a sufficiently thick crystal (thickness d), the absorption coefficient $\alpha(\omega) = 2.3026\frac{A(\omega)}{d}$ is related to the imaginary part of the dielectric function by the relation:

$$\alpha(\omega) = \frac{2\pi\omega\epsilon_2(\omega)}{n_1(\omega)} = 4\pi\omega n_2(\omega). \tag{4.41}$$

In the range of vibrational transitions, the dielectric function has the form of the equation (4.37) and the absorbance can be fully described by the sum of Lorentzian

peaks centred at the TO phonon frequencies ω_ν^{TO}.

Factor Group Analysis

The number of the active phonon modes for an arbitrary crystal can be calculated by applying the so-called factor group analysis [135], which is based upon the fact that a particular mode can be infrared active only if its symmetry is the same as that of at least one of the component of the dipole moment. Indeed, as described in subsection 4.3.1, an IR vibrational transition is allowed when $\langle\nu|\mathbf{M}|0\rangle$ is different from zero. In term of group theory, this can be expressed as:

$$\Gamma(\nu) \otimes \Gamma(\mathbf{M}) \supset \Gamma(0) \tag{4.42}$$

where $\Gamma(0)$ and $\Gamma(\nu)$ are the irreducible representations of the initial state (zero phonon) and the final state (one phonon ν). $\Gamma(\mathbf{M})$ is the irreducible representation of the dipole operator $\mathbf{M}$, which has the same symmetry than the translation vector. The irreducible representation of the initial state corresponds to the totally symmetric $\Gamma(0) = A$ and, in the case in which ν is non-degenerate, we have $\Gamma(\nu) = \Gamma(\mathbf{M})$.

First, we have to calculate the total irreducible representation Γ_{vib} of the vibrations at $\mathbf{Q} = \mathbf{0}$. To use the factor group analysis, the crystal structure and the factor group of the compound must be known. In a single unit cell we have N atoms occupying a particular site with its own symmetry at the equilibrium position (equipoint). For every element of the factor group we construct $3N \times 3N$ reducible representations which transform the structure into itself in block of 3×3 (one for every atoms N) of the form

$$R(\theta) = \begin{bmatrix} \cos\theta & \sin\theta & 0 \\ -\sin\theta & \cos\theta & 0 \\ 0 & 0 & \pm 1 \end{bmatrix} \tag{4.43}$$

where θ represents the angle of rotation about the particular symmetry axis. The blocks on the diagonal of the $3N \times 3N$ matrix will contribute to the reducible character and these correspond to the blocks assigned to atoms which remain fixed during the symmetry operation. The contribution of a particular $R(\theta)$ block is

$$\chi^{\mathrm{vib}}(R) = \omega(R)(\pm 1 + 2\cos\theta) \tag{4.44}$$

where $\omega(R)$ is the number of fixed atoms during R. The distribution of vibrational modes Γ_{vib} is made by the ensemble of n_j^{vib}, one for every irreducible representation of the crystal, equal to

$$n_j^{\mathrm{vib}} = \frac{1}{g} \sum_k a_k \chi^{\mathrm{vib}}(R_k) \chi^j(R_k)^* \tag{4.45}$$

where g is the order of the factor group, a_k is the order of the class R_k, $\chi^{\mathrm{vib}}(R_k)$ is the reducible character defined in (4.44) and $\chi^j(R_k)$ is the character of class R in the j-th irreducible representation.

Γ_{vib} contains optical and acoustical vibrations. Therefore, we will have to subtract the irreducible representation of the acoustical phonons that have the same character as the translations (and, hence, as the dipole moment). Finally, the IR active modes are the acoustical ones which are contained in the irreducible representation of the translation of the crystal.

An example of the application of the factor group analysis is given in 6.3.1, where we consider the phonon modes of $Li_2Cu_2O(SO_4)_2$.

4.3.2 Magnetic Excitation

An important part of this work is concerned with the investigation of magnetic excitations in low-dimensional spin systems. In this section, we analyze the optical spectroscopy processes by means of phonon-assisted infrared absorption of these magnetic excitations.

Lorenzana and Sawatzky - Bimagnon-plus-Phonon Absorption

One of the first evidence of these fascinating excitations observed in infrared spectra was given by Newman and Cherenko in 1959 [136] in the antiferromagnet NiO and in 1964 Mizuno and Koide [137] proposed the presence of two-magnon and one phonon in the spectra. The process was well explained only in 1995 by Lorenzana and Sawatzky in the mid-infrared absorption of high-T_c 2D-cuprates [138] on the basis of spin-wave theory. Experimental measurements of real systems also confirm this hypothesis [139, 140, 141].

In general, excitations leading to a change of the total spin are not allowed in IR spectroscopy. The lowest order process to have $\Delta S = 0$ would be to excite two $S = 1$ magnons with total spin $S_{tot} = 0$. However, in cuprates, the absorption of two magnons is not IR active due to inversion symmetry. Lorenzana and Sawatzky [138] presented the excitation of two magnons when an additionally symmetry-breaking phonon is excited. In this case the total momentum is also conserved: $k_{tot} = k_{ph} + k_{bimagnon} = 0$, and, from the energy conservation, the energy positions of the magnetic peaks are shifted by the energy of the phonon $\hbar\omega_{ph}$.

We consider linear Cu-O-Cu bonds in the presence of an electric field $\mathbf{E}$ and an excited phonon which creates a displacement $\mathbf{u}$ in the oxygen atom. The Hamiltonian is given by:

$$H = \sum_{i,\delta} J_{i,\delta}(\mathbf{E}, \{\mathbf{u}_{i+\delta/2}\})\mathbf{S}_i\mathbf{S}_{i+\delta} + H_{ph} - \mathbf{E}\cdot\mathbf{P}_{ph} \tag{4.46}$$

where i labels the Cu sites and δ runs over nearest-neighbour sites, the superexchange coupling $J_{i,\delta}$ is dependent on the electric field $\mathbf{E}$ and on the displacements of the oxygen ions $\mathbf{u}$. H_{ph} is the phonon Hamiltonian and $\mathbf{P}_{ph}$ is the phonon dipole moment $\mathbf{P}_{ph} = -\dfrac{\partial H}{\partial \mathbf{E}}$.

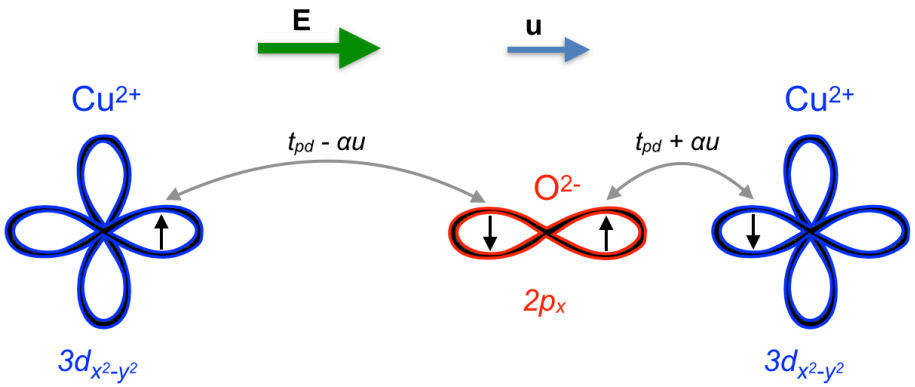

FIGURE 4.5: Illustration of the Cu-O-Cu bond in the presence of a virtual phonon and an electric field $\mathbf{E}$ parallel to the Cu-O-Cu axis (x axis). The phonon shifts the oxygen atom (along the x direction) and changes the values of the hopping integral t_{pd}.

The phonon breaks the symmetry of the Cu-O-Cu bonds, modulating the inter-site hopping and the on-site energies on both Cu and O sites (Figure 4.5). In [138] $J(\mathbf{E}, \mathbf{u})$ is expanded to order $\partial^2 J/\partial \mathbf{E} \partial \mathbf{u}$, leading to a coupling of a photon to a phonon and two neighboring spins. The dipole moment is then associated with a two-magnon plus phonon absorption, a process that is now IR active.

Dzyaloshinskii-Moriya Interaction (DMI)

Here we analyze the interaction of one single magnon with one phonon. The dynamic Dzyaloshinskii-Moriya mechanism is invoked in this case to explain the possible IR absorption of light.

Dimer system For simplicity, we consider isolated exchange coupled spins $S = 1/2$ (dimers). The effective Hamiltonian is

$$H = J\mathbf{S}_1 \cdot \mathbf{S}_2 \tag{4.47}$$

where J is the exchange coupling between the spins $\mathbf{S}_1$ and $\mathbf{S}_2$. Taking $\mathbf{S} = \mathbf{S}_1 + \mathbf{S}_2$, we chose as basis of eigenstates the common eigenstates of $\mathbf{S}^2$ and S_z, that are the singlet state

$$|S_0\rangle \equiv |0,0\rangle = \frac{1}{\sqrt{2}} \left(|\uparrow\downarrow\rangle - |\downarrow\uparrow\rangle\right), \tag{4.48}$$

and the triplet states

$$\begin{cases} |T_+\rangle \equiv |1,1\rangle = |\uparrow\uparrow\rangle, \\ |T_0\rangle \equiv |1,0\rangle = \frac{1}{\sqrt{2}} \left(|\uparrow\downarrow\rangle + |\downarrow\uparrow\rangle\right), \\ |T_-\rangle \equiv |1,-1\rangle = |\downarrow\downarrow\rangle. \end{cases} \tag{4.49}$$

The eigenvalue of $\mathbf{S}^2$ is $S(S+1)$ with $S = 0$ for the singlet and $S = 1$ for the triplet. The Hamiltonian can be rewritten as

$$\begin{aligned} H_0 |S, S_z\rangle &= \left[\frac{1}{2} J(\mathbf{S}^2 - \mathbf{S}_1^2 - \mathbf{S}_2^2)\right] |S, S_z\rangle \\ &= \left[\frac{1}{2} JS(S+1) - \frac{3}{4} J\right] |S, S_z\rangle . \end{aligned} \tag{4.50}$$

The energies of the eigenstates are in the table 4.1.

Eigenstate	S	S_z	E
$\|0,0\rangle$	0	0	$-\frac{3}{4}J$
$\|1,1\rangle$	1	1	$\frac{1}{4}J$
$\|1,0\rangle$	1	0	$\frac{1}{4}J$
$\|1,-1\rangle$	1	-1	$\frac{1}{4}J$

TABLE 4.1: Eigenstates of H_0 and their respective energies.

Optical absorption Light consists of electromagnetic waves (or their quanta, photons), which are synchronized oscillations of electric $\mathbf{E}_1^\omega$ and magnetic $\mathbf{H}_1^\omega$ fields propagating through space-time. Therefore, the interaction with matter could be of two

types, electric or magnetic. The magnetic field operator is

$$g\mu_B \mathbf{H}_1^{\omega} \cdot (\mathbf{S}_1 + \mathbf{S}_2) \tag{4.51}$$

The transition from the ground-state to triplet excitations induced by the magnetic dipole operator $g\mu_B \mathbf{H}_1^{\omega} \cdot (\mathbf{S}_1 + \mathbf{S}_2)$ is possible if the transition probability

$$I_i^j \propto |\langle T_j | S_{1i} + S_{2i} | S_0 \rangle|, \quad i = x, y, z, \quad j = +1, 0, 1 \tag{4.52}$$

is different from zero. Using relations (4.48) and (4.49) one can explicitly see that the magnetic dipole operator does not couple singlet and triplet states.

On the other hand, the electric dipole operator will not couple to spin states without an extra term in the Hamiltonian and we get a zero transition probability by default.

In general, the excitations from the singlet state ($S = 0$) to the triplet state ($S = 1$) induced by electric and magnetic dipole operators are not allowed in optical spectroscopy. Nevertheless, such excitations can be observed if the singlet and triplet states are mixed, and this is possible in the presence of an antisymmetric interaction.

DMI The Dzyaloshinskii-Moriya interaction (DMI) is an anisotropic exchange interaction arising from the interplay of the spin-orbit coupling and the super-exchange interaction [142, 143]. Such an interaction exists only when the crystal symmetry is sufficiently low.

The antisymmetrical Dzyaloshinskii-Moriya contribution to the Hamiltonian is expressed by

$$\mathbf{D} \cdot (\mathbf{S}_1 \times \mathbf{S}_2) \tag{4.53}$$

where $\mathbf{D}$ is the DM vector. The direction of $\mathbf{D}$ can be determined by pure symmetry considerations. Let the spins $\mathbf{S}_1$ and $\mathbf{S}_2$ be located at the points $\mathbf{R}_1$ and $\mathbf{R}_2$ of the crystal, and the middle point denoted by $\mathbf{R}_c = (\mathbf{R}_1 + \mathbf{R}_2)/2$

(i) If a centre of inversion is located at $\mathbf{R}_c$, $\mathbf{D} = 0$.

(ii) If a mirror plane perpendicular to the line $(\mathbf{R}_1 - \mathbf{R}_2)$ bisects it, $\mathbf{D} \perp (\mathbf{R}_1 - \mathbf{R}_2)$.

(iii) If there is a mirror plane including $\mathbf{R}_1$ and $\mathbf{R}_2$, $\mathbf{D}$ is perpendicular to the mirror plane.

(iv) If a 2-fold rotation axis is perpendicular to $(\mathbf{R}_1 - \mathbf{R}_2)$ and bisects it, $\mathbf{D}$ is perpendicular to the rotation axis.

(v) If there is an n-fold rotation axis ($n > 2$) along $(\mathbf{R}_1 - \mathbf{R}_2)$, $\mathbf{D}$ is parallel to $(\mathbf{R}_1 - \mathbf{R}_2)$.

The DMI can be treated as a perturbation in the Hamiltonian $H = H_0 + W$,

$$H_0 = J\mathbf{S}_1 \cdot \mathbf{S}_2, \tag{4.54}$$

where W with the first and second order corrections [144, 145] is

$$W = -\frac{|\mathbf{D}|^2}{4J}\mathbf{S}_1 \cdot \mathbf{S}_2 + \frac{1}{2J}\mathbf{S}_1 \cdot \mathbf{D}\mathbf{D} \cdot \mathbf{S}_2 + \mathbf{D} \cdot (\mathbf{S}_1 \times \mathbf{S}_2), \tag{4.55}$$

where $\mathbf{DD}$ is the dyadic term, pointed out by Shekhtman [145], which gives correction to both isotropic and anisotropic part of the spin Hamiltonian. This Hamiltomian can be represented as a 4×4 matrix in the basis $\{|T_+\rangle, |T_0\rangle, |T_-\rangle, |S_0\rangle\}$. The

Dzyaloshinskii-Moriya term gives nonzero off-diagonal elements which mixes singlet and triplet states. Depending on the direction of the DM vector $\mathbf{D}$, the singlet state is mixed with $|T_0\rangle$ or $|T_{\pm 1}\rangle$.

When $\mathbf{D} \parallel z$, the Hamiltonian in the matrix representation is

$$H = \begin{pmatrix} \frac{J}{4} + \frac{D^2}{16J} & 0 & 0 & 0 \\ 0 & \frac{J}{4} - \frac{3D^2}{16J} & 0 & -\frac{iD}{2} \\ 0 & 0 & \frac{J}{4} + \frac{D^2}{16J} & 0 \\ 0 & \frac{iD}{2} & 0 & -\frac{3}{4}J + \frac{D^2}{16J} \end{pmatrix} \tag{4.56}$$

The diagonalization of the matrix gives the eigenvalues

$$\begin{aligned} \lambda_{t_+} &= \frac{J}{4} + \frac{D^2}{16J} \\ \lambda_{t_0} &= \frac{J}{4} + \frac{D^2}{16J} \\ \lambda_{t_-} &= \frac{J}{4} + \frac{D^2}{16J} \\ \lambda_{s_0} &= -\frac{3}{4}J - \frac{3D^2}{16J} \end{aligned} \tag{4.57}$$

and the respective eigenvectors $|t_+\rangle, |t_0\rangle, |t_-\rangle, |s_0\rangle$. The states $|t_+\rangle$ and $|t_-\rangle$ still remain the pure states $|T_+\rangle$ and $|T_-\rangle$, instead $|s_0\rangle$ and $|t_0\rangle$ are linear combinations of $|S_0\rangle$ and $|T_0\rangle$

$$|s_0\rangle = |S_0\rangle + \frac{iD}{2J}|T_0\rangle, \tag{4.58}$$

$$|t_0\rangle = -\frac{D^2}{4J^2}|S_0\rangle + \frac{iD}{2J}|T_0\rangle. \tag{4.59}$$

When $\mathbf{B}_0 \perp \mathbf{D} \parallel y$,

$$H = \begin{pmatrix} \frac{J}{4} - \frac{D^2}{16J} & 0 & -\frac{D^2}{8J} & \frac{\sqrt{2}D}{4} \\ 0 & \frac{J}{4} + \frac{D^2}{16J} & 0 & 0 \\ -\frac{D^2}{8J} & 0 & \frac{J}{4} - \frac{D^2}{16J} & \frac{\sqrt{2}D}{4} \\ \frac{\sqrt{2}D}{4} & 0 & \frac{\sqrt{2}D}{4} & -\frac{3}{4}J + \frac{D^2}{16J} \end{pmatrix} \tag{4.60}$$

In this case, $|t_0\rangle \equiv |T_0\rangle$, while $|T_+\rangle$ and $|T_-\rangle$ are mixed with the singlet state $|S_0\rangle$ to create the new eigenstates $|t_+\rangle, |t_-\rangle, |s_0\rangle$.

Static DMI The terms off diagonal in the Hamiltonians (4.56) and (4.60) mix singlet and triplet states. The transition probability for the magnetic dipole operator defined in Eq. (4.52) becomes non-zero and the magnetic excitation could be detectable experimentally by optical singlet to triplet transitions. These transition probabilities for the magnetic dipole operator with DM interactions are calculated by Rõõm et al. [146].

Dynamic DMI The electric dipole transition between singlet and triplet states could be allowed when an optically active phonon is coupled with the electric component $\mathbf{E}_1$ of the electromagnetic radiation of the light, creating a dynamic DMI interaction [147, 148] .

Electric dipole coupling between the phonon and the light in the long wavelength limit is

$$V = e\mathbf{q}\mathbf{E}_1 \tag{4.61}$$

where e is an effective charge associated with a lattice normal coordinate $\mathbf{u}$.

The DM vector is expanded in a power series of u

$$\mathbf{D}(u) = \mathbf{D}(0) + \left.\frac{\partial \mathbf{D}}{\partial u}\right|_{u=0} u + ..., \tag{4.62}$$

where $\mathbf{D}(0)$ is the static DM vactor. Here we chose $\mathbf{D}(0) = 0$. The dynamic DMI is given by

$$H_{DMQ} = u\mathbf{D}_u \cdot (\mathbf{S}_1 \times \mathbf{S}_2), \tag{4.63}$$

with $\mathbf{D}_u = \left.\frac{\partial \mathbf{D}}{\partial u}\right|_{u=0}$.

In the Hamiltonian we have to take into account also the phonon term $\hbar\omega_p a^\dagger a$, where $\hbar\omega_p$ is the phonon energy and $a^\dagger$ and a are the creation and annihilation operators. We consider the phonon states with 0 or 1 phonon. The Hamiltonian becomes:

$$H = \hbar\omega_p a^\dagger a + J\mathbf{S}_1 \cdot \mathbf{S}_2 + H_{DMQ}. \tag{4.64}$$

In this case the dynamic DMI represented by the term H_{DMQ} mix the singlet and the triplet states, *i.e.* it creates off diagonal terms in the Hamiltonian written in the basis $\{|T_+, \nu\rangle, |T_0, \nu\rangle, |T_-, \nu\rangle, |S_0, \nu\rangle\}$, where $\nu = 0, 1$ is associated to 0 or 1 phonon state. As in the static DMI, in order to see the magnetic excitations the transition probability from the ground to the excited states induced by the electric dipole operator (4.61) has to be non-zero. All the calculations are described in [146].

4.3.3 Experimental Setup

In this work, the Fourier Transform infrared (FTIR) spectrometers Bruker IFS 66V/S has been used. This system has a very wide spectral domain from the near to far infrared (between 20000 to 80 cm^{-1}) in both transmission, reflection and emission modes. The spectrometer is mainly composed of the source, the Michelson interferometer, the sample and the detector, as illustrated in Figure 4.6.

The radiation coming from the external source is focused by parabolic mirrors and a parallel beam enters the Michelson interferometer. Here the radiation is divided in two directions by a beamsplitter. One beam is reflected onto a stationary mirror, M1. The other is transmitted by the beamsplitter and goes to a moving mirror, M2. Both beams return again to the beamsplitter where they recombine. The path difference, created by the motion of M2, gives constructive and destructive interference producing an interferogram. The relationship between the interferogram function $I(x)$ and the source intensity $S(\omega)$ is given by the Fourier transform:

$$S(\omega) \propto \int_0^\infty \left(I(x) - \frac{1}{2}I(0)\right) \cos(2\pi\omega x) dx \tag{4.65}$$

where $I(0)$ is the intensity detected when M1 and M2 have the same distance with respect to the beamsplitter (zero path difference). A laser beam (usually a He-Ne Laser) with well know frequency is superimposed to provide the position of the moving mirror M2 in a very precise way.

The recombined beam is now focussed onto the sample inside a cryostat, with which measurements in a temperature range from 5K to 800K are possible. The

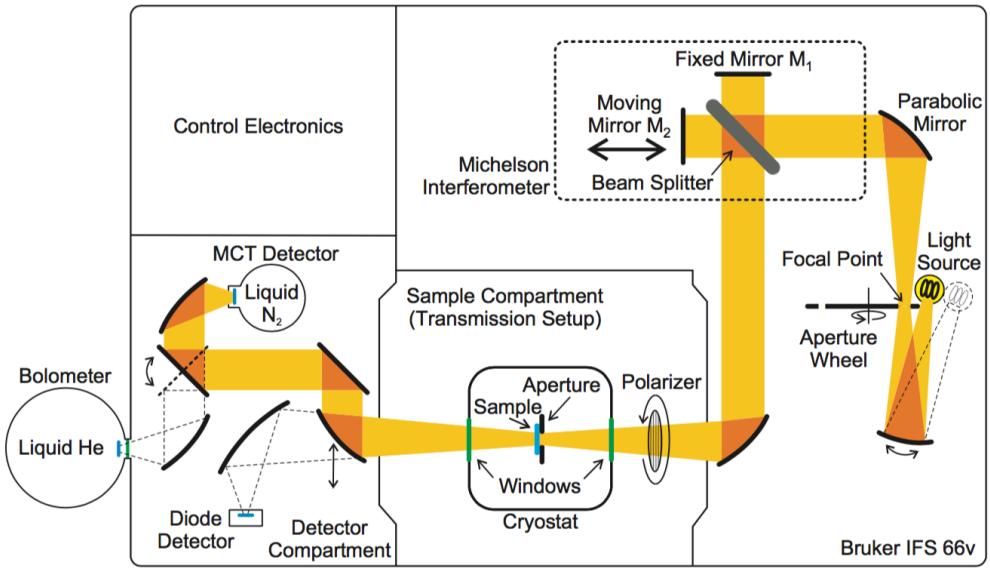

FIGURE 4.6: Schematic diagram of the Bruker IFS 66V/S spectrometer.

sample absorbs all the different wavelengths characteristic of its spectrum, and this subtracts specific wavelengths from the interferogram. Finally, the detector reports the spectrum of the sample $S_{\text{sample}}(\omega)$. The typical transmittance $T(\omega)$ is taken as the ratio of the sample spectrum to the reference.

$$T(\omega) = \frac{S_{\text{sample}}(\omega)}{S_{\text{ref}}(\omega)}. \tag{4.66}$$

In order to cover the suitable spectral range, there exist different light sources, beamsplitter and detector. In our setup, the light source is a Globar source, which is optimized for far and mid infrared regions. A combination of a KBR beamsplitter and MCT (Mercury Cadmium Telluride) detector is required in the MIR and in the FIR a multilayer (T222) and a Si bolometer were used.

Chapter 5

The new frustrated spin ladder $Li_2Cu_2O(SO_4)_2$

"How wonderful that we have met with a paradox.
Now we have some hope of making progress."

Niels Bohr

In this chapter we investigate the magnetic properties of the new compound $Li_2Cu_2O(SO_4)_2$ recently synthesized at the College de France.

In its high-temperature phase it has a tetragonal structure which appears topologically equivalent to a two-leg spin-ladder system. Magnetic susceptibility measurements show a clear spin-singlet ground-state and a spin-gapped behavior indicative of dominant AFM couplings. We perform electronic structure calculation in the framework of Density Functional Theory, as it is currently implemented in QUANTUM ESPRESSO, in order to qualitatively study the magnetic properties of this compound and to determine the sign and strength of the dominant magnetic couplings. Calculations carried out at the DFT+U level clearly confirm the quasi-1D magnetism of the compound as well as the presence of strong frustration. As a result, this compound appears as a rare material realization of a frustrated spin-1/2 two-leg ladder, where magnetic frustration arises from competing nearest (NN) and next-nearest (NNN) interactions along the legs.

Furthermore, experimental investigations reveal the occurrence of a weak and progressive structural transition from the tetragonal to the triclinic group at around 125 K. Magnetic couplings obtained from DFT calculations carried out using the experimental temperature-dependent atomic structure of $Li_2Cu_2O(SO_4)_2$ (Rietveld refinement of synchrotron X-ray and neutron diffraction data) reveal a very strong magnetic dimerization of the spins along the legs of the ladder as a result of the triclinic structural distortion, lifting most of the magnetic frustration.

Results and discussions of this chapter are strongly inspired by our recent articles [14] and [15].

5.1 A new frustrated spin ladder $Li_2Cu_2O(SO_4)_2$

5.1.1 Crystallographic structure

$Li_2Cu_2O(SO_4)_2$ has been synthetized for the first time in 2015 [13]. This compound was obtained from Li_2O (Alfa Aesar, 99.5 %) and $CuSO_4$ (Alfa Aesar, Reagent grade) according to the reaction $Li_2O + 2\ CuSO_4 \rightarrow Li_2Cu_2O(SO_4)_2$ as an emerald-green powder.

TABLE 5.1: Structural parameters for $Li_2Cu_2O(SO_4)_2$, deduced from the combined Rietveld refinement of the Synchrotron XRD and neutron diffraction patterns at 300 K. A bond valence sum analysis (BVS) is also reported for each atom.

$Li_2Cu_2O(SO_4)_2$, high temperature phase						
Space Group: $P4_2/m$						
$a = 8.324560(12)$ Å, $c = 5.089952(14)$ Å, $V = 352.725(1)$ Å^3						
Atom	Wyckoff site	x	y	z	B(Å^2)	BVS
Li1	$2d$	0	0.5	0.5	2.6(2)	0.91(2)
Li2	$2f$	0.5	0.5	0.25	0.56(14)	1.23(3)
Cu	$4j$	0.16055(9)	0.06465(8)	0	0.554(11)	2.05(3)
S	$4j$	0.31687(17)	0.22596(16)	0.5	0.60(2)	6.08(2)
O1	$8k$	0.32953(19)	0.12343(16)	0.7375(3)	1.28(3)	2.02(2)
O2	$4j$	0.1687(3)	0.3128(2)	0.5	0.96(4)	2.05(2)
O3	$4j$	0.4570(2)	0.3359(3)	0.5	0.59(4)	2.08(2)
O4	$2e$	0	0	0.25	0.40(6)	2.03(2)

The interest in this compound lies in its peculiar room-temperature crystallographic structure, shown in Figure 5.1 (a) and (b), solved from combined neutron and synchrotron X-ray powder diffraction. The structure has a tetragonal symmetry, with space group $P4_2/m$. Table 5.1 gathers the structural parameters obtained from the Rietveld refinement. Li atoms sit in $2d$ and $2f$ Wyckoff positions. The former position, occupied with Li1, is octahedrally coordinated with O1 and O2 oxygen atoms, while the latter, occupied with Li2, is in the middle of a tetrahedron made of O3 oxygen atoms. All O1, O2, and O3 are also part of a SO_4 tetrahedron. O4 is the only oxygen atom not being linked to a sulfur atom. It is on the $2e$ Wyckoff position and bridges the four copper atoms of the unit cell which are placed on the $4j$ position. Cu^{2+} is therefore surrounded by two O1 and two O4 oxygen atoms, so as to form a square planar environment, commonly observed for this Jahn-Teller ion. The room-temperature tetragonal structure of $Li_2Cu_2O(SO_4)_2$ is shown in Fig. 5.1 (a). Among all these atoms, only the copper is magnetic. It's a Cu^{2+} in a $3d^9$ electronic configuration, that carries the spin-1/2 because of a hole in its electronic structure (see Figure 2.2).

The resulting square-planar structural units CuO_4 are grouped by two, sharing an edge to form $[Cu_2O_6]^{4-}$ platelets. These platelets are connected one to each other at 90°, sharing an oxygen atom. Under the effect of the 4_2 helical axis, this leads to infinite $[Cu_2O_5]$ chains running along the c axis of the crystal. Tetrahedral polyatomic anions SO_4 further link every second platelet along the chains by sharing two oxygen ions with them. These chains are finally well separated from each other by the Li^+ ions (see Fig. 5.1 (b)).

If we only consider the coppers, we obtain an ensemble of tetrahedra linked by edges (Figure 5.1 (c)). From magnetostructural considerations, dominant magnetic couplings should occur in this structure. In particular, we recognize the superexchange mechanisms supported by Cu-O-Cu bonds that are related to an intra-platelet coupling $J_\perp$ and inter-platelet coupling J. Furthermore, the presence of the sulfate group SO_4 creates a non-magnetic bridge that can play a preponderant role in mediating strong and long ranged antiferromagnetic (AFM) interactions, leading in

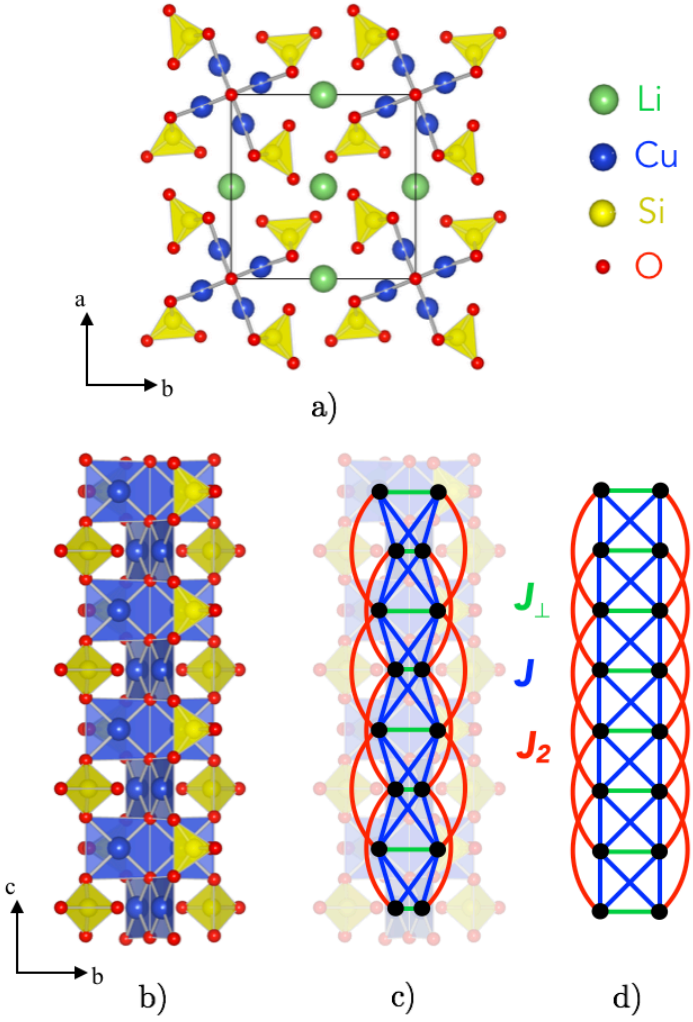

FIGURE 5.1: a) Atomic structure of $Li_2O(CuSO_4)_2$. Cu are in blue, O in red, S in yellow and Li in green. b) Detail of the atomic structure of the copper chain. c) Magnetic model deduced from the atomic structure, with the tree dominant interactions along the chain, $J_\perp$ in green, J in blue and J_2 in red. d) Topologically equivalent frustrated two-leg spin ladder.

the present case to sizeable second-nearest neighbor interaction along the chains J_2 (see 5.1 (c)). As additional interchain interactions are expected to be weak due to the absence of well-defined covalent superexchange paths, this compound should exhibit a strong quasi-1D character. This system is thus topologically equivalent to the two-leg ladder system represented in Figure 5.1 (d).

If we assume AFM interactions the system should be *frustrated*, meaning that whichever direction it points, it is unable to simultaneously satisfy the other two AFM interactions. We are therefore in the presence of a very rare example of frustrated spin-1/2 two-leg ladder.

We used Density Functional Theory (DFT) calculation as the first step to understand the electronic structure and the magnetic properties of this system, as illustrated in 3.1.

5.1.2 Electronic structure calculation

In this work, we carry out DFT calculation in the QUANTUM ESPRESSO simulation package [149]. We use a plane-wave basis set methods with ultrasoft pseudopotentials [150]. We choose the GGA paramagnetic approximation [97] parametrized by Perdew-Burkew-Enzerhof (PBE) exchange correlation to have a qualitative result of the electronic band structure independent of the spin that could be mapped onto an Hubbard model. This mapping in the strongly correlated limit, at half filling, reduces the Hubbard model to an AFM Heisenberg model and provides a link between the hopping integrals (independent of the magnetism) and the coupling terms (See Appendix A).

In order to have a good balance between accuracy and computational cost, we choose a k-grid $4 \times 4 \times 7$ with a plane-wave and charge density cutoffs of 60 and 480 Ry, respectively. The result of the DFT calculation is shown in Fig. 5.2, where we have set the value of the Fermi energy to zero.

The band structure reveals the presence of four bands (two of them are almost degenerate) close to the Fermi level well separated from the continuum manifold, related to the four copper atoms in the unit cell that interact with the oxygens creating hybridized orbitals between the Cu-$3d_{x^2-y^2}$ orbitals and the $2p$ states of the oxygens. In Figure 5.3 we focus around the Fermi level. We recognize the four bands and

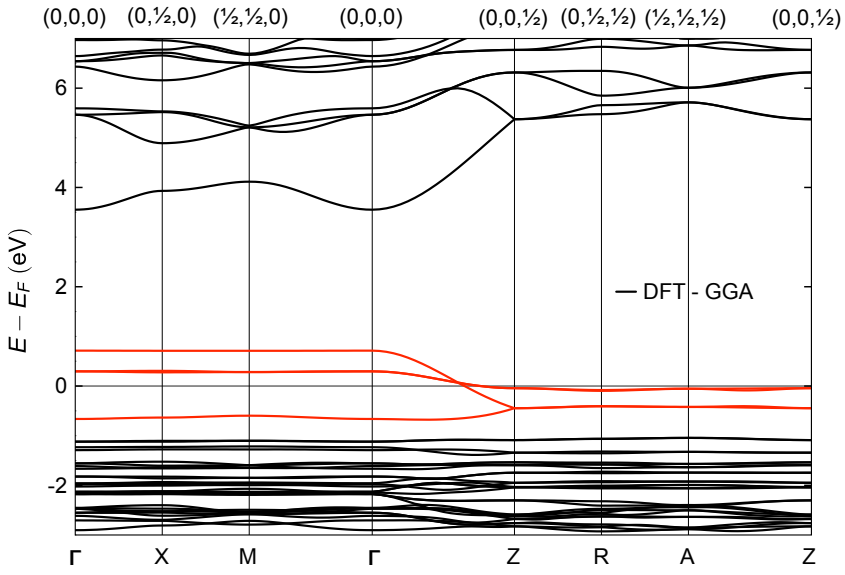

FIGURE 5.2: Paramagnetic band structure of $Li_2Cu_2O(SO_4)_2$ calculated using GGA-PBE.

the corresponding DOS, which show that the major contribution comes from the Cu-$3d_{x^2-y^2}$ orbital hybridized with the O-$2p$. Furthermore, the four bands are almost dispersionless, the only significant dispersion is along Γ - Z, which corresponds to the direction of the chains. This confirms the quasi-1D character of these electronic states, expected from structural considerations.

As illustrated in 3.1.3, Maximally localized Wannier function (MLWF) interpolation of the band structure is performed using WANNIER90 and is shown in Fig. 5.3. We obtain the four Wannier orbitals in the unit cell, centered on the Cu sites, which have the shape of the typical $3d_{x^2-y^2}$ orbitals with the large antibonding O-$2p$ tails

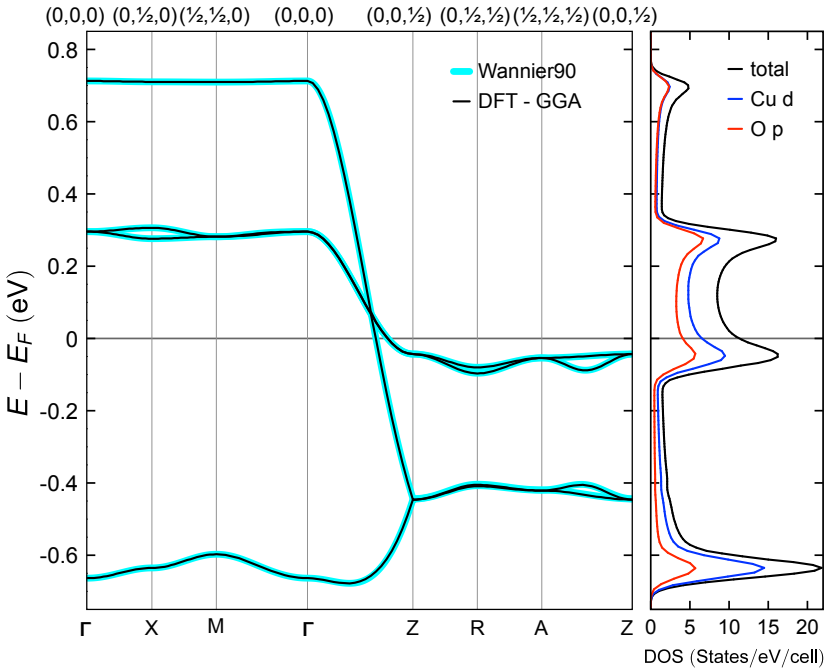

FIGURE 5.3: Detail of the paramagnetic band structure of $Li_2Cu_2O(SO_4)_2$ around the Fermi level, calculated using GGA-PBE and interpolated with MLWFs (left panel) and corresponding total and partial density of states (right panel).

clearly visible on neighboring atoms (Figure 5.4). This interpolation allows the extrac-

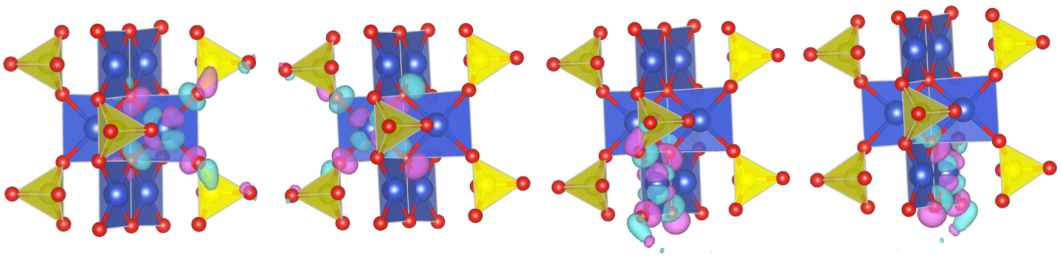

FIGURE 5.4: The four MLWFs extracted from the Wannier90 post processing.

tion of the effective hopping integrals between magnetic orbitals and reveals that three interactions largely dominate the dispersion: the intraplatelet hopping $t_\perp = -146$ meV, the NN interplatelet hopping $t = 161$ meV, and the NNN hopping along the legs $t_2 = 101$ meV.

To verify whether only three hopping parameters can accurately describe the properties of the system, we solve a tight-binding model assuming four localized orbitals on the copper atoms as a basis set. We have 4 coppers in the unit cell and one atomic

orbital for each copper, so we construct the 4×4 effective Hamiltonian:

$$H_{eff} = \begin{bmatrix} \epsilon_{3d} + 2t_2\cos(2\pi k_z) & t_\perp & t(1+e^{-i2\pi k_z}) & t(1+e^{-i2\pi k_z}) \\ t_\perp & \epsilon_{3d} + 2t_2\cos(2\pi k_z) & t(1+e^{-i2\pi k_z}) & t(1+e^{-i2\pi k_z}) \\ t(1+e^{+i2\pi k_z}) & t(1+e^{+i2\pi k_z}) & \epsilon_{3d} + 2t_2\cos(2\pi k_z) & t_\perp \\ t(1+e^{+i2\pi k_z}) & t(1+e^{+i2\pi k_z}) & t_\perp & \epsilon_{3d} + 2t_2\cos(2\pi k_z) \end{bmatrix} \tag{5.1}$$

The resulting analytical four bands are:

$$\begin{cases} \epsilon_{1,2}(\mathbf{k}) = \epsilon_{3d} - t_\perp + 2t_2\cos(2\pi k_z) \\ \epsilon_3(\mathbf{k}) = \epsilon_{3d} + t_\perp - 4t\cos(\pi k_z) + 2t_2\cos(2\pi k_z) \\ \epsilon_4(\mathbf{k}) = \epsilon_{3d} + t_\perp + 4t\cos(\pi k_z) + 2t_2\cos(2\pi k_z) \end{cases} \tag{5.2}$$

The hopping integrals are extracted through a least-square fit of the numerical DFT bands, giving

$$\begin{cases} t_\perp = -154.551 \text{ meV} \\ t = 167.705 \text{ meV} \\ t_2 = 101.980 \text{ meV} \end{cases} \tag{5.3}$$

These values for the hopping parameters are consistent with the ones extracted from the WANNIER90 calculation. Figure 5.5 shows the result of the corresponding tight-binding analysis, represented in red, which reproduces fairly well the DFT electronic band structure. The model with the 3 dominant interactions could therefore be a realistic model for the quasi-1D compound $Li_2Cu_2O(SO_4)_2$.

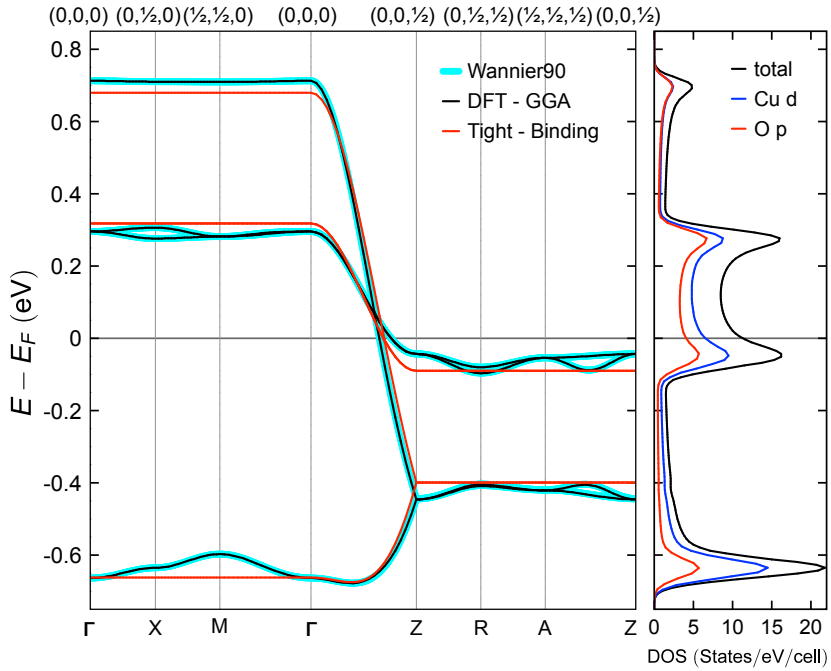

FIGURE 5.5: Paramagnetic band structure (left panel), total and partially density of states of $Li_2O(CuSO_4)_2$ (right panel). In black the GGA-PBE paramagnetic band structure, interpolation with MLWFs in sky-blue and in red the result of the tight-binding fit.

We can now map the paramagnetic band structure onto a single-band Hubbard

model that, in the strongly correlated limit and at half-filling, is reducing to an antiferromagnetic Heisenberg model. This mapping provides a direct link between the hopping parameters and the AFM component of the magnetic couplings, through the expression $J_{AFM} = 4t^2/U_{eff}$. As we have three dominant hopping terms of the order of 100 meV, one could expect three dominant couplings $J_\perp$, J , and J_2 essentially AFM, with $J_\perp$ and J of the same order of magnitude and J_2 is about half. However, this simple analysis overlooks the presence of potentially large ferromagnetic (FM) contributions which, depending on the detailed atomic arrangement supporting the superexchange mechanisms, could partially balance or even dominate their AFM counterparts. The three expected dominant couplings are shown in Fig. 5.1 (d). J_2 corresponds to a long-range interaction mediated by the bridging SO_4 group, the Cu-O-S-O-Cu bond, also called super-super-exchange interaction (see 2.1.2). J and $J_\perp$ goes through the Cu-O-Cu super-exchange mechanism and as the Cu-O-Cu angle increases, the coupling between the copper ions switches from FM to AFM. In particular, the J couplings are related to the Cu-O-Cu bonds with an angle of 116°, corresponding to a dominant AFM component. Indeed, for $J_\perp$ we find a Cu-O-Cu angle of 97°, close to the FM-AFM crossover [24].

5.1.3 Evaluation of the couplings in DFT+U

In order to calculate these three couplings we construct a supercell $1\times1\times2$ by doubling the tetragonal unit cell along the c direction. As we have four magnetic centers per unit cell, we obtain $2^8 = 256$ configurations, among which 18 inequivalent configurations with degeneracies g_α because of spin reversal and crystalline symmetries. In Figs. 5.6 (a) and (b) are shown two simple possible configurations, the ferromagnetic (a), that has degeneracy $g = 2$, and two of the 4 possible "antiferromagnetic" order (b).

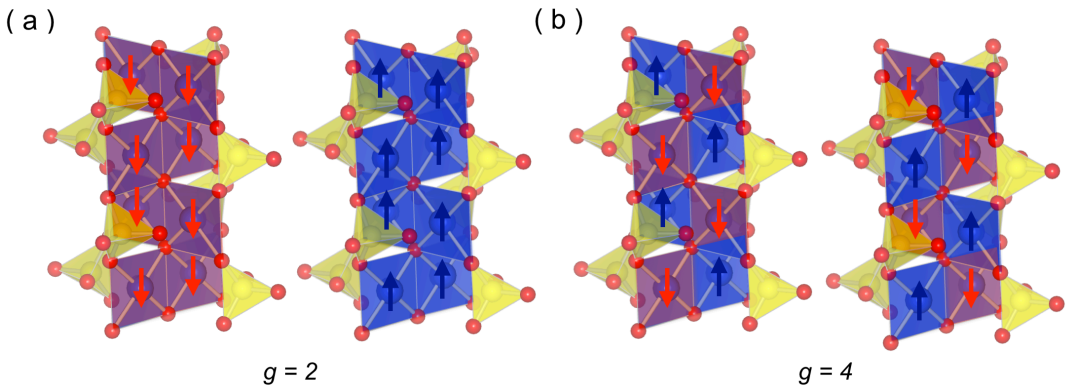

FIGURE 5.6: Ferromagnetic (a) and antiferromagnetic (b) configurations in the supercell $1 \times 1 \times 2$.

A rigorous evaluation of the exchange couplings is based on the broken-symmetry formalism in DFT+U [151, 152], as described in 3.1.4.

Hubbard U term In order to take into account the strongly correlated character of the Cu-3d electrons, we have to add an Hubbard U term in the DFT calculation. In the linear-response approach, as described in 3.1.1, the Hubbard U term is calculated from the inverse of the response matrix $\chi_{IJ} = \dfrac{\partial n_I}{\partial \alpha_J}$, where α represents a small perturbation applicable to the copper atoms. We have to subtract the non-interacting contribution, calculated from the first iteration, thus $U = (\chi_0^{-1} - \chi_1^{-1})_{II}$. The self-consistent U_{scf} is

determined for a $1 \times 1 \times 2$ supercell from the extrapolation of U_{out} calculated over a range of U_{in} (from 0 to 5 eV), where the relationship is linear (Figure 5.7). We obtain

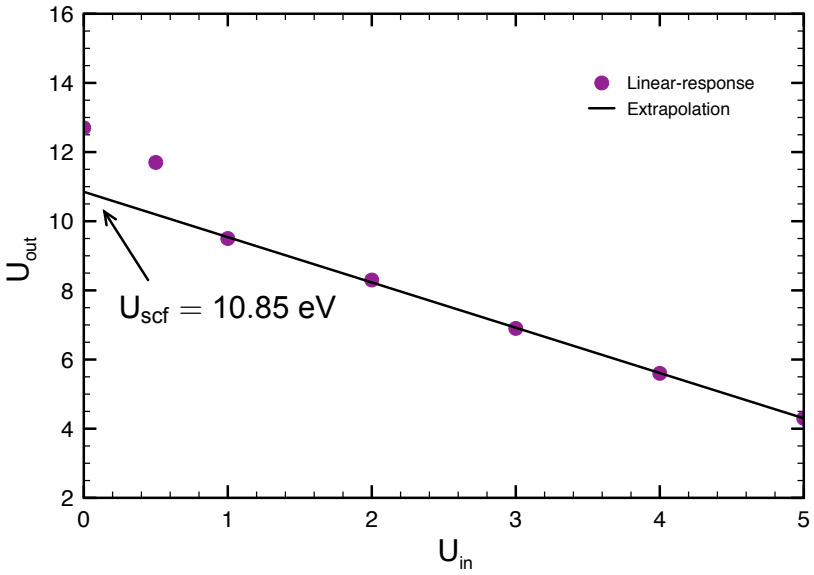

FIGURE 5.7: Calculation of the self-consistent U_{scf}.

a value of $U_{scf} = 10.85$ eV for the effective self-consistent Hubbard term.

Broken symmetry formalism We can now use the GGA-PBE semilocal exchange-correlation functional [97] with the self-consistent Hubbard term $U_{scf} = 10.85$ eV to find the values of the couplings. Following the approach proposed in [118], we assumed that the magnetic excitations in $Li_2Cu_2O(SO_4)_2$ can be described with an Heisenberg Hamiltonian

$$\hat{H} = \hat{H}_0 + \sum_{i>j} J_{ij}\, \hat{\mathbf{S}}_i \cdot \hat{\mathbf{S}}_j \tag{5.4}$$

where $\hat{H}_0$ represents the spin-independent part of the Hamiltonian, $\hat{\mathbf{S}}_i$ and $\hat{\mathbf{S}}_j$ stem for the spin-1/2 operators localized on sites i and j and J_{ij} is the magnetic coupling between these moments. We prepared the state $|\alpha\rangle$ characterized by a particular collinear spin arrangement in the supercell and obtained by a self-consistent loop until convergence. The expectation value of the Hamiltonian 5.4 on the state $|\alpha\rangle$ is:

$$\epsilon_\alpha^{DFT} = \langle\alpha|\hat{H}|\alpha\rangle = \epsilon_0 + \sum_{ij} \frac{J_{ij}}{4}\sigma_i\sigma_j \tag{5.5}$$

with $\sigma_i = \pm 1$. The total energy can be expressed also in term of the three expected Ising couplings as:

$$\epsilon_{Ising} = \epsilon_0 + \sum_{k=0}^{3} a_{\alpha k} J_k \tag{5.6}$$

where $a_{\alpha k}$ depends on the configuration. Numerical total energies obtained from DFT calculations for a set of distinct spin configurations can thus be analysed in terms of these Ising expressions involving the unknown magnetic couplings. For large sets of configurations, an overdetermined system of equations is obtained and solved using standard least-squares fitting procedures [118, 119, 120], i.e. by minimizing the

difference between DFT and Ising energies:

$$F = \sum_{\alpha=1}^{N_{conf}} g_\alpha \left(\epsilon_\alpha^{DFT} - \epsilon_{Ising}\right)^2 . \tag{5.7}$$

where N_{conf} is the number of spin-configurations and g_α represents the degeneracy of the particular α configuration. The mapping has been carried out using the total energies of 42 spin configurations calculated in a $1 \times 1 \times 2$ supercell containing four formula units and based on the experimental structure determined at ~ 300 K. Fig. (5.8) shows the results of the least-squares fitting procedure.

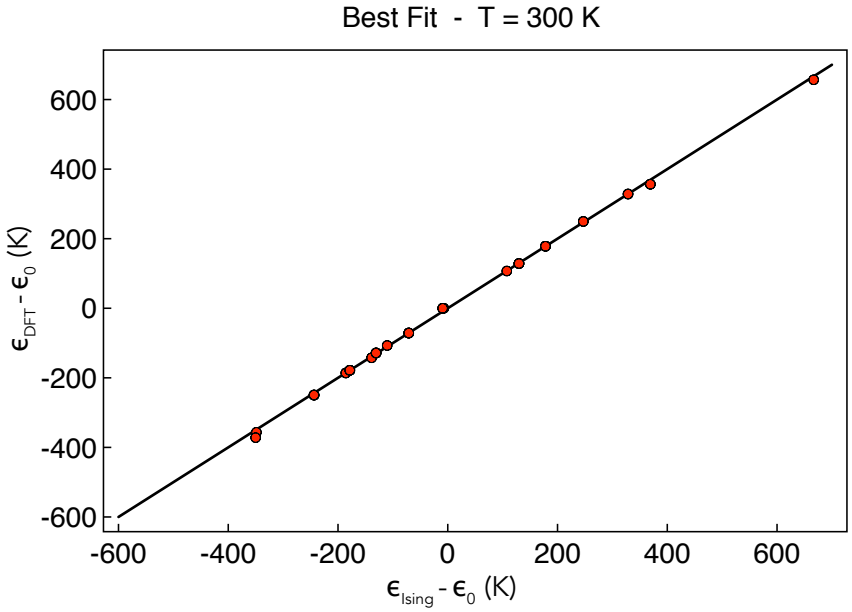

FIGURE 5.8: Graphical representation of the results obtained by using the least-square fitting procedure of the magnetic couplings for the tetragonal phase at T= 300 K.

The resulting couplings are:

$$\begin{cases} J_\perp = -100 \text{ K} \\ J \approx J_2 = 127 \text{ K} \end{cases} \tag{5.8}$$

We obtained, as expected, antiferromagnetic couplings J and J_2, but $J_\perp$ turned out to be ferromagnetic. This is a confirmation of the partially frustrated character of the system, where the geometrical frustration arises from competing nearest (NN) and next-nearest neighbour (NNN) interactions along the legs (i.e. J v.s. J_2).

Furthermore, the values of the magnetic couplings mark a region of the phase diagram that has not been studied so far in literature. Vekua and Honecker [9] have determined the full phase diagram only for $0 \ll J_\times \ll J$, $0 \ll J_\perp$ in the plane $J_2 = J/2$, where rung singlet, Haldane, columnar singlet and staggered singlet phases can be distinguished (see 2.4.3). In our system, we have found a ferromagnetic coupling $J_\perp$ and a ratio $J_2/J \approx 1$. The realization of a Haldane ground-state seems therefore highly probable in the high temperature phase of this compound.

5.1.4 Magnetic susceptibility

The temperature dependence of the magnetic susceptibility was measured using a SQUID (XL, Quantum Design), between 2 and 400 K under a magnetic field of 5000 Oe (Figure 5.9).

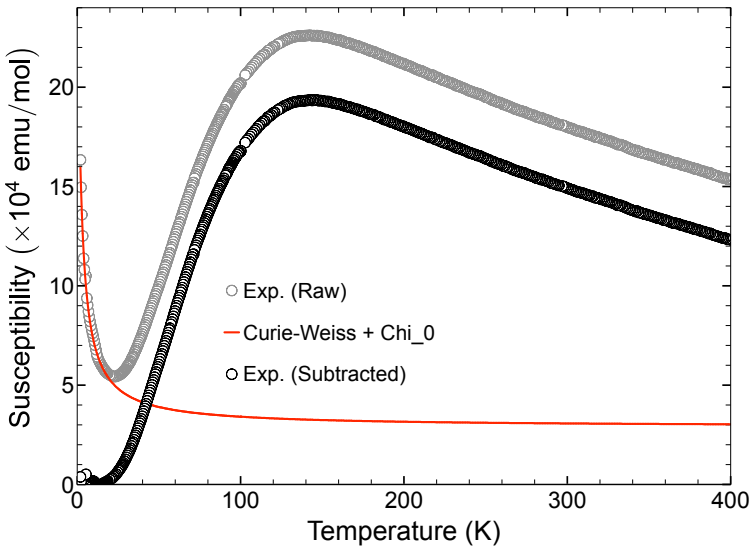

FIGURE 5.9: Magnetic susceptibility (under 5000 Oe). The raw susceptibility (gray circles) was corrected from a paramagnetic and temperature independent contributions (red line), to obtain the $Li_2Cu_2O(SO_4)_2$ susceptibility (black circles).

The susceptibility shows a smooth increase down to 150 K, followed by a exponential decrease and a subsequent sharp increase at very low temperature. The latter varies in amplitude from one batch to another and likely arises from a small amount of paramagnetic impurities. It has been shown [14] that Li_2SO_4 and $CuSO_4$ are likely impurities. Therefore the experimental susceptibility has been corrected from both the paramagnetic tail, fitted through a Curie Weiss law, $\chi_{\text{imp}} = C_{\text{imp}}/(T - \theta_{\text{imp}})$, where C_{imp} and θ_{imp} are, respectively, the Curie-Weiss constant and temperature of the impurity, and from a temperature-independent contribution χ_0 arising from the sample holder and core diamagnetism of the compound. The following values were used: $\chi_0 = 2.2 \times 10^{-4}$ emu mol^{-1}, $\theta_{\text{imp}} = -2.6$ K, and $C_{\text{imp}} = 6.4 \times 10^{-3}$ emu K mol^{-1}. These contributions were then subtracted from the total susceptibility, to obtain a signal coming from $Li_2Cu_2O(SO_4)_2$ only.

The resulting susceptibility exhibits a broad maximum at about 125 K, characteristic behavior for low-dimensional 1D antiferromagnetic system, and decreases exponentially at lower temperatures. This development describes a clear spin-singlet ground-state and a spin-gapped behavior which confirms the presence of dominant AFM couplings of the order of 100 - 200 K.

However, before engaging in a thorough study of the magnetic properties, it is of utmost importance to check the structural behavior of $Li_2Cu_2O(SO_4)_2$ below room temperature, in order to spot possible structural transitions. Indeed, many Cu^{2+}-based compounds present structural distortions at low temperature, such as the spin-Peierls transition in $CuGeO_3$ [35]. The aim of the next section is to investigate, via complementary synchrotron X-ray and neutron powder diffraction, the structural features of $Li_2Cu_2O(SO_4)_2$ down to 2 K.

5.2 Structural phase transition

The structure of $Li_2Cu_2O(SO_4)_2$ was explored by complementary synchrotron X-ray diffraction data (XRD) at the ID22 beamline at ESRF (Grenoble, France) and neutron powder diffraction data measured at the D20 neutron diffractometer at Institut Laue Langevin (Grenoble, France) in Figs. 5.10 and 5.11, respectively. This way, the structure can be assessed with confidence as the extreme resolution of the synchrotron allows a precise determination of the lattice parameters, while neutron diffraction provides accurate atomic positions.

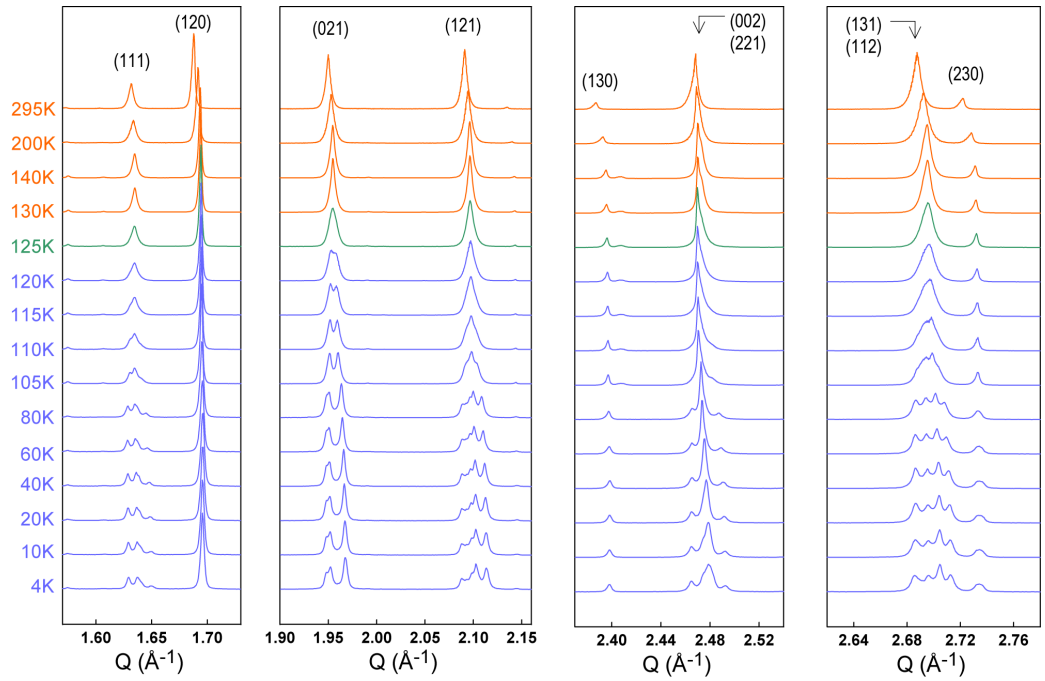

FIGURE 5.10: Evolution of the synchrotron X-ray powder patterns of $Li_2Cu_2O(SO_4)_2$ between 295 and 4 K. Note the splitting of some (hkl) reflections when the temperature is decreased below 125 K (green pattern).

The powder neutron diffraction on D20 confirmed the absence of magnetic long-range order down to 2 K. Moreover, at 125 K, some (hkl) reflections split and the splitting expands continuously on cooling down to 4 K. The relative intensities remain similar between the high and the low-temperature phase, so that this behaviour is typical of a progressive and weak transition.

The structure at 2 K is refined in the $P\bar{1}$ triclinic space group. The refined atomic positions and structure parameters for the low-temperature triclinic phase are gathered in Table 5.2.

The low-temperature structure is plotted in Fig. 5.12 (a) super-imposed with the structure at 300 K shown with gray atoms. It appears clearly that both structures are very close to each other. In particular, Li positions are almost superimposable, so are O2, O3 and O4 atoms (labels refer to the tetragonal description). O1, S, and to a lesser extent Cu appear to experience the largest displacements, so that the symmetry breaking induces a tilt in the Cu_2O_6 platelets, as highlighted by arrows in Fig. 5.12 (b). Even though atomic displacements are small, this transition has important effects on the Cu-Cu framework. The edge-sharing Cu_4 tetrahedra become distorted, as can

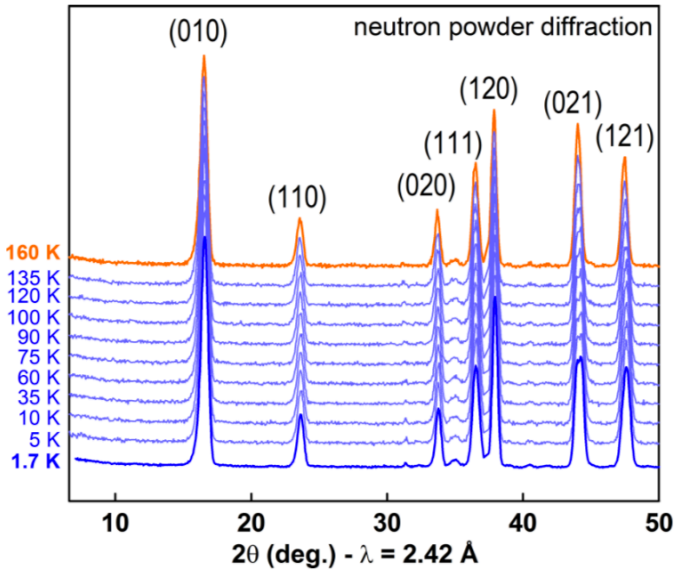

FIGURE 5.11: Evolution of the neutron powder diffraction patterns of $Li_2Cu_2O(SO_4)_2$ while cooling the sample from 160 K down to 1.7 K. (hkl) indexes refer to the tetragonal cell.

be observed in Fig. 5.12 (c). At 300 K, interplatelet bonds have all the same length imposed by symmetry [3.2602(7) Å], whereas the intraplatelet bond, perpendicular to [001], and shared between two adjacent tetrahedra, is 2.8816(10) Å. The triclinic distortion leads to six individual distances for each tetrahedron. The edge-sharing Cu-Cu intraplatelet distance is split into two, with distances of 2.8744(19) Å (Cu1-Cu1) and 2.8833(18) Å (Cu2-Cu2), echoing the splitting of Cu into Cu1 and Cu2. The splitting in distances is more severe for the four previously equivalent interplatelet bonds: the shortest, shown in yellow in Fig. 5.12, has a distance of 3.139(3) Å and the longest (shown in red) has a distance of 3.363(3) Å.

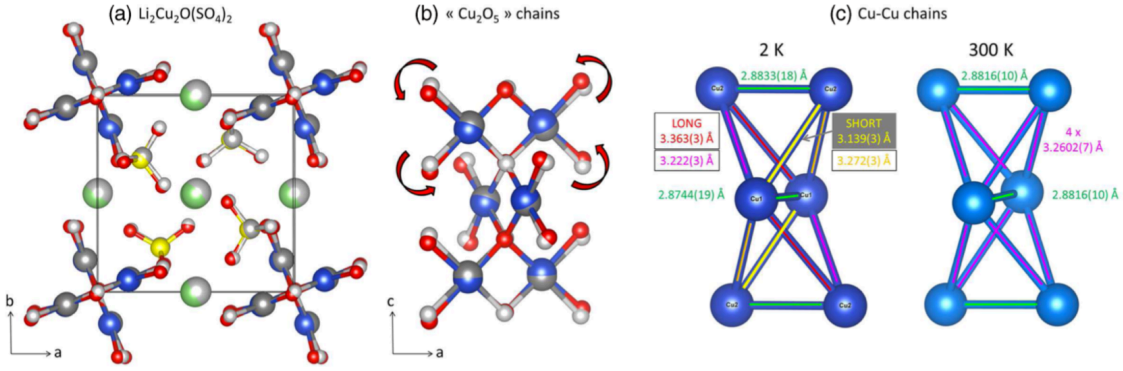

FIGURE 5.12: (a) and (b) Superposition of the room temperature tetragonal and low-temperature triclinic structures of $Li_2Cu_2O(SO_4)_2$. The structure of the low-temperature triclinic phase at 2 K is shown with colors: Cu is blue, Li is green, S is yellow, and O is red. The atoms shown in gray are those of the room temperature tetragonal phase. (c) View of the edge-sharing Cu tetrahedral chains at 2 and 300 K, with Cu-Cu distances reported.

TABLE 5.2: Structural parameters for $Li_2Cu_2O(SO_4)_2$, deduced from the combined Rietveld refinement of the Synchrotron XRD at 4 K and neutron diffraction patterns at 2 K. A bond valence sum analysis (BVS) is also reported for each atom.

$Li_2Cu_2O(SO_4)_2$, low-temperature phase
Space Group: $P\bar{1}$
Synchrotron, 4 K:
$a = 8.29197(3)$ Å, $b = 8.27975(2)$ Å, $c = 5.06688(2)$ Å
$\alpha = 90.4362(3)$ deg., $\beta = 90.5984(3)$ deg., $\gamma = 90.0666(3)$ deg.
$V = 347.839(2)$ Å^3
Neutrons, 2 K:
$a = 8.2889(6)$ Å, $b = 8.2791(6)$ Å, $c = 5.07645(4)$ Å
$\alpha = 90.4332(17)$ deg., $\beta = 90.5385(16)$ deg., $\gamma = 90.0838(13)$ deg.
$V = 348.34(4)$ Å^3

Atom	Wyckoff site	x	y	z	B(Å^2)	BVS
Li1	1d	0.5	0	0	0.42(12)	0.95(2)
Li2	1g	0	0.5	0.5	0.42(12)	0.96(2)
Li3	2i	0.5048(15)	0.5039(16)	0.753(3)	0.42(12)	1.22(2)
Cu1	2i	0.16085(16)	0.06400(17)	0.0209(3)	0.17(2)	2.12(2)
Cu2	2i	0.93570(17)	0.16156(15)	0.4899(3)	0.17(2)	2.02(2)
S1	2i	0.3196(3)	0.2250(3)	0.5278(6)	0.25(3)	5.91(2)
S2	2i	0.7764(4)	0.3207(3)	0.9921(6)	0.25(3)	6.02(2)
O1	2i	0.3362(5)	0.1372(6)	0.7831(9)	0.205(17)	2.04(2)
O2	2i	0.6751(5)	0.8955(6)	0.6918(9)	0.205(17)	1.95(2)
O3	2i	0.8950(5)	0.3300(5)	0.2161(9)	0.205(17)	1.98(2)
O4	2i	0.1389(6)	0.6660(5)	0.2623(9)	0.205(17)	2.05(2)
O5	2i	0.8322(5)	0.6877(5)	0.4832(8)	0.205(17)	1.96(2)
O6	2i	0.6867(5)	0.1712(5)	0.0089(8)	0.205(17)	1.97(2)
O7	2i	0.4614(6)	0.3331(5)	0.5043(8)	0.205(17)	2.06(3)
O8	2i	0.6674(5)	0.4604(6)	0.0118(9)	0.205(17)	2.18(3)
O9	2i	- 0.0032(5)	0.9902(5)	0.2440(9)	0.205(17)	2.094(13)

For sake of completion, all synchrotron X-ray diffraction patterns were refined using this triclinic cell up to 125 K, and with the tetragonal cell between 130 and 300 K. The lattice parameter evolution is shown in Fig. 5.13 (a) and (b) and shows that the triclinic distortion gets larger on cooling, as already guessed from examination of the peaks splitting (Fig. 5.10). Fig. 5.13 (c) reports the evolution of the unit cell volume versus temperature. It is worth noting that, within the experimental error, the tetragonal-triclinic transition is not accompanied by a discontinuous change in the unit cell volume.

Therefore, neutron diffraction and synchrotron X-ray reveal the occurrence of a continuous, weak and progressive structural phase transition in $Li_2Cu_2O(SO_4)_2$, starting from $\sim$ 125 K, from the tetragonal $P4_2/m$ to the triclinic $P\bar{1}$ space group. The compound, which appears as a rare realization of a spin-1/2 frustrated spin ladder in

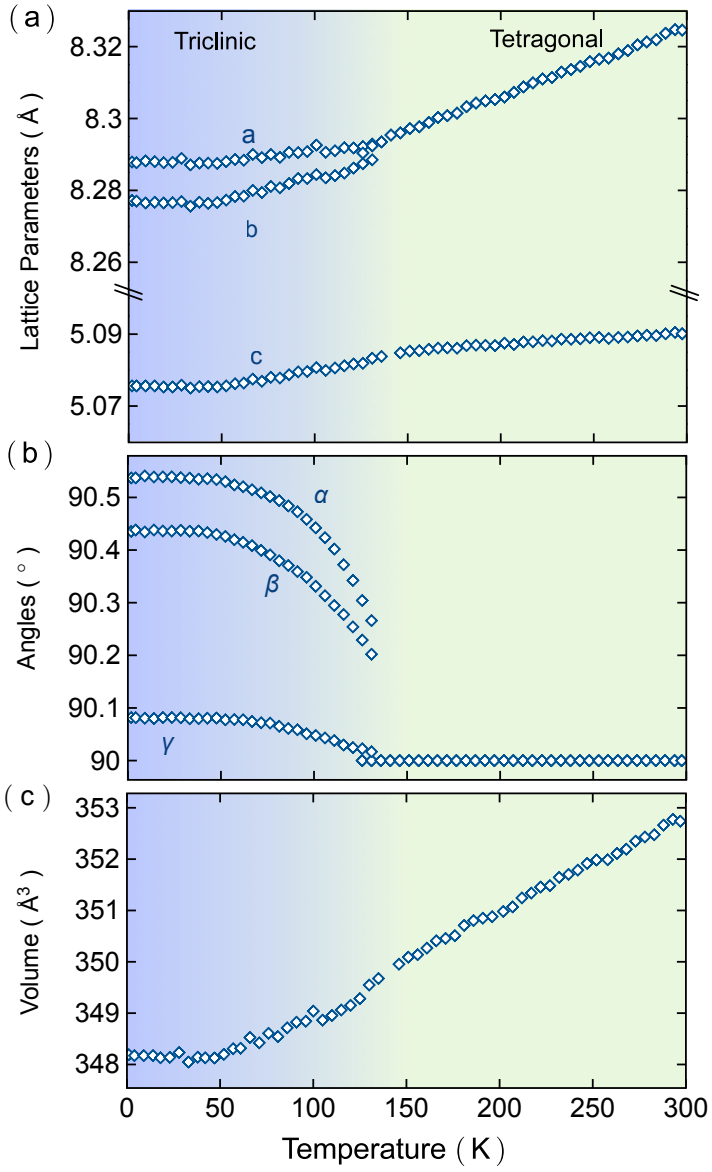

FIGURE 5.13: Evolution of the lattice parameters ((a) and (b)) and unit cell volume (c) versus temperature, deduced from the synchrotron X-ray diffraction Rietveld refinements.

its high-temperature phase, undergoes this triclinic distortion involving a very weak modification of the lattice parameters and no volume changing. Thus, it may be a weak first-order transition. Moreover, the fact that this transition occurs at the same temperature (125 K) as the broad maximum observed in the magnetic susceptibility seems to indicate that the structural modifications have an impact on the magnetism of this compound, which should be associated to the spitting in distance of the copper atoms already reported.

5.2.1 Extraction of the magnetic couplings as a function of the temperature

In order to evaluate the impact of this distortion on the magnetic couplings, broken-symmetry calculations performed using the experimental crystal structure determined

at 300 K have been extended to a set of 61 structures obtained from the Rietveld refinement of neutron powder diffraction experiments carried out from 2 to 300 K.

In the high temperature tetragonal structure, we have evaluated three magnetic couplings: $J_\perp = -100$ K corresponding to the intra-platelet coupling along the rungs of the ladders; $J = J_\times = 127$ K corresponding to the nearest-neighbour coupling along the legs and, by symmetry, to the diagonal coupling between the legs and finally, $J_2 = 127$ K corresponding to the next-nearest-neighbour interaction along the legs. In the triclinic structure, the symmetry lowering further splits these couplings. Two rung couplings $J_\perp^a$ and $J_\perp^b$ should be considered and the four interactions between adjacent platelets, J, give rise to J^a, $J_\times^b$, $J_\times^c$, J^d. Finally, J_2 remains almost unaffected. The particular arrangement of the magnetic couplings in the triclinic structure along a ladder is represented schematically in Fig. 5.14.

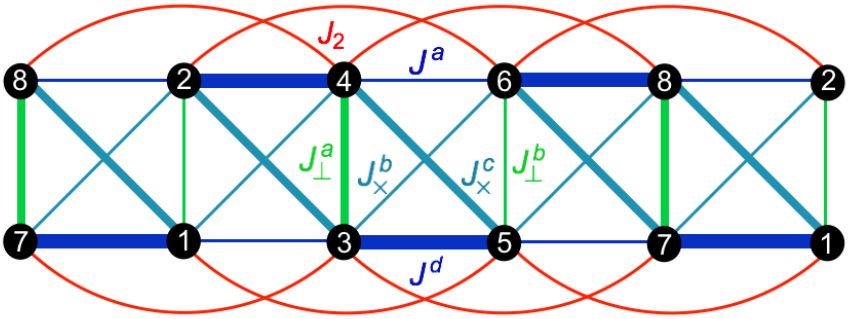

FIGURE 5.14: Schematic representation of the magnetic couplings in the triclinic phase. The inequivalent interactions along the legs J^a and J^d, diagonal interactions between the legs $J_\times^b$ and $J_\times^c$, and between the legs along the rungs $J_\perp^a$ and $J_\perp^b$, are represented in dark blue, blue, and green respectively. The next-nearest-neighbour interaction along the legs J_2 is represented in red. Cu^{2+} numbering, as used in Tab. (5.3), is also indicated.

In the triclinic phase, out of a total of $2^8 = 256$ possible spin configurations obtained for a $1 \times 1 \times 2$ supercell, we have to calculate the total energies of 42 inequivalent configurations with distinct Ising expressions and total magnetizations. Although these configurations have been determined using the low-temperature triclinic structure, the same set has been employed for every temperature, up to the high-temperature tetragonal phase. Note that in this latter case, the higher symmetry induces a number of additional degeneracies among these configurations, that as we already see, it is reduced to 18 inequivalent configurations.

Tab. (5.3) provides a detailed description of the 42 configurations. In each case, the spin state (up or down) of each of the eight Cu^{2+} ions indexed according to the convention shown in Fig. 5.14 is given, followed by the degeneracy of the configuration and the corresponding Ising expression. The first 16 configurations are shown in Fig. 5.15.

TABLE 5.3: Detail of the 42 spin configurations employed to estimate the magnetic couplings in $Li_2Cu_2O(SO_4)_2$ using the broken symmetry formalism. + and − symbols represent up and down spins on the Cu^{2+} ions respectively. The sum of the configuration degeneracies is equal to $2^8 = 256$.

Conf.	Cu1	Cu2	Cu3	Cu4	Cu5	Cu6	Cu7	Cu8	Deg.	Ising Expression
1	+	+	+	+	+	+	+	−	8	$\frac{1}{4}\left(2J_1 + 0J_\perp^b + 2J^a + 2J_\times^b + 2J_\times^c + 2J^d + 4J_2\right)$
2	+	+	+	−	−	+	−	−	8	$\frac{1}{4}\left(0J_\perp^a + 0J_\perp^b + 0J^a + 0J_\times^b + 0J_\times^c - 4J^d + 0J_2\right)$
3	+	+	+	+	−	−	−	−	4	$\frac{1}{4}\left(2J_\perp^a + 2J_\perp^b + 0J^a + 0J_\times^b + 0J_\times^c + 0J^d - 8J_2\right)$
4	+	+	+	+	−	+	+	−	8	$\frac{1}{4}\left(0J_\perp^a + 0J_\perp^b + 0J^a + 4J_\times^b + 0J_\times^c + 0J^d + 0J_2\right)$
5	+	+	+	−	+	+	+	−	4	$\frac{1}{4}\left(2J_\perp^a - 2J_\perp^b + 0J^a + 0J_\times^b + 0J_\times^c + 0J^d + 8J_2\right)$
6	+	+	+	+	+	+	−	−	8	$\frac{1}{4}\left(2J_\perp^a + 2J_\perp^b + 0J^a + 0J_\times^b + 0J_\times^c + 0J^d + 0J_2\right)$
7	+	+	+	+	+	−	+	+	8	$\frac{1}{4}\left(0J_\perp^a + 2J_\perp^b + 2J^a + 2J_\times^b + 2J_\times^c + 2J^d + 4J_2\right)$
8	+	+	+	+	−	+	−	−	8	$\frac{1}{4}\left(0J_\perp^a + 2J_\perp^b + 2J^a + 2J_\times^b - 2J_\times^c - 2J^d - 4J_2\right)$
9	+	−	+	−	+	−	−	+	8	$\frac{1}{4}\left(-2J_\perp^a - 2J_\perp^b + 0J^a + 0J_\times^b + 0J_\times^c + 0J^d + 0J_2\right)$
10	+	+	−	−	+	−	−	−	8	$\frac{1}{4}\left(0J_\perp^a + 2J_\perp^b - 2J^a - 2J_\times^b - 2J_\times^c - 2J^d + 4J_2\right)$
11	+	+	+	−	+	+	−	−	8	$\frac{1}{4}\left(2J_\perp^a + 0J_\perp^b - 2J^a - 2J_\times^b - 2J_\times^c - 2J^d + 4J_2\right)$
12	+	+	+	+	+	+	+	+	2	$\frac{1}{4}\left(2J_\perp^a + 2J_\perp^b + 4J^a + 4J_\times^b + 4J_\times^c + 4J^d + 8J_2\right)$
13	+	+	+	+	+	−	−	+	8	$\frac{1}{4}\left(0J_\perp^a + 0J_\perp^b + 0J^a + 0J_\times^b + 4J_\times^c + 0J^d + 0J_2\right)$
14	+	+	+	+	+	−	+	−	8	$\frac{1}{4}\left(0J_\perp^a + 0J_\perp^b + 0J^a + 0J_\times^b + 0J_\times^c + 4J^d + 0J_2\right)$
15	+	+	+	+	−	+	−	+	8	$\frac{1}{4}\left(0J_\perp^a + 0J_\perp^b + 4J^a + 0J_\times^b + 0J_\times^c + 0J^d + 0J_2\right)$
16	+	−	+	+	−	+	+	+	4	$\frac{1}{4}\left(-2J_\perp^a + 2J_\perp^b + 0J^a + 0J_\times^b + 0J_\times^c + 0J^d + 0J_2\right)$
17	+	+	+	−	+	−	−	−	8	$\frac{1}{4}\left(0J_\perp^a + 0J_\perp^b + 0J^a - 4J_\times^b + 0J_\times^c + 0J^d + 0J_2\right)$
18	+	−	−	+	+	−	−	+	2	$\frac{1}{4}\left(-2J_\perp^a - 2J_\perp^b - 4J^a + 4J_\times^b + 4J_\times^c - 4J^d + 8J_2\right)$
19	+	+	+	−	−	+	+	−	8	$\frac{1}{4}\left(0J_\perp^a - 2J_\perp^b - 2J^a + 2J_\times^b + 2J_\times^c - 2J^d + 4J_2\right)$
20	+	+	−	+	+	−	+	−	8	$\frac{1}{4}\left(0J_\perp^a - 2J_\perp^b - 2J^a + 2J_\times^b - 2J_\times^c + 2J^d - 4J_2\right)$
21	+	−	+	+	+	−	+	+	4	$\frac{1}{4}\left(-2J_\perp^a + 2J_\perp^b + 0J^a + 0J_\times^b + 0J_\times^c + 0J^d + 8J_2\right)$
22	+	−	+	+	+	−	+	−	8	$\frac{1}{4}\left(-2J_\perp^a + 0J_\perp^b + 2J^a - 2J_\times^b - 2J_\times^c + 2J^d + 4J_2\right)$
23	+	+	+	−	+	−	−	+	8	$\frac{1}{4}\left(0J_\perp^a - 2J_\perp^b + 2J^a - 2J_\times^b + 2J_\times^c - 2J^d - 4J_2\right)$
24	+	+	+	−	+	+	−	+	4	$\frac{1}{4}\left(2J_\perp^a - 2J_\perp^b + 0J^a + 0J_\times^b + 0J_\times^c + 0J^d + 0J_2\right)$
25	+	+	+	−	−	−	+	−	4	$\frac{1}{4}\left(2J_\perp^a - 2J_\perp^b + 0J^a + 0J_\times^b + 0J_\times^c + 0J^d + 0J_2\right)$
26	+	+	+	+	+	−	−	−	8	$\frac{1}{4}\left(0J_\perp^a + 2J_\perp^b - 2J^a - 2J_\times^b + 2J_\times^c + 2J^d - 4J_2\right)$
27	+	−	+	+	−	+	−	−	2	$\frac{1}{4}\left(-2J_\perp^a + 2J_\perp^b + 4J^a + 4J_\times^b - 4J_\times^c - 4J^d - 8J_2\right)$
28	+	−	+	−	−	+	−	+	4	$\frac{1}{4}\left(-2J_\perp^a - 2J_\perp^b + 0J^a + 0J_\times^b + 0J_\times^c + 0J^d - 8J_2\right)$
29	+	+	+	−	−	−	−	+	2	$\frac{1}{4}\left(2J_\perp^a - 2J_\perp^b + 4J^a - 4J_\times^b + 4J_\times^c - 4J^d - 8J_2\right)$
30	+	−	+	+	+	−	−	+	8	$\frac{1}{4}\left(-2J_\perp^a + 0J_\perp^b - 2J^a + 2J_\times^b + 2J_\times^c - 2J^d + 4J_2\right)$
31	+	−	−	−	−	+	+	+	2	$\frac{1}{4}\left(-2J_\perp^a + 2J_\perp^b - 4J^a - 4J_\times^b + 4J_\times^c + 4J^d - 8J_2\right)$
32	+	−	+	−	+	−	+	−	2	$\frac{1}{4}\left(-2J_\perp^a - 2J_\perp^b + 4J^a - 4J_\times^b - 4J_\times^c + 4J^d + 8J_2\right)$
33	+	+	+	−	+	−	+	−	8	$\frac{1}{4}\left(0J_\perp^a - 2J_\perp^b + 2J^a - 2J_\times^b - 2J_\times^c + 2J^d + 4J_2\right)$
34	+	+	−	+	−	−	+	−	2	$\frac{1}{4}\left(2J_\perp^a - 2J_\perp^b - 4J^a + 4J_\times^b - 4J_\times^c + 4J^d - 8J_2\right)$
35	+	+	−	+	+	−	−	−	8	$\frac{1}{4}\left(0J_\perp^a + 0J_\perp^b - 4J^a + 0J_\times^b + 0J_\times^c + 0J^d + 0J_2\right)$
36	+	−	+	+	+	−	−	−	4	$\frac{1}{4}\left(-2J_\perp^a + 2J_\perp^b + 0J^a + 0J_\times^b + 0J_\times^c + 0J^d + 0J_2\right)$
37	+	−	+	−	−	+	+	+	8	$\frac{1}{4}\left(-2J_\perp^a + 0J_\perp^b - 2J^a - 2J_\times^b + 2J_\times^c + 2J^d - 4J_2\right)$
38	+	+	−	−	+	+	−	−	2	$\frac{1}{4}\left(2J_\perp^a + 2J_\perp^b - 4J^a - 4J_\times^b - 4J_\times^c - 4J^d + 8J_2\right)$
39	+	−	+	+	−	+	+	−	8	$\frac{1}{4}\left(-2J_\perp^a + 0J_\perp^b + 2J^a + 2J_\times^b - 2J_\times^c - 2J^d - 4J_2\right)$
40	+	+	+	+	−	−	+	−	8	$\frac{1}{4}\left(2J_\perp^a + 0J_\perp^b - 2J^a + 2J_\times^b - 2J_\times^c + 2J^d - 4J_2\right)$
41	+	+	−	+	−	+	−	−	8	$\frac{1}{4}\left(0J_\perp^a + 0J_\perp^b + 0J^a + 0J_\times^b - 4J_\times^c + 0J^d + 0J_2\right)$
42	+	+	+	+	−	−	−	+	8	$\frac{1}{4}\left(2J_\perp^a + 0J_\perp^b + 2J^a - 2J_\times^b + 2J_\times^c - 2J^d - 4J_2\right)$

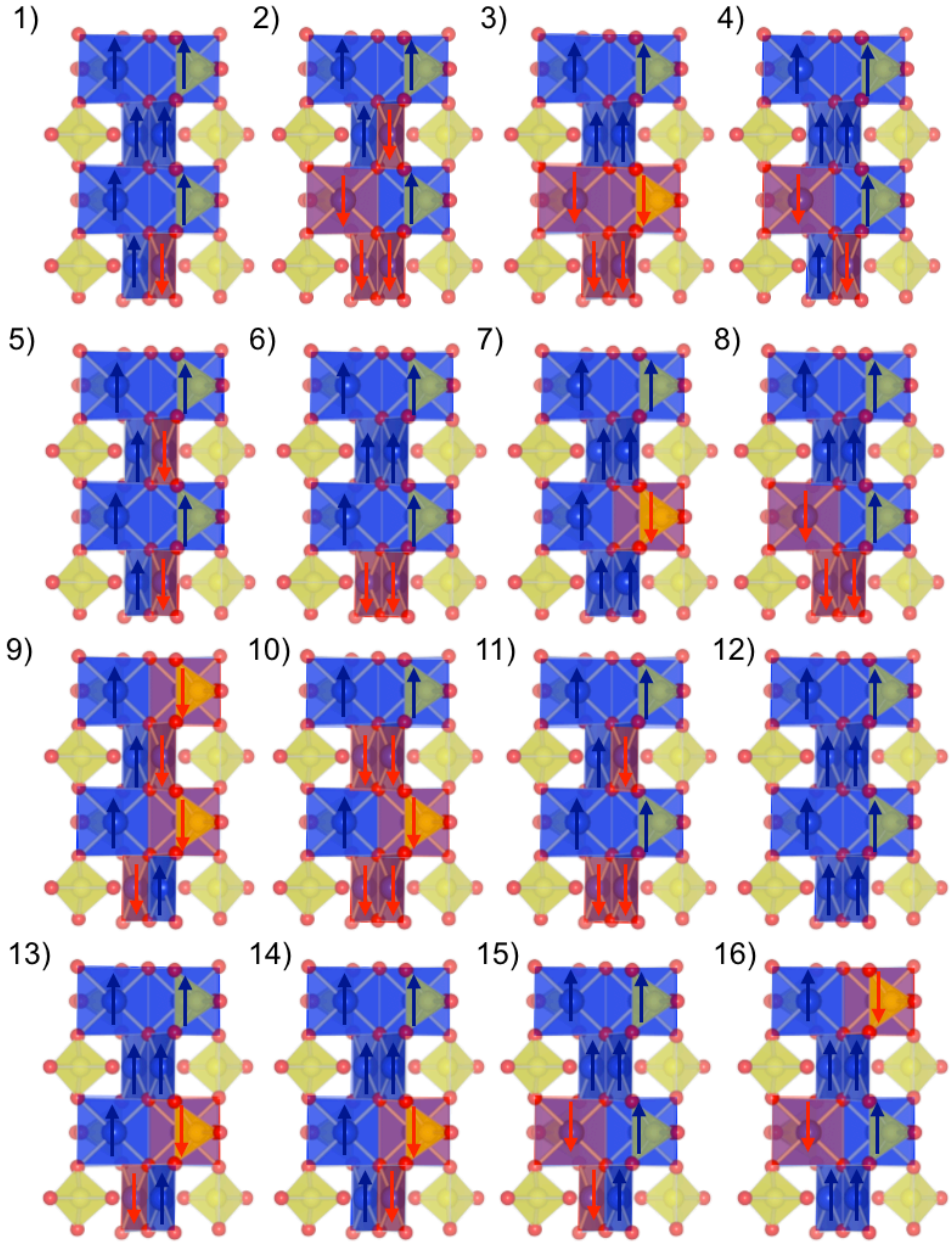

FIGURE 5.15: Graphical representation of the first 16 spin configurations.

Finally, Fig. 5.16 shows the results of the least-squares fitting procedure for a subset of six temperatures. Note the additional degeneracies visible for all temperatures above the transition.

The results are summarized in Fig. 5.17 (a) where data points are represented by dots and a smooth interpolation using Boltzmann sigmoids $J(T)$ is superimposed [153],

$$J(T) = J_0 + \frac{J_c - J_0}{1 + Ae^{-\frac{T-T_c}{\alpha}}}, \tag{5.9}$$

where J_0 is the initial value of the coupling (at low-temperature), J_c is the critical one, which is constant in the tetragonal phase, above the transition temperature $T_c = 125$ K. A and α are constant values which determines the width of the transition. It should be noted that the sigmoids are only a guide for the eyes, this means that

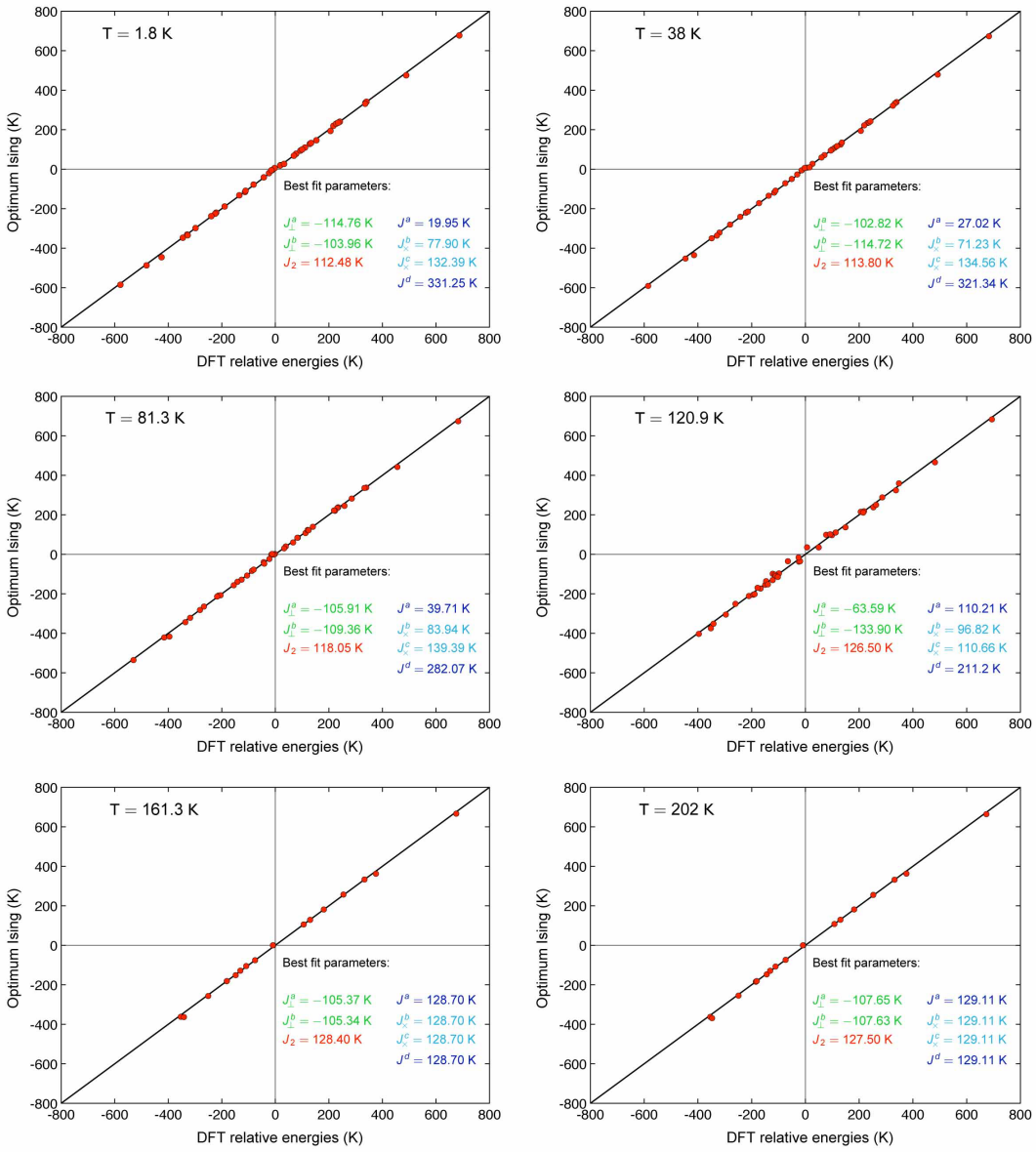

FIGURE 5.16: Graphical representation of the results obtained by using the least-square fitting procedure of the magnetic couplings for six representative temperatures. For each configuration, the DFT relative energy $\epsilon_\alpha^{\mathrm{DFT}} - \epsilon_0$ is represented as a function of the optimized Ising energy. The best fit values are given for each temperature.

the involved parameters have not real physical meaning in this context.

It should be mentioned that the weakness of the triclinic distortion close to the transition temperature leads to large standard deviations in the Rietveld refinements and partly explains the noise visible in the results shown in Fig. 5.17. Moreover, the use of this interpolation was motivated by the fact that, in the 125-140 K range, neutron refinements were carried out using the tetragonal symmetry even if the synchrotron X-ray diffraction patterns revealed the presence of large microstrain effects (lattice parameter fluctuations). These fluctuations indeed indicate that substantial deviations of local bond lengths and angles from the ideal tetragonal structure already occur above the transition temperature.

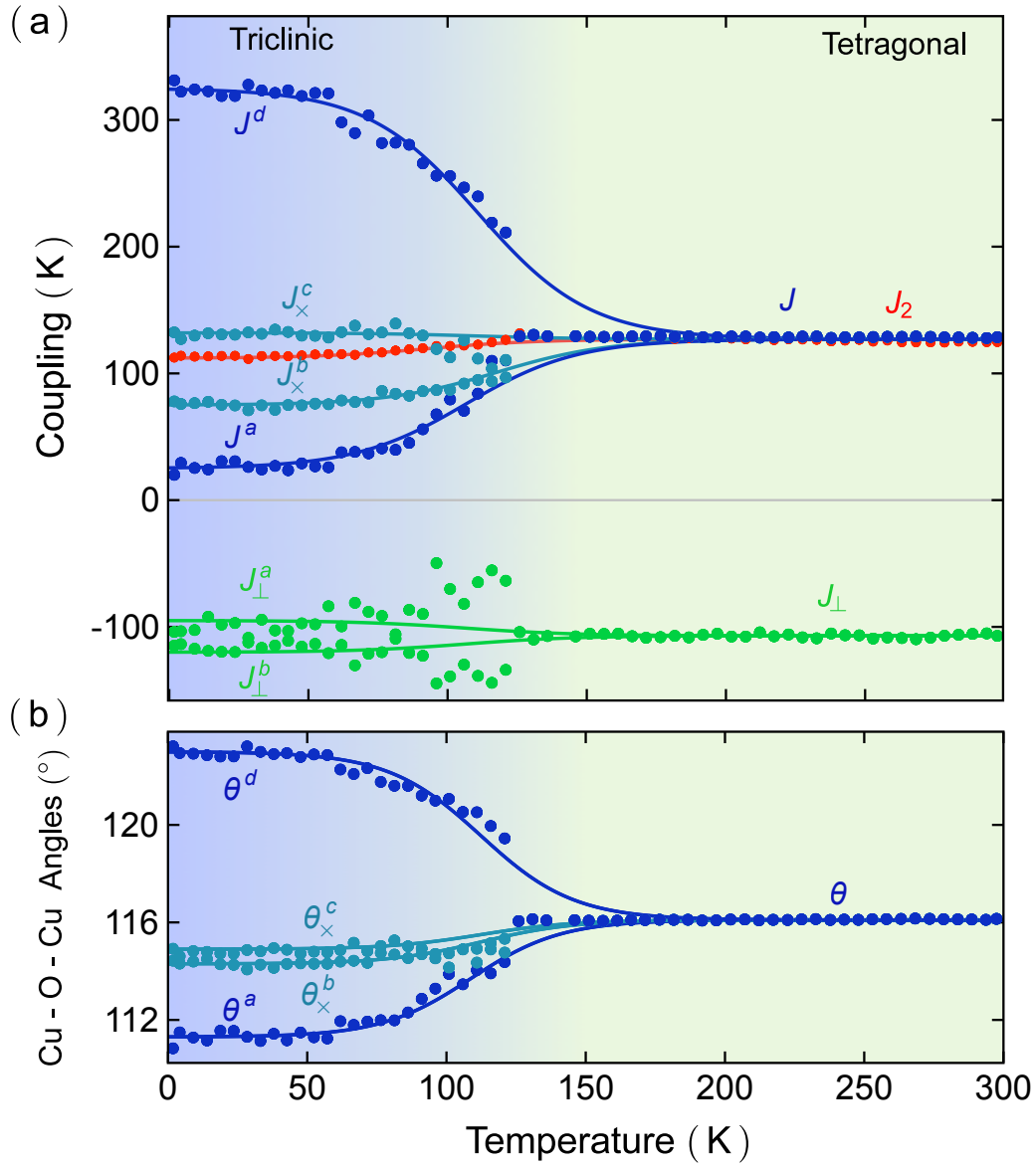

FIGURE 5.17: (a)Temperature dependence of the magnetic couplings in $Li_2Cu_2O(SO_4)_2$ calculated in GGA+U . Data points are represented with dots; the Boltzmann sigmoid fits are represented with lines. (b) Experimental temperature dependence of the interplatelet Cu-O-Cu superexchange angles.

Whereas the triclinic distortion has only a marginal effect on $J_\perp$ and J_2, it drastically impacts the interplatelet coupling J. Firstly, the crystal symmetry lowering in the triclinic phase lifts its original degeneracy, leading to four distinct couplings instead of a single one in the tetragonal phase. Secondly, each of these couplings follows a distinct trend as the temperature is lowered: two of them largely reduce their amplitude (J^a and $J^b_\times$), one remains almost constant ($J^c_\times$), whereas the last one experiences a drastic increase (J^d), raising its amplitude to almost three times its room-temperature value. This very strong variation of the predicted magnetic couplings with the temperature is not surprising if we consider the detailed evolution of the atomic arrangement inside the unit cell. Indeed, although the triclinic distortion has only a modest impact on the lattice parameters, it involves a sizable variation of

the interplatelet Cu-O-Cu superexchange angle, as shown in Fig. 5.17 (b). As the Cu-3d/O-2p hopping is directly related to this angle and as the superexchange interaction directly scales with this integral, the amplitude of the resulting AFM couplings correlates exactly with the Cu-O-Cu angle [see Figs. 5.17 (a) and 5.17 (b)]. The picture resulting from these calculations is therefore that the weak triclinic structural distortion involves a strong magnetic dimerization.

5.2.2 Exact Diagonalization

Experimental investigations have been associated with theoretical studies at the DFT+U level in order to estimate the strength and sign of the dominant magnetic couplings for different temperatures. Therefore it has been possible to establish a relevant spin Hamiltonian on the basis of *ab initio* results for all the temperatures.

The study of the properties of these Hamiltonians have been investigated numerically, through Exact Diagonalization (ED) calculations, to model the thermodynamic of the compound and verify the scenario revealed by DFT+U calculations.

The model studied for the tetragonal phase is described in Fig. 5.1 (d). It has only tree dominant magnetic couplings ($J_\perp$, J and J_2) and the ED can be carried out using fixed-magnetization blocks and exploiting rotational, translational and reflexion symmetries. The system in the low-temperature phase (Fig. 5.14) loses the reflexion symmetry and it becomes invariant with respect to translation doubling the size of the unit cell.

One specific advantage of ED is that we have access to the theoretical magnetic susceptibility of the compound that could be compared to the experimental result (Figure 5.9). We have calculated the theoretical susceptibility for (i) a set of fixed, i.e., temperature-independent couplings determined from the experimental tetragonal structure determined at 300 K; (ii) a set of fixed couplings determined from the experimental triclinic structure at 2 K.

The temperature dependence of the magnetic susceptibility has been evaluated using full diagonalization calculations for $N = 16$ spin ladders and using periodic boundary conditions. This choice has been motivated by the fact that only very small finite-size variations are observed when comparing the results obtained for $N = 16$ and $N = 20$ site systems. As shown in Fig. (5.18), whereas a small variation is still visible close to the maximum in the susceptibility calculated for the tetragonal phase, the calculations performed for the dimerized phase are almost exactly superimposed and point therefore to a very short correlation length.

In addition, taking into account the structural transition, we have constructed for every temperature (from 0 K to 400 K) different Hamiltonians with the magnetic couplings extracted from the interpolation of the Fig. 5.17 (a) and we have calculated the magnetic susceptibility for every different temperatures. The results are shown in Fig. 5.19 where the fit of the experimental data is solely based on the adjustment of the g factor, set to $g = 2.10$, a reasonable value for Cu^{2+} [154].

The best agreement is clearly obtained for the model with the temperature-dependent exchange interactions, confirming the large impact of the structural distortion on the magnetism of this compound. Remaining discrepancies, particularly visible at low temperature through a substantial overestimation of the spin gap, are directly attributable to the semiquantitative nature of the magnetic couplings calculated in DFT. These quantities indeed strongly depend on the approximations used in the treatment of exchange and correlation and are often overestimated.

It should be noted that the smooth sigmoid-shaped functions used to interpolate the data around the transition temperature $T_c \sim 125$ K can be now justified

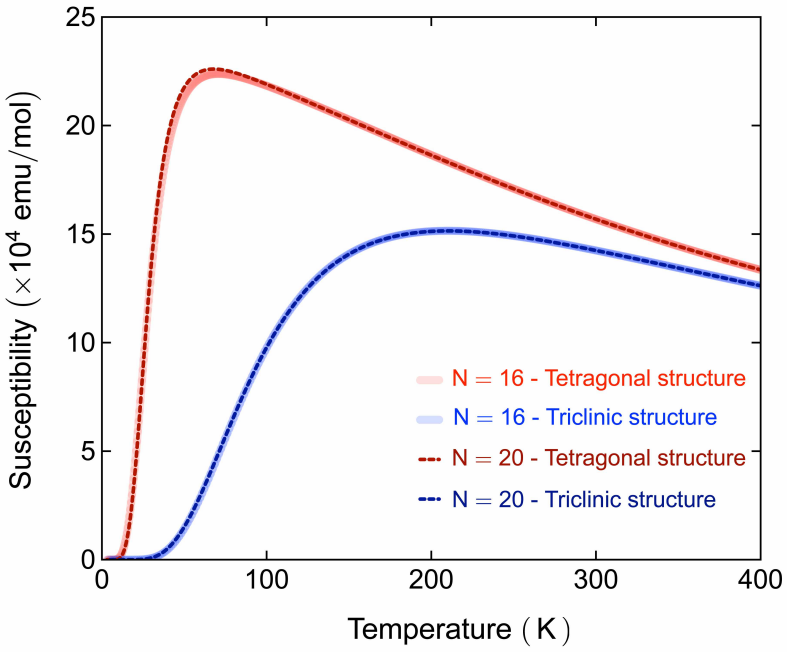

FIGURE 5.18: Comparison of the calculated temperature dependent magnetic susceptibility for $N = 16$ and $N = 20$ spin ladders. The two sets of results shown here correspond respectively to calculations performed using couplings determined in the tetragonal phase at 300 K and using couplings determined in the triclinic phase at 2 K.

in order to represent the experimental magnetic susceptibility. In fact, the magnetic susceptibility does not show any obvious discontinuity around T_c but rather a broad maximum before the exponential decay at low temperature. Any discontinuity introduced to interpolate the angles and magnetic couplings would be reflected as a clear discontinuity at the same temperature in the magnetic susceptibility, which is not observed experimentally. As an example, Fig. 5.20 (a) and (b) show possible power-law interpolations superimposed to the couplings and angles. The resulting erroneous discontinuous magnetic susceptibility is represented in Fig. 5.20 (c).

Moreover, as we already mentioned, the evolution of the lattice parameters (measured from synchrotron X-ray powder diffraction) shows that this distortion is continuous and extends over a wide range of temperature with no crystal unit cell volume discontinuity. The apparent discontinuity in the bond angles and reflected in the magnetic couplings is therefore due to the impossibility to detected the very weak atomic displacements in the temperature range around the transition.

In summary, $Li_2Cu_2O(SO_4)_2$ appears, in its tetragonal structure, as a very rare realization of a $S = 1/2$ frustrated two-leg spin ladder where frustration arises from competing NN and NNN interactions along the legs. The unusual triclinic distortion occurring in this compound at about 125 K is accompanied by a drastic modification of its magnetic properties. We indeed showed that a strong magnetoelastic coupling is responsible for the formation of a staggered $S = 1/2$ dimer structure, lifting most of the magnetic frustration.

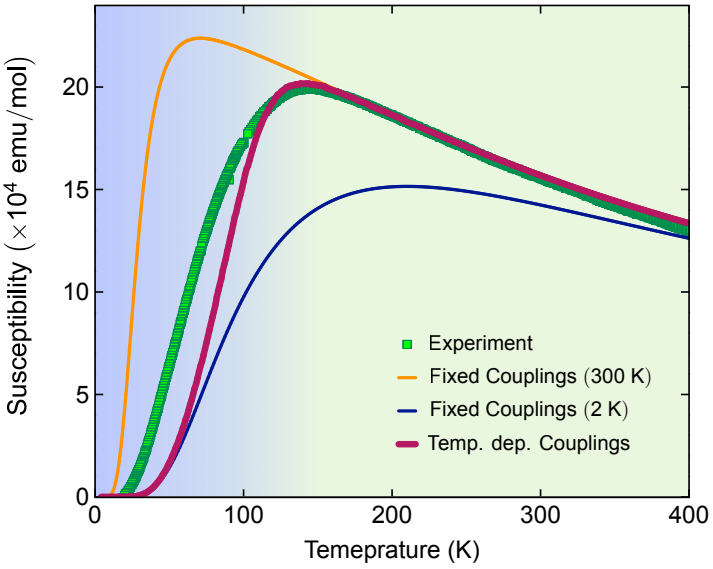

FIGURE 5.19: Temperature dependence of the magnetic susceptibility of $Li_2Cu_2O(SO_4)_2$. The experimental points are shown in green. The calculations performed with the fixed couplings corresponding to the high-temperature (300 K) structure are shown in orange, with the fixed couplings corresponding to the low-temperature (2 K) structure in dark blue, and with temperature-dependent couplings shown by a thick purple line.

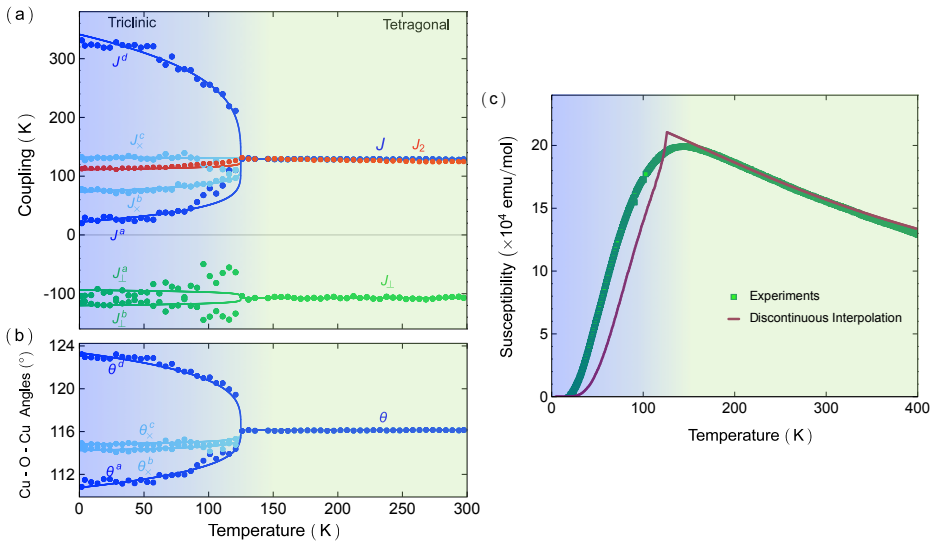

FIGURE 5.20: (a)Temperature dependence of the magnetic couplings in $Li_2Cu_2O(SO_4)_2$ calculated in GGA+U. Data points are represented with dots; the power-law fits are represented with lines. (b) Experimental temperature dependence of the interplatelet Cu-O-Cu superexchange angles. (c) Temperature dependence of the magnetic susceptibility of $Li_2Cu_2O(SO_4)_2$. The experimental points are shown in green. The calculations with temperature-dependent couplings interpolated with the power-law is shown by a thick purple line.

Chapter 6

Magnetic excitations

"Nothing in life is to be feared,
it is only to be understood.
Now is the time to understand more,
so that we may fear less."

Marie Curie

In this chapter, we report the first detailed investigation of the low-temperature magnetic excitations of $Li_2Cu_2O(SO_4)_2$ combining magnetic susceptibility, inelastic neutron scattering (INS) and infrared (IR) spectroscopy measurements carried out on powder samples.

6.1 Inelastic Neutron Scattering

The present neutron scattering study was intended to investigate the magnetic excitations of the unconventional low-dimensional spin system $Li_2Cu_2O(SO_4)_2$ in its low-temperature phase (triclinic structure).

The inelastic-neutron-scattering measurements were performed at the Institut Laue-Langevin in Grenoble on the Time-of-Flight spectrometer IN4 to map the magnetic excitations of $Li_2Cu_2O(SO_4)_2$. A total of 6.8 g of powder sample of $Li_2Cu_2O(SO_4)_2$ was synthesized according to the procedure described in Ref. [14], put in a flat plate holder ($4.0 \times 2.8 \times 0.2$ cm^3) made of aluminium and thermalized using a standard Orange cryostat. Spectra were recorded using neutrons with an initial incident energy E_i at specific values of the temperature. Additionally, absorption corrections were applied taking into account the shape of the sample and the different absorption of the scattered neutrons depending on their angle and final energy. Moreover, a vanadium standard and an empty cell were measured to account for background and detector efficiency. The raw data have been corrected for background and neutron absorption and were normalised to vanadium employing the program package LAMP.

We start exploring a wide range of energy for the low-temperature phase, where we expected the presence of a magnetic contribution and, because of the quasi-1D nature of the system, any dispersive magnetic scattering is plausibly assumed to originate from the spin dynamics along the chain direction. We investigated this large energy-region using neutrons with $E_i = 66$ meV for a limited acquisition time of 1 h. Figure 6.1 shows the maps of the dynamic susceptibility $\chi''(|Q|, E)$ as a function of momentum transfer, Q, expressed in units of reciprocal length, and energy transfer, E, obtained by normalizing the background-subtracted neutron scattering intensity $S(|Q|, E)$ by the thermal occupancy factor $1-e^{-E/k_BT}$, with $T = 1.5$ K. The temperature dependence of the dynamic susceptibility clearly reveals the absence of excitations

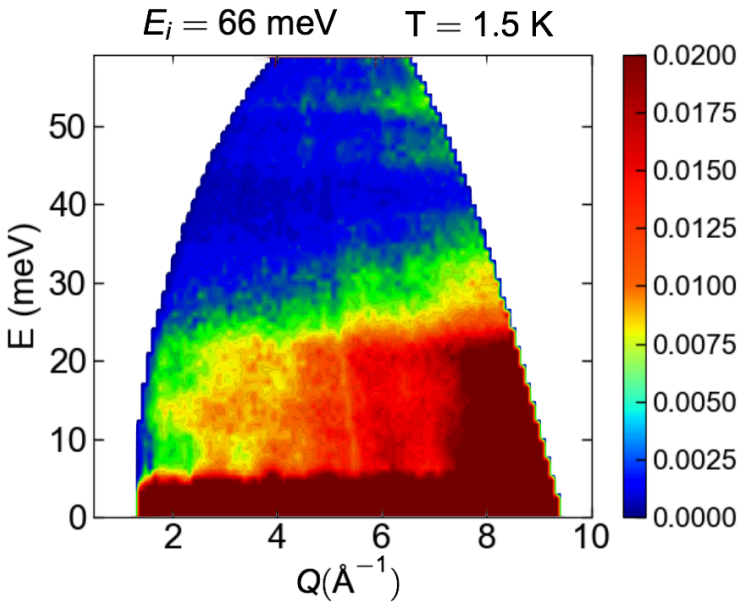

FIGURE 6.1: Experimental dynamic susceptibility $\chi''(|Q|, E)$ plots for $Li_2Cu_2O(SO_4)_2$ measured at $T = 1.5$ K, with an initial energy $E_i = 66$ meV.

in the high energy range, but indicates the presence of excitations below ~ 25 meV. In order to focus on the low-energy zone, we have changed the initial energy of the incident neutrons to $E_i = 16.6$ meV and at two different temperatures, $T = 1.5$ K and $T = 80$ K, respectively, for an acquisition time of 2 h. The resulting dynamic susceptibility $\chi''(|Q|, E)$ (obtained from the neutron scattering intensity $S(|Q|, E)$) are shown in Figs. 6.2 (a) and (b).

The spectra clearly reveal the presence of a dominant phonon contribution, responsible for the strong increase in intensity as $|Q|^2$ [126, 155] which are present for the two temperatures. In particular, we recognize an acoustic phonon related to a Bragg peak (at $E = 0$ meV) for $Q = 4$ Å^{-1} and an excitation at $Q = 2.8$ Å^{-1} that is already visible for $T = 80$ K (thus, it is not a magnetic excitation) and could be a spurious feature. Moreover, we identify the presence of an excitation at around $E = 11$ meV at low temperature that seems to disappear at $T = 80$ K. We decided to change another time the initial energy of incident neutrons to verify the presence of this excitation and to understand its origin. Spectra were thus recorded using neutrons with an incident energy $E_i = 31.5$ meV at $T = 1.5$, 40, 60, 80 and 100 K for a typical acquisition time of 12 h. Again, measurements carried out with and without the empty Al-holder were also performed, allowing for a complete background, self- shielding, and absorption correction. Figures 6.3 (a)-(e) show the maps of the dynamic susceptibility $\chi''(|Q|, E)$, still obtained by normalizing the background-subtracted neutron scattering intensity $S(|Q|, E)$ by the thermal occupancy factor $1 - e^{-E/k_B T}$ at 1.5, 40, 60, 80 and 100 K, respectively.

The temperature dependence of the dynamic susceptibility clearly reveals the presence of two dominant contributions arising from phonon and magnetic excitations. Whereas the scattering cross-section of the former scales as $|Q|^2$, that arising from magnetism scales with the square of the form factor associated with the magnetic ions, and falls off with increasing $|Q|$ (as described in section 4.2.1), vanishing progressively in increasing T [156]. The high-temperature dynamic susceptibility is therefore largely

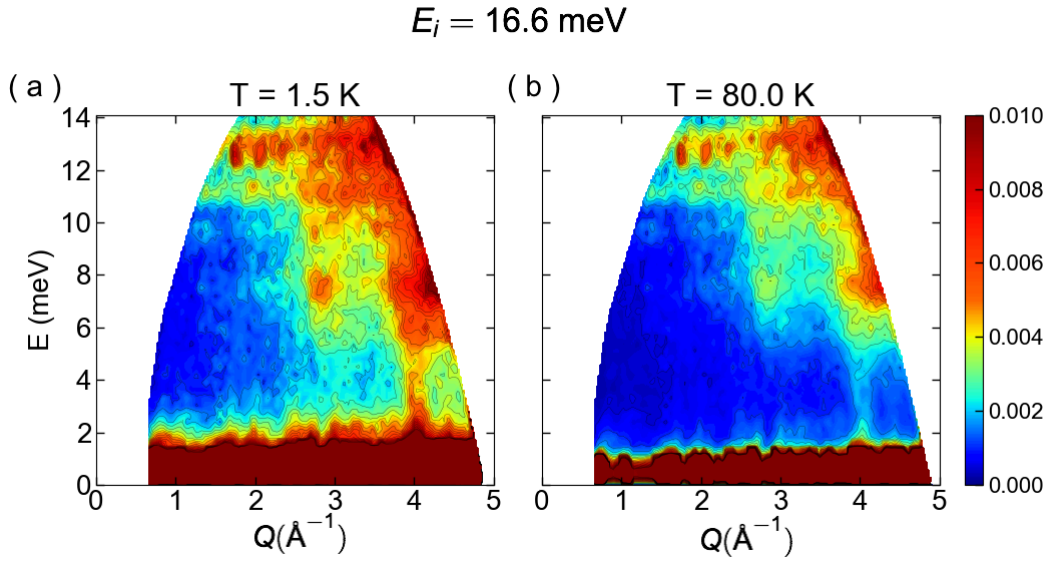

FIGURE 6.2: Experimental dynamic susceptibility $\chi''(|Q|, E)$ plot for $Li_2Cu_2O(SO_4)_2$ measured at $T = 1.5$ K (a) and $T = 80$ K (b), with an initial energy $E_i = 16.6$ meV.

dominated by phonon scattering (see Fig. 6.3(d)-(e)) whereas the weight of the magnetic contribution progressively increases with decreasing temperatures, as it can be observed in the low-$|Q|$ region of Fig. 6.3(a)-(c). Assuming, in first approximation, that the intensity is entirely associated with phonons scattering for the highest temperature measurement ($T = 100$ K in our case), the magnetic contribution to the dynamic susceptibility at low-temperature can simply be isolated by plotting the difference [157]

$$\Delta\chi''(|Q|, E) = \chi''(|Q|, E)|_{1.5\text{K}} - \chi''(|Q|, E)|_{100\text{K}}. \tag{6.1}$$

The corresponding difference map is shown in Fig. 6.3 (f) and clearly reveals the presence of dispersive magnetic excitations at energy transfer $E \approx 15$ meV of bandwidth ≈ 5 meV, with an intensity suppressed at higher values of Q.

E-scans extracted for a fixed $|Q|$ value of 2 ± 0.1 Å^{-1} for each temperature measured experimentally are shown in Fig. 6.4. The magnetic contribution is clearly visible for low temperature, $T = 1.5$ K, and vanishes progressively with increasing temperatures. From the $T = 1.5$ K profile (in blue in Fig. 6.4), we first extract the value of the spin gap, $\Delta = 10.6$ meV, measured as the inflection point of first peak (A). The continuum of states, extending over 5 meV above the spin gap, includes the first low-intensity peak (A) centred at 11.2 meV followed by the most intense structure (C) at 14.7 meV. A low-energy shoulder (B) of this dominant structure is also present at about 13.5 meV, particularly visible on the data obtained at 1.5 K.

Inelastic neutron scattering experiments therefore clearly reveal the presence of dispersive magnetic excitations despite the dimerizaion, which means that the dimers in the low-temperature phase are not totally isolated. This magnetic excitation, mostly localized at low-$|Q| < 3.5$ Å^{-1} and vanishing at temperatures above ~ 80 K, is consistent with spin triplet excitations out of the singlet ground-state of this compound [14, 15].

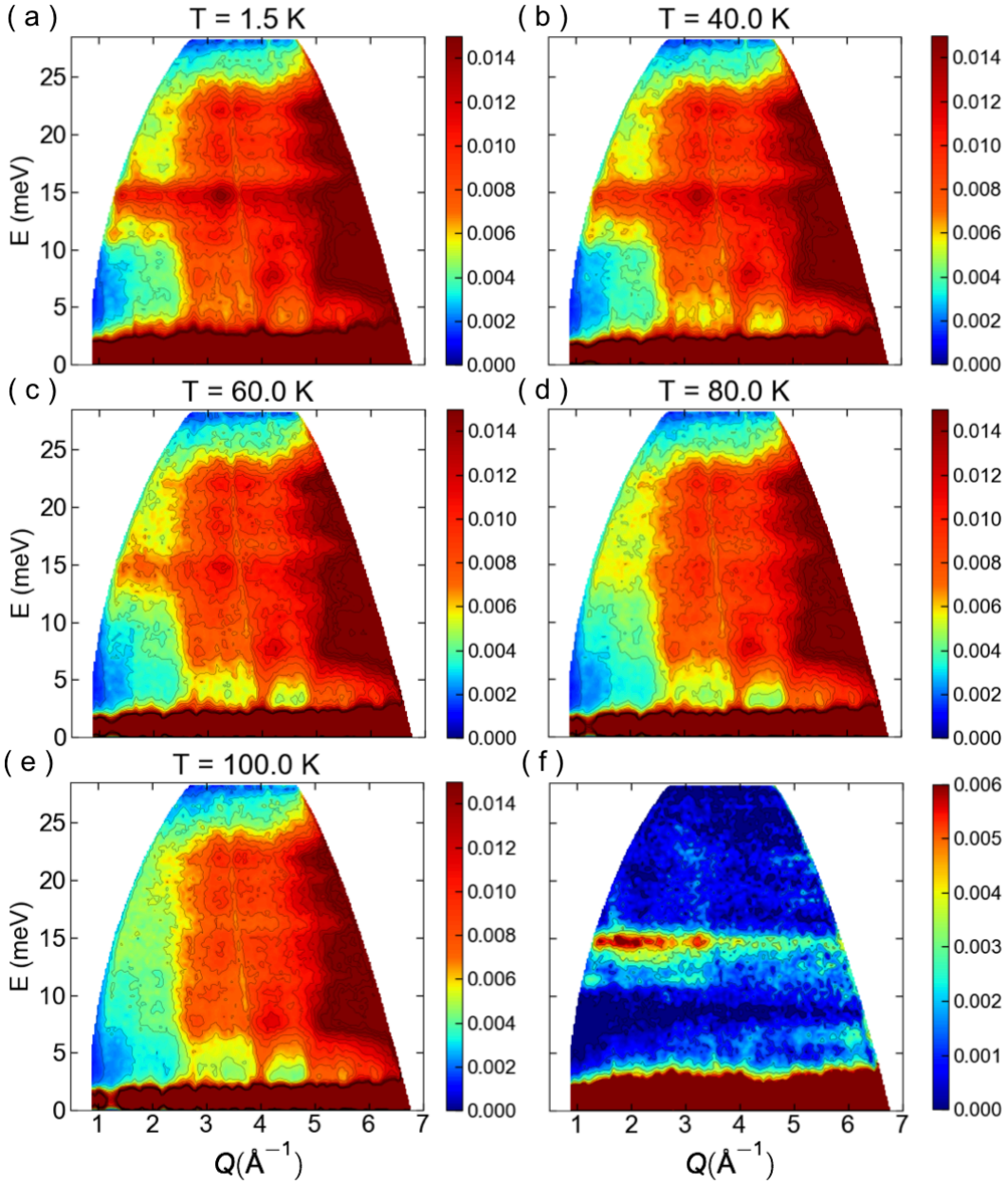

FIGURE 6.3: Experimental dynamic susceptibility $\chi''(|Q|, E)$ plots for $Li_2Cu_2O(SO_4)_2$ measured with an initial incident energy E_i = 16.6 meV at different temperatures: (a) $T = 1.5$ K, (b) $T = 40$ K, (c) $T = 60$ K, (d) $T = 80$ K and (e) $T = 100$ K. Magnetic contributions are isolated in (f) by displaying the difference $\Delta\chi''(|Q|, E)$ from Eq. (6.1).

6.2 Magnetic Susceptibility

These results can be further confirmed by analyzing the low-temperature behavior of the experimental magnetic susceptibility.

Fig. 6.5 reproduces the experimental data corrected from paramagnetic impurities and temperature-independent contributions, already analysed in the previous chapter. The susceptibility exhibits the typical behavior of a gapped low-dimensional antiferromagnet with a high-temperature paramagnetic regime reaching a broad maximum at about 125 K and an exponential decay at low-temperature. Note, however, that

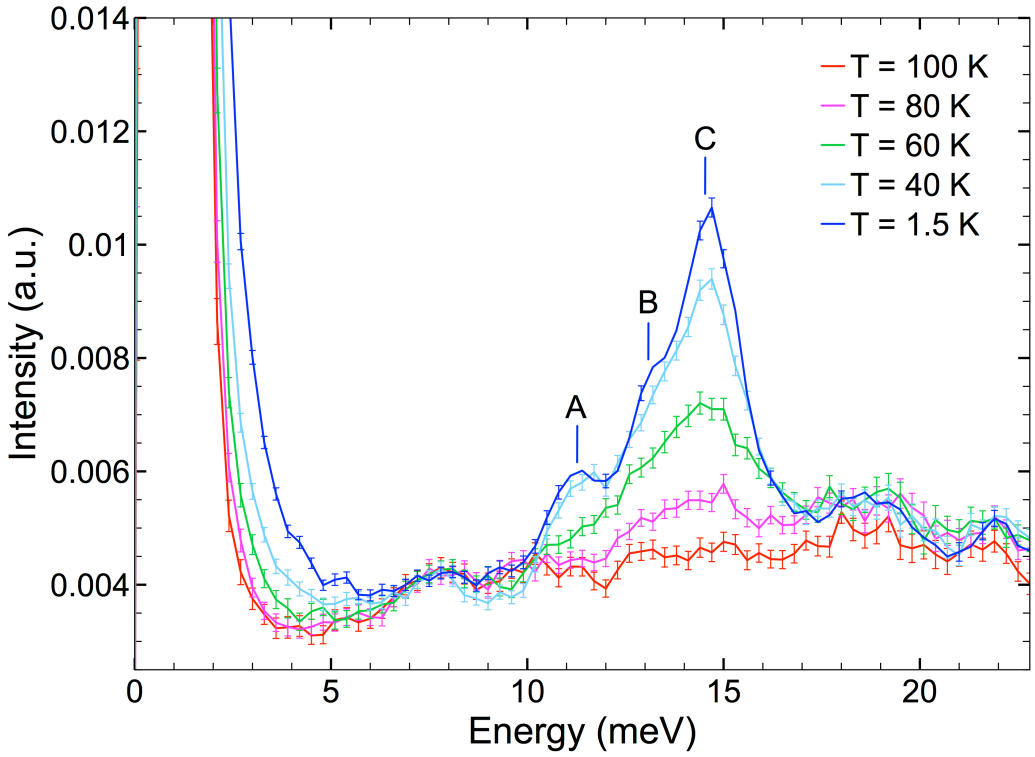

FIGURE 6.4: E-scans of the dynamic susceptibility $\chi''(|Q|, E)$ extracted for a fixed $|Q|$ value of 2 Å^{-1} from the plots shown in Fig. 6.3(a)-(e).

the temperature dependence of the magnetic susceptibility is largely affected by the structural transition occurring at the same temperature as the maximum (125 K) since it is accompanied by a substantial magnetic dimerization within the ladders. As reported in Ref. [15], although this transition extends over a large temperature range, the low-temperature triclinic phase is already mostly stabilized at about 80 K, and the 2-80 K range can therefore be used to estimate the corresponding spin gap.

A rough estimate can be obtained by fitting the experimental data using the general expression for thermally activated processes

$$\chi(T) \propto e^{-\Delta/T} \tag{6.2}$$

leading to a value of $\Delta \approx 9.1$ meV. It should however be noted that (6.2) would be valid for non-interacting particles, but magnons are not free particles. A suitable expression that takes the hard-core repulsion between the magnons into account is given by [52]

$$\chi_{\text{lad.}}(T) \propto T^{-1/2}\, e^{-\Delta/T} \tag{6.3}$$

for a quadratic band minimum. Equation (6.3) has also been employed (see Fig. 6.5). The resulting estimate for the spin gap, $\Delta \approx 11.6$ meV, is slightly larger than the value obtained with the previous expression.

Despite these small variations, essentially related to the rather low accuracy of this approach and to the limited applicability of the simple ladder model to $Li_2Cu_2O(SO_4)_2$, these estimates are however fully consistent with the spin gap value obtained from inelastic neutron scattering.

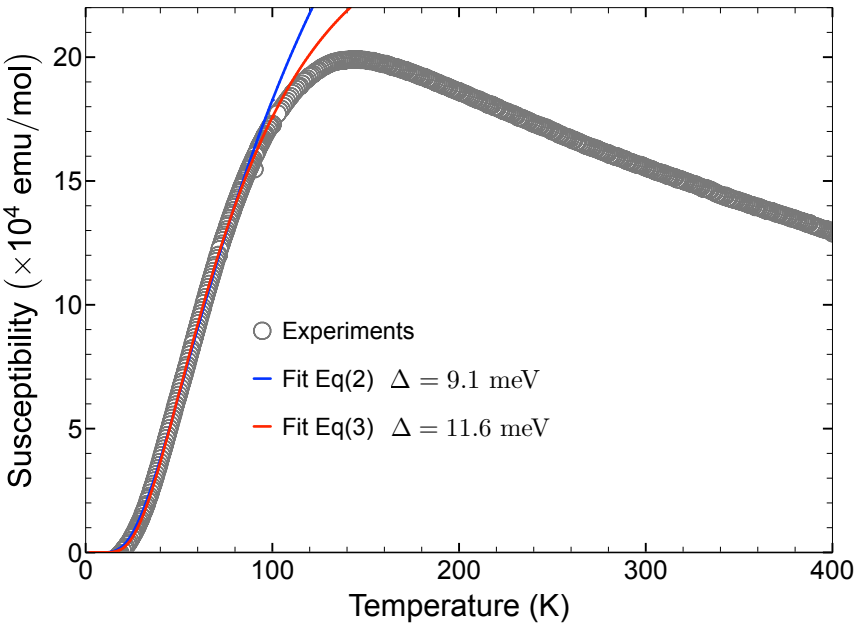

FIGURE 6.5: Temperature dependence of the magnetic susceptibility of $Li_2Cu_2O(SO_4)_2$ corrected from paramagnetic impurities and temperature-independent contributions. Grey circles correspond to the experimental points, the solid blue and red lines correspond, respectively, to the best fit obtained using the general expression (6.2) or a spin-1/2 two-leg ladder Heisenberg model (6.3). The corresponding values of the extracted spin gap are indicated.

6.3 Infrared spectroscopy

Infrared absorption spectroscopy was finally employed as a complementary technique to investigate the low-energy excitations of $Li_2Cu_2O(SO_4)_2$. These experiments were performed using a Fourier transform Bruker IFS66 v/s spectrometer at the IMPMC-Sorbonne University spectroscopy platform. The instrument was aligned in transmission geometry. Isotropic pellets of $\sim$ 13 mm diameter were prepared by mixing the original powder samples with transparent matrix materials. Pure KBr powder was used as a matrix in the middle-infrared (MIR), whereas polyethylene (PE) was employed to prepare pellets for the far infrared (FIR) measurements. The former was obtained with a mixture of 2.5 mg of sample and 80 mg of pure PE; for the KBr pellets, 1.4 mg of sample was mixed with 200 mg of KBr powder, placed in an oven at T = 150°C in order to remove water contamination from the KBr powder, and then pressed to obtain high quality pellets.

Transmission spectra were taken as a function of temperature from 10 to 300 K using a continuous Janis liquid helium cryostat working in vacuum. Each spectrum was acquired in the frequency region ($20 - 600$ cm^{-1} for the FIR measurements and $600 - 4000$ cm^{-1} for the spectrum in the MIR), with a spectral resolution of about 2 cm^{-1}. The absorption spectra are derived from the logarithm of the transmission given by the ratio between the spectrum of the sample pellet and the spectrum of the reference pellet.

The temperature dependence of the transmission IR powder spectrum of $Li_2Cu_2O(SO_4)_2$ measured between 10 and 300 K in the frequency region $80 - 4000$ cm^{-1}, represented in logarithmic scale, is shown in Fig. 6.6. The phonon excitations are clearly restricted in the low-energy region. The only visible group of high-energy modes (wavenumber

> 1500 cm^{-1}) is associated with the presence of water contamination which is uninteresting in our investigation.

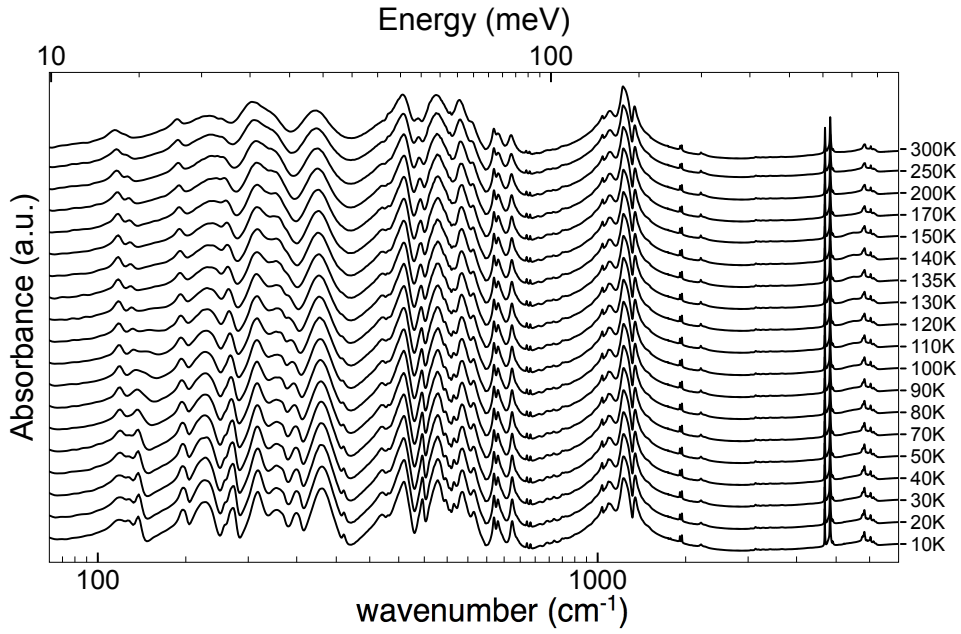

FIGURE 6.6: Temperature dependence of the powder transmission infrared spectrum of $Li_2Cu_2O(SO_4)_2$ in logarithmic scale for the frequency (energy) axis.

In Fig. 6.7 we restrict the spectrum in the frequency region $80 - 1300$ cm^{-1}. Most of the absorption bands visible between 100 and 1300 cm^{-1} are associated with the electric dipole excitation of optical phonons. The group of high-energy modes located around 1100 cm^{-1} is exclusively associated with internal $[SO_4]^{2-}$ bond stretching [158]. The $500 - 700$ cm^{-1} range is dominated by $[SO_4]^{2-}$ tetrahedra bending modes involving progressively the displacement of Cu and O atoms forming the chain backbone, as the frequency decreases.

6.3.1 Factor group analysis

Symmetry can be employed to determine the maximum number of infrared active optical phonons in both phases of this compound. In its high temperature phase, $Li_2Cu_2O(SO_4)_2$ belongs to the $P4_2/m$ space group, which corresponds to the point group C_{4h}. A factor group analysis is used to calculate the symmetry properties and selection rules for vibration modes of the crystal [159, 160], as illustrated in 4.3.1. The character table for the point group C_{4h} is represented in Tab. (6.1). Starting from this table, we determined the irreducible representation for the vibrational modes of $Li_2Cu_2O(SO_4)_2$. The important steps are presented in Tab. (6.2).

The point group symmetry of the Wyckoff positions for each atom in the unit cell are given in the left column. The next step is to calculate the number of atoms that are invariant under symmetry operations of the crystal point group. Their sum gives $\omega(R)$, that is related to the (mechanical) representation character by $\chi^{\text{vib}}(R) = \omega(R)\chi(R)$, with $\chi(R) = \pm 1 + 2\cos\theta(R)$.

The resulting irreducible representation is obtained by the ensemble of n_j^{vib}, one for every Mulliken symbols in the character table. For example, $n_{A_g} = \frac{1}{8}(90 - 6 - 6 +$

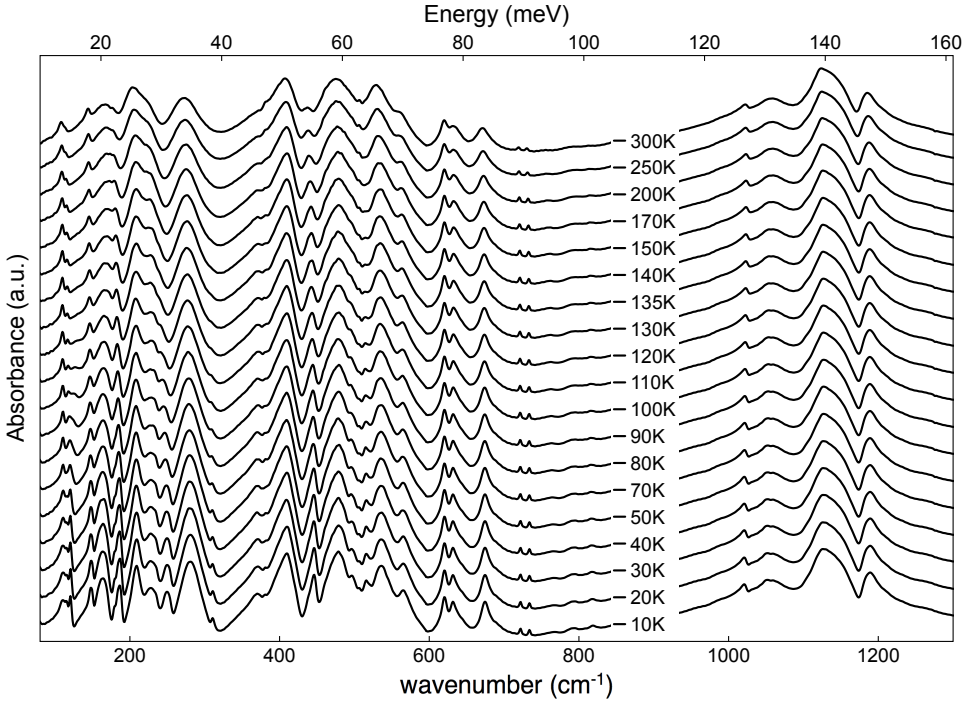

FIGURE 6.7: Temperature dependence of the powder transmission infrared spectrum of $Li_2Cu_2O(SO_4)_2$ in the frequency region 80 − 1300 cm^{-1}.

TABLE 6.1: Character table for the point group C_{4h}

	E	C_2	C_4	C_4^3	i	σ_h	S_4	S_4^3
A_g	1	1	1	1	1	1	1	1
B_g	1	1	-1	-1	1	1	-1	-1
^1E_g	1	-1	-i	i	1	-1	-i	i
^2E_g	1	-1	i	-i	1	-1	i	-i
A_u	1	1	1	1	-1	-1	-1	-1
B_u	1	1	-1	-1	-1	-1	1	1
^1E_u	1	-1	-i	i	-1	1	i	-i
^2E_u	1	-1	i	-i	-1	1	-i	i

$18 - 4 - 4) = 11A_g$. Finally, the vibrational degrees of freedom decompose as:

$$\Gamma_{\mathrm{HT}} = 11A_g + 13B_g + 9E_g + 10A_u + 8B_u + 15E_u. \tag{6.4}$$

Subtracting the $A_u + E_u$ acoustic modes, we find 37 IR-active modes, decomposed in 27 potentially distinct $\Gamma_{\mathrm{HT}}^{\mathrm{IR}} = 9A_u + 14E_u$ bands.

The triclinic distortion, occurring below 125 K, further reduces the crystal symmetry to $P\bar{1}$. A similar analysis leads to the following decomposition on the only two irreducible representations of C_i

$$\Gamma_{\mathrm{LT}} = 42A_g + 48A_u. \tag{6.5}$$

The acoustic active modes are $\Gamma_{\mathrm{LT}}^{\mathrm{ac}} = 3A_u$, therefore $\Gamma_{\mathrm{LT}}^{\mathrm{IR}} = 45A_u$.

As it can be observed in Fig. 6.7, the exact number of bands detected in these experiments is difficult to assess, due to the broad and asymmetric profile of certain

TABLE 6.2: Invariance conditions for $Li_2Cu_2O(SO_4)_2$ structure

	E	C_2	C_4	C_4^3	i	σ_h	S_4	S_4^3
Li1 $(2d)$ $[C_{2h}(2/m)]$	2	2	0	0	2	2	0	0
Li2 $(2f)$ $[\ S_4(4)]$	2	2	0	0	0	0	2	2
Cu $(4j)$ $[\ C_{1h}(m)]$	4	0	0	0	0	4	0	0
S $(4j)$ $[\ C_{1h}(h)]$	4	0	0	0	0	4	0	0
01 $(8k)$ $[\ C_1(1)]$	8	0	0	0	0	0	0	0
02 $(4j)$ $[\ C_{1h}(m)]$	4	0	0	0	0	4	0	0
03 $(4j)$ $[\ C_{1h}(m)]$	4	0	0	0	0	4	0	0
04 $(\bar{4})$ $[S_4(\bar{4})]$	2	2	0	0	0	0	2	2
$\omega(R)$	30	6	0	0	2	18	4	4
$\chi(R)$	3	-1	1	1	-3	1	-1	-1
$\chi^{\text{vib}}(R)$	90	-6	0	0	-6	18	-4	-4

peaks. The above group theoretical analysis therefore only provides an upper bound for the number of bands distinguishable in the experimental spectra. Qualitatively, however, the large increase of active modes due to the symmetry lowering triggered by the triclinic distortion is clearly visible on the experimental spectra when decreasing the temperature below the transition ($\sim$ 125 K) and therefore consistent with the structural data.

Besides this increase in the number of phonon lines, the main effects of decreasing the temperature consist in a slight hardening and narrowing of most of the bands, usually attributed to anharmonic effects and in particular, for the former, to the overall unit cell volume contraction (discussed in the previous chapter). However, a few bands display a softening in the temperature range of the structural transition, characteristic of magneto-elastic effects associated in our case to the rise of the dimerization [161].

6.3.2 Unusual band

At low energy a pronounced transfer of spectral weight toward low frequencies reveals the rise of a weak excitation at 115 cm^{-1} (14.3 meV). This band is indicated by a blue arrow in Fig. 6.10(a).

In order to quantify these spectral changes, a least-square fit of the low-frequency range of the spectra based on a superposition of Lorentzians has been carried out. Figs. 6.8 and 6.9 show two Lorenzian fits of the spectrum in the low-frequencies region (from 80 to 600 $cm^{-}1$) at two different temperatures, at T = 10 and 300 K. The peak associated to the particular band is represented in green. It is clearly visible in the low-temperature spectrum at $T = 10$ K and it vanishes for $T = 300$ K.

The temperature dependence of the energy of the different modes observed in the $105-152$ cm^{-1} range resulting from this fit is displayed in Fig. 6.10(b). A weak hardening of the modes identified as polar phonons (grey filled diamonds) is visible with decreasing temperature except in the transition temperature range ($80-130$ K) where a sizable jump is observed. Concomitantly, the band shown in blue in Fig. 6.10(b) has an energy of 14.3 meV, that falls precisely in the continuum of magnetic excitations observed by INS, in a region characterized by a large spectral weight. Moreover, this excitation is only visible at temperatures well below the structural transition, i.e. in the magnetic dimerized phase. These observations therefore suggest that this excitation might involve, to a certain extent, the spin degrees of freedom of this system.

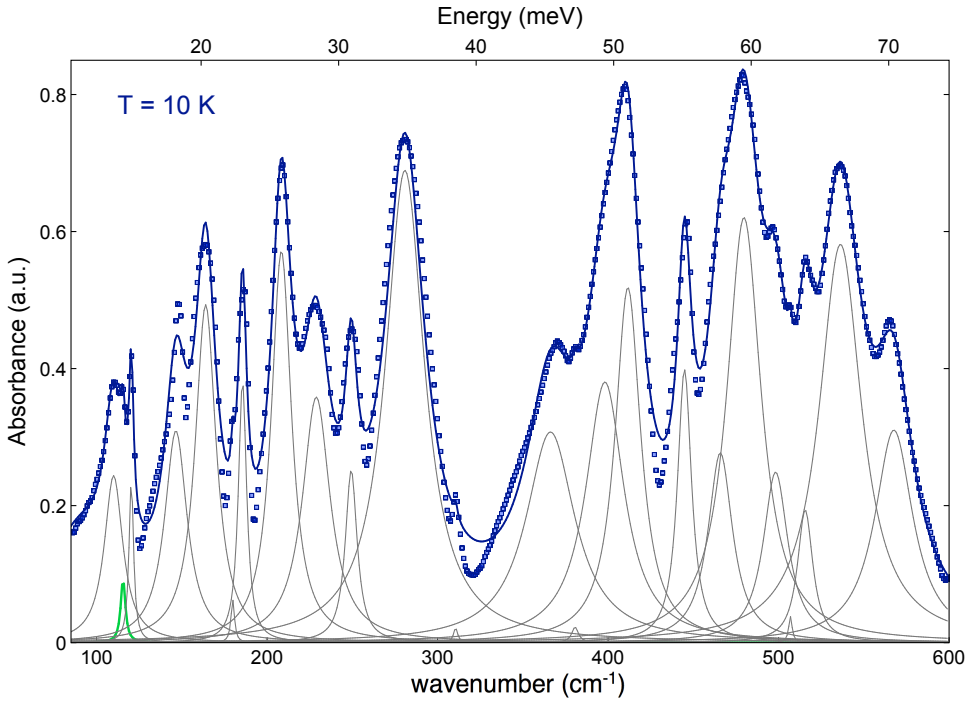

FIGURE 6.8: Infrared spectra of $Li_2Cu_2O(SO_4)_2$ at T = 10 K. The open square blocks are the experimental data. The solid lines represent the Lorentzian fit. In blue the overall fit and in green the particular band.

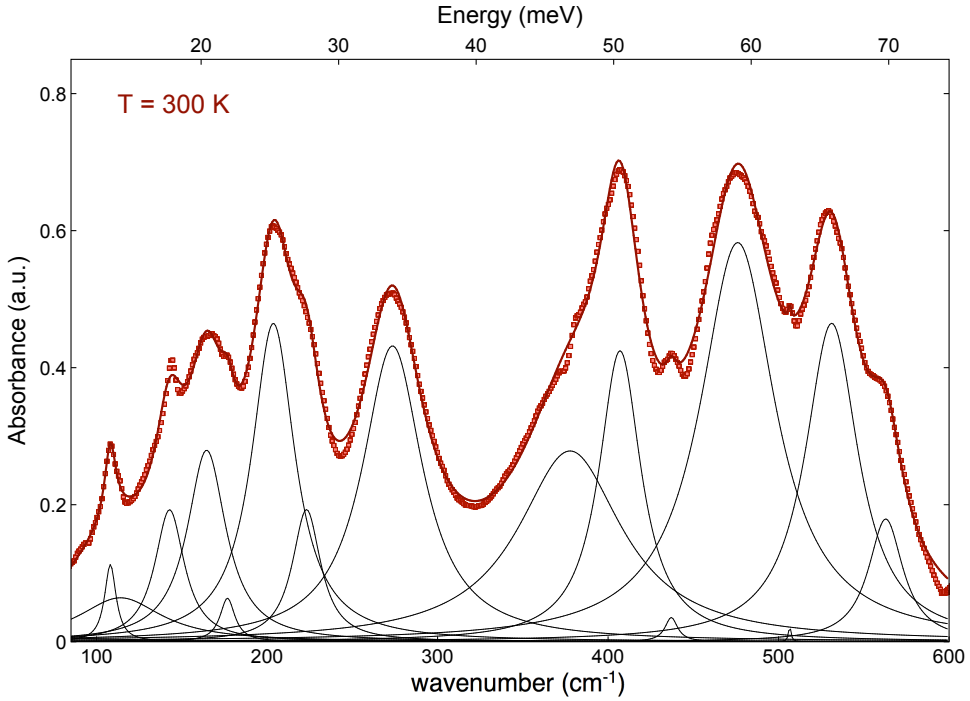

FIGURE 6.9: Infrared spectra of $Li_2Cu_2O(SO_4)_2$ at T = 300 K. The open square blocks are the experimental data. The solid lines represent the Lorentzian fit. In red the overall fit.

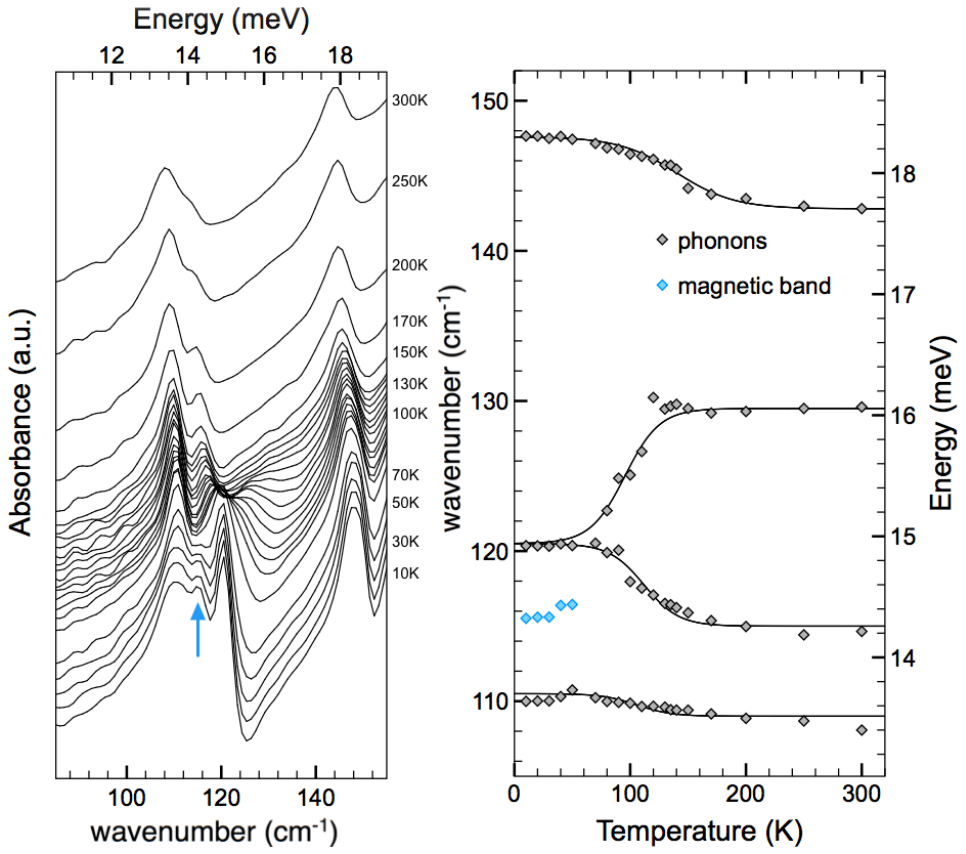

FIGURE 6.10: (a) Enlarged view of the powder transmission infrared spectra in the 80−155 cm^{-1} range. The blue solid line is a guide to the eye following the anomalous softening of the band. (b) Temperature-dependence of the mode frequencies extracted from the Lorentzian fit. Experimental data are represented with filled diamond symbols, lines are only guides for the eye. The phonon bands are represented in black whereas the magnetic band is in blue.

6.4 Perturbation Theory

In order to explain this set of experimental findings and explore the landscape of low-energy magnetic excitations in $Li_2Cu_2O(SO_4)_2$ higher-order perturbation theory calculations have been carried out.

A realistic spin Hamiltonian susceptible to describe the magnetism of this compound in the triclinic phase has been derived previously from first-principle calculations and requires seven distinct couplings to account for the low symmetry of the crystal.

The resulting staggered $S = 1/2$ dimer structure of this model is depicted in Fig. 6.11(e). For the coupling constants we use the relative amplitudes determined by DFT+U [15] for the 2 K structure. $J^d = 1$ and $J^a = 20/330 = 2/33$ are antiferromagnetic and alternate along the legs of the ladder so as to form a staggered dimer structure, $J^a_\perp \approx J^b_\perp = -110/330 = -1/3$ are the ferromagnetic couplings along the rungs of the ladder, $J^b_\times = 78/330 = 13/55$ and $J^c_\times = 133/330$ are antiferromagnetic diagonal couplings between the legs and, finally, $J_2 = 112/330 = 56/165$ is the antiferromagnetic NNN interaction along the legs. This model therefore neglects the supposedly very weak inter-ladder couplings [15] as well as any other term beyond the bilinear, Heisenberg like, interactions.

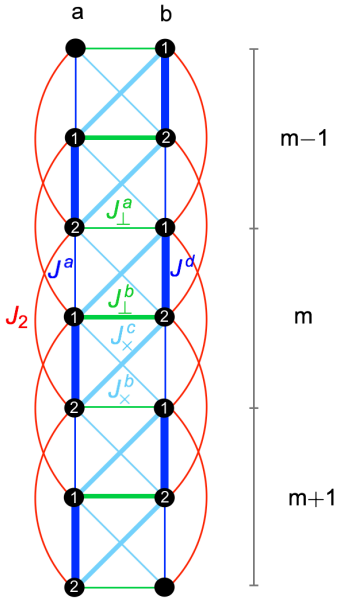

FIGURE 6.11: Schematic representation of the staggered-dimer structure in the triclinic phase (T< 125K). J^a and J^d in blue represent the exchange couplings along the legs, $J^b_\times$ and $J^c_\times$ in light blue the diagonal inter-chain couplings, $J^a_\perp$ and $J^b_\perp$ in green the couplings between the chains along the rungs and the NNN coupling along the legs J_2 in red. Other symbols are described in text.

Perturbation expansion of the one-triplet dispersion relation up to the fifth order has been carried out around the limit of isolated dimers, where the triclinic spin Hamiltonian is considered as the sum of an unperturbed part $\mathbf{H}_0$, for decoupled dimers along the legs (bold blue lines in Fig. 6.11(e)) and a perturbation $\mathbf{W}$, accounting for the coupling between the dimers, with:

$$\mathbf{H}_0 = \sum_m \left[J^d \left(\mathbf{S}^m_{1,a} \cdot \mathbf{S}^m_{2,a} + \mathbf{S}^m_{1,b} \cdot \mathbf{S}^m_{2,b} \right) \right] \tag{6.6}$$

and

$$\begin{aligned} \mathbf{W} = \sum_m \Big[& J_\perp \left(\mathbf{S}^m_{1,a} \cdot \mathbf{S}^m_{2,b} + \mathbf{S}^{m-1}_{2,a} \cdot \mathbf{S}^m_{1,b} \right) + J^a \left(\mathbf{S}^m_{1,a} \cdot \mathbf{S}^{m-1}_{2,a} + \mathbf{S}^m_{1,b} \cdot \mathbf{S}^{m-1}_{2,b} \right) \\ & + J^b_\times \left(\mathbf{S}^{m-1}_{1,a} \cdot \mathbf{S}^m_{1,b} + \mathbf{S}^{m-1}_{2,a} \cdot \mathbf{S}^m_{2,b} \right) + J^c_\times \left(\mathbf{S}^m_{1,a} \cdot \mathbf{S}^m_{1,b} + \mathbf{S}^m_{2,a} \cdot \mathbf{S}^m_{2,b} \right) \\ & + J_2 \left(\mathbf{S}^m_{1,a} \cdot \mathbf{S}^{m+1}_{1,a} + \mathbf{S}^m_{2,a} \cdot \mathbf{S}^{m+1}_{2,a} + \mathbf{S}^m_{1,b} \cdot \mathbf{S}^{m+1}_{1,b} + \mathbf{S}^m_{2,b} \cdot \mathbf{S}^{m+1}_{2,b} \right) \Big]. \end{aligned} \tag{6.7}$$

where m is the cell index, a and b denote the two legs of the ladder, the number 1 or 2 distinguishes the upper and the lower spin-site of a dimer and $\mathbf{S}^m_{i,\alpha}$ with $\alpha = \{a, b\}$ and $i = \{1, 2\}$, are the spin 1/2 operators. In our calculations, we imposed periodic boundary conditions, such that $\mathbf{S}^{m+N} = \mathbf{S}^m$, where $2N$ is the number of the dimers in the chain.

At $\mathbf{W} = 0$, the system consists of isolated dimers and the unperturbed ground-state corresponds to product state of singlets $|0\rangle = \prod_{i=1}^{N} |s\rangle$ on the leg dimers defined by the dominant antiferromagnetic coupling J^d. Low-energy magnetic excitations of this system are obtained by promoting one dimer into a triplet state, $|t_{-1}\rangle = |\downarrow\downarrow\rangle$,

$|t_0\rangle = (|\uparrow\downarrow\rangle + |\downarrow\uparrow\rangle)/\sqrt{2}$ or $|t_1\rangle = |\uparrow\uparrow\rangle$. Therefore, the first excited state is the one-triplet state $|t\rangle_\alpha^m$, a state with a single triplet on a dimer $(m.\alpha)$ and all singlets on the other dimers. As $Li_2Cu_2O(SO_4)_2$ contains two dimers per unit cell, a 2×2 effective Hamiltonian, $\mathbf{W}$, has to be computed for each value of k in Fourier space. This leads to two separate bands of triplets.

The dispersion relation is obtained by diagonalizing the effective Hamiltonian up to the fifth-order in the Bloch states $|T\rangle_\alpha = \frac{1}{\sqrt{N}} \sum_m e^{ikm} |t\rangle_\alpha^m$, $\alpha = \{a, b\}$.

6.4.1 First-order: analytical solution

Our goal is to find the one-triplon dispersion relation at the first order. Therefore, we have to determine how the perturbation can lead to a jump of the triplet from a dimer to another. The calculations have been carried out using two different methods.

Method 1

We introduce the operators $\mathbf{T}_\alpha^m$ and $\mathbf{D}_\alpha^m$

$$\begin{cases} \mathbf{T}_\alpha^m &= \mathbf{S}_{1,\alpha}^m + \mathbf{S}_{2,\alpha}^m \\ \mathbf{D}_\alpha^m &= \mathbf{S}_{1,\alpha}^m - \mathbf{S}_{2,\alpha}^m \end{cases} \iff \begin{cases} \mathbf{S}_{1,\alpha}^m &= \frac{1}{2}\left(\mathbf{T}_\alpha^m + \mathbf{D}_\alpha^m\right) \\ \mathbf{S}_{2,\alpha}^m &= \frac{1}{2}\left(\mathbf{T}_\alpha^m - \mathbf{D}_\alpha^m\right) \end{cases} \tag{6.8}$$

The action of these operators to the local basis states is summarized in the table

	$(\mathbf{T}_\alpha^m)^2$	$\mathbf{T}_\alpha^{m,z}$	$\mathbf{T}_\alpha^{m,+}$	$\mathbf{T}_\alpha^{m,-}$	$\mathbf{D}_\alpha^{m,z}$	$\mathbf{D}_\alpha^{m,+}$	$\mathbf{D}_\alpha^{m,-}$
$\lvert s\rangle_\alpha^m$	0	0	0	0	$\lvert t^0\rangle_\alpha^m$	$-\sqrt{2}\lvert t^+\rangle_\alpha^m$	$\sqrt{2}\lvert t^-\rangle_\alpha^m$
$\lvert t^0\rangle_\alpha^m$	$2\lvert t^0\rangle_\alpha^m$	0	$\sqrt{2}\lvert t^+\rangle_\alpha^m$	$\sqrt{2}\lvert t^-\rangle_\alpha^m$	$\lvert s\rangle_\alpha^m$	0	0
$\lvert t^+\rangle_\alpha^m$	$2\lvert t^+\rangle_\alpha^m$	$\lvert t^+\rangle_\alpha^m$	0	$\sqrt{2}\lvert t^0\rangle_\alpha^m$	0	0	$\sqrt{2}\lvert s\rangle_\alpha^m$
$\lvert t^-\rangle_\alpha^m$	$2\lvert t^-\rangle_\alpha^m$	$-\lvert t^-\rangle_\alpha^m$	$\sqrt{2}\lvert t^0\rangle_\alpha^m$	0	0	$\sqrt{2}\lvert s\rangle_\alpha^m$	0

The $\mathbf{T}_\alpha^m$ operators don't create transitions between singlet and triplet, therefore cannot lead to a triplet jump. The only non-zero terms at the first order are the $\mathbf{D}_\alpha^{m,+}\mathbf{D}_\beta^{m',-}$ terms that permute a singlet and a triplet

$$\mathbf{D}_\alpha^{m,+}\mathbf{D}_\beta^{m',-} |s\rangle_\alpha^m |t\rangle_\beta^{m'} \propto |t\rangle_\alpha^m |s\rangle_\beta^{m'} . \tag{6.9}$$

The Hamiltonian $\mathbf{H} = \mathbf{H}_0 + \mathbf{W}$ can be rewritten in the form

$$\begin{aligned}
\mathbf{H} = \sum_m \Bigg\{ & \frac{J_\perp}{4}\Big[\Big(\mathbf{T}_a^m + \mathbf{D}_a^m\Big)\Big(\mathbf{T}_b^m - \mathbf{D}_b^m\Big) + \Big(\mathbf{T}_a^{m-1} - \mathbf{D}_a^{m-1}\Big)\Big(\mathbf{T}_b^m + \mathbf{D}_b^m\Big)\Big] \\
& + \frac{J_2}{4}\Big[\Big(\mathbf{T}_a^m + \mathbf{D}_a^m\Big)\Big(\mathbf{T}_a^{m-1} + \mathbf{D}_a^{m-1}\Big) + \Big(\mathbf{T}_a^m - \mathbf{D}_a^m\Big)\Big(\mathbf{T}_a^{m-1} - \mathbf{D}_a^{m-1}\Big) \\
& \quad + \Big(\mathbf{T}_b^m + \mathbf{D}_b^m\Big)\Big(\mathbf{T}_b^{m-1} + \mathbf{D}_b^{m-1}\Big) + \Big(\mathbf{T}_b^m - \mathbf{D}_b^m\Big)\Big(\mathbf{T}_b^{m-1} - \mathbf{D}_b^{m-1}\Big)\Big] \\
& + \frac{J^a}{4}\Big[\Big(\mathbf{T}_a^m + \mathbf{D}_a^m\Big)\Big(\mathbf{T}_a^{m-1} - \mathbf{D}_a^{m-1}\Big) + \Big(\mathbf{T}_b^m + \mathbf{D}_b^m\Big)\Big(\mathbf{T}_b^{m-1} - \mathbf{D}_b^{m-1}\Big)\Big] \\
& + \frac{J_\times^b}{4}\Big[\Big(\mathbf{T}_a^{m-1} + \mathbf{D}_a^{m-1}\Big)\Big(\mathbf{T}_b^m + \mathbf{D}_b^m\Big) + \Big(\mathbf{T}_a^{m-1} - \mathbf{D}_a^{m-1}\Big)\Big(\mathbf{T}_b^m - \mathbf{D}_b^m\Big)\Big] \\
& + \frac{J_\times^c}{4}\Big[\Big(\mathbf{T}_a^m + \mathbf{D}_a^m\Big)\Big(\mathbf{T}_b^m + \mathbf{D}_b^m\Big) + \Big(\mathbf{T}_a^m - \mathbf{D}_a^m\Big)\Big(\mathbf{T}_b^m - \mathbf{D}_b^m\Big)\Big] \\
& + \frac{J^d}{4}\Big[\Big(\mathbf{T}_a^m + \mathbf{D}_a^m\Big)\Big(\mathbf{T}_a^m - \mathbf{D}_a^m\Big) + \Big(\mathbf{T}_b^m + \mathbf{D}_b^m\Big)\Big(\mathbf{T}_b^m - \mathbf{D}_b^m\Big)\Big].
\end{aligned} \tag{6.10}$$

The perturbed Hamiltonian (6.7), taking only the $\mathbf{D}_\alpha^m \mathbf{D}_\beta^{m'}$ terms, becomes

$$\begin{aligned}
\mathbf{W} = \sum_n \Bigg[& -\frac{J_\perp}{4}\Big(\mathbf{D}_a^m\mathbf{D}_b^m + \mathbf{D}_a^{m-1}\mathbf{D}_b^m + \frac{J_2}{2}\Big(\mathbf{D}_a^m\mathbf{D}_a^{m-1} + \mathbf{D}_b^m\mathbf{D}_b^{m-1}\Big) \\
& - \frac{J^a}{4}\Big(\mathbf{D}_a^m\mathbf{D}_a^{m-1} + \mathbf{D}_b^m\mathbf{D}_b^{m-1}\Big) + \frac{J_\times^b}{2}\Big(\mathbf{D}_a^{m-1}\mathbf{D}_b^m\Big) + \frac{J_\times^c}{2}\Big(\mathbf{D}_a^m\mathbf{D}_b^m\Big)\Bigg].
\end{aligned} \tag{6.11}$$

Using the translational invariance of the lattice we switch from L single dimer states to Bloch states

$$|T\rangle_\alpha = \frac{1}{\sqrt{N}}\sum_m e^{ikm}\,|t\rangle_\alpha^m \tag{6.12}$$

where $N = L/2$ (two dimers for unit cell), *i.e.*, we switch from a $L \times L$ diagonalization problem to a 2×2 matrix. The diagonal terms of the perturbed matrix in the Bloch basis $|T\rangle_\alpha$, $\alpha = \{a, b\}$, is

$$\begin{aligned}
{}_\alpha\langle T|\mathbf{W}|T\rangle_\alpha = & + \frac{J_2}{2}\frac{1}{N}\sum_{m,m',l}\Big[e^{ik(m-m')}\,{}_\alpha^m\Big\langle t\Big|\mathbf{D}_\alpha^l\mathbf{D}_\alpha^{l-1}\Big|t\Big\rangle_\alpha^{m'}\Big] \\
& - \frac{J^\alpha}{4}\frac{1}{N}\sum_{m,m',l}\Big[e^{ik(m-m')}\,{}_\alpha^m\Big\langle t\Big|\mathbf{D}_\alpha^l\mathbf{D}_\alpha^{l-1}\Big|t\Big\rangle_\alpha^{m'}\Big] \\
= & + \frac{J_2}{2}\Big(e^{ik} + e^{-ik}\Big) - \frac{J^a}{4}\Big(e^{ik} + e^{-ik}\Big) = \Big(J_2 - \frac{J^\alpha}{2}\Big)\cos k.
\end{aligned} \tag{6.13}$$

The off diagonal terms

$$
\begin{aligned}
{}_a\langle T|\mathbf{W}|T\rangle_b = &-\frac{J_\perp}{4}\frac{1}{N}\sum_{m,m',l}\left[e^{ik(m-m')}\,{}^m_a\Big\langle t\Big|\mathbf{D}_a^l\mathbf{D}_b l\Big|t\Big\rangle_b^{m'} + e^{ik(m-m')}\,{}^m_a\Big\langle t\Big|\mathbf{D}_a^{l-1}\mathbf{D}_b^l\Big|t\Big\rangle_b^{m'}\right]\\
&+\frac{J_\times^b}{2}\frac{1}{N}\sum_{m,m',l}\left[e^{ik(m-m')}\,{}^m_a\Big\langle t\Big|\mathbf{D}_a^{l-1}\mathbf{D}_b^l\Big|t\Big\rangle_b^{m'}\right]\\
&+\frac{J_\times^c}{2}\frac{1}{N}\sum_{m,m',l}\left[e^{ik(m-m')}\,{}^m_a\Big\langle t\Big|\mathbf{D}_a^l\mathbf{D}_b^l\Big|t\Big\rangle_b^{m'}\right]\\
= &-\frac{J_\perp}{4}\left(1+e^{ik}\right)+\frac{J_\times^b}{2}e^{ik}+\frac{J_\times^c}{2}
\end{aligned}
\tag{6.14}
$$

and

$$
{}_b\langle T|\mathbf{W}|T\rangle_a = -\frac{J_\perp}{4}\left(1+e^{-ik}\right)+\frac{J_\times^b}{2}e^{-ik}+\frac{J_\times^c}{2}. \tag{6.15}
$$

Method 2

The perturbed Hamiltonian (6.7) can be written as the sum of different terms

$$
\mathbf{W} = \mathbf{H}_\perp + \mathbf{H}_2 + \mathbf{H}^a + \mathbf{H}_\times^b + \mathbf{H}_\times^c \tag{6.16}
$$

$$
\begin{cases}
\mathbf{H}_\perp = J_\perp \sum_m \left(\mathbf{S}_{1,a}^m\mathbf{S}_{2,b}^m + \mathbf{S}_{2,a}^{m-1}\mathbf{S}_{1,b}^m\right)\\
\mathbf{H}_2 = J_2 \sum_m \left(\mathbf{S}_{1,a}^m\mathbf{S}_{1,a}^{m+1} + \mathbf{S}_{2,a}^m\mathbf{S}_{2,a}^{m+1} + \mathbf{S}_{1,b}^m\mathbf{S}_{1,b}^{m+1} + \mathbf{S}_{2,b}^m\mathbf{S}_{2,b}^{m+1}\right)\\
\mathbf{H}^a = J^a \sum_m \left(\mathbf{S}_{1,a}^m\mathbf{S}_{2,a}^{m-1} + \mathbf{S}_{1,b}^m\mathbf{S}_{2,b}^{m-1}\right)\\
\mathbf{H}_\times^b = J_\times^b \sum_m \left(\mathbf{S}_{1,a}^{m-1}\mathbf{S}_{1,b}^m + \mathbf{S}_{2,a}^{m-1}\mathbf{S}_{2,b}^m\right)\\
\mathbf{H}_\times^c = J_\times^c \sum_m \left(\mathbf{S}_{1,a}^m\mathbf{S}_{1,b}^m + \mathbf{S}_{2,a}^m\mathbf{S}_{2,b}^m\right)
\end{cases}
\tag{6.17}
$$

For every term, we have to determine how the perturbation can lead to a triplet jump. As explained before, we switch from a $N \times N$ to a 2×2 problem using the Bloch states 6.12.

$\mathbf{H}_\perp$ hamiltonian The contribution of $\mathbf{H}_\perp$ in the 2×2 Hamiltonian is

$$
\begin{aligned}
{}_a\langle T|\mathbf{H}_\perp|T\rangle_b &= \frac{J_\perp}{N}\sum_{m,m',l} e^{ik(m-m')}\,{}^m_a\Big\langle t\Big|\mathbf{S}_{1,a}^l\mathbf{S}_{2,b}^l + \mathbf{S}_{2,a}^{l-1}\mathbf{S}_{1,b}^l\Big|t\Big\rangle_b^{m'}\\
&= \frac{J_\perp}{N}\sum_m \left[e^{ik(0)}\,{}^m_a\langle t|\mathbf{S}_{1,a}^m\mathbf{S}_{2,b}^m|t\rangle_b^m + e^{ik(1)}\,{}^m_a\Big\langle t\Big|\mathbf{S}_{2,a}^{m-1}\mathbf{S}_{1,b}^m\Big|t\Big\rangle_b^{m-1}\right].
\end{aligned}
\tag{6.18}
$$

To solve the first term of the eq. (6.18), we take the state

$$
\mathbf{S}_{1,a}^m\mathbf{S}_{2,b}^m\,|s\rangle_a^m\,|t^+\rangle_b^m \tag{6.19}
$$

and we find the permutation between the singlet and the triplet [1].

[1] Here we take the triplet state $|t^+\rangle$, but the calculation is the same for $|t^0\rangle$ and $|t^-\rangle$.

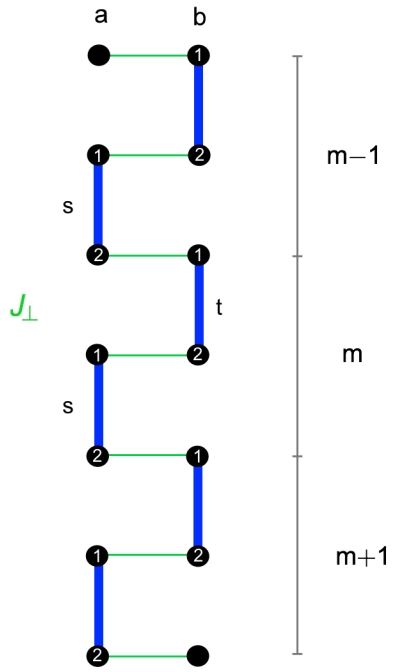

FIGURE 6.12

The spin operator could be decomposed as follows

$$\mathbf{S}^m_{1,a}\mathbf{S}^m_{2,b} = \mathbf{S}^{m,z}_{1,a}\mathbf{S}^{m,z}_{2,b} + \frac{1}{2}\left(\mathbf{S}^{m,+}_{1,a}\mathbf{S}^{m,-}_{2,b} + \mathbf{S}^{m,-}_{1,a}\mathbf{S}^{m,+}_{2,b}\right). \tag{6.20}$$

Therefore, we calculate

$$\begin{aligned}\mathbf{S}^{m,z}_{1,a}\mathbf{S}^{m,z}_{2,b}\left|s\right\rangle^m_a\left|t^+\right\rangle^m_b &= \mathbf{S}^{m,z}_{1,a}\mathbf{S}^{m,z}_{2,b}\frac{1}{\sqrt{2}}\left(\left|\uparrow_1\downarrow_2\right\rangle^m_a - \left|\downarrow_1\uparrow_2\right\rangle^m_a\right)\left|\uparrow_1\uparrow_2\right\rangle^m_b \\ &= \frac{1}{\sqrt{2}}\frac{1}{4}\left(\left|\uparrow\downarrow\right\rangle^m_a + \left|\downarrow\uparrow\right\rangle^m_a\right)\left|\uparrow\uparrow\right\rangle^m_b = \frac{1}{4\sqrt{2}}\left|t^0\right\rangle^m_a\left|t^+\right\rangle^m_b,\end{aligned} \tag{6.21}$$

$$\begin{aligned}\frac{1}{2}\,\mathbf{S}^{m,+}_{1,a}\mathbf{S}^{m,-}_{2,b}\left|s\right\rangle^m_a\left|t^+\right\rangle^m_b &= \frac{1}{2}\,\mathbf{S}^{m,+}_{1,a}\mathbf{S}^{m,-}_{2,b}\frac{1}{\sqrt{2}}\left(\left|\uparrow_1\downarrow_2\right\rangle^m_a - \left|\downarrow_1\uparrow_2\right\rangle^m_a\right)\left|\uparrow_1\uparrow_2\right\rangle^m_b \\ &= -\frac{1}{2}\frac{1}{\sqrt{2}}\left|\uparrow\uparrow\right\rangle^m_a\left|\uparrow\downarrow\right\rangle^m_b = -\frac{1}{4}\left|t^+\right\rangle^m_a\left(\left|t^0\right\rangle^m_b + \left|s\right\rangle^m_b\right),\end{aligned} \tag{6.22}$$

$$\frac{1}{2}\,\mathbf{S}^{m,-}_{1,a}\mathbf{S}^{m,+}_{2,b}\left|s\right\rangle^m_a\left|t^+\right\rangle^m_b = \frac{1}{2}\,\mathbf{S}^{m,-}_{1,a}\mathbf{S}^{m,+}_{2,b}\frac{1}{\sqrt{2}}\left(\left|\uparrow_1\downarrow_2\right\rangle^m_a - \left|\downarrow_1\uparrow_2\right\rangle^m_a\right)\left|\uparrow_1\uparrow_2\right\rangle^m_b = 0. \tag{6.23}$$

The result at the first order is

$$\mathbf{S}^m_{1,a}\mathbf{S}^m_{2,b}\left|s\right\rangle^m_a\left|t^+\right\rangle^m_b \to -\frac{1}{4}\left|t^+\right\rangle^m_a\left|s\right\rangle^m_b. \tag{6.24}$$

For the second term in eq. (6.18), we analyse

$$\mathbf{S}^{m-1}_{2,a}\mathbf{S}^m_{1,b}\left|s\right\rangle^{m-1}_a\left|t^+\right\rangle^m_b. \tag{6.25}$$

The only contributing term is given by $\frac{1}{2}\mathbf{S}^{m-1,+}_{2,a}\mathbf{S}^{m,-}_{1,b}$

$$\begin{aligned}\frac{1}{2}\,\mathbf{S}^{m-1,+}_{2,a}\mathbf{S}^{m,-}_{1,b}\,|s\rangle^{m-1}_{a}\,|t^{+}\rangle^{m}_{b} &= \frac{1}{2}\,\mathbf{S}^{m-1,+}_{2,a}\mathbf{S}^{m,-}_{1,b}\,\frac{1}{\sqrt{2}}\left(|\uparrow_1\downarrow_2\rangle^{m}_{a}-|\downarrow_1\uparrow_2\rangle^{m}_{a}\right)|\uparrow_1\uparrow_2\rangle^{m}_{b}\\ &= \frac{1}{2}\frac{1}{\sqrt{2}}\,|\uparrow\uparrow\rangle^{m}_{a}\,|\downarrow\uparrow\rangle^{m}_{b} = \frac{1}{4}\,|t^{+}\rangle^{m-1}_{a}\left(|t^{0}\rangle^{m}_{b}-|s\rangle^{m}_{b}\right).\end{aligned} \tag{6.26}$$

At the first order, we obtain

$$\mathbf{S}^{m-1}_{2,a}\mathbf{S}^{m}_{1,b}\,|s\rangle^{m-1}_{a}\,|t^{+}\rangle^{m}_{b} \to -\frac{1}{4}\,|t^{+}\rangle^{m-1}_{a}\,|s\rangle^{m}_{b}\,. \tag{6.27}$$

The two summing terms in the equation (6.18) are equal to

$${}^{m}_{a}\langle t|\mathbf{S}^{m}_{1,a}\mathbf{S}^{m}_{2,b}|t\rangle^{m}_{b} = {}^{m}_{a}\left\langle t\middle|\mathbf{S}^{m-1}_{2,a}\mathbf{S}^{m}_{1,b}\middle|t\right\rangle^{m-1}_{b} = -\frac{1}{4}. \tag{6.28}$$

The contribution of $\mathbf{H}_{\perp}$, at the first order, is

$${}_{a}\langle T|\mathbf{H}_{\perp}|T\rangle_{b} = -\frac{J_{\perp}}{4}\left(1+e^{ik}\right). \tag{6.29}$$

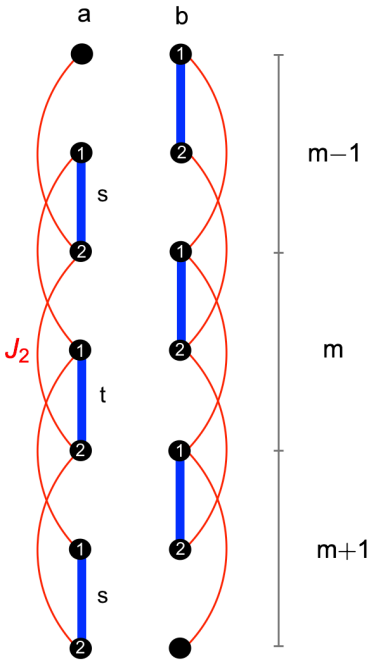

FIGURE 6.13

$\mathbf{H}_2$ hamiltonian

$$
\begin{aligned}
{}_a\langle T|\mathbf{H}_2|T\rangle_a &= \frac{J_2}{N}\sum_{m,m',l} e^{ik(m-m')}\,{}^m_a\!\left\langle t\middle|\mathbf{S}^l_{1,a}\mathbf{S}^{l+1}_{1,a}+\mathbf{S}^l_{2,a}\mathbf{S}^{l+1}_{2,a}\middle|t\right\rangle^{m'}_a \\
&= \frac{J_2}{N}\sum_m \Big[e^{ik(-1)}\,{}^m_a\!\left\langle t\middle|\mathbf{S}^m_{1,a}\mathbf{S}^{m+1}_{1,a}\middle|t\right\rangle^{m+1}_a + e^{ik(1)}\,{}^m_a\!\left\langle t\middle|\mathbf{S}^{m-1}_{1,a}\mathbf{S}^{m}_{1,a}\middle|t\right\rangle^{m-1}_a \\
&\quad + e^{ik(-1)}\,{}^m_a\!\left\langle t\middle|\mathbf{S}^m_{2,a}\mathbf{S}^{m+1}_{2,a}\middle|t\right\rangle^{m+1}_a + e^{ik(1)}\,{}^m_a\!\left\langle t\middle|\mathbf{S}^{m-1}_{2,a}\mathbf{S}^{m}_{2,a}\middle|t\right\rangle^{m-1}_a\Big].
\end{aligned}
\tag{6.30}
$$

To establish the first matrix term in the sum over the square brackets, we calculate

$$
\mathbf{S}^m_{1,a}\mathbf{S}^{m+1}_{1,a}\,|s\rangle^m_a\,|t^+\rangle^{m+1}_a\,. \tag{6.31}
$$

The only contributing term at the first order is given by $\frac{1}{2}\mathbf{S}^{m,+}_{1,a}\mathbf{S}^{m+1,-}_{1,a}$

$$
\begin{aligned}
\frac{1}{2}\,\mathbf{S}^{m,+}_{1,a}\mathbf{S}^{m+1,-}_{1,a}\,|s\rangle^m_a\,|t^+\rangle^{m+1}_a &= \frac{1}{2}\,\mathbf{S}^{m,+}_{1,a}\mathbf{S}^{m+1,-}_{1,a}\,\frac{1}{\sqrt{2}}\left(|\uparrow_1\downarrow_2\rangle^m_a - |\downarrow_1\uparrow_2\rangle^m_a\right)|\uparrow_1\uparrow_2\rangle^{m+1}_a \\
&= -\frac{1}{2}\frac{1}{\sqrt{2}}\,|\uparrow\uparrow\rangle^m_a\,|\downarrow\uparrow\rangle^{m+1}_a \\
&= -\frac{1}{4}\,|t^+\rangle^m_a\left(|t^0\rangle^{m+1}_b - |s\rangle^{m+1}_a\right).
\end{aligned}
\tag{6.32}
$$

The (6.31) becomes

$$
\mathbf{S}^m_{1,a}\mathbf{S}^{m+1}_{1,a}\,|s\rangle^m_a\,|t^+\rangle^{m+1}_a \to \frac{1}{4}\,|t^+\rangle^m_a\,|s\rangle^{m+1}_a\,. \tag{6.33}
$$

All the other terms over the square brackets in (6.30) can be calculated in the same way

$$
\begin{aligned}
{}^m_a\!\left\langle t\middle|\mathbf{S}^m_{1,a}\mathbf{S}^{m+1}_{1,a}\middle|t\right\rangle^{m+1}_a &= {}^m_a\!\left\langle t\middle|\mathbf{S}^{m-1}_{1,a}\mathbf{S}^{m}_{1,a}\middle|t\right\rangle^{m-1}_a = \\
= {}^m_a\!\left\langle t\middle|\mathbf{S}^m_{2,a}\mathbf{S}^{m+1}_{2,a}\middle|t\right\rangle^{m+1}_a &= {}^m_a\!\left\langle t\middle|\mathbf{S}^{m-1}_{2,a}\mathbf{S}^{m}_{2,a}\middle|t\right\rangle^{m-1}_a = \frac{1}{4}.
\end{aligned}
\tag{6.34}
$$

Therefore, the contribution of $\mathbf{H}_2$, at the first order, is

$$
{}_a\langle T|\mathbf{H}_2|T\rangle_a = \frac{J_2}{2}\left(e^{ik}+e^{-ik}\right) = J_2\cos k. \tag{6.35}
$$

$\mathbf{H}^a$ hamiltonian

$$
\begin{aligned}
{}_a\langle T|\mathbf{H}^a|T\rangle_a &= \frac{J^a}{N}\sum_{m,m',l} e^{ik(m-m')}\,{}^m_a\!\left\langle t\middle|\mathbf{S}^l_{1,a}\mathbf{S}^{l+1}_{2,a}\middle|t\right\rangle^{m'}_a \\
&= \frac{J^a}{N}\sum_m \left[e^{ik(-1)}\,{}^m_a\!\left\langle t\middle|\mathbf{S}^m_{1,a}\mathbf{S}^{m+1}_{2,a}\middle|t\right\rangle^{m+1}_a + e^{ik(1)}\,{}^m_a\!\left\langle t\middle|\mathbf{S}^{m-1}_{1,a}\mathbf{S}^{m}_{2,a}\middle|t\right\rangle^{m-1}_a\right] \\
&= -\frac{J^a}{4}\left(e^{ik}+e^{-ik}\right) = -\frac{J^a}{2}\cos k,
\end{aligned}
\tag{6.36}
$$

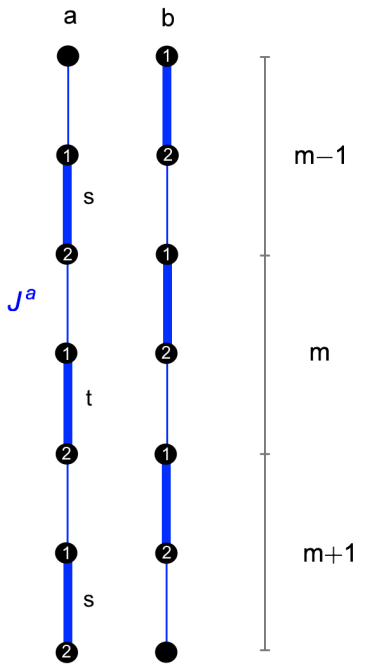

FIGURE 6.14

with the terms in the brackets being calculated in the same way

$$ {}^{m}_{a}\Big\langle t\Big|\mathbf{S}^{m}_{1,a}\mathbf{S}^{m+1}_{2,a}\Big|t\Big\rangle^{m+1}_{a} = {}^{m}_{a}\Big\langle t\Big|\mathbf{S}^{m-1}_{1,a}\mathbf{S}^{m}_{2,a}\Big|t\Big\rangle^{m-1}_{a} = -\frac{1}{4}. \tag{6.37} $$

$\mathbf{H}^b$ hamiltonian

$$ \begin{aligned} {}_a\langle T|\mathbf{H}^b_\times|T\rangle_b &= \frac{J^b_\times}{N}\sum_{m,m',l} e^{ik(m-m')}\,{}^{m}_{a}\Big\langle t\Big|\mathbf{S}^{l}_{1,a}\mathbf{S}^{l-1}_{1,b}+\mathbf{S}^{l}_{2,a}\mathbf{S}^{l-1}_{2,b}\Big|t\Big\rangle^{m'}_{b} \\ &= \frac{J^b_\times}{N}\sum_{m}\Big[e^{ik(+1)}\,{}^{m}_{a}\Big\langle t\Big|\mathbf{S}^{m}_{1,a}\mathbf{S}^{m-1}_{1,b}+\mathbf{S}^{m}_{2,a}\mathbf{S}^{m-1}_{2,b}\Big|t\Big\rangle^{m-1}_{b}\Big] \\ &= \frac{J^b_\times}{2}e^{ik}, \end{aligned} \tag{6.38} $$

where we have used

$$ {}^{m}_{a}\Big\langle t\Big|\mathbf{S}^{m}_{1,a}\mathbf{S}^{m-1}_{1,b}\Big|t\Big\rangle^{m-1}_{b} = {}^{m}_{a}\Big\langle t\Big|\mathbf{S}^{m}_{2,a}\mathbf{S}^{m-1}_{2,b}\Big|t\Big\rangle^{m-1}_{b} = \frac{1}{4}. \tag{6.39} $$

$\mathbf{H}^c$ hamiltonian

$$ \begin{aligned} {}_a\langle T|\mathbf{H}^c_\times|T\rangle_b &= \frac{J^c_\times}{N}\sum_{m,m',l} e^{ik(m-m')}\,{}^{m}_{a}\Big\langle t\Big|\mathbf{S}^{l}_{1,a}\mathbf{S}^{l}_{1,b}+\mathbf{S}^{l}_{2,a}\mathbf{S}^{l}_{2,b}\Big|t\Big\rangle^{m'}_{b} \\ &= \frac{J^c_\times}{N}\sum_{m}\Big[e^{ik(0)}\,{}^{m}_{a}\langle t|\mathbf{S}^{m}_{1,a}\mathbf{S}^{m}_{1,b}+\mathbf{S}^{m}_{2,a}\mathbf{S}^{m}_{2,b}|t\rangle^{m}_{b}\Big] \\ &= \frac{J^c_\times}{2}, \end{aligned} \tag{6.40} $$

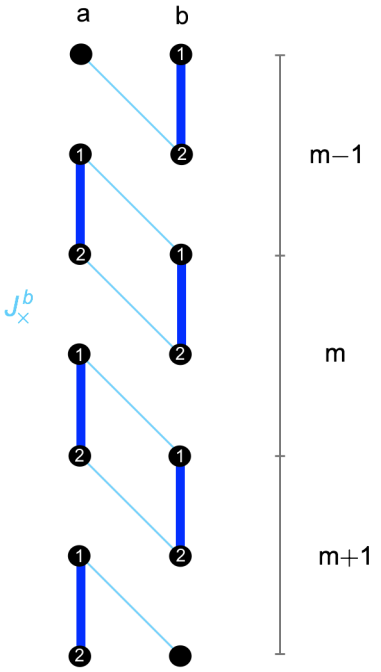

FIGURE 6.15

where

$$ {}^{m}_{a}\langle t|\mathbf{S}^m_{1,a}\mathbf{S}^m_{1,b}|t\rangle^{m}_{b} = {}^{m}_{a}\langle t|\mathbf{S}^m_{2,a}\mathbf{S}^m_{2,b}|t\rangle^{m}_{b} = \frac{1}{4}. \tag{6.41} $$

Perturbed Hamiltonian W Summing all contributions we found, the diagonal term of the 2×2 Hamiltonian reads

$$ {}_a\langle T|\mathbf{W}|T\rangle_a = \left(J_2 - \frac{J^a}{2}\right)\cos k \tag{6.42} $$

and the off diagonal term is given by

$$ {}_a\langle T|\mathbf{H}_{eff}|T\rangle_b = -\frac{J_\perp}{4}\left(1+e^{ik}\right) + \frac{J^b_\times}{2}e^{ik} + \frac{J^c_\times}{2}. \tag{6.43} $$

As can been seen above (equations (6.13) and (6.14)), we have got the same results as with the Method 1.

Dispersion Relation

The perturbation $\mathbf{W}$ reads in the $|T\rangle_\alpha$ basis, $\alpha = \{a, b\}$, at the first-order is:

$$ \mathbf{W} = \begin{pmatrix} \left(J_2 - \frac{J^a}{2}\right)\cos k & -\frac{J_\perp}{4}\left(1+e^{ik}\right) + \frac{J^b_\times}{2}e^{ik} + \frac{J^c_\times}{2} \\ -\frac{J_\perp}{4}\left(1+e^{-ik}\right) + \frac{J^b_\times}{2}e^{-ik} + \frac{J^c_\times}{2} & \left(J_2 - \frac{J^a}{2}\right)\cos k \end{pmatrix} \tag{6.44} $$

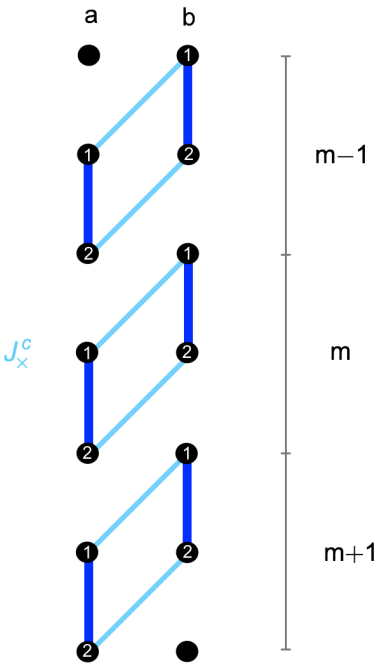

FIGURE 6.16

Solving the eigenvalue equation $\det\left[\mathbf{W}-\omega\mathbb{1}\right]=0$, we find the dispersion relation

$$\omega_\pm(k) = J^d + \left(J_2 - \frac{J^a}{2}\right)\cos k \pm \frac{\sqrt{2}}{4}\Big(2[(J_\times^b)^2 + (J_\times^c)^2] - 2J_\perp(J_\times^b + J_\times^c) + J_\perp^2 - (2J_\times^b - J_\perp)(-2J_\times^c + J_\perp)\cos k\Big)^{1/2} \tag{6.45}$$

Substituting the DFT values of the coupling, we obtain:

$$\omega_\pm(k) = 1 + 0.31\cos k \pm \sqrt{0.12 + 0.11\cos k}. \tag{6.46}$$

6.4.2 Perturbation theory up to the fifth order

Perturbation theory is implemented up to the fifth-order. All orders beyond the first have been calculated with a computer code developed by Andreas Honecker. When looking at the complexity of the formula, we decided to report directly the Mathematica code in the Annex C. In Annex B, we verify the validity of the calculations by comparing the results with results taken from the literature on simpler limit cases.

Numerical results are summarized in Fig. 6.17. Fig. 6.17(a) and (b) show the convergence of the perturbation expansion by comparing, respectively, the one-triplet dispersion relations obtained at different expansion orders and the highest order perturbation theory with exact diagonalization results, performed using finite lattices of $N = 12,\ 16,\ 20\ ,\ 24,\ 28$ and 32 sites with periodic boundary conditions along the legs. For system sizes exceeding $N = 20$ we have used the Lanczos algorithm in order to compute low-lying eigenvalues. As it clearly appears, a remarkable convergence towards the exact results is achieved for the higher-order expansions.

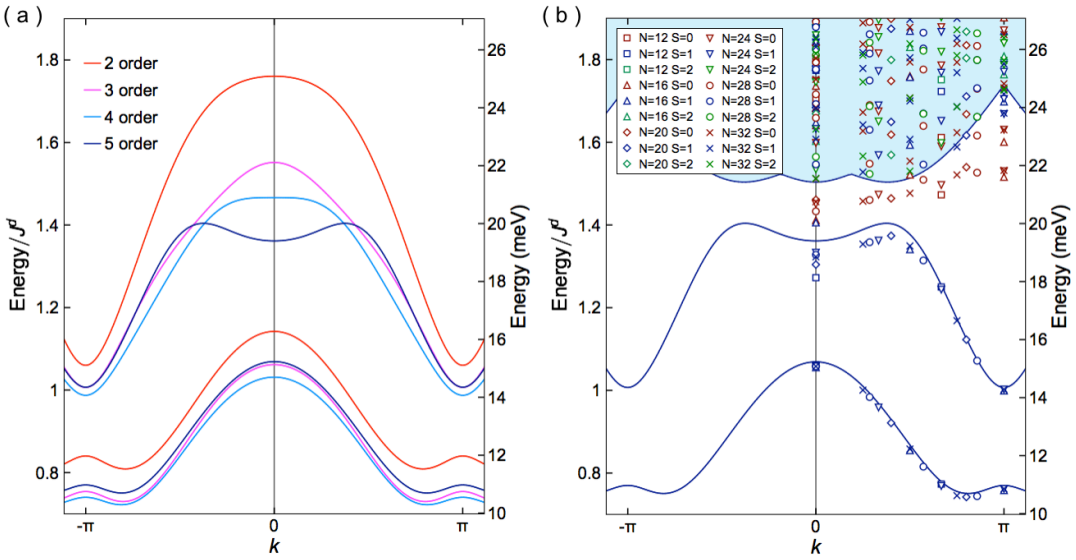

FIGURE 6.17: (a) One-triplet dispersion relation calculated from second to fifth order perturbation theory. (b) Comparison of the one-triplet dispersion relation obtained for the fifth order perturbation theory with exact diagonalization results obtained on finite lattices up to $N = 32$ sites. First few lowest-lying singlets (in red) and triplet (in blue) obtained from ED are shown. The blue filled area corresponds to the free two-triplet continuum. Energies given in meV have been obtained by downscaling the DFT isotropic magnetic couplings by 50 %.

These calculations indicate the presence of two dispersive and slightly overlapping triplet bands above a large spin gap. The lowest band displays a behavior characteristic of antiferromagnetically coupled dimers with a maximum at the zone center and a minimum close the Brillouin zone edge. The actual minimum arises at an incommensurate wave vector and results from the presence of frustrating couplings.

In addition to the one-triplet excitation bands, the lower boundary of the two-triplet continuum, calculated as

$$E_2(k) = \min_{\substack{q\in 1\mathrm{BZ} \\ m,n=1,2}} [\omega_m(k-q) + w_n(q)] \tag{6.47}$$

and where $\omega_1(k)$ and $\omega_2(k)$ represent the two one-triplet bands, is also shown in Fig. 6.17(b). The large value of the spin gap compared to the modest triplet excitation band-width, pushes this continuum lower bound well above the maximum of the highest one-triplet band. The ED results are close to the fifth-order expansion, i.e., both of them can be considered accurate. The exception is the top of the upper band where proximity to the continuum leads to larger finite-size effects and slower convergence of the series.

Figure 6.18 shows the ED energies of the triplet excitations for two different value of k, $k = 0$ and $k = \pi$, as a function of the inverse of the size, $1/N$. One observes that the values of the energies for $k = \pi$ and for the lower band of the triplet at $k = 0$ converge rapidly. Larger finite-size effects are only observed at the top of the upper band at $k = \pi$. This corresponds to the region where the series also show a slow convergence (see Fig. 6.17(a)) and we speculate that this is again due to the proximity with the continuum. Still, for systems with $N > 20$, the data can also be

considered to converge to the thermodynamic limit. Even in this least favorable case, finite-size corrections to the $N = 32$ data are presumably negligible for both bands and all values of k.

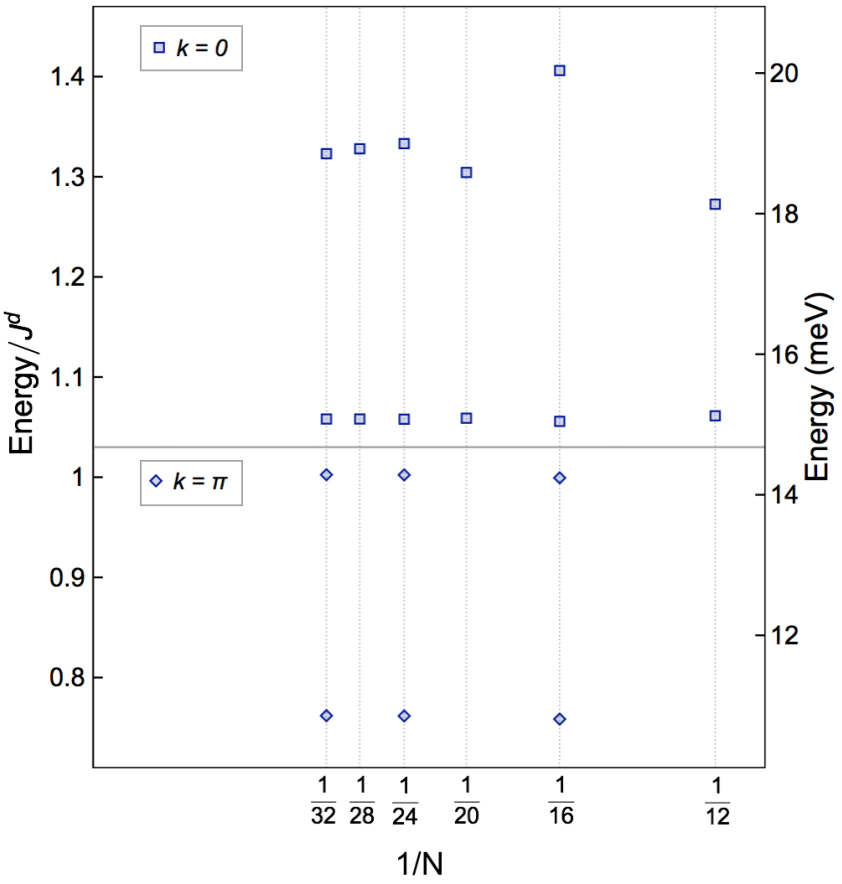

FIGURE 6.18: Extraction of the exact digaonalization results obtained on finite lattices up to $N = 32$ sites. The triplet energies ($S = 1$) for $k = 0$ and $k = \pi$ are plotted in function of $1/N$.

Exact diagonalization, furthermore, reveals the presence of lower-lying singlets above and below the continuum, which do not interfere with the upper triplet band, as it can be seen in Fig. 6.17(b). Similar excitations have already been reported in ladder systems where they can be understood as bound states of two triplets [162, 163, 12].

It should be mentioned, however, that we only have a powder sample, thus we do not have experimental access to the actual triplet dispersion. Nevertheless, we can investigate the density of state (DOS), which is numerically computed starting from the perturbation expression at fifth-order of the one-triplet dispersion bands. The result is shown in Fig. 6.19.

6.5 Discussion

The theoretical results presented in the previous section provide solid ground for analyzing the experimental results obtained on $Li_2Cu_2O(SO_4)_2$. It should be noted, however, that the global energy scale, given by $J^d \approx 28$ meV and obtained from first-principle calculations [15], is not consistent with our experimental observations. Indeed, as already reported, a straightforward use of the magnetic couplings provided

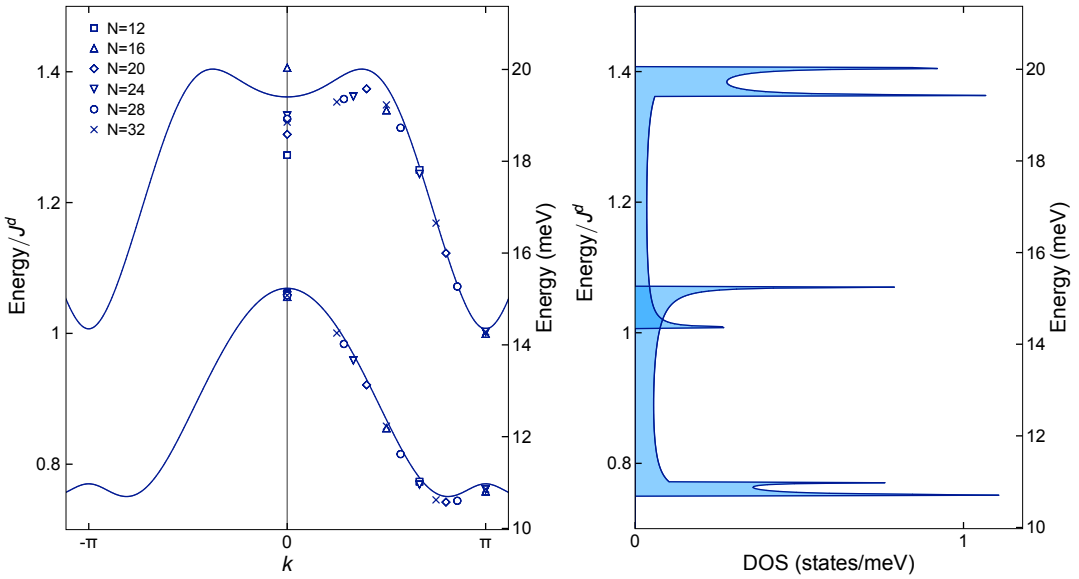

FIGURE 6.19: (a) Comparison of the one-triplet dispersion relation obtained for the fifth order perturbation theory with exact diagonalization results of triplet excitations obtained on finite lattices up to $N = 32$ sites. (b) One-triplet density of states obtained from fifth order perturbation theory dispersion relations. Energies given in meV have been obtained by downscaling the DFT isotropic magnetic couplings by 50 %.

by density functional theory (DFT) calculations leads to a substantial overestimation of the experimental spin gap [15]. Although the amplitudes of these couplings are often overestimated and strongly depend on the approximate treatment of exchange and correlation employed in the calculations [164, 165], their ratios are expected to be subject to smaller errors [166]. In this framework, the ratios between the seven couplings involved in the spin Hamiltonian were considered as fixed. The global energy scale was thus taken as the only variable parameter, adjusted so as to reproduce the experimental value of the spin gap. This led to an approximate 50 % downscaling of the DFT coupling amplitudes. The resulting energy scale in millivolts is shown on the vertical axes of Fig 6.17.

Under these assumptions, powder INS can be qualitatively discussed in terms of one-triplet excitation density-of-states (DOS) shown in Fig. 6.19(b). In first approximation, the experimental peaks A, B and C shown in Fig. 6.4 can indeed be interpreted as arising from the DOS singularities, at the bottom of the lowest band for peak A and in the overlapping region of the two bands for peaks B (bottom of the upper band) and C (top of the lower band). Although this qualitative analysis provides a satisfying explanation regarding the origins of the low-energy part of the INS data, it also predicts the presence of higher-lying features corresponding to the top of the highest one-triplet band, *i.e.* at $\sim$ 20 meV, which are not observed experimentally. This could simply be a matrix element effect. Alternatively, although our model locates the two-triplet continuum lower bound above the highest one-triplet branch over the entire first Brillouin zone (see Fig. 6.17(b)), they remain close in energy. Therefore, only minor modifications of the model employed in this work would be necessary to change this picture and, in particular, restore a significant overlap between the highest triplet quasi-particle mode and the two-particle continuum. This overlap will provide spontaneous decay channels [167, 168] leading to significant damping of these

quasi-particles and therefore to the absence of visible signatures in INS data.

A second important question arises from the likely detection of triplet excitations in IR spectroscopy presented in Sec. 6.3. Indeed, dominant electric dipole transitions induced by light are strictly confined to spin-conserving excitations ($\Delta S = 0$) and are therefore, in principle, unable to reveal singlet-to-triplet transitions. However, it has been shown that, in a number of low-dimensional quantum magnets, this selection rule can be circumvented through essentially two mechanisms relying on the presence of spin-phonon coupling and involving one or multiple magnetic excitations.

A successful and now well-established model employed to describe the infrared optical absorption of one and two-dimensional undoped cuprates is based on phonon-assisted bi-magnon absorption [169, 138, 170, 171, 163]. The excitation of singlet bound states, resulting from the coupling of two spin-carrying modes (triplets, in our case) in such a way that the total spin amounts to zero, indeed obeys the imposed spin selection rule (see 4.3.2). Lorenzana and Sawatzky further showed that, when a center of inversion is present, dipole-allowed absorption is only possible if a symmetry-breaking phonon is also involved in the process [169, 138]. In our case, an attribution of the IR band observed at 14.3 meV for $T < 70$ K to the absorption of phonon-assisted bi-magnons is very unlikely as the typical energy of these excitations, already of the order of $\sim 2\Delta = 21.2$ meV when neglecting the phonon energy, are much larger.

An alternative mechanism, arising from the spin-orbit coupling, has been proposed to explain the detection of singlet-to-triplet excitations in dimerized quantum magnets using IR absorption [172, 161]. As discussed in 4.3.2, it can be described qualitatively as a process where light excites the system into a virtual spin-singlet one-phonon state coupled, through a *dynamic* Dzyaloshinskii-Moriya (DM) interaction, to a spin-triplet zero-phonon state [173]. This mechanism thus relies on the assumption that the virtual polar phonon involved in the process is associated with atomic displacements able to induce an instantaneous variation of the DM vector. Assuming that such a mechanism is effective in the low-temperature phase of $Li_2Cu_2O(SO_4)_2$, the 14.3 meV IR absorption band would, quite accurately, match the zone center maximum of the lowest one-triplet excitation and the corresponding Van Hove singularity in the DOS.

6.6 Conclusion

In this chapter we have analysed the first experimental investigation of magnetic excitations in the low-temperature, dimerized phase of the recently discovered frustrated spin-1/2 two-leg ladder $Li_2Cu_2O(SO_4)_2$.

The inelastic neutron scattering measurements obtained on powder samples reveal the presence of a dispersive triplet excitation of bandwidth of the order of 5 meV above a large spin gap of 10.6 meV at 1.5 K. In particular, the continuum of states includes two intense peaks at 11.2 meV and 14.7 meV plus a shoulder at 13.5 meV, associated to the second peak. It should be noted that the dispersive character shows a non-complete dimerization of the system at the low-temperature phase. Moreover, the value of the spin gap is consistent with the estimates extracted from the magnetic susceptibility.

In addition, an absorption band showing an unusual softening with decreasing temperature, is observed in IR spectroscopy and attributed to a triplet excitation arising at 14.3 meV at 10 K. The dynamic Dzyaloshinskii-Moriya mechanism is invoked in this case to explain the absorption of light by this low-dimensional spin system.

Exact diagonalization and higher-order perturbation theory calculations allowed for an overall consistent interpretation of these results in terms of one-triplet quasi-particle excitations above the singlet ground-state. These calculations were carried out on the basis of the dimerized geometry derived from first-principle calculations, presented in the previous chapter. While experiments and theory show an overall good agreement, the only exception lies in the high-energy part of the triplet excitation spectrum, where a possible coupling between the quasi-particles and the high-lying many-particle continuum may be responsible for the absence of high-energy structure in the INS spectra. This calls for further experimental and theoretical investigations of this very rare example of frustrated spin-1/2 ladder, which will heavily rely on the future availability of single crystals.

Chapter 7

Conclusion

The main focus of this thesis was the investigation of the magnetic properties of the low-dimensional spin system $Li_2Cu_2O(SO_4)_2$, recently synthetized at the College de France. In its high-temperature tetragonal phase this cuprate displays a very peculiar crystal structure. The magnetic Cu^{2+} ions are localized in square planar environments grouped by two to form platelets. These platelets are connected one to each other at 90° through an oxygen atom. Moreover a sulphate group SO_4 creates a bridge between the copper in the platelets which point in the same direction. These environments form copper chains, well separated from each other by lithium atoms. Considering super-exchange mechanisms supported by Cu-O-Cu bonds, this geometry is exactly that of a linked-tetrahedra spin chains with nearest neighbour interaction between the copper in the same platelets $J_\perp$ and interplatelets interaction J. Furthermore, the non-magnetic bridging units, such as SO_4, play a preponderant role to mediate strong and long ranged antiferromagnetic interactions, leading in the present case to sizeable second-nearest neighbor interaction along the chains J_2. This system is thus topologically equivalent to a spin-1/2 two-leg ladder system where frustration arises from next-nearest interactions along the legs.

We are therefore in the presence of a very rare example of frustrated spin ladder, a system at the center of a very impressive amount of theoretical work over the past decades with fairly rare example of real realizations, as described in Chapter 2. Electronic structure calculations have been undertaken to determine the sign and strength of the dominant magnetic couplings and to establish a spin Hamiltonian on the basis of ab initio results. Calculations carried out at the DFT+U level clearly confirm the quasi-1D magnetism of the compound as well as the presence of strong frustration: out of three dominant couplings, two are AFM (J and J_2) and one is FM ($J_\perp$).

Temperature dependent magnetic susceptibility measurements showed a behavior typical for a 1D antiferromagnetic system, with a spin-singlet ground-state and a singlet-triplet spin-gap. In agreement with these results, powder neutron diffraction confirmed the absence of magnetic long-range order down to 2 K, but also revealed the occurrence of a structural phase transition at about 125 K from the tetragonal to the triclinic symmetry. This transition is not accompanied by any volume discontinuity and only involves a very weak distortion in the structure. Combining experimental and theoretical approaches, we have demonstrated that this weak distortion involves a strong splitting in the interplatelet couplings, with a strong increase of one of the couplings along the legs. The triclinic phase can thus be described by a staggered $S = 1/2$ dimer structure, removing most of the magnetic frustration.

Moreover, we have investigated the magnetic excitations of the powder sample $Li_2Cu_2O(SO_4)_2$. Despite the presence of a magnetic dimerization, neutron scattering experiments revealed the presence of dispersive triplet excitations above a spin gap of $\Delta = 10.6 \pm 0.2$ meV, a value consistent with the estimates extracted from

magnetic susceptibility. In addition, these spin excitations seem to be responsible of an unusual softening of mode when the temperature decrease, likely detected in the absorption band of the IR spectroscopy. The dynamic Dzyaloshinskii-Moriya mechanism is invoked in this case to explain the absorption of light by this low-dimensional spin system. Higher-order perturbation and exact diagonalization calculations of these low-energy triplet excitations based on a spin Hamiltonian derived from first-principles provided an overall qualitative interpretation of these results.

Despite these various interesting observations and findings, other challenging questions await further investigations. In particular, an important step would be the successful synthesis of single crystals, which would give more quantitative results by revealing the dispersion of magnetic excitations and probably solve the open questions about the theoretically expected third excitation that is missing in the experimental INS measurements. Single crystal would also help clarifying the results obtained in IR spectroscopy through polarization-dependent measurements or experiments carried out under magnetic field.

Further researches in solid-state chemistry and synthesis, for instance by substituting Li ions or sulfate groups could lead to new types of interesting geometries or even suppress the structural transition responsible for the magnetic dimerization in an isostructural compound allowing for the low-temperature study of the still-missing frustrated and undistorted two-leg spin ladder.

Appendix A

Derivation of the Heisenberg Hamiltonian from the Hubbard model at half filling

The Hubbard model is a model which takes into account quantum mechanical motion of electrons in a solid and repulsive interaction between electrons. The model describes fermions whose quantum dynamics is governed by the Hamiltonian

$$H = \sum_{ij\sigma}{}' t_{ij} c^\dagger_{i\sigma} c_{j\sigma} + \sum_i U \mathbf{n}_{i\uparrow}\mathbf{n}_{i\downarrow}. \tag{A.1}$$

The prime over the first sum excludes the terms $i = j$. Indices i and j represent lattice sites, corresponding to the atomic sites in a crystal, σ is a spin index $\{\sigma = \uparrow, \downarrow\}$. The operators $c^\dagger_{i\sigma}$ and $c_{i\sigma}$ are the fermionic creation and annihilation operators for a particle in the spin state σ (up or down) at lattice sites i, they create and destroys an electron with spin σ at site $i \in \Lambda$. The number operator $\mathbf{n}_{i\sigma} = c^\dagger_{i\sigma} c_{i\sigma}$ counts the number of electrons of spin σ on site i. These fermion operators obey the canonical anticommutation relations

$$\{c^\dagger_{i\sigma}, c_{j\tau}\} = \delta_{i,j}\delta_{\sigma,\tau} \tag{A.2}$$

and

$$\{c^\dagger_{i\sigma}, c^\dagger_{j\tau}\} = \{c_{i\sigma}, c_{j\tau}\} = 0. \tag{A.3}$$

The first term in (A.1) is the *hopping hamiltonian*. It contains the hopping amplitude t_{ij} such that $t_{ij} = t_{ji}$, which represents the tunnelling matrix element between adjacent lattice sites. This part describes the hopping of the electrons from site i to j (or from j to i). The second term in (A.1) is the *Coulomb repulsion hamiltonian*, it describes the interaction energy in the system determined by the on-site interaction U, i.e. the electrostatic energy of two electrons on the same site.

In the standard Hubbard model each site has only one electron orbital, it can either be vacant, occupied by an $\uparrow$ or $\downarrow$ electron, or occupied by both $\uparrow$ and $\downarrow$ electrons. In the limit $U/t \to \infty$ the particles are almost perfectly localized, it does not matter whether the neighbour of a particle has the same or the opposite spin. Therefore, there are a large number of energetically equivalent ways of arranging the particles in the lattice. This degeneracy is lifted for smaller U, where an effective magnetic coupling between the spins emerges. This is because the system tries to lower energy by having at least some tunneling. At large interaction $U \gg t$ this is done by the so-called superexchange process: neighboring fermions tunnel (hop) via an intermediate highly energetic doubly occupied state. Due to Pauli blocking the doubly occupied state is only possible for fermions of different spin. Therefore the superexchange

can occur only for fermions of opposite spins, and the arising effective coupling is antiferromagnetic.

We consider strong coupling limit of the Hubbard model ($U \gg t$) at half-filling, i.e. a system in which the electron number N_e is equal to the number of sites N. The perturbative treatment of the half-filled Hubbard model leads to an effective spin-1/2 Heisenberg Hamiltonian

$$H = \sum_{ij} J_{ij} \mathbf{S}_i \mathbf{S}_j \tag{A.4}$$

where the antiferromagnetic exchange costant $J_{ij} = 4t_{ij}^2/U$.

Since $U \gg t$, it is reasonable to choose the Coulomb term as the unperturbed part of the Hamiltonian H_0 and the remaining hopping term as a perturbation V.

The Hamiltonian of the Hubbard model, in the limit $U \gg t$, can be divided in two terms, the Coulomb term as the unperturbed part

$$H_0 = \sum_j U \mathbf{n}_{j\uparrow} \mathbf{n}_{j\downarrow}, \tag{A.5}$$

and the hopping term as a perturbation

$$V = {\sum_{ij\sigma}}' t_{ij} c_{i\sigma}^\dagger c_{j\sigma}. \tag{A.6}$$

We have to consider the eigenvalue equation for the ground-state of the Hamiltonian H_0. The operator $H_0 = \sum_j U \mathbf{n}_{j\uparrow} \mathbf{n}_{j\downarrow}$ counts the number of site with a pair of electrons n and the GS space describes a highly localized situation, for which there is one and only one electron on each site. The energy ϵ_0 is therfore equal to zero.

$$H_0 |\varphi_n^i\rangle = \epsilon_0 |\varphi_n^i\rangle = nU |\varphi_n^i\rangle, \tag{A.7}$$

$$H_0 |\varphi_0^i\rangle = \epsilon_0 |\varphi_0^i\rangle = 0. \tag{A.8}$$

The electron on its site can be with spin up $|\uparrow\rangle$ or spin down $|\downarrow\rangle$ and, consequently, the degeneracy of the GS is 2^N, where N is the total number of sites.

The lowest excited state is connected to the first order of perturbation theory $\langle \psi_0^i | V | \psi_0^j \rangle$, where the operator $V = {\sum_{ij\sigma}}' t_{ij} c_{i\sigma}^\dagger c_{j\sigma}$ acting on the state $|\psi_0^i\rangle$ with one electron on each site, produce a state $|\psi_1^i\rangle$ with one pair of electrons in one site of the chain and energy, from the (A.7),

$$\epsilon_1 = \langle \psi_1^\gamma | H_0 | \psi_1^\gamma \rangle = U, \tag{A.9}$$

therefore the lowest exicted state has one doubly occupied site and its degeneracy is $N(N-1)2^{N-2}$. Consequently the fist order correction of the perturbation theory is equal to zero:

$$\langle \psi_n^i | V | \psi_0^j \rangle \propto \langle \psi_n^i | \psi_1^j \rangle \neq 0 \quad \text{only if } n = 1 \tag{A.10}$$

$$\implies \quad \langle \psi_0^i | V | \psi_0^j \rangle = 0. \tag{A.11}$$

The second order term is equal to

$$\sum_{m\gamma} \frac{\langle \psi_0^i | V | \psi_m^\gamma \rangle \langle \psi_m^\gamma | V | \psi_0^j \rangle}{\epsilon_0 - \epsilon_m}. \tag{A.12}$$

From the (A.10) we can reduce the sum in the term with $m = 1$ that has energy $\epsilon_1 = U$, independent of the sum over γ

$$\sum_{m\gamma} \frac{\langle\psi_0^i|V|\psi_m^\gamma\rangle\langle\psi_m^\gamma|V|\psi_0^j\rangle}{\epsilon_0 - \epsilon_m} = \sum_{\gamma} \frac{\langle\psi_0^i|V|\psi_1^\gamma\rangle\langle\psi_1^\gamma|V|\psi_0^j\rangle}{-\epsilon_1} =$$
$$= -\frac{\langle\psi_0^i|V\left(\sum_\gamma |\psi_1^\gamma\rangle\langle\psi_1^\gamma|\right)V|\psi_0^j\rangle}{U} = -\frac{\langle\psi_0^i|V^2|\psi_0^j\rangle}{U}$$

where we have used the identity $\sum_\gamma |\psi_1^\gamma\rangle\langle\psi_1^\gamma| = \mathbb{1}$.

We define the effective Hamiltonian as

$$\langle\psi_0^i|H_{eff}|\psi_0^j\rangle = -\frac{\langle\psi_0^i|V^2|\psi_0^j\rangle}{U}. \tag{A.13}$$

Therefore

$$H_{eff} = P_0\left(-V^2/U\right)P_0, \tag{A.14}$$

where $P_0 = \sum_i |\psi_0^i\rangle\langle\psi_0^i|$ is the projection operator. Replacing V by its explicit expression, we obtain

$$H_{eff} = P_0\left(-{\sum_{ij\sigma}}' {\sum_{kl\eta}}' t_{ij}t_{kl}c_{i\sigma}^\dagger c_{j\sigma}c_{k\eta}^\dagger c_{l\eta}/U\right)P_0. \tag{A.15}$$

The creation and annihilation operators are acting on the subspace with one electron on each site because of the projection operators on the left and on the right, therefore only the terms with $j = k$ and $i = l$ contribute. Taking into account the anticommutation rules that are ruling the fermionic systems (A.2) and (A.3) and remembering that $t_{ij} = t_{ij}^\star$, we can easily get

$$H_{eff} = P_0\left({\sum_{ij}}' |t_{ij}|^2 \sum_\sigma \left(\mathbf{n}_{i\sigma}\mathbf{n}_{j\sigma} + c_{i\sigma}^\dagger c_{i-\sigma}c_{j-\sigma}^\dagger c_{j\sigma} - \mathbf{n}_{i\sigma}\right)/U\right)P_0. \tag{A.16}$$

where $\mathbf{n}_{i\sigma} = c_{i\sigma}^\dagger c_{i\sigma}$ is the number operator.

The Heisenberg spin-spin interaction can be obtained from the many-particles Hubbard Hamiltonian using a representation in which the spin operator are specified in terms of the fermionic creation and annihilation operator:

$$S_{iz} = \frac{1}{2}\sum_\sigma c_{i\sigma}^\dagger c_{i\sigma} = \frac{1}{2}\sum_\sigma \mathbf{n}_{i\sigma} \tag{A.17}$$

i.e., simply subtract the number of particles with spin down from those with spin up to find the spin in the z-direction. In addition

$$S_{i+} = S_{ix} + iS_{iy} = c_{i\sigma}^\dagger c_{i-\sigma} \tag{A.18}$$
$$S_{i-} = S_{ix} - iS_{iy} = c_{i-\sigma}^\dagger c_{i\sigma} \tag{A.19}$$

raise or lower the total spin by flipping spins down into spins up or viceversa.

Equation (A.16) becomes

$$H_{eff} = P_0 \left(\sum_{ij}{}' \frac{4|t_{ij}|^2}{U} \mathbf{S}_i \mathbf{S}_j \right) P_0. \tag{A.20}$$

We can conclude that in the limit $U \gg t$ the effective Hamiltonian is given by the Heisenberg hamiltonian

$$H_J = \sum_{ij}{}' J_{ij} \mathbf{S}_i \mathbf{S}_j$$

with $J_{ij} = 4t_{ij}^2/U$.

Appendix B

Perturbation Theory: Comparison with simpler limit cases

The evaluation of the one-triplet dispersion dispersion relation has been carried out solving the spin Hamiltonian parametrized *ab-initio* (DFT) around the limit of isolated dimer (low-temperature phase), implementing a hight-order perturbative approach in the strong coupling expansion.

Following [15], the triclinic phase (T> 125K) can be described by the staggered $S = 1/2$ dimer structure schematized in Fig. B.1 (a). In this structure one of the couplings along the legs, J^d, is much higher that the others.

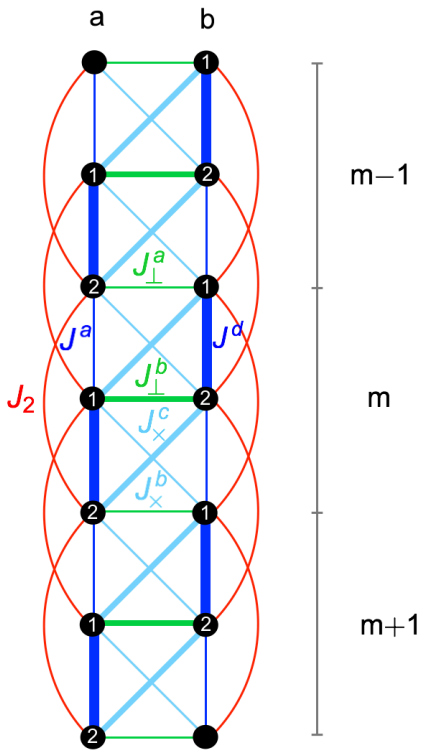

FIGURE B.1: (a) Schematic representation of the staggered-dimer structure: J^a and J^d in blue represent the alternating couplings along the legs, $J_\times^b$ and $J_\times^c$ in light blue the diagonal inter-chain couplings, $J_\perp^a$ and $J_\perp^b$ in green the couplings between the chains along the rungs and the NNN coupling along the legs J_2 in red.

As illustrated in section 6.4, the triclinic Hamiltonian H can be written the sum of an unperturbed, $\mathbf{H}_0$, and a perturbed part, $\mathbf{W}$, with:

$$\mathbf{H}_0 = \sum_m \left[J^d \left(\mathbf{S}^m_{1,a} \cdot \mathbf{S}^m_{2,a} + \mathbf{S}^m_{1,b} \cdot \mathbf{S}^m_{2,b} \right) \right] \tag{B.1}$$

and

$$\begin{aligned} \mathbf{W} = \sum_m \Big[& J_\perp \left(\mathbf{S}^m_{1,a} \cdot \mathbf{S}^m_{2,b} + \mathbf{S}^{m-1}_{2,a} \cdot \mathbf{S}^m_{1,b} \right) + J_2 \left(\mathbf{S}^m_{1,a} \cdot \mathbf{S}^{m+1}_{1,a} + \mathbf{S}^m_{2,a} \cdot \mathbf{S}^{m+1}_{2,a} \right. \\ & \left. + \mathbf{S}^m_{1,b} \cdot \mathbf{S}^{m+1}_{1,b} + \mathbf{S}^m_{2,b} \cdot \mathbf{S}^{m+1}_{2,b} \right) + J^a \left(\mathbf{S}^m_{1,a} \cdot \mathbf{S}^{m-1}_{2,a} + \mathbf{S}^m_{1,b} \cdot \mathbf{S}^{m-1}_{2,b} \right) \\ & + J^b_\times \left(\mathbf{S}^{m-1}_{1,a} \cdot \mathbf{S}^m_{1,b} + \mathbf{S}^{m-1}_{2,a} \cdot \mathbf{S}^m_{2,b} \right) + J^c_\times \left(\mathbf{S}^m_{1,a} \cdot \mathbf{S}^m_{1,b} + \mathbf{S}^m_{2,a} \cdot \mathbf{S}^m_{2,b} \right) \Big], \end{aligned} \tag{B.2}$$

where m is the cell index, a and b denote the two legs of the ladder, the number 1 or 2 distinguishes the upper and the lower spin-site of a dimer and $\mathbf{S}^m_{i,\alpha}$ with $\alpha = \{a, b\}$ and $i = \{1, 2\}$, are the spin 1/2 operators. In our calculations, we will impose periodic boundary conditions, such that $\mathbf{S}^{m+N} = \mathbf{S}^m$, where $2N$ is the number of the dimers in the chain.

Perturbation theory is implemented up to the fifth-order. When looking at the complexity of the formula, we decided to report directly the Mathematica code in the Annex C. Here, we verify the validity of the calculations by comparing the results with results taken from the literature on simpler limit cases.

B.1 Limit case 1: The simple spin-1/2 two-leg ladder

The first system is the simple spin-1/2 two leg ladder represented in Figure B.2 (a) with an intrachain coupling J and a dominant interchain coupling $J_\perp$ (dimerization). The Hamiltonian of the system has the form

$$\mathbf{H} = \mathbf{H}_0 + \mathbf{H}_1 \tag{B.3}$$

where

$$\mathbf{H}_0 = \sum_n J_\perp \left(\mathbf{S}^n_a \mathbf{S}^n_b \right) \tag{B.4}$$

$$\mathbf{H}_1 = \sum_n J \left(\mathbf{S}^n_a \mathbf{S}^{n+1}_a + \mathbf{S}^n_b \mathbf{S}^{n+1}_b \right). \tag{B.5}$$

Reigrotzki, Tsunetsugu and Rice [48] studied the excitation energy $\omega(k)$ for magnon excitation up to the third order $J/J_\perp$ in the strong-coupling limit ($J_\perp \gg J$) and they found

$$\begin{aligned} \frac{\omega(k)}{J_\perp} = & 1 + \frac{J}{J_\perp} \cos k + \frac{1}{4} \left(\frac{J}{J_\perp} \right)^2 (3 - \cos(2k)) \\ & - \frac{1}{8} \left(\frac{J}{J_\perp} \right)^3 (2 \cos k + 2 \cos(2k) - \cos(3k) - 3). \end{aligned} \tag{B.6}$$

Starting from the triclinc structure shown in Figure B.1, we reconstruct the simple spin-1/2 two-leg ladder taking $J^a \equiv J_\perp \equiv J_2 = 0$ and $J^b_\times \equiv J^c_\times = J_\times$. In our case the dimerized coupling is J^d and the intrachain coupling is $J_\times$. Our system is represented in Figure B.2 (b) that is formally equivalent to the system in Figure B.2 (c).

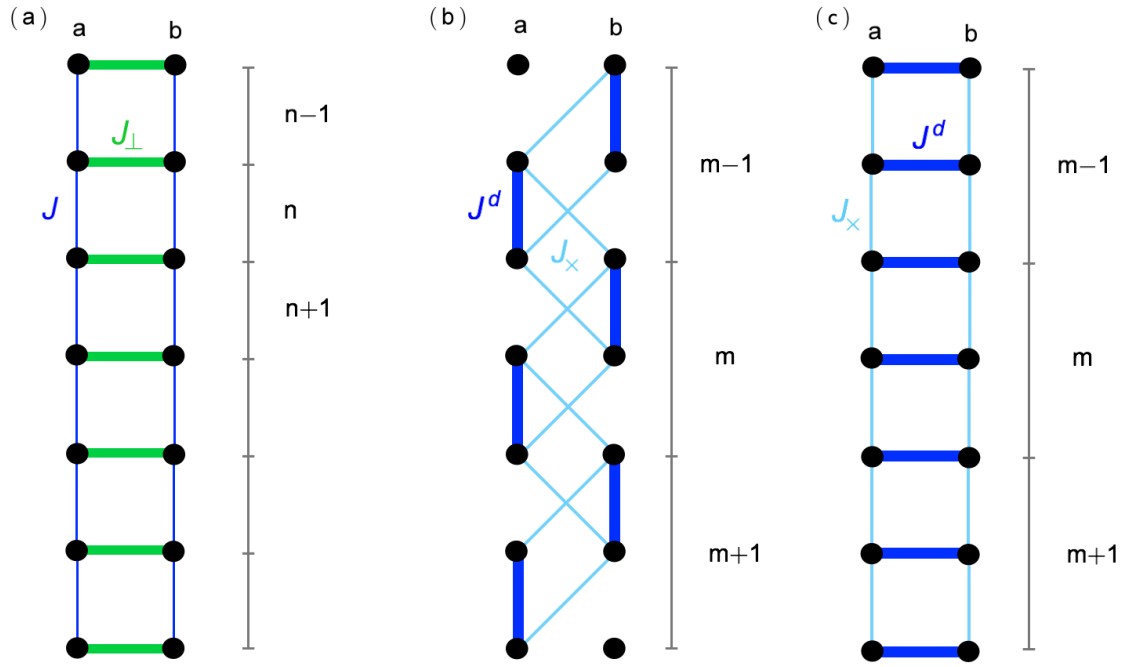

FIGURE B.2

The elements of the perturbation matrix (B.2), up to the third order, become

$$\mathbf{W}(1,1) \equiv \mathbf{W}(2,2) = 1 + \frac{1}{8}\Big(3J_\times^2(2+J_\times) - 2J_\times^2(1+J_\times)\cos(k)\Big) \tag{B.7}$$

$$\mathbf{W}(1,2) = \mathbf{W}^*(2,1) = \frac{e^{-\frac{ik}{2}}}{8} J_\times \cos\frac{k}{2}\Big(8 - 3J_\times^2 + 2J_\times^2\cos k\Big) \tag{B.8}$$

and the dispersion relation

$$\begin{aligned}\omega_\pm(k) &= 1 + \frac{1}{8}\Big(3J_\times^2(2+J_\times) - 2J_\times^2(1+J_\times)\cos(k) \pm \\ &\qquad \sqrt{J_\times^2\cos^2\frac{k}{2}\Big(8 - 3J_\times^2 + 2J_\times^2\cos k\Big)^2}\Big) \\ &= 1 + \frac{1}{8}\Big(3J_\times^2(2+J_\times) - 2J_\times^2(1+J_\times)\cos(k) \pm \\ &\qquad \left|J_\times\cos\frac{k}{2}\Big(8 - 3J_\times^2 + 2J_\times^2\cos k\Big)\right|\Big)\end{aligned} \tag{B.9}$$

The unit cell is twice the unit cell of the simple spin ladder, as we can see when comparing figures B.2 (a) and (c), so that the Brillouin Zone (BZ) is half that of the ladder model. Therefore the band structure calculated for the supercell can be unfolded into the BZ of the unit cell two times smaller and we should have only one

band. We obtain

$$\omega(k) = 1 + J_\times \cos(k) + \frac{1}{4}J_\times^2\big(3 - \cos(2k)\big) - \frac{1}{8}J_\times^3\big(2\cos(k) + 2\cos(2k) - \cos(3k) - 3\big) \tag{B.10}$$

i.e. the result up to the third order of Reigrotzki, Tsunetsugu and Rice in eq. (B.6) substituting $J_\times$ with J and remembering that our results are expressed in unit of J^d (where J^d correspond to J fo the ladder model in Figure B.2 (a)).

B.2 Limit case 2: the frustrated chain

Knetter and Uhrig [174] studied the frustrated and dimerized $S = 1/2$ chain described by the Hamiltonian

$$\mathbf{H} = \mathbf{H}_0 + \lambda \mathbf{H}_1 \tag{B.11}$$

with

$$\mathbf{H}_0 = \sum_i J\left[\mathbf{S}_{2i}\mathbf{S}_{2i+1} + 3/4\right] \tag{B.12}$$

$$\mathbf{H}_1 = \sum_i J\left[\mathbf{S}_{2i}\mathbf{S}_{2i-1} + \alpha\left(\mathbf{S}_{2i}\mathbf{S}_{2i-2} + \mathbf{S}_{2i-1}\mathbf{S}_{2i+1}\right)\right]. \tag{B.13}$$

where the subscript i counts the dimers and λ is the perturbation parameter supposed to be small $\lambda < 1$. The ground-state is a product of singlets on the dimers and the perturbative calculation is obtained as polynomials in λ and α.

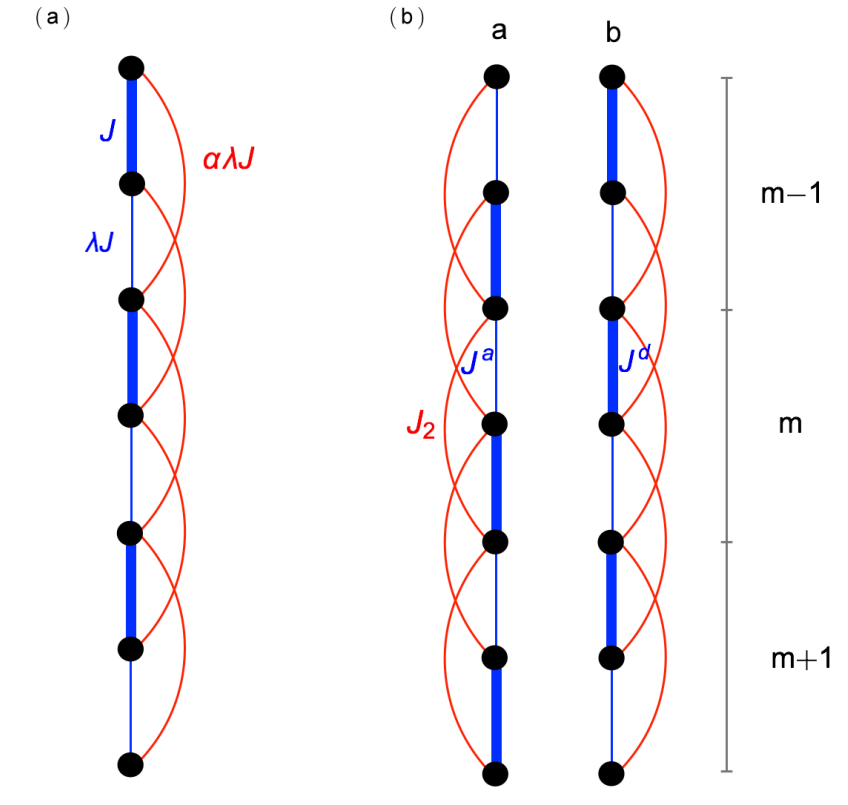

FIGURE B.3

The resulting one magnon dispersion is given by[1]

$$\frac{\omega(k)}{J} = \sum_j a_j \cos(jk) \tag{B.14}$$

where the effective hopping elements are given up to order 6 (with $\bar{\alpha} = 1 - 2\alpha$ and $\bar{\lambda} = \frac{1}{4}\lambda$).

$$\begin{aligned}
a_0 =& 1 - \left(4 - 3\bar{\alpha}^2\right)\bar{\lambda}^2 - \left(8 - 8\bar{\alpha} - 6\bar{\alpha}^2 + 3\bar{\alpha}^3\right)\bar{\lambda}^3 \\
&- \left(2 - 24\bar{\alpha} + 5\bar{\alpha}^2 + 8\bar{\alpha}^3 + \frac{13}{4}\bar{\alpha}^4\right)\bar{\lambda}^4 \\
&+ \left(56 - 82\bar{\alpha} - 22\bar{\alpha}^2 + 55\bar{\alpha}^3 - 39\bar{\alpha}^4 + 20\bar{\alpha}^5\right)\bar{\lambda}^5 \\
&+ \left(\frac{367}{3} - \frac{7328}{9}\bar{\alpha} + \frac{22976}{27}\bar{\alpha}^2 + \frac{6442}{27}\bar{\alpha}^3 - \frac{28895}{54}\bar{\alpha}^4 + 193\bar{\alpha}^5 - 32\bar{\alpha}^6\right)\bar{\lambda}^6 \\
a_1 =& -2\bar{\alpha}\bar{\lambda} - 4\bar{\lambda}^2 - \left(8 - 8\bar{\alpha} - 2\bar{\alpha}^3\right)\lambda^3 + \left(4 + 20\bar{\alpha} - 24\bar{\alpha}^2 + 10\bar{\alpha}^3 - 5\bar{\alpha}^4\right)\bar{\lambda}^4 \\
&\left(92 - \frac{499}{3}\bar{\alpha} - \frac{164}{3}\bar{\alpha}^2 + 152\bar{\alpha}^3 - 47\bar{\alpha}^4 + \frac{13}{2}\bar{\alpha}^5\right)\bar{\lambda}^5 \\
&+ \left(\frac{532}{3} - \frac{11906}{9}\bar{\alpha} + \frac{11960}{9}\bar{\alpha}^2 + \frac{1648}{3}\bar{\alpha}^3 - \frac{41357}{54}\bar{\alpha}^4 + 85\bar{\alpha}^5 + 6\bar{\alpha}^6\right)\bar{\lambda}^6 \\
a_2 =& -\bar{\alpha}^2\bar{\lambda}^2 - \left(4\bar{\alpha}^2 - 2\bar{\alpha}^3\right)\bar{\lambda}^3 + \left(6 - 4\bar{\alpha} - 23\bar{\alpha}^2 + 14\bar{\alpha}^3 - \frac{1}{2}\bar{\alpha}^4\right)\bar{\lambda}^4 \\
&+ \left(36 - \frac{272}{3}\bar{\alpha} - \frac{220}{3}\bar{\alpha}^2 + \frac{1150}{9}\bar{\alpha}^3 - 9\bar{\alpha}^4 - \frac{13}{2}\bar{\alpha}^5\right)\bar{\lambda}^5 \\
&+ \left(\frac{107}{3} - \frac{1630}{3}\bar{\alpha} + \frac{1126}{3}\bar{\alpha}^2 + \frac{5102}{9}\bar{\alpha}^3 - \frac{13205}{36}\bar{\alpha}^4 - 59\bar{\alpha}^5 + 11\bar{\alpha}^6\right)\bar{\lambda}^6 \\
a_3 =& -\bar{\alpha}^3\bar{\lambda}^3 - \left(\frac{10}{3}\bar{\alpha}^2 + 4\bar{\alpha}^3 - 2\bar{\alpha}^4\right)\bar{\lambda}^4 \\
&- \left(\frac{19}{3}\bar{\alpha} + 20\bar{\alpha}^2 - \frac{10}{3}\bar{\alpha}^3 - 11\bar{\alpha}^4 - 3\bar{\alpha}^5\right)\bar{\lambda}^5 \\
&- \frac{58}{3} + \frac{104}{3}\bar{\alpha} - \frac{224}{9}\bar{\alpha}^2 - 63\bar{\alpha}^3 + \frac{103}{2}\bar{\alpha}^4 - \frac{57}{2}\bar{\alpha}^5 + \frac{81}{4}\bar{\alpha}^6\Big)\bar{\lambda}^6 \\
a_4 =& -\frac{5}{4}\bar{\alpha}^4\bar{\lambda}^4 - \left(\frac{40}{9}\bar{\alpha}^3 + 6\bar{\alpha}^4 - 3\bar{\alpha}^5\right)\bar{\lambda}^5 \\
&+ \left(\frac{11}{3}\bar{\alpha}^2 - \frac{827}{27}\bar{\alpha}^3 - \frac{1127}{36}\bar{\alpha}^4 + \frac{91}{4}\bar{\alpha}^5 + \frac{73}{16}\bar{\alpha}^6\right)\bar{\lambda}^6 \\
a_5 =& -\frac{7}{4}\bar{\alpha}^5\bar{\lambda}^5 - \left(\frac{497}{54}\bar{\alpha}^4 + 10\bar{\alpha}^5 - 5\bar{\alpha}^6\right)\bar{\lambda}^6 \\
a_6 =& -\frac{21}{8}\bar{\alpha}^6\bar{\lambda}^6
\end{aligned} \tag{B.15}$$

In our case we should obtain the same result taking $J^b_\times \equiv J^b_\times \equiv J_\perp = 0$ and substituting

$$\begin{cases} J = J^d \\ \lambda J = J^a \\ \lambda\alpha J = J_2 \end{cases} \tag{B.16}$$

[1]The formula (39b) in [174] has probably a typo error. The relation (B.14) is also consistent with the studies of Barnes, Riera and Tennant [175] (equation (31)) that we analyze in the next section.

The diagonal term of the perturbation matrix (B.2) are

$$\begin{aligned}\mathbf{W}(1,1) \equiv \mathbf{W}(2,2) = \frac{1}{36864}\Big(&36(1024 - 640J_2^5 + 16J_2^4(-13 + 61J^a) + 24J_2^3(16 + (28 - 33J^a)J^a) \\ &+ 2J_2J^a(24 + 17J^a)(-16 + J^a(4 + J^a)) - (J^a)^2(-8 + 3J^a)(-8 + J^a(3 + 4J^a)) \\ &+ 4J_2^2(192 + (-2 + J^a)J^a(24 + 109J^a))) - 6(96J_2(-64 + J_2^2(16 + J_2(20 + 13J_2))) \\ &+ 48(64 + J_2^2(-48 + J_2(-40 + 29J_2)))J^a + 48(32 + J_2(56 + J_2(48 + 29J_2)))(J^a)^2 \\ &- 8(24 + J_2(108 + 553J_2))(J^a)^3 + 2(-60 + 149J_2)(J^a)^4 + 105(J^a)^5)\cos(k) \\ &+ 2(288J_2^2(-16 + J_2(-16 + J_2(-2 + 13J_2))) - 144J_2(-32 + J_2(-16 + J_2(48 + 83J_2)))J^a \\ &- 16(72 + J_2(-72 + J_2(-288 + 241J_2)))(J^a)^2 + 72(-8 + J_2(20 + 191J_2))(J^a)^3 \\ &- 90(6 + 31J_2)(J^a)^4 - 283(J^a)^5)\cos(2k) - 12(2J_2 - J^a)(48(-2 + J_2)J_2^2(2 + 3J_2) \\ &+ 24J_2(8 + (4 - 23J_2)J_2)J^a + 4(-12 + J_2(32 + 163J_2))(J^a)^2 - 2(32 + 95J_2)(J^a)^3 \\ &- 27(J^a)^4)\cos(3k) - 4(2J_2 - J^a)^3(18J_2(5 + 6J_2) - J^a(45 + 67J^a))\cos(4k) \\ &+ 63(2J_2 - J^a)^5\cos(5k)\Big)\end{aligned} \tag{B.17}$$

and indeed the off diagonal terms are equal to zero $\mathbf{W}(1,2) \equiv \mathbf{W}(2,1) = 0$. Consequently the two dispersion bands are equivalent and exactly equal to the diagonal terms. We can easily demonstrate, doing the appropriate substitutions, that this result is strictly identical to the result of Knetter and Uhrig expressed in eq. (B.14).

B.3 Limit case 3: The alternating chain

The alternating Heisenberg chain, representing in Figure B.4 (a), is described by the Hamiltonian

$$\mathbf{H} = \sum_i J\mathbf{S}_{2i}\mathbf{S}_{2i+1} + \lambda J\mathbf{S}_{2i}\mathbf{S}_{2i-1}. \tag{B.18}$$

The system is studied by Barnes, Riera and Tennant[2] [175] and it could also be represented by the Knetter and Uhrig chain with $\alpha = 0$.

The dispersion relation is expressed by the equation (B.14) with the coefficients a_j up to the $O(\alpha^5)$

$$\begin{aligned}a_0 =& 1 - \frac{1}{16}\lambda^2 + \frac{3}{64}\lambda^3 + \frac{23}{1024}\lambda^4 - \frac{3}{256}\lambda^5 \\ a_1 =& -\frac{1}{2}\lambda - \frac{1}{4}\lambda^2 + \frac{1}{32}\lambda^3 + \frac{5}{256}\lambda^4 - \frac{35}{2048}\lambda^5 \\ a_2 =& -\frac{1}{16}\lambda^2 - \frac{1}{32}\lambda^3 - \frac{15}{512}\lambda^4 - \frac{283}{18432}\lambda^5 \\ a_3 =& -\frac{1}{64}\lambda^3 - \frac{1}{48}\lambda^4 - \frac{9}{1024}\lambda^5 \\ a_4 =& -\frac{5}{1024}\lambda^4 - \frac{67}{9216}\lambda^5 \\ a_5 =& -\frac{7}{4096}\lambda^5.\end{aligned} \tag{B.19}$$

that can be also easily derived from (B.15) taking $\alpha = 0$.

[2] In [175] λ is replaced by α

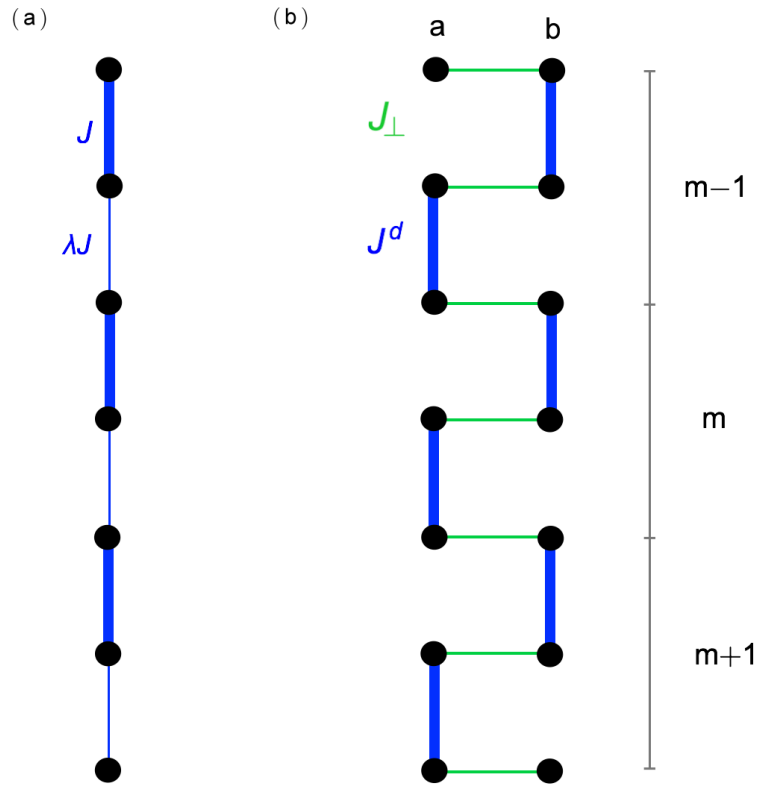

FIGURE B.4

The system could be reproduced by the triclinic Hamiltonian with $J^a \equiv J^b_\times \equiv J^b_\times = 0$ and doing the substitution

$$\begin{cases} J = J^d \\ \lambda J = J_\perp \end{cases} \tag{B.20}$$

We obtain the chain in Figure B.4 (b) that is equivalent to the chain in Figure B.4 (a), but with a double unit cell.

The diagonal elements of perturbation matrix are

$$\begin{aligned} \mathbf{W}(1,1) \equiv \mathbf{W}(2,2) = 1 &+ \frac{1}{64} J_\perp^3 (3 - 2\cos(k)) - \frac{1}{16} J_\perp^2 (1 + \cos(k)) \\ &- \frac{1}{1024} \Big(J_\perp^4 (-23 + 30\cos(k) + 5\cos(2k)) \Big) \\ &- \frac{1}{18432} \Big(J_\perp^5 (216 + 283\cos(k) + 134\cos(2k)) \Big) \end{aligned} \tag{B.21}$$

and the off-diagonal terms $\mathbf{W}(1,2)$ and $\mathbf{W}(2,1) = \mathbf{W}^*(1,2)$

$$\begin{aligned} \mathbf{W}(1,2) \equiv \mathbf{W}(2,2) = \frac{1}{12288} e^{\frac{ik}{2}} J_\perp \cos\left(\frac{k}{2}\right) \Big(&6144 + J_\perp (3072 + J_\perp (-576 \\ &+ J_\perp (-496 + 123 J_\perp))) + 2 J_\perp^2 (192 + J_\perp (256 + 87 J_\perp)) \cos(k) \\ &+ 42 J_\perp^4 \cos(2k) \Big) \end{aligned} \tag{B.22}$$

Solving the eigenvalues equation we obtain the bands

$$\begin{aligned}\omega_{\pm}(k) =&\frac{1}{36864}\Big(- 2J_{\perp}^{2}(1152 + J_{\perp}(576 + J_{\perp}(540 + 283J_{\perp}))) \cos(k) - 4J_{\perp}^{4}(45 \\ &+ 67J_{\perp}) \cos(2k) - 3\Big(- 12288 + 12J_{\perp}^{2}(-8 + 3J_{\perp})(-8 + J_{\perp}(3 + 4J_{\perp})) \\ &\pm \Big|6J_{\perp}(1024 + J_{\perp}(512 + J_{\perp}(-64 + 5J_{\perp}(-8 + 7J_{\perp})))) \cos\left(\frac{k}{2}\right) \\ &+ 4J_{\perp}^{3}(48 + J_{\perp}(64 + 27J_{\perp})) \cos\left(\frac{3k}{2}\right) + 21J_{\perp}^{5} \cos\left(\frac{5k}{2}\right)\Big|\Big)\Big).\end{aligned} \tag{B.23}$$

As in section B.1, we have a unit cell two times larger so that the BZ is half of the system in Figure B.4 (a). Unfolding the bands gives

$$\begin{aligned}\omega(k) =&1 - J_{\perp}\frac{\cos(k)}{2} + J_{\perp}^{2}\left(-\frac{1}{16} - \frac{\cos(k)}{4} - \frac{\cos(2k)}{16}\right) \\ &+ J_{\perp}^{3}\left(\frac{3}{64} + \frac{\cos(k)}{32} - \frac{\cos(2k)}{32} - \frac{\cos(3k)}{64}\right) \\ &+ J_{\perp}^{4}\left(\frac{23}{1024} + \frac{5\cos(k)}{256} - \frac{15\cos(2k)}{512} - \frac{\cos(3k)}{48} - \frac{5\cos(4k)}{1024}\right) \\ &+ J_{\perp}^{5}\left(-\frac{3}{256} - \frac{35\cos(k)}{2048} - \frac{283\cos(2k)}{18432} - \frac{9\cos(3k)}{1024} - \frac{67\cos(4k)}{9216} - \frac{7\cos(5k)}{4096}\right)\end{aligned} \tag{B.24}$$

which is equivalent to the dispersion relation found by Barnes, Riera and Tennant.

Appendix C

Mathematica expression: Perturbation Theory

We report the perturbed matrix $\mathbf{W}$, written in Mathematica, reads in the $|T\rangle_\alpha$ basis computed up to the fifth-order. In our Mathematica code, we have: `JpA` $\equiv J^a_\perp \equiv$ `JpB` $\equiv J^b_\perp = -0.33$, `Ja` $\equiv J^a = 0.06$, `JdB` $\equiv J^b_\times = 0.24$, `JdC` $\equiv J^c_\times = 0.40$, `J2` $\equiv J_2 = 0.34$.

C.1 First-order

As discussed in B, the first-order expression can be found analytically. For sake of completion, we rewrite the resulting first-order perturbed expression. The diagonal elements `W11o1` and `W22o1`≡`W11o1`, and the out-of-diagonal `W12o1` and `W21o1`≡`Conjugate[W12o1]` are, respectively:

```
W11o1[k_, Ja_, J2_, JdB_, JpA_, JpB_, JdC_] := (J2 - Ja/2) Cos[k]

W12o1[k_, Ja_, J2_, JdB_, JpA_, JpB_,  JdC_] := ((Cos[k] - I Sin[k])(2JdB - JpA) + 2JdC - JpB)/4
```

We report the resulting numerical dispersion relation, obtained substituting the DFT values of the coupling:

$$\omega_\pm(k) = 1 + 0.31\cos k \pm \sqrt{0.12 + 0.11\cos k}. \tag{C.1}$$

C.2 Second-order

The second-order expressions of the $\mathbf{W}$'s elements `W11o2`, `W22o2`≡`W11o2`, `W12o2` and `W21o2`≡`Conjugate[W12o2]`

```
W11o2[k_, Ja_, J2_, JdB_, JpA_, JpB_, JdC_] := 1/32 (24 J2^2 - 24 J2 Ja - 2 Ja^2 + 12 JdB^2 + 12 JdC^2
   - 12 JdB JpA - JpA^2 - 12 JdC JpB - JpB^2 - 2 (4 Ja^2 + (2 JdB - JpA) (2 JdC - JpB)) Cos[k]
   - 2 (-2 J2 + Ja)^2 Cos[2 k]) 1/16 (-2 JpB^2 - 2 E^(-I k) (2 J2 - Ja) (2 JdB - JpA) Cos[k]
   - 2 (4 J2 JdC - 2 Ja JdC + JpA^2 - 2 J2 JpB + Ja JpB) Cos[k] + 2 I JpA^2 Sin[k])

W12o2[k_, Ja_, J2_, JdB_, JpA_, JpB_, JdC_] := 1/16 (-2 JpB^2 - 2 E^(-I k) (2 J2 - Ja) (2 JdB - JpA) Cos[k]
   - 2 (4 J2 JdC - 2 Ja JdC + JpA^2 - 2 J2 JpB + Ja JpB) Cos[k] + 2 I JpA^2 Sin[k])
```

We solve the eigenvalue equation adding the 2-order expression for the perturbed matrix. We obtain:

$$\omega_\pm(k) = 1.25 + (0.25 - 0.048\cos(k))\cos(k) \pm \sqrt{0.11 + (0.031 + (-0.055 + 0.011\cos(k))\cos(k))\cos(k)} \tag{C.2}$$

C.3 Third-order

For the third-order expressions of the perturbed Hamiltonian, it turns out that even the diagonal elements are complex and one is the complex conjugate of the other, we thus have`W11o3`, `W22o3`≡`Conjugate[W11o3]`, `W12o3` and `W21o3`≡`Conjugate[W12o3]`,

```
W11o3[k_, Ja_, J2_, JdB_, JpA_, JpB_, JdC_] := 1/128 (48 J2^3 - 24 J2^2 Ja + 6 Ja^3 + 24 JdB^3 + 24 JdC^3
   - 12 JdB^2 JpA - 22 JdB JpA^2 + 3 JpA^3 - 12 JdC^2 JpB - 22 JdC JpB^2 + 3 JpB^3 - 4 J2 (11 Ja^2 + 60 JdB JdC
   - 30 JdC JpA - 30 JdB JpB + 23 JpA JpB) + 2 Ja (2 JdB (30 JdC - 7 JpB) + 7 JpA (-2 JdC + JpB)) - 2 (16 J2^3
   - 24 J2^2 Ja - 2 Ja^3 + 2 JdC (4 JdB (JdB + JdC) - 2 JdC JpA + JpA^2) + (-4 JdB^2 - 4 (JdB + JdC) JpA
   + JpA^2) JpB + (2 JdB + JpA) JpB^2 - Ja (4 JdB^2 + 4 JdB JdC + 4 JdC^2 - 4 JdB JpA + 10 JdC JpA + 5 JpA^2
   + 10 JdB JpB - 4 JdC JpB - 7 JpA JpB + 5 JpB^2) + 2 J2 (14 Ja^2 + 4 JdB^2 + 4 JdC^2 + 2 JdC JpA + 5 JpA^2
   - 4 JdC JpB + 3 JpA JpB + 5 JpB^2 + 2 JdB (-2 (JdC + JpA) + JpB))) Cos[k] - 2 (2 J2 - Ja) (8 J2^2 - 2 Ja^2
   - 3 (2 JdB - JpA) (2 JdC - JpB)) Cos[2 k] + 2 (2 J2 - Ja)^3 Cos[3 k] + 4 I (2 JdC JpA^2 + JpB (-2 JdB JpB
   + JpA (-JpA + JpB))) Sin[k])

W12o3[k_, Ja_, J2_, JdB_, JpA_, JpB_, JdC_] := 1/128 (3 E^(-3 I k) (-2 J2 + Ja)^2 (2 JdB - JpA) + 8 J2^2 (-2 JdB
   - 2 JdC + JpA + JpB) + 2 Ja^2 (-2 JdB - 10 JdC + 3 JpA + 5 JpB) + 2 Ja (4 JdB^2 - 4 JdB (JdC + JpA)
   + JpA (10 JdC + 3 JpA - 3 JpB) + 10 JdB JpB) - 2 (-8 JdB JdC JpA + 6 JdC JpA^2 + JdB^2 (8 JdC - 4 JpB)
   - JpA^2 JpB + 8 JdC JpB^2) - 4 J2 (4 JdB^2 - 2 JdB (2 JdC + JpB) + 2 Ja (-2 JdC + JpA + JpB) + JpA (2 JdC
   + JpA + 7 JpB)) - (Ja^2 (14 JdB + 8 JdC - 7 JpA - 4 JpB) + 4 J2^2 (-2 JdB + 8 JdC + JpA - 4 JpB) - JpA (2 JdC
   + JpB)^2 - 2 Ja (-4 JdB JdC + 8 JdC^2 + 10 JdC JpA + 10 JdB JpB - 3 JpA JpB + 2 JpB^2) + 4 J2 (Ja (2 JdB - JpA)
   - 2 JdC (2 JdB - 4 JdC + JpA) + (2 JdB + 7 JpA) JpB + 2 JpB^2) + 2 JdB (8 JpA^2 + 4 JdC (JdC - JpB)
   + 5 JpB^2)) Cos[k] + (Ja (8 JdB^2 + 8 JdB JpA - 2 JpA^2) + 8 J2^2 (-2 JdB + 6 JdC + JpA - 3 JpB) + (-2 JdB
   + JpA)^2 (2 JdC - JpB) - 2 Ja^2 (2 JdB - 6 JdC + JpA + 3 JpB) - 4 J2 (4 JdB^2 + 12 Ja JdC - 2 Ja JpA + JpA^2
   - 6 Ja JpB)) Cos[2 k] + I (20 J2^2 (2 JdB - JpA) + Ja^2 (26 JdB - 13 JpA - 8 JpB) + 2 Ja (4 JdB JdC - 10 JdC JpA
   - 10 JdB JpB + 8 JdC JpB + 3 JpA JpB - 4 JpB^2) + JpA (-12 JdC^2 + 4 JdC JpB - 3 JpB^2) + 2 JdB (8 JpA^2
   + 12 JdC (JdC - JpB) + 7 JpB^2) + 4 J2 (-2 JdC JpA + 7 JpA JpB + 2 JdB (-2 JdC + JpB) + Ja (-10 JdB + 5 JpA
   + 4 JpB))) Sin[k] - I (8 J2^2 (-2 JdB + JpA) - 2 Ja^2 (2 JdB + JpA) + Ja (8 JdB^2 + 8 JdB JpA - 2 JpA^2)
   - 4 J2 (4 JdB^2 + JpA (-2 Ja + JpA)) + (-2 JdB + JpA)^2 (2 JdC - JpB)) Sin[2 k])
```

The dispersion relation becomes:

$$\begin{aligned}\omega_{\pm}(k) =& 1.01 + 0.21\cos(k) - 0.0061\cos(2k) + 0.0037\cos(3k) \\ &+ \Big(0.052 + 0.015\cos(k) - 0.013\cos(2k) + 0.0072\cos(3k) - 0.0012\cos(4k) + 0.00015\cos(5k)\Big)^{1/2}\end{aligned} \tag{C.3}$$

C.4 Forth-order

The results of the forth-order expressions `W11o4`, `W22o4`≡`Conjugate[W11o4]`, `W12o4` and `W21o4`≡`Conjugate[W12o4]` are

```
W11o4[k_, Ja_, J2_, JdB_, JpA_, JpB_, JdC_] := (1/6144)(3 (-416 J2^4 + 1344 J2^3 Ja + 46 Ja^4 + 48 JdB^4
   - 512 JdB^2 JdC^2 + 48 JdC^4 + 288 JdB^3 JpA + 384 JdB JdC^2 JpA - 568 JdB^2 JpA^2 - 224 JdC^2 JpA^2
   + 72 JdB JpA^3 + 67 JpA^4 + 16 JdC (24 JdB^2 + 18 JdC^2 + 2 JdB JpA + 7 JpA^2) JpB -  8 (28 JdB^2 + 71 JdC^2
   - 14 JdB JpA + 11 JpA^2) JpB^2 + 72 JdC JpB^3 + 67 JpB^4 + 4 Ja^2 (28 JdB^2 + 28 JdC^2 - 56 JdC JpA
   - 13 JpA^2 + 4 JdB (34 JdC - 11 JpA - 14 JpB) - 44 JdC JpB + 18 JpA JpB - 13 JpB^2) - 16 J2^2 (97 Ja^2
   - 76 JdB^2 - 76 JdC^2 - 44 JdC JpA - 7 JpA^2 + JdB (72 JdC + 92 JpA - 44 JpB) + 92 JdC JpB + 38 JpA JpB
   - 7 JpB^2) + 8 Ja (4 JdB^2 (22 JdC + JpB) + 4 JdB (22 JdC^2 + 9 JdC (JpA + JpB) - 7 JpB (JpA + JpB))
   + JpA (4 JdC^2 - 28 JdC (JpA + JpB) + 15 JpB (JpA + JpB))) + 16 J2 (23 Ja^3 - 72 JdB JdC (JdB + JdC)
   + 4 JdC (-2 JdB + 11 JdC) JpA + 34 JdC JpA^2 - 2 (-22 JdB^2 + 4 JdB JdC + 13 (JdB + JdC) JpA + 8 JpA^2) JpB
   + 2 (17 JdB - 8 JpA) JpB^2 - Ja (92 JdB^2 + 92 JdC^2 + 11 JpA^2 + 4 JpA JpB + 11 JpB^2 - 18 JdC (JpA + 6 JpB)
   + 2 JdB (4 JdC - 9 (6 JpA + JpB))))) - 4 (480 J2^4 - 480 J2^3 Ja - 30 Ja^4 + 2 Ja^2 (52 JdB^2 - 82 JdB JdC
   + 52 JdC^2 - 52 JdB JpA + 125 JdC JpA + 33 JpA^2) + 6 JdC (-8 JdB (JdB^2 - 3 JdB JdC + JdC^2) + 4 (11 JdB^2
   + JdC^2) JpA + 2 (JdB - 3 JdC) JpA^2 + 5 JpA^3) - 4 Ja (24 (JdB^3 + JdC^3) + 4 (-3 JdB^2 + 26 JdB JdC
   + 14 JdC^2) JpA + 2 (15 JdB - 13 JdC) JpA^2 + 9 JpA^3) + (Ja^2 (250 JdB - 104 JdC - 105 JpA) + 8 Ja (-28 JdB^2
   - 52 JdB JdC + 6 JdC^2 + 11 JdB JpA + 11 JdC JpA + 8 JpA^2) + 3 (8 JdB (JdB^2 + 11 JdC^2) - 28 (3 JdB^2
```

```
   - 2 JdB JdC + 3 JdC^2) JpA + 6 (JdB - 6 JdC) JpA^2 + JpA^3)) JpB + (66 Ja^2 + 8 Ja (13 JdB - 15 JdC + 8 JpA)
   + 3 (-12 JdB^2 + 4 JdB (JdC - 9 JpA) + JpA (6 JdC + 13 JpA))) JpB^2 + 3 (-12 Ja + 10 JdB + JpA) JpB^3
   + 4 J2^2 (144 Ja^2 + 72 JdB^2 + 72 JdC^2 + 186 JdC JpA + 82 JpA^2 - 6 JdB (62 JdC + 12 JpA - 31 JpB)
   - 72 JdC JpB + 35 JpA JpB + 82 JpB^2) + 4 J2(-6 (9 Ja^3 - 66 Ja JdB JdC - 4(JdB - 2 JdC)(2 JdB - JdC)(JdB + JdC))
   - 6 (4 JdB^2 + 57 Ja JdC - 6 JdB JdC) JpA - 4 (16 Ja - 15 JdB + 2 JdC) JpA^2 + 18 JpA^3 + (12 (3 JdB - 2 JdC) JdC
   + 142 (JdB + JdC) JpA - 43 JpA^2 + Ja (-342 JdB + 115 JpA)) JpB - (64 Ja + 8 JdB - 60 JdC + 43 JpA) JpB^2
   + 18 JpB^3)) Cos[k] - 2 (96 J2^4 + 1152 J2^3 Ja + 90 Ja^4 + 15 (-2 JdB + JpA)^2 (-2 JdC + JpB)^2
   - 8 J2^2 (96 Ja^2 - 36 JdB^2 - 36 JdC^2 - 48 JdC JpA - 29 JpA^2 + 12 JdB (8 JdC + 3 JpA - 4 JpB) + 36 JdC JpB
   - 48 JpA JpB - 29 JpB^2) + 16 Ja (JdC (12 JdB (JdB + JdC) - 2 (JdB + JdC) JpA - 7 JpA^2) - 2 (JdB^2 + (JdC
   - 2 JpA) JpA + JdB (JdC + JpA)) JpB + (-7 JdB + 4 JpA) JpB^2) + Ja^2 (8 JdB^2 + 8 JdC^2 + 42 JpA^2
   + 8 JdB (88 JdC - JpA - 12 JpB) + 64 JpA JpB + 42 JpB^2 - 8 JdC (12 JpA + JpB)) + 8 J2 (-30 Ja^3
   + 8 JdC (-6 JdB (JdB + JdC) + 3 JdC JpA + 4 JpA^2) + 2 (12 JdB^2 - 2 (JdB + JdC) JpA - 7 JpA^2) JpB + 2 (16 JdB
   - 7 JpA) JpB^2 - Ja (36 JdB^2 + 36 JdC^2 - 36 JdB JpA + 64 JdC JpA + 29 JpA^2 + 64 JdB JpB - 36 JdC JpB
   + 8 JpA JpB + 29 JpB^2))) Cos[2 k] + 4 (-2 J2 + Ja)^2 (48 J2^2 - 32 Ja^2 - 45 (2 JdB - JpA) (2 JdC
   - JpB)) Cos[3 k] - 30 (-2 J2 + Ja)^4 Cos[4 k] + 12 I (-16 JdB (JdB - JdC) JdC (-2 J2 + Ja + 3 (JdB + JdC))
   - 8 (-3 Ja (-2 J2 + Ja - 2 JdB) JdB + (4 J2 - 10 Ja - 9 JdB) JdB JdC + 2 (J2 + 5 Ja) JdC^2 + 3 JdC^3) JpA
   + 4 (-3 Ja (Ja - 4 JdB) - (9 Ja + JdB) JdC + 2 J2 (3 Ja + JdC)) JpA^2 + 2 (-6 Ja + 11 JdC) JpA^3
   + (8 (JdB^2 (2 J2 + 10 Ja + 3 JdB) + (6 J2 Ja - 3 Ja^2 + 4 J2 JdB - 10 Ja JdB) JdC + 3 (2 Ja - 3 JdB) JdC^2)
   - 4 (JdB - JdC) (26 J2 + 17 Ja + 3 (JdB + JdC)) JpA + 2 (24 J2 + 7 Ja - 11 JdB) JpA^2 - 5 JpA^3) JpB
   - 2 (-6 Ja^2 - 18 Ja JdB + 24 Ja JdC - 2 JdB JdC + 7 Ja JpA - 11 JdC JpA + 4 J2 (3 Ja + JdB + 6 JpA)) JpB^2
   + (12 Ja - 22 JdB + 5 JpA) JpB^3) Sin[k] + 24 I (2 JdC (4 (2 J2 - Ja) JdB (JdB - JdC) + (J2 (-6 Ja + 4 JdC)
   + Ja (3 Ja - 2 (3 JdB + JdC))) JpA + (4 J2 + Ja) JpA^2) + (2 JdB ((-2 J2 + Ja) (-3 Ja + 2 JdB) + 6 Ja JdC)
   + 6 Ja (JdB - JdC) JpA - (4 J2 + Ja) JpA^2) JpB - (4 J2 + Ja) (2 JdB - JpA) JpB^2) Sin[2 k])

W12o4[k_, Ja_, J2_, JdB_, JpA_, JpB_, JdC_] := (1/1536)(6 JdC (-8 JdB^2 (4 JdB + JdC) + 8 JdB (2 JdB + JdC) JpA
  - 2 (5 JdB + JdC) JpA^2 - 11 JpA^3) + 6 (16 JdB^3 + 14 JdB^2 JpA + 3 JpA^2 (JdC + JpA)
  - JdB JpA (6 JdC + JpA)) JpB - 3 (24 JdB^2 + 64 JdC^2 - 54 JdB JpA + 17 JpA^2) JpB^2 + 48 JpB^4
  + 24 J2^3 (6 JdB - 8 JdC - 3 JpA + 4 JpB) + Ja^3 (-10 JdB - 72 JdC + 19 JpA + 36 JpB) - Ja^2 (124 JdB^2
  + 328 JdC^2 + 31 JpA^2 + 4 JdC (33 JpA - 64 JpB) - 4 JdB (8 JdC + 35 JpA - 26 JpB) - 60 JpA JpB + 66 JpB^2)
  - 4 J2^2 (36 (JdB^2 - 2 JdB JdC + 2 JdC^2) + 31 JpA^2 + 92 JpA JpB + 26 JpB^2 + Ja (102 JdB - 24 JdC
  - 17 JpA + 12 JpB)) + Ja (-24 JdB^3 - 12 JdB^2 (4 JdC + JpA - 11 JpB) + 2 JdB (-84 JdC^2 + 114 JdC JpA
  + 27 JpA^2 + 272 JdC JpB - 93 JpA JpB - 71 JpB^2) + JpA (340 JdC^2 - 6 JdC JpA + 27 JpA^2 - 272 JdC JpB
  + 24 JpA JpB + 43 JpB^2)) + 2 J2 (3 (8 JdB (JdB^2 + 4 JdB JdC + 7 JdC^2) - 4 (11 JdB^2 + 2 JdB JdC
  + 7 JdC^2) JpA - 2 (JdB + 2 JdC) JpA^2 - 5 JpA^3) + 2 (12 JdB (JdB - 9 JdC) - 2 (24 JdB + 37 JdC) JpA
  - 9 JpA^2) JpB + (98 JdB + 19 JpA) JpB^2 + Ja^2 (-2 JdB - 120 JdC + 21 JpA + 60 JpB) + Ja (144 JdC^2
  + 212 JdC JpA + 70 JpA^2 - 4 JdB (18 JdC + JpA - 52 JpB) - 20 JpA JpB + 52 JpB^2)) + (-48 JdB JdC^2 (JdB
  + 2 JdC) + 48 JdC^3 JpA - 4 (48 JdB^2 + 19 JdC^2) JpA^2 + 48 JpA^4 + 144 J2^3 (2 JdC - JpB)
  + 8 JdC (6 JdB (JdB + JdC) - (JdB - 12 JdC) JpA + 19 JpA^2) JpB + (-28 JdB^2 + (36 JdC - 49 JpA) JpA
  + 20 JdB (-6 JdC + JpA)) JpB^2 - 36 JdB JpB^3 + 2 Ja^3 (-8 JdB - 10 JdC + 6 JpA + 5 JpB) - 2 Ja^2 (160 JdB^2
  + 124 JdC^2 + 45 JpA^2 - 2 JdB (12 JdC + 70 JpA - 35 JpB) + 32 JdC (4 JpA - 5 JpB) - 34 JpA JpB + 53 JpB^2)
  + 2 J2 (-4 Ja^2 (44 JdB + JdC - 20 JpA) + 2 JdC (108 JdB^2 + 72 JdB JdC + 24 JdC^2 - 132 JdB JpA + 35 JpA^2)
  + 8 Ja (12 JdB^2 - JdB (21 JdC + JpA) + JpA (50 JdC + 11 JpA)) + (2 (Ja^2 + 106 Ja JdB - 6 (9 JdB^2 + 6 JdB JdC
  + 22 JdC^2)) + 4 (11 Ja - 29 JdB - 34 JdC) JpA + 29 JpA^2) JpB + 4 (40 Ja - 4 JdB - 3 JdC + 4 JpA) JpB^2
  - 30 JpB^3) + Ja (-2 JdC (108 JdB^2 + 24 JdC^2 - 4 (69 JdB + 28 JdC) JpA + 47 JpA^2) + (4 (99 JdB^2
  + 62 JdB JdC + 66 JdC^2) - 4 (79 JdB + 62 JdC) JpA + 31 JpA^2) JpB + 12 (-JdB + JdC + 2 JpA) JpB^2
  + 30 JpB^3) - 8 J2^2 (24 JdB^2 + 36 JdC^2 + 12 JdC JpA + 21 JpA^2 + Ja (102 JdC - 2 JpA - 51 JpB)
  + 86 JpA JpB + 31 JpB^2 - 12 JdB(5 JdC + JpB)))Cos[k] - (48 J2^3(2 JdB - 8 JdC - JpA + 4 JpB) + 4 Ja^3(-5 JdB
  - 28 JdC + 6 JpA + 14 JpB) + Ja^2 (124 JdB^2 - 16 JdC^2 + 8 JdC JpA + 75 JpA^2 - 4 JdB (4 JdC + 45 JpA
  - 38 JpB) - 8 (4 JdC + JpA) JpB + 40 JpB^2) + 4 J2^2 (36 JdB^2 - 48 JdC^2 - 24 JdC JpA + 31 JpA^2
  + 4 Ja (3 JdB + 12 JdC - 10 JpA - 6 JpB) + 80 JpA JpB + 32 JpB^2 + 24 JdB (-2 JdC + JpB)) + 2 (24 JdB^3 (-2 JdC
  + JpB) + JdB JpA (30 JdC JpA - 7 (2 JdC + 3 JpA) JpB + 5 JpB^2) + 2 JdB^2 (12 JdC JpA + JpB (-3 JpA + JpB))
  - JpA^2 (-8 JdC^2 + JpB (-9 JpA + JpB) + JdC (15 JpA + JpB))) + 2 J2 (-24 JdB^3 + 2 Ja^2 (46 JdB + 56 JdC
  - 13 JpA - 28 JpB) + 12 JdB^2 (-4 JdC + 11 JpA + 2 JpB) + 2 Ja (48 JdB JdC + 48 JdC^2 - 2 JdB JpA - 45 JpA^2
  - 32 (3 JdB + JpA) JpB - 32 JpB^2) + JdB (72 JdC^2 + 48 JdC JpA + 6 JpA^2 - 72 JdC JpB + 40 JpA JpB
  + 58 JpB^2) + JpA (-36 JdC^2 + 15 JpA^2 - 34 JpA JpB - 25 JpB^2 + 4 JdC (JpA + 7 JpB))) + Ja (24 JdB^3
  + JpA (4 JdC^2 + 6 JdC JpA - 3 JpA^2 - 16 JdC JpB + 27 JpB^2) - 4 JdB^2 (12 JdC + 23 (3 JpA + JpB))
  + JdB (-72 JdC^2 + 42 JpA^2 + 62 JpA JpB - 78 JpB^2 + 4 JdC (-5 JpA + 28 JpB)))) Cos[2 k]
  + (-4 J2 (2 Ja^2 (14 JdB + 45 JdC - 9 JpA) + 15 JdC (-2 JdB + JpA)^2 + 2 Ja (12 JdB^2 - 2 JdB JpA - 7 JpA^2))
  + 8 J2^2 (12 JdB^2 - 8 JpA^2 + Ja (-12 JdB + 90 JdC + 4 JpA - 45 JpB)) + Ja (8 Ja (JdB - JpA) (JdB + 2 JpA)
  + Ja^2 (56 JdB + 60 JdC - 32 JpA - 30 JpB) + 15 (-2 JdB + JpA)^2 (2 JdC - JpB)) + 30 J2 (6 Ja^2 + (-2 JdB
  + JpA)^2) JpB + 48 J2^3 (4 JdB - 2 (5 JdC + JpA) + 5 JpB)) Cos[3 k] - 15 (2 J2 - Ja)^3 (2 JdB - JpA) Cos[4 k]
  + I (8 JdB (16 Ja^3 + Ja^2(42 JdB - 2 JdC) + 3 Ja JdC(5 JdB + 4 JdC) + 6 JdC^2(JdB + 6 JdC)) + 192 J2^3(2 JdB
```

```
- JpA) - 4 (15 Ja^3 + 36 JdC^3 + 2 Ja JdC (67 JdB + 5 JdC) + 2 Ja^2 (29 JdB + 6 JdC)) JpA + 2 (21 Ja^2
+ 96 JdB^2 + 95 Ja JdC + 34 JdC^2) JpA^2 - 48 JpA^4 + 4 J2 (4 Ja^2 (8 JdB - 5 JpA) - 3 JdC (20 JdB^2
+ 8 JdB JdC - 28 JdB JpA + 8 JdC JpA + 21 JpA^2) - 4 Ja (24 JdB^2 + 2 JpA (JdC + JpA) + JdB (3 JdC + JpA)))
- 2 J2 (4 (10 Ja^2 + 53 Ja JdB - 15 JdB^2 - 2 Ja JdC + 6 JdB JdC) - 4 (21 Ja + 45 JdB + 14 JdC) JpA
+ 9 JpA^2) JpB - (28 Ja^3 - 4 Ja^2 (31 JdB + 10 JdC - 13 JpA) + 4 JdC (12 JdB (JdB + 3 JdC) + 2 (-8 JdB
+ 9 JdC) JpA + 43 JpA^2) + Ja (4 (71 JdB^2 + 52 JdB JdC - 72 JdC^2) - 4 (57 JdB + 31 JdC) JpA + 55 JpA^2)) JpB
+ 8 J2 (5 Ja + 2 JdB + 13 JpA) JpB^2 - (44 Ja^2 + 4 JdB^2 + 16 (JdB - 3 JdC) JpA - 53 JpA^2
+ 24 Ja (4 JdC + JpA)) JpB^2 - 12 (2 Ja - 8 JdB + 3 JpA) JpB^3 + 8 J2^2 (48 JdB^2 + 12 JdB (-JdC + JpB)
+ JpA (-12 JdC + 5 JpA + 6 JpB) + Ja (-24 JdB + 14 JpA + 34 JpB))) Sin[k] - I (192 J2^3 (2 JdB - JpA)
- 2 JdC (-48 JdB^3 + 24 JdB^2 JpA + 30 JdB JpA^2 + (8 JdC - 15 JpA) JpA^2) + 2 (-24 JdB^3 + 6 JdB^2 JpA
+ (JdC - 9 JpA)JpA^2 + 7 JdB JpA(2 JdC + 3 JpA))JpB + 2(-2 JdB^2 - 5 JdB JpA + JpA^2)JpB^2 + Ja^3(-40 JdB
+ 6 JpA + 8 JpB) + Ja^2(-124 JdB^2 - JpA (8 JdC + 75 JpA) + 4 JdB(4 JdC + 45 JpA - 38 JpB) + 8(2 JdC + JpA)JpB
- 8 JpB^2) - 4 J2^2 (36 JdB^2 + 2 Ja (96 JdB - 65 JpA - 4 JpB) + 24 JdB (-2 JdC + JpB) + JpA (-24 JdC + 31 JpA
+ 80 JpB)) + 2 J2 (24 JdB^3 + 12 JdB^2 (4 JdC - 11 JpA - 2 JpB) - JpA (84 JdC^2 + 15 JpA^2 + 4 JdC (JpA
- 23 JpB) - 34 JpA JpB + 5 JpB^2) + 8 Ja^2(11 JdB - 2(4 JpA + JpB)) + 2 JdB (84 JdC^2 - 3 JpA^2 - 20 JpA JpB
+ JpB^2 - 12 JdC(2 JpA + 7 JpB)) + 2 Ja(45 JpA^2 + 32 JpA JpB + 4 JpB(-2 JdC + JpB) + 2 JdB(-24 JdC + JpA
+ 48 JpB))) + Ja(-24 JdB^3 + 2 JdB(-84 JdC^2 + 10 JdC JpA - 21 JpA^2 + 64 JdC JpB - 31 JpA JpB + 9 JpB^2)
+ 4 JdB^2(12 JdC + 23(3 JpA + JpB)) + JpA(116 JdC^2 - 2 JdC(3 JpA + 52 JpB) + 3(JpA^2 + JpB^2))))Sin[2 k]
- I (96 J2^3 (2 JdB - JpA) + 32 J2^2 (3 JdB (-Ja + JdB) + Ja JpA - 2 JpA^2) + 4 J2 (-15 JdC (-2 JdB + JpA)^2
+ Ja^2 (-28 JdB + 18 JpA) + Ja (-24 JdB^2 + 4 JdB JpA + 14 JpA^2)) + Ja (8 Ja^2 (7 JdB - 4 JpA)
+ 8 Ja (JdB - JpA) (JdB + 2 JpA) + 15 (-2 JdB + JpA)^2 (2 JdC - JpB)) + 30 J2 (-2 JdB + JpA)^2 JpB) Sin[3 k]
+ 15 I (2 J2 - Ja)^3 (2 JdB - JpA) Sin[4 k])
```

The dispersion relation

$$\begin{aligned}\omega_{o4\,\pm}(k) =& 1.071 + 0.12\cos(k) - 0.012\cos(2k) - 0.0053\cos(3k) - 0.007\cos(4k) \\ &\pm \frac{1}{2}\Big(0.18 + 0.055\cos(k) - 0.053\cos(2k) + 0.0082\cos(3k) - 0.0062\cos(4k) \\ &+ 0.0011\cos(5k) - 0.00011\cos(6k) + 0.000039\cos(7k)\Big)^{1/2}\end{aligned} \tag{C.4}$$

C.5 Fifth-order

The results of the forth-order expressions `W11o5`, `W22o5`≡`Conjugate[W11o5]`, `W12o5` and `W21o5`≡`Conjugate[W12o5]` are

```
W11o5[k_, Ja_, J2_, JdB_, JpA_, JpB_, JdC_] := (1/73728)(-46080 J2^5 + 70272 J2^4 Ja - 864 Ja^5
- 16 J2^3(3564 Ja^2 - 612 JdB^2 - 612 JdC^2 - 810 JdC JpA + 431 JpA^2 + 18 JdB(50 JdC + 74 JpA - 45 JpB)
+ 1332 JdC JpB + 1609 JpA JpB + 431 JpB^2) + 2 Ja(2 JdC(-504 JdB(15 JdB^2 - 4 JdB JdC + 15 JdC^2)
+ 4(5339 JdB^2 + 396 JdB JdC + 1421 JdC^2)JpA - 18(671 JdB + 26 JdC)JpA^2 + 709 JpA^3)
+(8 JdB(1421 JdB^2 + 396 JdB JdC + 5339 JdC^2) - 4(4447 JdB^2 + 1080 JdB JdC + 4447 JdC^2)JpA
+ 2(3691 JdB - 216 JdC)JpA^2 - 953 JpA^3)JpB - 2(468 JdB^2 + 18 JdB(671 JdC + 12 JpA) - JpA(3691 JdC
+ 126 JpA))JpB^2 +(1418 JdB - 953 JpA)JpB^3) + 9(-160(3 JdB^5 + 13 JdB^3 JdC^2 + 13 JdB^2 JdC^3 + 3 JdC^5)
+ 16 JdB(93 JdB^3 + 61 JdB JdC^2 + 90 JdC^3)JpA - 8(206 JdB^3 + 75 JdB JdC^2 + 25 JdC^3)JpA^2
- 4(78 JdB^2 + 89 JdC^2)JpA^3 + 954 JdB JpA^4 - 15 JpA^5 + 4 JdC(4(90 JdB^3 + 61 JdB^2 JdC + 93 JdC^3)
- 180 JdB(JdB + JdC)JpA +(574 JdB + 29 JdC)JpA^2 - 79 JpA^3)JpB -(8(25 JdB^3 + 75 JdB^2 JdC + 206 JdC^3)
- 4 JdB(29 JdB + 574 JdC)JpA + 502(JdB + JdC)JpA^2 + 33 JpA^3)JpB^2 -(356 JdB^2 + 312 JdC^2 + 316 JdB JpA
+ 33 JpA^2)JpB^3 + 954 JdC JpB^4 - 15 JpB^5) + 2 Ja^3(4516 JdB^2 + 4516 JdC^2 + 446 JdC JpA + 345 JpA^2
- 4084 JdC JpB + 917 JpA JpB + 345 JpB^2 + JdB(2388 JdC - 4084 JpA + 446 JpB)) - 2 Ja^2(3448 JdB^3
+ 3448 JdC^3 + JdC^2(548 JpA - 9132 JpB) - 4 JdB^2(658 JdC + 2283 JpA - 137 JpB) -(JpA + JpB)(345 JpA^2
+ 1612 JpA JpB + 345 JpB^2) + 2 JdC(841 JpA^2 + 1330 JpA JpB + 3997 JpB^2) + JdB(-2632 JdC^2 + 7994 JpA^2
+ 2660 JpA JpB + 1682 JpB^2 + 3224 JdC(JpA + JpB))) + 8 J2^2(3924 Ja^3 + 1224 JdB^3 + 1656 JdB^2 JdC
+ 1656 JdB JdC^2 + 1224 JdC^3 - 756 JdB^2 JpA - 2952 JdB JdC JpA + 2196 JdC^2 JpA - 5210 JdB JpA^2
+ 658 JdC JpA^2 + 1129 JpA^3 +(36(61 JdB^2 - 82 JdB JdC - 21 JdC^2) - 3900(JdB + JdC)JpA + 415 JpA^2)JpB
+(658 JdB - 5210 JdC + 415 JpA)JpB^2 + 1129 JpB^3 + Ja(-756 JdB^2 - 756 JdC^2 + 2594 JdC JpA + 2283 JpA^2
+ 1476 JdC JpB + 1603 JpA JpB + 2283 JpB^2 + 2 JdB(918 JdC + 738 JpA + 1297 JpB))) + 4 J2(612 Ja^4
+ 2 JdC(360 JdB(25 JdB^2 + 2 JdB JdC + 25 JdC^2) - 108(173 JdB^2 + 12 JdB JdC + 35 JdC^2)JpA + 2(4667 JdB
+ 504 JdC)JpA^2 - 1409 JpA^3) +(-216 JdB(35 JdB^2 + 12 JdB JdC + 173 JdC^2) + 4(2819 JdB^2 - 1800 JdB JdC
```

```
+ 2819 JdC^2)JpA + 18(-287 JdB + 128 JdC)JpA^2 + 2221 JpA^3)JpB + 2(1008 JdB^2 - 9 JpA(287 JdC + 71 JpA)
+ 2 JdB(4667 JdC + 576 JpA))JpB^2 +(-2818 JdB + 2221 JpA)JpB^3 - Ja^2(10420 JdB^2 + 10420 JdC^2
+ 3706 JdC JpA + 3997 JpA^2 - 9988 JdC JpB + 191 JpA JpB + 3997 JpB^2 + JdB(6780 JdC - 9988 JpA + 3706 JpB))
+ 2 Ja(-2664 JdB^3 - 2664 JdC^3 + 12 JdB^2(-246 JdC + 123 JpA + 79 JpB) + 12 JdC^2(79 JpA + 123 JpB)
- (JpA + JpB)(1021 JpA^2 - 224 JpA JpB + 1021 JpB^2) + JdC(-806 JpA^2 + 428 JpA JpB + 4994 JpB^2)
+ JdB(-2952 JdC^2 + 4994 JpA^2 + 428 JpA JpB - 806 JpB^2 + 8216 JdC(JpA + JpB)))) + 2(-(7488 J2^5
+ 8352 J2^4 Ja + 630 Ja^5 + 4 JdC(-72 JdB(JdB + JdC)(14 JdB^2 - 15 JdB JdC + 14 JdC^2) + 36(44 JdB^3
+ 25 JdB^2 JdC + 14 JdC^3)JpA + 2(540 JdB^2 - 265 JdB JdC + 371 JdC^2)JpA^2 +(-180 JdB + 31 JdC)JpA^3
- 315 JpA^4) + 2(72 JdB(14 JdB^3 + 25 JdB JdC^2 + 44 JdC^3) - 16(JdB + JdC)(162 JdB^2 - 283 JdB JdC
+ 162 JdC^2)JpA - 2(720 JdB^2 + 264 JdB JdC + 2305 JdC^2)JpA^2 + 4(252 JdB - 97 JdC)JpA^3 + 117 JpA^4)JpB
+(8 JdB(371 JdB^2 - 265 JdB JdC + 540 JdC^2) - 4(2305 JdB^2 + 264 JdB JdC + 720 JdC^2)JpA + 2810(JdB
+ JdC)JpA^2 + 49 JpA^3)JpB^2 +(124 JdB^2 + 7 JpA(288 JdC + 7 JpA) - 8 JdB(90 JdC + 97 JpA))JpB^3
+ 18(-70 JdB + 13 JpA)JpB^4 + 8 J2^3(1044 Ja^2 + 2484 JdB^2 - 5904 JdB JdC + 2484 JdC^2 - 2052 JdB JpA
+ 2664 JdC JpA + 2333 JpA^2 + 36(74 JdB - 57 JdC + 55 JpA)JpB + 2333 JpB^2) - Ja^3(5748 JdB^2 + 5748 JdC^2
+ 4396 JdC JpA + 2037 JpA^2 - 4548 JdC JpB - 700 JpA JpB + 2037 JpB^2 + JdB(-6784 JdC - 4548 JpA + 4396 JpB))
+ 2 Ja^2(2808 JdB^3 + 2808 JdC^3 + 4 JdC^2(326 JpA - 1543 JpB) + 4 JdB^2(1100 JdC - 1543 JpA + 326 JpB)
- (JpA + JpB)(469 JpA^2 - 422 JpA JpB + 469 JpB^2) + 2 JdC(755 JpA^2 - 71 JpA JpB + 1893 JpB^2)
+ 2 JdB(2200 JdC^2 + 1893 JpA^2 - 71 JpA JpB + 755 JpB^2 - 1186 JdC(JpA + JpB))) + Ja(-432 JdB^4 - 432 JdC^4
+ 1485 JpA^4 + 216 JdB^3(6 JdC - 12 JpA - 25 JpB) + 1393 JpA^3 JpB - 2093 JpA^2 JpB^2 + 1393 JpA JpB^3
+ 1485 JpB^4 - 216 JdC^3(25 JpA + 12 JpB) - 4 JdC^2(853 JpA^2 - 3291 JpA JpB + 378 JpB^2) - 4 JdB^2(2772 JdC^2
+ 3954 JdC JpA + 378 JpA^2 - 100 JdC JpB - 3291 JpA JpB + 853 JpB^2) + 2 JdC(1453 JpA^3 + 2898 JpA^2 JpB
- 2993 JpA JpB^2 - 756 JpB^3) + 2 JdB(648 JdC^3 - 756 JpA^3 + 4 JdC^2(50 JpA - 1977 JpB) - 2993 JpA^2 JpB
+ 2898 JpA JpB^2 + 1453 JpB^3 + 6 JdC(401 JpA^2 - 188 JpA JpB + 401 JpB^2))) + 2 J2(894 Ja^4 + 432 JdB^4
+ 432 JdC^4 - 648 JdC^3 JpA + 3828 JdC^2 JpA^2 - 786 JdC JpA^3 - 1773 JpA^4 +(2592 JdC^3 + 4724 JdC^2 JpA
- 8492 JdC JpA^2 - 2361 JpA^3)JpB +(360 JdC^2 + 346 JdC JpA + 2969 JpA^2)JpB^2 + 3(888 JdC - 787 JpA)JpB^3
- 1773 JpB^4 - 72 JdB^3(34 JdC + 9(-4 JpA + JpB)) + 4 JdB^2(2052 JdC^2 + 90 JpA^2 + 1181 JpA JpB + 957 JpB^2
- 54 JdC(JpA + 42 JpB)) + Ja^2(13996 JdB^2 + 13996 JdC^2 + 12032 JdC JpA + 7491 JpA^2 - 4(2983 JdC
+ 842 JpA)JpB + 7491 JpB^2 + 4 JdB(952 JdC - 2983 JpA + 3008 JpB)) + 2 JdB(-1224 JdC^3 + 1332 JpA^3
+ 173 JpA^2 JpB - 4246 JpA JpB^2 - 393 JpB^3 - 108 JdC^2(42 JpA + JpB) + 2 JdC(461 JpA^2 + 5676 JpA JpB
+ 461 JpB^2)) + 2 Ja(-6544 JdC^2 JpA + 16 JdB^2(261 JdC - 409 JpB) +(JpA + JpB)(816 JpA^2 - 359 JpA JpB
+ 816 JpB^2) - 2 JdC(659 JpA^2 - 741 JpA JpB + 2288 JpB^2) + 2 JdB(2088 JdC^2 - 2288 JpA^2 + 741 JpA JpB
- 659 JpB^2 - 3130 JdC(JpA + JpB)))) + 4 J2^2(-6636 Ja^3 - Ja(5292 JdB^2 - 6480 JdB JdC + 5292 JdC^2
- 3996 JdB JpA + 11252 JdC JpA + 6427 JpA^2 + 4(2813 JdB - 999 JdC + 288 JpA)JpB + 6427 JpB^2)
+ 2(936 JdB^3 + 936 JdC^3 - 36 JdB^2(62 JdC + 13 JpA - 21 JpB) + 36 JdC^2(21 JpA - 13 JpB) - 9(JpA
+ JpB)(27 JpA^2 + 38 JpA JpB + 27 JpB^2) + 2 JdC(573 JpA^2 + 1340 JpA JpB + 979 JpB^2) + 2 JdB(-1116 JdC^2
+ 979 JpA^2 + 1340 JpA JpB + 573 JpB^2 + 180 JdC(JpA + JpB)))))Cos[ k] +(7488 J2^5 - 23904 J2^4 Ja
- 566 Ja^5 - 8 JdC^2(216 JdB^2(JdB + JdC) - 108 JdB(JdB + 2 JdC)JpA + 2(-25 JdB + 23 JdC)JpA^2 + 25 JpA^3)
+ 8 JdC(108 JdB^2(2 JdB + JdC) - 32 JdB(JdB + JdC)JpA -(126 JdB + 23 JdC)JpA^2 + 44 JpA^3)JpB - 2(8 JdB^2(23 JdB
- 25 JdC) + 4 JdB(23 JdB + 126 JdC)JpA - 226(JdB + JdC)JpA^2 + 67 JpA^3)JpB^2 - 2(100 JdB^2 - 176 JdB JpA
+ 67 JpA^2)JpB^3 + Ja^3(2(720 JdB^2 + 720 JdC^2 + 775 JdC JpA + 524 JpA^2 - 2 JdB(539 JdC + 360 JpA))
+ 5(310 JdB - 9(32 JdC + 23 JpA))JpB + 1048 JpB^2) - 8 J2^3(964 Ja^2 - 1530 JdC JpA + 1376 JpA^2
+ 1530 JdB(2 JdC - JpB) + 3037 JpA JpB + 1376 JpB^2) + 4 J2^2(36(191 Ja^3 + 371 Ja JdB JdC - 4(JdB + JdC)(JdB^2
+ 3 JdB JdC + JdC^2)) + 6(-337 Ja JdC + 12(JdB^2 + 16 JdB JdC - 12 JdC^2))JpA + 4(1016 Ja - 183 JdB
- 468 JdC)JpA^2 - 290 JpA^3 +(Ja(-2022 JdB + 4571 JpA) + 8(9(-12 JdB^2 + 16 JdB JdC + JdC^2)
- 194(JdB + JdC)JpA + 81 JpA^2))JpB + 4(1016 Ja - 468 JdB - 183 JdC + 162 JpA)JpB^2 - 290 JpB^3)
+ 2 J2(-2790 Ja^4 + 4 JdC(-36 JdB(20 JdB^2 + 3 JdB JdC + 20 JdC^2) + 72(23 JdB^2 + 3 JdB JdC + 5 JdC^2)JpA
- 3(404 JdB + 19 JdC)JpA^2 - 46 JpA^3) + 8(36 JdB(5 JdB^2 + 3 JdB JdC + 23 JdC^2) - 12(24 JdB^2 + 43 JdB JdC
+ 24 JdC^2)JpA +(241 JdB + 242 JdC)JpA^2 + 11 JpA^3)JpB +(-12 JdB(19 JdB + 404 JdC) + 8(242 JdB
+ 241 JdC)JpA - 295 JpA^2)JpB^2 + 8(-23 JdB + 11 JpA)JpB^3 - Ja^2(1184 JdB^2 + 1184 JdC^2 - 694 JdC JpA
+ 3672 JpA^2 + 2 JdB(8006 JdC - 592 JpA - 347 JpB) - 1184 JdC JpB + 283 JpA JpB + 3672 JpB^2) + 2 Ja(144(JdB
+ JdC)(JdB^2 + 7 JdB JdC + JdC^2) + 4(-18 JdB^2 + 422 JdB JdC + 627 JdC^2)JpA + 4(183 JdB + 329 JdC)JpA^2
+ 290 JpA^3 +(4(627 JdB^2 + 422 JdB JdC - 18 JdC^2) - 1644(JdB + JdC)JpA - 373 JpA^2)JpB +(1316 JdB
+ 732 JdC - 373 JpA)JpB^2 + 290 JpB^3)) + 2 Ja^2(536 JdB^3 + 536 JdC^3 - 4 JdC^2(126 JpA + 83 JpB)
- 4 JdB^2(1034 JdC + 83 JpA + 126 JpB) - 5(JpA + JpB)(17 JpA^2 + JpA JpB + 17 JpB^2) - 2 JdC(25 JpA^2
- 512 JpA JpB + 227 JpB^2) + JdB(-4136 JdC^2 - 454 JpA^2 + 1024 JpA JpB - 50 JpB^2 + 488 JdC(JpA + JpB)))
+ Ja(32 JdB^3(90 JdC - 83 JpB) - 4 JdB^2(324 JdC^2 + 1456 JdC JpA - 932 JdC JpB - 660 JpA JpB + 465 JpB^2)
+ 4 JdB(4 JdC(180 JdC^2 + 233 JdC JpA + 317 JpA^2) - 2(728 JdC^2 + 604 JdC JpA + 233 JpA^2)JpB +(1268 JdC
+ 291 JpA)JpB^2 - 32 JpB^3) - JpA(2656 JdC^3 + 60 JdC^2(31 JpA - 44 JpB) + JpB(52 JpA^2 + 561 JpA JpB
+ 52 JpB^2) + 4 JdC(32 JpA^2 - 291 JpA JpB + 466 JpB^2))))Cos[ 2 k] +(-3456 J2^5 + 14976 J2^4 Ja
- 16 J2^3(1392 Ja^2 - 540 JdB^2 - 540 JdC^2 - 378 JdC JpA - 131 JpA^2 + 54 JdB(14 JdC + 10 JpA - 7 JpB)
+ 540 JdC JpB + 329 JpA JpB - 131 JpB^2) + Ja(-324 Ja^4 - 315(-2 JdB + JpA)^2(-2 JdC + JpB)^2 - 2 Ja^2(508 JdB^2
+ 508 JdC^2 - 886 JdC JpA + 123 JpA^2 + JdB(660 JdC - 508 JpA - 886 JpB) - 508 JdC JpB + 581 JpA JpB
```

```
+ 123 JpB^2) + 2 Ja(2 JdC(-308 JdB(JdB + JdC) + 6(-28 JdB + 23 JdC)JpA + 155 JpA^2) + 3(4 JdB(23 JdB - 28 JdC)
+ 92(JdB + JdC)JpA - 67 JpA^2)JpB +(310 JdB - 201 JpA)JpB^2)) + 8 J2^2(1548 Ja^3 + 6 JdC(-108 JdB(JdB + JdC)
+ 54 JdC JpA + 25 JpA^2) +(324 JdB^2 + 76(JdB + JdC)JpA - 113 JpA^2)JpB +(150 JdB - 113 JpA)JpB^2
+ Ja(-1620 JdB^2 - 1620 JdC^2 + 178 JdC JpA - 393 JpA^2 + 1620 JdC JpB + 53 JpA JpB - 393 JpB^2 + 2 JdB(378 JdC
+ 810 JpA + 89 JpB))) + 2 J2(-816 Ja^4 + 315(-2 JdB + JpA)^2(-2 JdC + JpB)^2 + 2 Ja^2(1588 JdB^2 + 1588 JdC^2
+ 385 JpA^2 + 2 JdB(330 JdC - 794 JpA - 721 JpB) + 857 JpA JpB + 385 JpB^2 - 2 JdC(721 JpA + 794 JpB))
+ 4 Ja(4 JdB^2(162 JdC - 77 JpB) + JpA(-308 JdC^2 + 155 JpB(JpA + JpB) - 2 JdC(113 JpA + 84 JpB)) + 2 JdB(324 JdC^2
+ 76 JdC(JpA + JpB) - JpB(84 JpA + 113 JpB)))))Cos[3 k] - 2(2 J2 - Ja)^3(216 J2^2 - 134 Ja^2 - 315(2 JdB
- JpA)(2 JdC - JpB))Cos[4 k] + 63(2 J2 - Ja)^5 Cos[5 k] + I(4 JdC(-216 JdB(JdB - JdC)(6 JdB^2 + 7 JdB JdC + 6 JdC^2)
+ 324(4 JdB^3 + JdB^2 JdC - 2 JdC^3)JpA + 2(348 JdB^2 - 37 JdB JdC + 325 JdC^2)JpA^2 -(156 JdB + 17 JdC)JpA^3
- 33 JpA^4) + 2(648 JdB(2 JdB^3 - JdB JdC^2 - 4 JdC^3) + 16(JdB - JdC)(33 JdB^2 - 62 JdB JdC + 33 JdC^2)JpA
- 2(1068 JdB^2 - 672 JdB JdC + 1787 JdC^2)JpA^2 + 4(39 JdB - 73 JdC)JpA^3 + 165 JpA^4)JpB +(-8 JdB(325 JdB^2
- 37 JdB JdC + 348 JdC^2) + 4(1787 JdB^2 - 672 JdB JdC + 1068 JdC^2)JpA - 5326(JdB - JdC)JpA^2 + 913 JpA^3)JpB^2
+ (68 JdB^2 + 8 JdB(78 JdC + 73 JpA) - JpA(312 JdC + 913 JpA))JpB^3 + 66(2 JdB - 5 JpA)JpB^4 + 8 Ja^3((110 JdB
+ 14 JdC - 55 JpA)JpA - 2(7 JdB + 55 JdC)JpB + 55 JpB^2) + 2 Ja^2(5432 JdB(JdB - JdC)JdC - 4(200 JdB^2
+ 1481 JdB JdC - 408 JdC^2)JpA + 32(34 JdB + 71 JdC)JpA^2 - 416 JpA^3 +(-1632 JdB^2 + 5924 JdB JdC + 800 JdC^2
+ 2226 JdB JpA - 2226 JdC JpA - 1039 JpA^2)JpB +(-32(71 JdB + 34 JdC) + 1039 JpA)JpB^2 + 416 JpB^3)
+ 4 J2(72 JdB(JdB - JdC)JdC(-19 Ja + 6(JdB + JdC)) + 4(4 Ja^2(26 JdB - 7 JdC) + 108(JdB - JdC)JdC^2 + Ja(56 JdB^2
+ 726 JdB JdC - 323 JdC^2))JpA - 2(8 Ja(13 Ja + 32 JdB) + 37(35 Ja + 2 JdB)JdC + 624 JdC^2)JpA^2 + 4(68 Ja
+ 5 JdC)JpA^3 +(16 Ja^2(7 JdB - 26 JdC) + 432 JdB^2(JdB - JdC) + 4 Ja(323 JdB^2 - 726 JdB JdC - 56 JdC^2)
- 4(JdB - JdC)(401 Ja + 277(JdB + JdC))JpA +(1219 Ja - 312 JdB + 2220 JdC)JpA^2 + 559 JpA^3)JpB +(208 Ja^2
+ Ja(2590 JdB + 512 JdC - 1219 JpA) + 4(312 JdB^2 + 37 JdB(JdC - 15 JpA) + 78 JdC JpA))JpB^2 -(272 Ja + 20 JdB
+ 559 JpA)JpB^3) + 16 J2^2(18 JdB^2(28 JdC - 5 JpB) - JdB(504 JdC^2 + 428 Ja JpA + 162 JdC(JpA - JpB) + 28 Ja JpB
+ 123 JpA JpB + 325 JpB^2) + Ja(214(JpA - JpB)(JpA + JpB) + 4 JdC(7 JpA + 107 JpB)) + JpA(90 JdC^2 + 101 JpB(-JpA
+ JpB) + JdC(325 JpA + 123 JpB))) + 4 Ja(-4 JdB^3(108 JdC + 456 JpA - 73 JpB) + 4 JdC^3(-73 JpA + 456 JpB)
+ 12 JdC^2(9 JpA^2 + 80 JpA JpB - 120 JpB^2) + 4 JdB^2(JpA(457 JdC + 360 JpA) + 48(7 JdC - 5 JpA)JpB - 27 JpB^2)
- JdC JpA(183 JpA^2 + 132 JpA JpB + 317 JpB^2) - 3(44 JpA^4 - 9 JpA^3 JpB + 9 JpA JpB^3 - 44 JpB^4) + JdB(432 JdC^3
- 4 JdC^2(336 JpA + 457 JpB) + 728 JdC(-JpA^2 + JpB^2) + JpB(317 JpA^2 + 132 JpA JpB + 183 JpB^2))))Sin[k]
+ I(8 JdC^2(-216 JdB^2(JdB - JdC) + 108 JdB(JdB - 2 JdC)JpA + 14(5 JdB + 7 JdC)JpA^2 - 35 JpA^3)
- 8 JdC(108 JdB^2(-2 JdB + JdC) + 8 JdB(-JdB + JdC)JpA +(186 JdB + 35 JdC)JpA^2 - 64 JpA^3)JpB - 2(56 JdB^2(7 JdB
+ 5 JdC) - 4 JdB(35 JdB + 186 JdC)JpA + 170(-JdB + JdC)JpA^2 + 71 JpA^3)JpB^2 + 2(140 JdB^2 - 256 JdB JpA
+ 71 JpA^2)JpB^3 + 8 Ja^3(28 JdB JpA + 55 JdC JpA - 14 JpA^2 - 55 JdB JpB - 28 JdC JpB + 14 JpB^2)
+ 4 J2^2(1368 JdB(JdB - JdC)JdC - 4(9 JdC(20 JdB + JdC) + Ja(-56 JdB + 214 JdC))JpA + 14(-8 Ja + 95 JdC)JpA^2
+(8 Ja(107 JdB - 28 JdC) + 36 JdB(JdB + 20 JdC) - 2024(JdB - JdC)JpA + 347 JpA^2)JpB +(112 Ja - 1330 JdB
- 347 JpA)JpB^2) + 2 J2(144 JdB(JdB - JdC)JdC(-10 Ja + 19(JdB + JdC)) - 8(8 Ja JdB(7 Ja + 4 JdB) +(-52 Ja^2
- 652 Ja JdB + 297 JdB^2)JdC + 18 Ja JdC^2 - 171 JdC^3)JpA + 4(56 Ja^2 + 64 Ja JdB - 1290 Ja JdC + 545 JdB JdC
+ 88 JdC^2)JpA^2 + 2(-32 Ja + 229 JdC)JpA^3 +(-8 JdB(52 Ja^2 - 18 Ja JdB + 171 JdB^2) + 32 Ja(14 Ja - 163 JdB)JdC
+ 8(32 Ja + 297 JdB)JdC^2 + 4(JdB - JdC)(324 Ja + 329(JdB + JdC))JpA + 2(350 Ja - 609 JdB - 176 JdC)JpA^2
- 197 JpA^3)JpB - 2(2(56 Ja^2 - 1290 Ja JdB + 88 JdB^2 + 64 Ja JdC + 545 JdB JdC) +(350 Ja - 176 JdB
- 609 JdC)JpA)JpB^2 +(64 Ja - 458 JdB + 197 JpA)JpB^3) + Ja^2(4 JdB^2(1154 JdC + 64 JpA - 613 JpB)
+ 4 JdC^2(613 JpA - 64 JpB) +(JpA - JpB)(64 JpA^2 - 1299 JpA JpB + 64 JpB^2) + JdC(4462 JpA^2 - 3288 JpA JpB
+ 256 JpB^2) - 2 JdB(2308 JdC^2 + 128 JpA^2 + 4808 JdC(JpA - JpB) - 1644 JpA JpB + 2231 JpB^2))
+ Ja(8 JdB^3(-342 JdC + 259 JpB) - 4 JdB^2(7(3 JpA - 40 JpB)JpB + JdC(550 JpA + 384 JpB)) + 2 JdB(1368 JdC^3
+ 4 JdC^2(192 JpA + 275 JpB) + 98 JdC(-JpA^2 + JpB^2) + JpB(377 JpA^2 - 296 JpA JpB + 153 JpB^2))
- JpA(2072 JdC^3 + 28 JdC^2(40 JpA - 3 JpB) + 33 JpB(-JpA^2 + JpB^2) + JdC(306 JpA^2 - 592 JpA JpB
+ 754 JpB^2))))Sin[2 k] - 8 I(2 JdC(2(72 J2^2 - 72 J2 Ja + 7 Ja^2)JdB(JdB - JdC) +(4 J2 Ja(7 Ja + 4 JdB - 18 JdC)
+ 7 Ja^2(-Ja + 2 JdB + JdC) + J2^2(-28 Ja + 72 JdC))JpA +(-70 J2^2 + 62 J2 Ja - 19 Ja^2)JpA^2) +(-2 JdB(J2^2(-28 Ja
+ 72 JdB) + 7 Ja^2(-Ja + JdB + 2 JdC) + 4 J2 Ja(7 Ja - 18 JdB + 4 JdC)) - 2 Ja(8 J2 + 7 Ja)(JdB - JdC)JpA +(70 J2^2
- 62 J2 Ja + 19 Ja^2)JpA^2)JpB +(70 J2^2 - 62 J2 Ja + 19 Ja^2)(2 JdB - JpA)JpB^2)Sin[3 k]))

W12o5[k_, Ja_, J2_, JdB_, JpA_, JpB_, JdC_] := (1/73728)(4 Ja^4(82 JdB + 150 JdC - 172 JpA - 3 JpB) + 576 J2^4(36 JdB
- 2(JdC + 9 JpA) + JpB) + 4 J2^2(-8(Ja^2(701 JdB + 528 JdC) + 9 Ja(34 JdB^2 + 47 JdB JdC - 26 JdC^2) + 9(8 JdB^3
+ 79 JdB^2 JdC - 36 JdB JdC^2 + 22 JdC^3)) + 4(520 Ja^2 - 358 Ja JdB - 288 JdB^2 + 3369 Ja JdC + 1638 JdB JdC
- 36 JdC^2)JpA + 2(3076 Ja - 1696 JdB - 2211 JdC)JpA^2 + 360 JpA^3 + (2400 Ja^2 + 4284 JdB^2 - 1368 JdC^2
- 4880 JdC JpA + 339 JpA^2 - 36 JdB(64 JdC + 163 JpA) + 2 Ja(5390 JdB + 879 JpA))JpB + 4(1543 Ja - 482 JdB
- 1877 JdC + 227 JpA)JpB^2 + 1670 JpB^3) + 3(4 JdC(-24 JdB^2(12 JdB^2 + 9 JdB JdC + 5 JdC^2) + 12 JdB(-48 JdB^2
+ 9 JdB JdC + 2 JdC^2)JpA + 2(160 JdB^2 + 27 JdB JdC - 287 JdC^2)JpA^2 - (392 JdB + 27 JdC)JpA^3 + 158 JpA^4)
+ 4(36 JdB^2(4 JdB^2 - 11 JdC^2) + 4 JdB(194 JdB^2 - 174 JdB JdC + 169 JdC^2)JpA + (-148 JdB^2 + 624 JdB JdC
+ 777 JdC^2)JpA^2 - 50(JdB + 3 JdC)JpA^3 - 20 JpA^4)JpB + (984 JdB^3 - 3072 JdC^3 - 3274 JdC JpA^2 - 357 JpA^3
+ 2 JdB JpA(1828 JdC + 153 JpA) + 4 JdB^2(-730 JdC + 441 JpA))JpB^2 + (92 JdB^2 + 236 JdB JpA + 227 JpA^2)JpB^3
+ 2304 JdC JpB^4) - 16 J2^3(-72 JdB^2 + 936 JdC^2 + 90 JdC JpA + 858 JpA^2 + 2 Ja(792 JdB + 432 JdC - 265 JpA
- 216 JpB) + 2275 JpA JpB + 702 JpB^2 - 90 JdB(14 JdC + JpB)) + 2 Ja^3(2768 JdB^2 + 1944 JdC^2 + 1366 JpA^2
```

```
+ 6 JdC(953 JpA - 544 JpB) - 2795 JpA JpB + 938 JpB^2 + JdB(-9044 JdC - 3060 JpA + 4938 JpB)) + Ja^2(-7488 JdB^3
- 14896 JdC^3 + 136 JpA^3 + 1783 JpA^2 JpB + 3524 JpA JpB^2 + 1302 JpB^3 + 4 JdB^2(-4534 JdC + 3096 JpA
+ 1187 JpB) + 8 JdC^2(-54 JpA + 2293 JpB) - 14 JdC(361 JpA^2 + 256 JpA JpB + 950 JpB^2) - 4 JdB(1736 JdC^2
+ 1276 JpA^2 + 551 JpA JpB + 1206 JpB^2 - 2 JdC(719 JpA + 228 JpB))) + 4 Ja(-1008 JdB^4 + JdB^3(-336 JpA
+ 2996 JpB) + 2 JdB^2(-360 JdC^2 + 1438 JdC JpA + 684 JpA^2 + 2366 JdC JpB - 2350 JpA JpB - 921 JpB^2)
- JdB(1296 JdC^3 - 468 JpA^3 - 613 JpA^2 JpB + 733 JpA JpB^2 + 626 JpB^3 - 4 JdC^2(757 JpA + 1834 JpB)
+ 4 JdC(195 JpA^2 + 468 JpA JpB + 1163 JpB^2)) + JpA(4264 JdC^3 - 471 JpA^3 + 2 JdC^2(509 JpA - 4014 JpB)
+ 308 JpA^2 JpB + 535 JpA JpB^2 - 1093 JpB^3 + JdC(-869 JpA^2 - 1535 JpA JpB + 4734 JpB^2)))
+ 4 J2(144 JdB(14 JdB^3 + 9 JdB^2 JdC + 31 JdB JdC^2 + 26 JdC^3) - 72(44 JdB^3 - 10 JdB^2 JdC + 21 JdB JdC^2
+ 18 JdC^3)JpA - 4(396 JdB^2 + 211 JdB JdC + 146 JdC^2)JpA^2 + 8(-27 JdB + 10 JdC)JpA^3 + 774 JpA^4
+ 2 Ja^3(2112 JdB + 1320 JdC - 613 JpA - 804 JpB) - (72 JdB JdC(53 JdB + 34 JdC) + 4(757 JdB^2 + 2400 JdB JdC
+ 794 JdC^2)JpA - 2(630 JdB + 1349 JdC)JpA^2 - 463 JpA^3)JpB + (824 JdB^2 + 1048 JdB JdC + 4314 JdB JpA
- 236 JdC JpA - 1163 JpA^2)JpB^2 + 2(-350 JdB + 1457 JpA)JpB^3 - Ja^2(5008 JdB^2 + 7832 JdC^2 + 15134 JdC JpA
+ 3724 JpA^2 - 2 JdB(4962 JdC + 3524 JpA - 5993 JpB) - 9152 JdC JpB - 6823 JpA JpB + 3786 JpB^2) + Ja(432 JdC^3
- 52 JpA^3 - 105 JpA^2 JpB - 1484 JpA JpB^2 - 1334 JpB^3 + 72 JdC^2(68 JpA + 43 JpB) + 4 JdB^2(1386 JdC - 92 JpA
+ 95 JpB) + 10 JdC(229 JpA^2 - 76 JpA JpB + 626 JpB^2) + 4 JdB(-288 JdC^2 + 884 JpA^2 - 471 JpA JpB + 558 JpB^2
+ 2 JdC(631 JpA + 866 JpB)))) - (288 JdB JdC^2(27 JdB^2 + 8 JdB JdC + 3 JdC^2) - 144 JdC^2(25 JdB^2 + 3 JdC^2)JpA
+ 8(1152 JdB^3 + 1585 JdB JdC^2 - 328 JdC^3)JpA^2 - 908 JdC^2 JpA^3 - 6912 JdB JpA^4 - 4 JdC(72 JdB(23 JdB^2
+ 4 JdB JdC - 18 JdC^2) + 4(239 JdB^2 - 836 JdB JdC + 414 JdC^2)JpA + 14(235 JdB + 144 JdC)JpA^2 - 19 JpA^3)JpB
+ (8 JdB(1195 JdB^2 - 520 JdB JdC + 378 JdC^2) - 4(2481 JdB^2 + 2368 JdB JdC + 738 JdC^2)JpA + 18(537 JdB
+ 8 JdC)JpA^2 - 779 JpA^3)JpB^2 + 8(316 JdB^2 + 5 JpA(45 JdC + 26 JpA) + JdB(378 JdC + 202 JpA))JpB^3
+ 99(-30 JdB + 7 JpA)JpB^4 + 144 J2^4(82 JdB - 288 JdC - 41 JpA + 144 JpB) + Ja^4(-726 JdB - 656 JdC + 119 JpA
+ 328 JpB) - 16 J2^3(-9(92 JdB^2 - 176 JdB JdC - 16 JdC^2 + 48 JdC JpA + 153 JpA^2 + Ja(-128 JdB + 352 JdC
+ 74 JpA)) + 2(792 Ja + 216 JdB - 1973 JpA)JpB - 1716 JpB^2) - 2 Ja^3(3180 JdB^2 + 5536 JdC^2 + 7044 JdC JpA
+ 1675 JpA^2 - 4 JdB(3280 JdC + 1245 JpA - 2354 JpB) - 5088 JdC JpB - 4404 JpA JpB + 1216 JpB^2)
+ 2 Ja(2 JdC(72(33 JdB^3 + 4 JdB^2 JdC - 9 JdB JdC^2 + 28 JdC^3) - 4(1585 JdB^2 + 1716 JdB JdC + 675 JdC^2)JpA
+ 6(471 JdB + 340 JdC)JpA^2 + 499 JpA^3) + (-8(1345 JdB^3 + 996 JdB^2 JdC + 1563 JdB JdC^2 + 792 JdC^3)
+ 4(4091 JdB^2 + 1914 JdB JdC + 2587 JdC^2)JpA + 2(-3785 JdB + 802 JdC)JpA^2 + 2095 JpA^3)JpB - 2(1068 JdB^2
+ 2160 JdC^2 + 1153 JdC JpA + 628 JpA^2 - 2 JdB(2173 JdC + 917 JpA))JpB^2 + (446 JdB + 720 JdC - 191 JpA)JpB^3
+ 1260 JpB^4) + 8 J2^2(1512 JdB^3 + 576 JdC^3 - 5544 JdC^2 JpA + 2614 JdC JpA^2 - 789 JpA^3 + Ja^2(6382 JdB
+ 5608 JdC - 3721 JpA - 2804 JpB) + (1152 JdC^2 + 9656 JdC JpA - 747 JpA^2)JpB + 4(848 JdC - 329 JpA)JpB^2
- 360 JpB^3 - 36 JdB^2(38 JdC + 27 JpA + 7 JpB) + 2 JdB(4824 JdC^2 + 432 JdC JpA + 2483 JpA^2 - 5508 JdC JpB
+ 1982 JpA JpB + 2082 JpB^2) - Ja(828 JdB^2 - 2448 JdC^2 + 9740 JdC JpA + 5491 JpA^2 - 4 JdB(324 JdC + 219 JpA
- 2186 JpB) + 2496 JpA JpB + 5156 JpB^2)) + 2 Ja^2(8776 JdB^3 + 7488 JdC^3 - 369 JpA^3 - 2201 JpA^2 JpB
- 1926 JpA JpB^2 + 400 JpB^3 + 4 JdB^2(1442 JdC - 2879 JpA + 149 JpB) - 8 JdC^2(235 JpA + 1408 JpB)
+ JdC(4338 JpA^2 + 5044 JpA JpB + 3760 JpB^2) + 2 JdB(9384 JdC^2 + 3791 JpA^2 + 588 JpA JpB + 2504 JpB^2
- 12 JdC(37 JpA + 522 JpB))) + 4 J2(2 JdC(-72(41 JdB^3 + 32 JdB^2 JdC + 17 JdB JdC^2 + 28 JdC^3) + 36(49 JdB^2
+ 48 JdB JdC + 9 JdC^2)JpA + 2(211 JdB - 108 JdC)JpA^2 + 533 JpA^3) + (72(33 JdB^3 + 28 JdB^2 JdC - 3 JdB JdC^2
+ 88 JdC^3) + 4(493 JdB^2 + 3414 JdB JdC + 1231 JdC^2)JpA - 2(279 JdB + 2818 JdC)JpA^2 - 3007 JpA^3)JpB
+ 2(708 JdB^2 + 122 JdB JdC + 1584 JdC^2 - 3178 JdB JpA - 893 JdC JpA + 958 JpA^2)JpB^2 + 3(154 JdB + 144 JdC
- 425 JpA)JpB^3 - 1548 JpB^4 + Ja^3(-5848 JdB - 8448 JdC + 3486 JpA + 4224 JpB) + Ja^2(9292 JdB^2 + 10016 JdC^2
+ 6537 JpA^2 - 8 JdB(1604 JdC + 1553 JpA - 2813 JpB) + 8 JdC(2425 JpA - 1484 JpB) - 9910 JpA JpB + 5056 JpB^2)
+ 2 Ja(-936 JdB^3 + 12 JdC^2 JpA + 533 JpA^3 + 4 JdB^2(234 JdC + 67 JpA - 831 JpB) + 862 JpA^2 JpB + 812 JpA JpB^2
+ 192 JpB^3 - 2 JdB(5004 JdC^2 + 2554 JdC JpA + 2123 JpA^2 - 2890 JdC JpB - 649 JpA JpB + 1530 JpB^2)
- 2 JdC(1420 JpA^2 + 1731 JpA JpB + 1888 JpB^2))))Cos[k] + (2 JdC(144 JdB^2(9 JdB^2 + JdB JdC - 15 JdC^2)
+ 72 JdB(12 JdB^2 - JdB JdC + 30 JdC^2)JpA - 4(858 JdB^2 - 439 JdB JdC + 271 JdC^2)JpA^2 + 2(420 JdB
- 551 JdC)JpA^3 + 537 JpA^4) + 2 Ja^4(784 JdB + 126 JdC - 38 JpA - 207 JpB) - (1296 JdB^4 + 2688 JdB^3 JpA
+ 16 JdB JpA(79 JdC^2 - 124 JdC JpA + 75 JpA^2) + JpA^2(156 JdC^2 - 184 JdC JpA + 453 JpA^2) - 8 JdB^2(666 JdC^2
- 628 JdC JpA + 591 JpA^2))JpB + (-8 JdB^2(41 JdB + 301 JdC) + 4 JdB(693 JdB + 170 JdC)JpA + 6(-177 JdB
+ 89 JdC)JpA^2 + 31 JpA^3)JpB^2 + (380 JdB^2 - 532 JdB JpA + 35 JpA^2)JpB^3 + 288 J2^4(36 JdB - 74 JdC - 18 JpA
+ 37 JpB) - 16 J2^3(36(26 Ja JdB + 4 JdB^2 - 112 Ja JdC - 3 JdB JdC - 6 JdC^2) - 2(319 Ja + 315 JdC)JpA + 808 JpA^2
+ 9(224 Ja + 70 JdB + 221 JpA)JpB + 1350 JpB^2) + 4 J2^2(-8(Ja^2(627 JdB + 2135 JdC) + 9 Ja(16 JdB^2 - 29 JdB JdC
+ 6 JdC^2) + 9(8 JdB^3 + 169 JdB^2 JdC + 22 JdB JdC^2 + 40 JdC^3)) + 4(946 Ja^2 + 282 Ja JdB - 288 JdB^2
+ 1121 Ja JdC + 3510 JdB JdC + 378 JdC^2)JpA + 2(2006 Ja - 1696 JdB - 1797 JdC)JpA^2 + 360 JpA^3 + (8252 Ja^2
+ 6084 JdB^2 + 6624 JdC^2 + 36 JdB(64 JdC - 345 JpA) - 5064 JdC JpA + 1985 JpA^2 + Ja(9588 JdB + 4462 JpA))JpB
+ 2(3974 Ja - 1834 JdB - 2424 JdC + 673 JpA)JpB^2 - 184 JpB^3) + 2 Ja^3(2952 JdB^2 + 2472 JdC^2 + 4454 JdC JpA
- 132 JpA^2 - 1856 JdC JpB - 1783 JpA JpB + 726 JpB^2 + JdB(-4468 JdC - 2148 JpA + 2638 JpB)) - Ja^2(7488 JdB^3
+ 5312 JdC^3 + 936 JpA^3 + 8 JdC^2(381 JpA - 1012 JpB) - 1769 JpA^2 JpB + 106 JpA JpB^2 + 424 JpB^3
+ 4 JdB^2(4522 JdC - 2536 JpA + 379 JpB) + 4 JdB(1356 JdC^2 - 4458 JdC JpA + 604 JpA^2 + 760 JdC JpB
+ 1743 JpA JpB + 521 JpB^2) + JdC(4602 JpA^2 - 4280 JpA JpB + 4496 JpB^2)) + 2 Ja(-2016 JdB^4 + 16 JdB^3(81 JdC
+ 438 JpA - 37 JpB) + 4 JdB^2(252 JdC^2 + 396 JpA^2 - 237 JpA JpB - 106 JpB^2 + 2 JdC(844 JpA + 523 JpB))
+ 2 JdB(144 JdC^3 - 828 JpA^3 + 4 JdC^2(187 JpA - 274 JpB) + 540 JpA^2 JpB - 23 JpA JpB^2 + 362 JpB^3
```

```
- 2 JdC(1783 JpA^2 + 956 JpA JpB - 550 JpB^2)) - JpA(-1072 JdC^3 + 318 JpA^3 + 425 JpA^2 JpB - 113 JpA JpB^2
+ 238 JpB^3 + 8 JdC^2(-17 JpA + 81 JpB) + JdC(-1292 JpA^2 + 486 JpA JpB + 780 JpB^2))) + 4 J2(Ja^3(2984 JdB
+ 6416 JdC - 2654 JpA - 2920 JpB) + Ja(72 JdC(181 JdB^2 - 10 JdB JdC + 40 JdC^2) + 16(23 JdB^2 - 943 JdB JdC
+ 194 JdC^2)JpA + 2(2008 JdB + 1739 JdC)JpA^2 - 332 JpA^3 + (252 JdB^2 + 5200 JdB JdC - 6624 JdC^2
+ 7808 JdB JpA - 2992 JdC JpA - 1207 JpA^2)JpB + 4(607 JdB + 1212 JdC + 8 JpA)JpB^2 + 184 JpB^3) - Ja^2(5624JdB^2
+ 2920 JdC^2 + 8470 JdC JpA + 1326 JpA^2 - 2304 JdC JpB - 2965 JpA JpB + 3462 JpB^2 + JdB(-2868 JdC - 5096 JpA
+ 8282 JpB)) + 2(1008 JdB^4 + 36 JdB^3(16 JdC - 44 JpA - 9 JpB) - 6 JdB^2(132 JpA^2 + 42 JdC(JpA - JpB)
+ 158 JpA JpB + 33 JpB^2) - JdB(144 JdC^3 + 108 JpA^3 + 36 JdC^2(7 JpA - 2 JpB) - 263 JpA^2 JpB - 579 JpA JpB^2
+ 290 JpB^3 + 12 JdC(-25 JpA^2 + 158 JpA JpB + 61 JpB^2)) + JpA(72 JdC^3 + 387 JpA^3 + 406 JpA^2 JpB
- 318 JpA JpB^2 + 143 JpB^3 + 6 JdC^2(-55 JpA + 78 JpB) + JdC(-271 JpA^2 + 1677 JpA JpB + 118 JpB^2)))))Cos[2 k]
- (288 J2^4(2 JdB + 72 JdC - JpA - 36 JpB) - 63(2 JdB - JpA)^3(-2 JdC + JpB)^2 + Ja^4(-756 JdB - 2480 JdC + 622 JpA
+ 1240 JpB) - 16 J2^3(9(12(7 Ja JdB + JdB^2 + 12 Ja JdC - 2 JdB JdC - 4 JdC^2) - 4(8 Ja + 3 JdC)JpA - 75 JpA^2)
- 6(108 Ja - 18 JdB + 53 JpA)JpB + 100 JpB^2) + 2 Ja^3(-1236 JdB^2 - 368 JdC^2 - 532 JdC JpA + 11 JpA^2
+ 28 JdB(14 JdC + 5 JpA - 27 JpB) - 64 JdC JpB + 174 JpA JpB + 116 JpB^2) + 2 Ja(8 JdB^3(-306 JdC + 145 JpB)
+ 2 JdB JpA(40 JdC^2 + 726 JdC JpA - 44 JdC JpB - 559 JpA JpB - 56 JpB^2) + 4 JdB^2(-36 JdC^2 + 50 JdC JpA
+ 104 JdC JpB + 85 JpA JpB - 9 JpB^2) + JpA^2(28 JdC^2 - 470 JdC JpA - 92 JdC JpB + 329 JpA JpB + 73 JpB^2))
+ 2 Ja^2(1328 JdB^3 + 8 JdB^2(52 JdC - 213 JpA + 143 JpB) + JpA(1524 JdC^2 - 70 JpA^2 + 492 JpA JpB + 465 JpB^2
- 52 JdC(17 JpA + 33 JpB)) + 2 JdB(-1588 JdC^2 + 658 JpA^2 - 762 JpA JpB - 405 JpB^2 + 44 JdC(17 JpA + 37 JpB)))
+ 8 J2^2(720 JdB^3 + 72 JdB^2(12 JdC - 23 JpA - 6 JpB) + 4 Ja^2(595 JdB - 148 JdC - 165 JpA + 74 JpB)
- 6 JdB(540 JdC^2 + 144 JdC JpA - 202 JpA^2 - 540 JdC JpB - 168 JpA JpB + 131 JpB^2) + JpA(1620 JdC^2
+ 184 JdC JpA + 46 JpA^2 - 1772 JdC JpB - 380 JpA JpB + 469 JpB^2) + Ja(108 JdB^2 - 3(432 JdC^2 + 148 JdC JpA
+ 523 JpA^2) - 614 JpA JpB + 300 JpB^2 - 4 JdB(162 JdC + 219 JpA + 59 JpB))) - 4 J2(1224 JdB^3(-2 JdC + JpB)
+ 4 Ja^3(487 JdB - 620 JdC - 103 JpA + 310 JpB) - Ja^2(1460 JdB^2 + 40 JdB JdC + 1232 JdC^2 + 968 JdB JpA
+ 868 JdC JpA + 711 JpA^2 + 2(550 JdB + 32 JdC + 61 JpA)JpB - 316 JpB^2) + 2 JdB JpA(72 JdC^2 + 214 JdC JpA
+ 132 JdC JpB - 279 JpA JpB - 152 JpB^2) - 4 JdB^2(36 JdC^2 - 306 JdC JpA + 67 JpA JpB - 43 JpB^2) + JpA^2(-4 JdC^2
- 214 JdC JpA - 164 JdC JpB + 193 JpA JpB + 117 JpB^2) + 2 Ja(720 JdB^3 + JdB^2(-1496 JpA + 676 JpB)
+ JdB(-3240 JdC^2 + 956 JdC JpA + 1308 JpA^2 + 3280 JdC JpB - 578 JpA JpB - 806 JpB^2) + JpA(1588 JdC^2
- 510 JdC JpA - 42 JpA^2 - 1760 JdC JpB + 136 JpA JpB + 471 JpB^2))))Cos[3 k] - 2(2 J2 - Ja)(-4 J2(Ja^2(310 JdB
+ 945 JdC - 247 JpA) + 315 JdC(-2 JdB + JpA)^2 + 4 Ja(54 JdB^2 + 19 JdB JpA - 22 JpA^2)) + Ja(2 Ja(92 JdB^2
+ 92 JdB JpA - 67 JpA^2) + Ja^2(620 JdB + 630 JdC - 402 JpA - 315 JpB) + 315(-2 JdB + JpA)^2(2 JdC - JpB))
+ 630 J2(3 Ja^2 + (-2 JdB + JpA)^2)JpB + 72 J2^3(36 JdB - 70 JdC - 18 JpA + 35 JpB) - 4 J2^2(-216 JdB^2 + 50 JpA^2
+ Ja(324 JdB - 70(27 JdC + JpA) + 945 JpB)))Cos[4 k] + 315(-2 J2 + Ja)^4(2 JdB - JpA)Cos[5 k] - I(4752 J2^4(2 JdB - JpA)
+ 4(-36 JdB^2 JdC^2(20 JdC + 91 JpA) + JdC^2 JpA(756 JdC^2 + 820 JdC JpA - 89 JpA^2) + 72 JdB^3(17 JdC^2
- 32 JpA^2) - 2 JdB(756 JdC^4 + 605 JdC^2 JpA^2 - 864 JpA^4)) + Ja^4(474 JdB + 95 JpA - 1048 JpB)
+ 4 JdC(-72 JdB(21 JdB^2 - 5 JdB JdC + 30 JdC^2) + 4(775 JdB^2 - 208 JdB JdC + 750 JdC^2)JpA + 2(1097 JdB
+ 315 JdC)JpA^2 + 373 JpA^3)JpB + (-8 JdB(527 JdB^2 + 358 JdB JdC - 1338 JdC^2) + 4(2181 JdB^2 + 1376 JdB JdC
- 1626 JdC^2)JpA + 6(-1663 JdB + 330 JdC)JpA^2 + 583 JpA^3)JpB^2 + 2(940 JdB^2 + (300 JdC - 551 JpA)JpA
- 8 JdB(399 JdC + 124 JpA))JpB^3 + 3(274 JdB + 71 JpA)JpB^4 - 16 J2^3(9(4 JdB(80 Ja + 29 JdB - 26 JdC) - 34(5 Ja
+ 2 JdC)JpA + 3 JpA^2) + 4(131 Ja + 153 JdB + 151 JpA)JpB) + 2 Ja^3(708 JdB^2 + 3 JpA(944 JdC + 67 JpA)
- 4 JdB(1242 JdC + 387 JpA - 505 JpB) - 2(516 JdC + 593 JpA)JpB + 1516 JpB^2) + 2 Ja(2 JdC(-72 JdB(3 JdB^2
+ 16 JdB JdC + 9 JdC^2) + 4(2083 JdB^2 + 650 JdB JdC + 823 JdC^2)JpA - 2(3239 JdB + 822 JdC)JpA^2 - 753 JpA^3)
+ (8(787 JdB^3 + 518 JdB^2 JdC - 125 JdB JdC^2 - 960 JdC^3) - 4(3937 JdB^2 - 42 JdB JdC + 2113 JdC^2)JpA
+ 2(5683 JdB - 664 JdC)JpA^2 - 2277 JpA^3)JpB + 2(968 JdB^2 + 2786 JdB JdC + 576 JdC^2 - 1236 JdB JpA
+ 73 JdC JpA + 442 JpA^2)JpB^2 + 3(-1010 JdB + 864 JdC + 347 JpA)JpB^3 - 624 JpB^4) - 2 Ja^2(6120 JdB^3
- 933 JpA^3 + 4 JdB^2(294 JdC - 1707 JpA - 41 JpB) - 1323 JpA^2 JpB + 143 JpA JpB^2 - 536 JpB^3 - 4 JdC^2(717 JpA
+ 280 JpB) + JdB(-632 JdC^2 - 936 JdC JpA + 5718 JpA^2 + 6776 JdC JpB + 2408 JpA JpB + 46 JpB^2) + 2 JdC(243 JpA^2
- 1420 JpA JpB + 672 JpB^2)) + 8 J2^2(-72 JdB^3 + Ja^2(2158 JdB - 1321 JpA - 724 JpB) + 36 JdB^2(34 JdC - 65 JpA
- 11 JpB) + JpA(-1260 JdC^2 + 686 JdC JpA + 881 JpA^2 + 3788 JdC JpB + 161 JpA JpB - 977 JpB^2) + 2 JdB(1980 JdC^2
- 1271 JpA^2 - 458 JpA JpB - 129 JpB^2 - 72 JdC(10 JpA + 31 JpB)) + Ja(1044 JdB^2 + 1040 JdC JpA + 681 JpA^2
- 1432 JdC JpB - 738 JpA JpB + 996 JpB^2 + JdB(-2088 JdC + 876 JpA + 4732 JpB))) + 4 J2(2 JdC(72 JdB(11 JdB^2
+ 30 JdB JdC + JdC^2) - 36(19 JdB^2 + 58 JdB JdC - 9 JdC^2)JpA + 2(735 JdB + 304 JdC)JpA^2 - 167 JpA^3)
- (72 JdB(JdB - JdC)(3 JdB + 17 JdC) + 4(1095 JdB^2 + 1386 JdB JdC + 283 JdC^2)JpA + 2(515 JdB - 1496 JdC)JpA^2
- 2821 JpA^3)JpB + 2(124 JdB^2 - 722 JdB JdC - 480 JdB JpA + 367 JdC JpA - 205 JpA^2)JpB^2 + (622 JdB
- 349 JpA)JpB^3 + Ja^3(-568 JdB + 270 JpA + 1772 JpB) + Ja^2(-6372 JdB^2 - 9 JpA(508 JdC + 115 JpA)
+ JdB(7016 JdC + 5880 JpA - 7764 JpB) + 8(278 JdC + 467 JpA)JpB - 2392 JpB^2) + 2 Ja(-504 JdB^3 - 801 JpA^3
+ 8 JdC^2(49 JpA - 46 JpB) - 622 JpA^2 JpB + 707 JpA JpB^2 + 140 JpB^3 + 4 JdB^2(-54 JdC + 841 JpA + 393 JpB)
+ 2 JdB(-2232 JdC^2 + 910 JdC JpA + 1007 JpA^2 + 5414 JdC JpB + 269 JpA JpB - 385 JpB^2) - 2 JdC(304 JpA^2
+ 2673 JpA JpB + 120 JpB^2))))Sin[k] - I(15552 J2^4(2 JdB - JpA) + 2 JdC(144 JdB^2(9 JdB^2 + JdB JdC - 29 JdC^2)
+ 72 JdB(12 JdB^2 - JdB JdC + 58 JdC^2)JpA - 4(858 JdB^2 - 439 JdB JdC + 397 JdC^2)JpA^2 + 2(420 JdB
- 551 JdC)JpA^3 + 537 JpA^4) + (-144 JdB^2(9 JdB^2 - 79 JdC^2) - 16 JdB(168 JdB^2 + 314 JdB JdC + 457 JdC^2)JpA
+ 4(1182 JdB^2 + 496 JdB JdC + 339 JdC^2)JpA^2 + 8(-150 JdB + 23 JdC)JpA^3 - 453 JpA^4)JpB + (-8 JdB^2(41 JdB
+ 679 JdC) + 4 JdB(693 JdB + 926 JdC)JpA - 6(177 JdB + 37 JdC)JpA^2 + 31 JpA^3)JpB^2 + (884 JdB^2 - 1036 JdB JpA
```

```
+ 161 JpA^2)JpB^3 + Ja^4(-912 JdB + 796 JpA + 200 JpB) + 2 Ja^3(2584 JdB^2 + 2942 JdC JpA - 168 JpA^2
- 2 JdB(1842 JdC + 954 JpA - 787 JpB) - 1576 JdC JpB - 1435 JpA JpB + 748 JpB^2) - 16 J2^3(-288 JdB^2
+ 6 Ja(372 JdB - 245 JpA + 30 JpB) + JdB(-540 JdC + 414 JpB) + JpA(-414 JdC + 908 JpA + 1353 JpB))
- Ja^2(7488 JdB^3 + 936 JpA^3 - 2369 JpA^2 JpB - 1862 JpA JpB^2 + 704 JpB^3 + 4 JdB^2(5178 JdC - 2536 JpA
+ 115 JpB) - 8 JdC^2(191 JpA + 160 JpB) + 2 JdC(2661 JpA^2 + 908 JpA JpB - 384 JpB^2) + 4 JdB(940 JdC^2
- 5194 JdC JpA + 604 JpA^2 - 736 JdC JpB + 2199 JpA JpB + 1405 JpB^2)) + 4 J2^2(-576 JdB^3 - 36 JdB^2(418 JdC
+ 32 JpA - 209 JpB) + 8 Ja^2(-775 JdB + 409 JpA + 229 JpB) + 4 JdB(468 JdC^2 + 4230 JdC JpA - 848 JpA^2
- 288 JdC JpB - 3617 JpA JpB - 733 JpB^2) - 3 JpA(72 JdC^2 + 1406 JdC JpA - 120 JpA^2 + 344 JdC JpB - 867 JpA JpB
+ 58 JpB^2) + 2 Ja(-1872 JdB^2 + 1770 JdC JpA + 2154 JpA^2 - 1752 JdC JpB + 1003 JpA JpB + 836 JpB^2
+ 14 JdB(-18 JdC + 62 JpA + 279 JpB))) + 2 Ja(-2016 JdB^4 + 16 JdB^3(81 JdC + 438 JpA - 37 JpB) + 4 JdB^2(180 JdC^2
+ 396 JpA^2 - 237 JpA JpB - 92 JpB^2 + 2 JdC(844 JpA + 543 JpB)) - 2 JdB(2304 JdC^3 + 828 JpA^3 - 540 JpA^2 JpB
+ 115 JpA JpB^2 + 108 JpB^3 + JdC^2(-1164 JpA + 896 JpB) + JdC(3566 JpA^2 + 2000 JpA JpB - 2552 JpB^2))
+ JpA(3392 JdC^3 - 318 JpA^3 - 425 JpA^2 JpB + 259 JpA JpB^2 + 420 JpB^3 + 32 JdC^2(2 JpA + JpB)
+ 2 JdC(646 JpA^2 - 355 JpA JpB - 1508 JpB^2))) + 4 J2(Ja^3(5464 JdB - 3342 JpA - 836 JpB) + Ja^2(-4392 JdB^2
- 6270 JdC JpA - 1338 JpA^2 + JdB(2948 JdC + 4552 JpA - 6546 JpB) + 4240 JdC JpB + 3209 JpA JpB - 2040 JpB^2)
+ Ja(2 JpA(200 JdC^2 + 2091 JdC JpA - 166 JpA^2) + 4 JdB^2(3978 JdC + 92 JpA - 265 JpB) - (640 JdC^2
+ 680 JdC JpA + 1831 JpA^2)JpB - 128(3 JdC + 4 JpA)JpB^2 + 352 JpB^3 + 4 JdB(-180 JdC^2 - 4532 JdC JpA
+ 1004 JpA^2 + 344 JdC JpB + 2452 JpA JpB + 1117 JpB^2)) + 2(1008 JdB^4 + 36 JdB^3(16 JdC - 44 JpA - 9 JpB)
+ 2 JdB^2(72 JdC^2 - 396 JpA^2 - 474 JpA JpB - 97 JpB^2 + 18 JdC(-7 JpA + 3 JpB)) + JdB(2304 JdC^3 - 108 JpA^3
+ 263 JpA^2 JpB + 743 JpA JpB^2 - 76 JpB^3 - 36 JdC^2(7 JpA + 32 JpB) + 20 JdC(15 JpA^2 - 108 JpA JpB - 58 JpB^2))
+ JpA(-1152 JdC^3 + 387 JpA^3 + 406 JpA^2 JpB - 435 JpA JpB^2 - 50 JpB^3 + JdC^2(-502 JpA + 736 JpB)
+ JdC(-271 JpA^2 + 1981 JpA JpB + 676 JpB^2)))))Sin[2 k] + I(10368 J2^4(2 JdB - JpA) + 8 Ja^4(63 JdB - JpA - 46 JpB)
- 63(2 JdB - JpA)^3(-2 JdC + JpB)^2 + 16 J2^3(9(-4 JdB(91 Ja + 3 JdB - 6 JdC) + 4(43 Ja + 3 JdC)JpA + 75 JpA^2)
+ 2(92 Ja - 54 JdB + 159 JpA)JpB) + 2 Ja^3(-1236 JdB^2 + 11 JpA^2 + 28 JdB(14 JdC + 5 JpA - 27 JpB) + 174 JpA JpB
- 152 JpB^2 + 76 JdC(-7 JpA + 4 JpB)) + 2 Ja(8 JdB^3(-306 JdC + 145 JpB) + 2 JdB JpA(40 JdC^2 + 726 JdC JpA
- 44 JdC JpB - 559 JpA JpB - 56 JpB^2) + 4 JdB^2(-36 JdC^2 + 50 JdC JpA + 104 JdC JpB + 85 JpA JpB - 9 JpB^2)
+ JpA^2(28 JdC^2 - 470 JdC JpA - 92 JdC JpB + 329 JpA JpB + 73 JpB^2)) + 2 Ja^2(1328 JdB^3 + 8 JdB^2(52 JdC
- 213 JpA + 143 JpB) - JpA(996 JdC^2 + 884 JdC JpA + 70 JpA^2 - 804 JdC JpB - 492 JpA JpB + 165 JpB^2)
+ 2 JdB(932 JdC^2 + 748 JdC JpA + 658 JpA^2 - 892 JdC JpB - 762 JpA JpB + 225 JpB^2)) + 8 J2^2(720 JdB^3
+ 72 JdB^2(12 JdC - 23 JpA - 6 JpB) + JpA(-900 JdC^2 + 184 JdC JpA + 46 JpA^2 + 748 JdC JpB - 380 JpA JpB
- 161 JpB^2) + 6 JdB(300 JdC^2 - 144 JdC JpA + 202 JpA^2 - 300 JdC JpB + 168 JpA JpB + 79 JpB^2) + Ja(108 JdB^2
- 444 JdC JpA - 1569 JpA^2 + 304 JdC JpB - 614 JpA JpB - 152 JpB^2 - 4 JdB(162 JdC + 219 JpA + 59 JpB))
+ Ja^2(6160 JdB - 6(425 JpA + 92 JpB))) - 4 J2(4 Ja^3(1117 JdB - 418 JpA - 138 JpB) + 1224 JdB^3(-2 JdC + JpB)
+ 2 JdB JpA(72 JdC^2 + 214 JdC JpA + 132 JdC JpB - 279 JpA JpB - 152 JpB^2) - 4 JdB^2(36 JdC^2 - 306 JdC JpA
+ 67 JpA JpB - 43 JpB^2) + JpA^2(-4 JdC^2 - 214 JdC JpA - 164 JdC JpB + 193 JpA JpB + 117 JpB^2) - Ja^2(1460 JdB^2
+ 40 JdB JdC + 968 JdB JpA + 868 JdC JpA + 711 JpA^2 + 2(550 JdB - 304 JdC + 61 JpA)JpB + 304 JpB^2)
+ 2 Ja(720 JdB^3 + JdB^2(-1496 JpA + 676 JpB) - JpA(932 JdC^2 + 510 JdC JpA + 42 JpA^2 - 760 JdC JpB
- 136 JpA JpB + 159 JpB^2) + 2 JdB(900 JdC^2 + 478 JdC JpA + 654 JpA^2 - 880 JdC JpB - 289 JpA JpB
+ 227 JpB^2))))Sin[3 k] + 2 I(2 J2 - Ja)(1296 J2^3(2 JdB - JpA) + 8 J2^2(54 JdB(-3 Ja + 2 JdB) + 35 Ja JpA - 25 JpA^2)
+ 4 J2(-315 JdC(-2 JdB + JpA)^2 + Ja^2(-310 JdB + 247 JpA) - 4 Ja(54 JdB^2 + 19 JdB JpA - 22 JpA^2))
+ Ja(Ja^2(620 JdB - 402 JpA) + 2 Ja(92 JdB^2 + 92 JdB JpA - 67 JpA^2) + 315(-2 JdB + JpA)^2(2 JdC - JpB))
+ 630 J2(-2 JdB + JpA)^2 JpB)Sin[4 k] - 315 I(-2 J2 + Ja)^4(2 JdB - JpA)Sin[5 k])
```

The dispersion relation

$$\begin{aligned}\omega_{\mathrm{o5}\,\pm}(k) =& 1.086 + 0.16\cos(k) - 0.035\cos(2k) - 0.0012\cos(3k) - 0.0027\cos(4k) + 0.00015\cos(5k) \\ &\pm \Big(0.041 - 0.00087\cos(k) - 0.023\cos(2k) + 0.0044\cos(3k) + 0.00077\cos(4k) \\ &+ 0.00019\cos(5k) - 0.00012\cos(6k) - 2.27\cdot 10^{-6}\cos(7k) + 1.04\cdot 10^{-6}\cos(8k) \\ &+ 7.15\cdot 10^{-7}\cos(9k)\Big)^{1/2}\end{aligned} \tag{C.5}$$

Bibliography

[1] P. W. Anderson. "Resonating valence bonds: A new kind of insulator?" In: *Materials Research Bulletin* 8.2 (1973), pp. 153 –160.

[2] P. W. Anderson et al. "Resonating valence-bond theory of phase transitions and superconductivity in La_2CuO_4-based compounds". In: *Phys. Rev. Lett.* 58 (26 1987), pp. 2790–2793.

[3] G. Toulouse. "Theory of the frustration effect in spin glasses I". In: *Commun Phys* 2 (1977), p. 115.

[4] C. K. Majumdar and D. K. Ghosh. "On Next Nearest Neighbor Interaction in Linear Chain. I". In: *Journal of Mathematical Physics* 10.8 (1969), pp. 1388–1398. DOI: 10.1063/1.1664978. eprint: https://doi.org/10.1063/1.1664978. URL: https://doi.org/10.1063/1.1664978.

[5] C. K. Majumdar and D. K. Ghosh. "On Next Nearest Neighbor Interaction in Linear Chain. II". In: *Journal of Mathematical Physics* 10.8 (1969), pp. 1399–1402. DOI: 10.1063/1.1664979. eprint: http://dx.doi.org/10.1063/1.1664979. URL: http://dx.doi.org/10.1063/1.1664979.

[6] B. S. Shastry and B. Sutherland. "Excitation Spectrum of a Dimerized Next-Neighbor Antiferromagnetic Chain". In: *Phys. Rev. Lett.* 47 (13 1981), pp. 964–967. DOI: 10.1103/PhysRevLett.47.964. URL: https://link.aps.org/doi/10.1103/PhysRevLett.47.964.

[7] M. P. Gelfand. "Series investigations of magnetically disordered ground states in two-dimensional frustrated quantum antiferromagnets". In: *Phys. Rev. B* 42 (13 1990), pp. 8206–8213. DOI: 10.1103/PhysRevB.42.8206. URL: http://link.aps.org/doi/10.1103/PhysRevB.42.8206.

[8] M. P. Gelfand. "Linked-tetrahedra spin chain: Exact ground state and excitations". In: *Phys. Rev. B* 43 (10 1991), pp. 8644–8645. DOI: 10.1103/PhysRevB.43.8644. URL: https://link.aps.org/doi/10.1103/PhysRevB.43.8644.

[9] T. Vekua and A. Honecker. "Quantum dimer phases in a frustrated spin ladder: Effective field theory approach and exact diagonalization". In: *Phys. Rev. B* 73 (21 2006), p. 214427. DOI: 10.1103/PhysRevB.73.214427. URL: https://link.aps.org/doi/10.1103/PhysRevB.73.214427.

[10] M. Azuma et al. "Observation of a Spin Gap in $SrCu_2O_3$ Comprising Spin-1/2 Quasi-1D Two-Leg Ladders". In: *Phys. Rev. Lett.* 73 (25 1994), pp. 3463–3466. DOI: 10.1103/PhysRevLett.73.3463. URL: http://link.aps.org/doi/10.1103/PhysRevLett.73.3463.

[11] H. Kageyama et al. "Exact Dimer Ground State and Quantized Magnetization Plateaus in the Two-Dimensional Spin System $SrCu_2(BO_3)_2$". In: *Phys. Rev. Lett.* 82 (15 1999), pp. 3168–3171. DOI: 10.1103/PhysRevLett.82.3168. URL: http://link.aps.org/doi/10.1103/PhysRevLett.82.3168.

[12] A. A. Tsirlin et al. "Bridging frustrated-spin-chain and spin-ladder physics: Quasi-one-dimensional magnetism of $BiCu_2PO_6$". In: *Phys. Rev. B* 82 (14 2010), p. 144426. DOI: 10.1103/PhysRevB.82.144426. URL: https://link.aps.org/doi/10.1103/PhysRevB.82.144426.

[13] M. Sun et al. "$Li_2Cu_2O(SO_4)_2$: a Possible Electrode for Sustainable Li-Based Batteries Showing a 4.7 V Redox Activity vs Li^+/Li^0". In: *Chem. Mater.* 27.8 (2015), pp. 3077–3087. DOI: 10.1021/acs.chemmater.5b00588. URL: https://doi.org/10.1021/acs.chemmater.5b00588.

[14] G. Rousse et al. "Low-temperature structural transition in the quasi-one-dimensional spin-$\frac{1}{2}$ compound $Li_2Cu_2O(SO_4)_2$". In: *Phys. Rev. B* 95 (14 2017), p. 144103. DOI: 10.1103/PhysRevB.95.144103. URL: https://link.aps.org/doi/10.1103/PhysRevB.95.144103.

[15] O. Vaccarelli et al. "Magnetic dimerization in the frustrated spin ladder $Li_2Cu_2O(SO_4)_2$". In: *Phys. Rev. B* 96 (18 2017), p. 180406. DOI: 10.1103/PhysRevB.96.180406. URL: https://link.aps.org/doi/10.1103/PhysRevB.96.180406.

[16] F. Hund. "Zur Deutung der Molekelspektren. IV". In: *Zeitschrift für Physik* 51.11 (1928), pp. 759–795. ISSN: 0044-3328. DOI: 10.1007/BF01400239. URL: https://doi.org/10.1007/BF01400239.

[17] S. S. Zumdahl and D. J. DeCoste. *Chemical principles*. Brooks/Cole Cengage Learning, 2013. ISBN: 1111580650 9781111580650.

[18] W. Heisenberg and P. Jordan. "Anwendung der Quantenmechanik auf das Problem der anomalen Zeemaneffekte". In: *Zeitschrift für Physik* 37.4 (1926), pp. 263–277. ISSN: 0044-3328. DOI: 10.1007/BF01397100. URL: https://doi.org/10.1007/BF01397100.

[19] P. A. M. Dirac. "Quantum mechanics and a preliminary investigation of the hydrogen atom". In: *Proceedings of the Royal Society of London A: Mathematical, Physical and Engineering Sciences* 110.755 (1926), pp. 561–579. ISSN: 0950-1207. DOI: 10.1098/rspa.1926.0034. URL: http://rspa.royalsocietypublishing.org/content/110/755/561.

[20] H. Eskes and J. H. Jefferson. "Superexchange in the cuprates". In: *Phys. Rev. B* 48 (13 1993), pp. 9788–9798. DOI: 10.1103/PhysRevB.48.9788. URL: https://link.aps.org/doi/10.1103/PhysRevB.48.9788.

[21] P. W. Anderson. "Antiferromagnetism. Theory of Superexchange Interaction". In: *Phys. Rev.* 79 (2 1950), pp. 350–356. DOI: 10.1103/PhysRev.79.350. URL: https://link.aps.org/doi/10.1103/PhysRev.79.350.

[22] J. Kanamori. "Theory of the Magnetic Properties of Ferrous and Cobaltous Oxides, I". In: *Progress of Theoretical Physics* 17.2 (1957), pp. 177–196. DOI: 10.1143/PTP.17.177. eprint: /oup/backfile/content_public/journal/ptp/17/2/10.1143/ptp.17.177/2/17-2-177.pdf. URL: http://dx.doi.org/10.1143/PTP.17.177.

[23] J. B. Goodenough. "An interpretation of the magnetic properties of the perovskite-type mixed crystals $La_{1-x}Sr_xCoO_{3-\lambda}$". In: *Journal of Physics and chemistry of Solids* 6.2-3 (1958), pp. 287–297. ISSN: 0022-3697. DOI: https://doi.org/10.1016/0022-3697(58)90107-0. URL: http://www.sciencedirect.com/science/article/pii/0022369758901070.

[24] V. H. Crawford et al. "Relation between the singlet-triplet splitting and the copper-oxygen-copper bridge angle in hydroxo-bridged copper dimers". In: *Inorganic Chemistry* 15.9 (1976), pp. 2107–2110.

[25] M. Reynaud et al. "Marinite $Li_2M(SO_4)_2$ (M = Co, Fe, Mn) and $Li_1Fe(SO_4)_2$: Model Compounds for Super-Super-Exchange Magnetic Interactions". In: *Inorganic Chemistry* 52.18 (2013). PMID: 23978225, pp. 10456–10466. DOI: 10.1021/ic401280e. eprint: https://doi.org/10.1021/ic401280e. URL: https://doi.org/10.1021/ic401280e.

[26] M. L. Néel. "Propriétés magnétiques du manganèse et du chrome en solution solide étendue". In: *J. Phys. Radium* 3.4 (1932), pp. 160–171. DOI: 10.1051/jphysrad:0193200304016000. URL: https://doi.org/10.1051/jphysrad:0193200304016000.

[27] M. L. Néel. "Propriétés magnétiques des ferrites ; ferrimagnétisme et antiferromagnétisme". In: *Ann. Phys.* 12.3 (1948), pp. 137–198. DOI: 10.1051/anphys/194812030137. URL: https://doi.org/10.1051/anphys/194812030137.

[28] N. D. Mermin and H. Wagner. "Absence of Ferromagnetism or Antiferromagnetism in One- or Two-Dimensional Isotropic Heisenberg Models". In: *Phys. Rev. Lett.* 17 (22 1966), pp. 1133–1136. DOI: 10.1103/PhysRevLett.17.1133. URL: https://link.aps.org/doi/10.1103/PhysRevLett.17.1133.

[29] Y. Endoh et al. "Dynamics of an $S = \frac{1}{2}$, One-Dimensional Heisenberg Antiferromagnet". In: *Phys. Rev. Lett.* 32 (4 1974), pp. 170–173. DOI: 10.1103/PhysRevLett.32.170. URL: https://link.aps.org/doi/10.1103/PhysRevLett.32.170.

[30] J. S. Miller. *Extended linear chain compounds*. Vol. 3. Springer Science & Business Media, 2012.

[31] H. Bethe. "Zur Theorie der Metalle". In: *Zeitschrift für Physik* 71.3 (1931), pp. 205–226. ISSN: 0044-3328. DOI: 10.1007/BF01341708. URL: https://doi.org/10.1007/BF01341708.

[32] J. des Cloizeaux and J. J. Pearson. "Spin-Wave Spectrum of the Antiferromagnetic Linear Chain". In: *Phys. Rev.* 128 (5 1962), pp. 2131–2135. DOI: 10.1103/PhysRev.128.2131. URL: https://link.aps.org/doi/10.1103/PhysRev.128.2131.

[33] L. D. Faddeev and L. A. Takhtajan. "What is the spin of a spin wave?" In: *Phys. Lett.* 85 (1981), p. 375.

[34] J. C. Bonner et al. "Susceptibility calculations for alternating antiferromagnetic chains". In: *Journal of Applied Physics* 50.B3 (1979), pp. 1810–1812. DOI: 10.1063/1.327177. eprint: https://doi.org/10.1063/1.327177. URL: https://doi.org/10.1063/1.327177.

[35] M. Hase, I. Terasaki, and K. Uchinokura. "Observation of the spin-Peierls transition in linear Cu^{2+} (spin-1/2) chains in an inorganic compound $CuGeO_3$". In: *Phys. Rev. Lett.* 70 (23 1993), pp. 3651–3654. DOI: 10.1103/PhysRevLett.70.3651. URL: https://link.aps.org/doi/10.1103/PhysRevLett.70.3651.

[36] A. Seidel et al. "$S = \frac{1}{2}$ chains and spin-Peierls transition in TiOCl". In: *Phys. Rev. B* 67 (2 2003), p. 020405. DOI: 10.1103/PhysRevB.67.020405. URL: https://link.aps.org/doi/10.1103/PhysRevB.67.020405.

[37] G. S. Uhrig and M. Gruninger. "Uberblick-Das Wechselspiel magnetischer Anregungen in Spinflussigkeiten". In: *Physik Journal* 2.1 (2003), pp. 41–47.

[38] G. S. Uhrig and H. J. Schulz. "Magnetic excitation spectrum of dimerized antiferromagnetic chains". In: *Phys. Rev. B* 54 (14 1996), R9624–R9627. DOI: 10.1103/PhysRevB.54.R9624. URL: https://link.aps.org/doi/10.1103/PhysRevB.54.R9624.

[39] K. P. Schmidt and G. S. Uhrig. "Excitations in One-Dimensional $S = \frac{1}{2}$ Quantum Antiferromagnets". In: *Phys. Rev. Lett.* 90 (22 2003), p. 227204. DOI: 10.1103/PhysRevLett.90.227204. URL: https://link.aps.org/doi/10.1103/PhysRevLett.90.227204.

[40] E. Dagotto and T. M. Rice. "Surprises on the Way from One- to Two-Dimensional Quantum Magnets: The Ladder Materials". In: *Science* 271.5249 (1996), pp. 618–623. ISSN: 0036-8075. DOI: 10.1126/science.271.5249.618. eprint: http://science.sciencemag.org/content/271/5249/618.full.pdf. URL: http://science.sciencemag.org/content/271/5249/618.

[41] D. G. Shelton, A. A. Nersesyan, and A. M. Tsvelik. "Antiferromagnetic spin ladders: Crossover between spin S=1/2 and S=1 chains". In: *Phys. Rev. B* 53 (13 1996), pp. 8521–8532. DOI: 10.1103/PhysRevB.53.8521. URL: https://link.aps.org/doi/10.1103/PhysRevB.53.8521.

[42] T. Barnes et al. "Excitation spectrum of Heisenberg spin ladders". In: *Phys. Rev. B* 47 (6 1993), pp. 3196–3203. DOI: 10.1103/PhysRevB.47.3196. URL: https://link.aps.org/doi/10.1103/PhysRevB.47.3196.

[43] S. Gopalan, T. M. Rice, and M. Sigrist. "Spin ladders with spin gaps: A description of a class of cuprates". In: *Phys. Rev. B* 49 (13 1994), pp. 8901–8910. DOI: 10.1103/PhysRevB.49.8901. URL: https://link.aps.org/doi/10.1103/PhysRevB.49.8901.

[44] S. R. White, R. M. Noack, and D. J. Scalapino. "Resonating Valence Bond Theory of Coupled Heisenberg Chains". In: *Phys. Rev. Lett.* 73 (6 1994), pp. 886–889. DOI: 10.1103/PhysRevLett.73.886. URL: https://link.aps.org/doi/10.1103/PhysRevLett.73.886.

[45] N. Hatano and Y. Nishiyama. "Scaling theory of antiferromagnetic Heisenberg ladder models". In: *Journal of Physics A: Mathematical and General* 28.14 (1995), p. 3911. URL: http://stacks.iop.org/0305-4470/28/i=14/a=012.

[46] E. Dagotto. "Experiments on ladders reveal a complex interplay between a spin-gapped normal state and superconductivity". In: *Reports on Progress in Physics* 62.11 (1999), p. 1525. URL: http://stacks.iop.org/0034-4885/62/i=11/a=202.

[47] D. Poilblanc, H. Tsunetsugu, and T. M. Rice. "Spin gaps in coupled t-J ladders". In: *Phys. Rev. B* 50 (9 1994), pp. 6511–6514. DOI: 10.1103/PhysRevB.50.6511. URL: https://link.aps.org/doi/10.1103/PhysRevB.50.6511.

[48] M. Reigrotzki, H. Tsunetsugu, and T. M. Rice. "Strong-coupling expansions for antiferromagnetic Heisenberg spin-one-half ladders". In: *Journal of Physics: Condensed Matter* 6.43 (1994), p. 9235. URL: http://stacks.iop.org/0953-8984/6/i=43/a=021.

[49] A. G. Rojo. "Absence of gap for infinite half-integer spin ladders with an odd number of legs". In: *Phys. Rev. B* 53 (14 1996), pp. 9172–9174. DOI: 10.1103/PhysRevB.53.9172. URL: https://link.aps.org/doi/10.1103/PhysRevB.53.9172.

[50] Z. Hiroi et al. "A new homologous series $Sr_nCu_{n+1}O_{2n+1}$ found in the SrO – CuO system treated under high pressure". In: *Journal of Solid State Chemistry* 95.1 (1991), pp. 230–238. ISSN: 0022-4596. DOI: https://doi.org/10.1016/0022-4596(91)90394-W. URL: Phttp://www.sciencedirect.com/science/article/pii/002245969190394W.

[51] T. M. Rice, S. Gopalan, and M. Sigrist. "Superconductivity, Spin Gaps and Luttinger Liquids in a Class of Cuprates". In: *EPL (Europhysics Letters)* 23.6 (1993), p. 445. URL: http://stacks.iop.org/0295-5075/23/i=6/a=011.

[52] M. Troyer, H. Tsunetsugu, and D. Würtz. "Thermodynamics and spin gap of the Heisenberg ladder calculated by the look-ahead Lanczos algorithm". In: *Phys. Rev. B* 50 (18 1994), pp. 13515–13527. DOI: 10.1103/PhysRevB.50.13515. URL: https://link.aps.org/doi/10.1103/PhysRevB.50.13515.

[53] K. Kojima et al. "Magnetic Behavior of the 2-Leg and 3-Leg Spin Ladder Cuprates $Sr_{n-1}Cu_{n+1}O_{2n}$". In: *Phys. Rev. Lett.* 74 (14 1995), pp. 2812–2815. DOI: 10.1103/PhysRevLett.74.2812. URL: https://link.aps.org/doi/10.1103/PhysRevLett.74.2812.

[54] M. Matsuda and K. Katsumata. "Observation of a dimerized state in the S=1/2 quasi-one-dimensional antiferromagnet $Sr_{14}Cu_{24}O_{41}$". In: *Phys. Rev. B* 53 (18 1996), pp. 12201–12205. DOI: 10.1103/PhysRevB.53.12201. URL: https://link.aps.org/doi/10.1103/PhysRevB.53.12201.

[55] R. S. Eccleston et al. "Spin Dynamics of the Spin-Ladder Dimer-Chain Material $Sr_{14}Cu_{24}O_{41}$". In: *Phys. Rev. Lett.* 81 (8 1998), pp. 1702–1705. DOI: 10.1103/PhysRevLett.81.1702. URL: https://link.aps.org/doi/10.1103/PhysRevLett.81.1702.

[56] C. Lacroix, P. Mendels, and F. Mila. *Introduction to Frustrated Magnetism: Materials, Experiments, Theory*. Vol. 164. Springer Series in Solid-State Sciences. Springer Berlin Heidelberg, 2011. ISBN: 978-3-642-10589-0. URL: https://books.google.com.au/books?id=F9SYngEACAAJ.

[57] F. D. M. Haldane. "Spontaneous dimerization in the $S = \frac{1}{2}$ Heisenberg antiferromagnetic chain with competing interactions". In: *Phys. Rev. B* 25 (7 1982), pp. 4925–4928. DOI: 10.1103/PhysRevB.25.4925. URL: https://link.aps.org/doi/10.1103/PhysRevB.25.4925.

[58] P. M. Van den Broek. "Exact value of the ground state energy of the linear antiferromagnetic Heisenberg chain with nearest and next-nearest neighbour interactions". In: *Physics Letters A* 77.4 (1980), pp. 261 –262. ISSN: 0375-9601. DOI: https://doi.org/10.1016/0375-9601(80)90662-3. URL: http://www.sciencedirect.com/science/article/pii/0375960180906623.

[59] I. Affleck et al. "Valence bond ground states in isotropic quantum antiferromagnets". In: *Commun. Math. Phys.* 115 (1988), p. 477.

[60] K. Okamoto and K. Nomura. "Fluid-dimer critical point in $S = \frac{1}{2}$ antiferromagnetic Heisenberg chain with next nearest neighbor interactions". In: *Physics Letters A* 169.6 (1992), pp. 433–437. ISSN: 0375-9601. DOI: https://doi.org/10.1016/0375-9601(92)90823-5. URL: http://www.sciencedirect.com/science/article/pii/0375960192908235.

[61] R. Chitra et al. "Density-matrix renormalization-group studies of the spin-1/2 Heisenberg system with dimerization and frustration". In: *Phys. Rev. B* 52 (9 1995), pp. 6581–6587. DOI: 10.1103/PhysRevB.52.6581. URL: https://link.aps.org/doi/10.1103/PhysRevB.52.6581.

[62] S. R. White and I. Affleck. "Dimerization and incommensurate spiral spin correlations in the zigzag spin chain: Analogies to the Kondo lattice". In: *Phys. Rev. B* 54 (14 1996), pp. 9862–9869. DOI: 10.1103/PhysRevB.54.9862. URL: https://link.aps.org/doi/10.1103/PhysRevB.54.9862.

[63] Y. Xian. "Rigorous results on a first-order phase transition in antiferromagnetic spin-1/2 coupled chains". In: *Phys. Rev. B* 52 (17 1995), pp. 12485–12488. DOI: 10.1103/PhysRevB.52.12485. URL: https://link.aps.org/doi/10.1103/PhysRevB.52.12485.

[64] F. D. M. Haldane. "Nonlinear Field Theory of Large-Spin Heisenberg Antiferromagnets: Semiclassically Quantized Solitons of the One-Dimensional Easy-Axis Néel State". In: *Phys. Rev. Lett.* 50 (15 1983), pp. 1153–1156. DOI: 10.1103/PhysRevLett.50.1153. URL: https://link.aps.org/doi/10.1103/PhysRevLett.50.1153.

[65] Z. Weihong, V. Kotov, and J. Oitmaa. "Two-chain spin ladder with frustrating second-neighbor interactions". In: *Phys. Rev. B* 57 (18 1998), pp. 11439–11445. DOI: 10.1103/PhysRevB.57.11439. URL: https://link.aps.org/doi/10.1103/PhysRevB.57.11439.

[66] E. H. Kim, Ö. Legeza, and J. Sólyom. "Topological order, dimerization, and spinon deconfinement in frustrated spin ladders". In: *Phys. Rev. B* 77 (20 2008), p. 205121. DOI: 10.1103/PhysRevB.77.205121. URL: https://link.aps.org/doi/10.1103/PhysRevB.77.205121.

[67] S. Wessel et al. "Efficient Quantum Monte Carlo simulations of highly frustrated magnets: the frustrated spin-1/2 ladder". In: *SciPost Phys.* 3 (1 2017), p. 005. DOI: 10.21468/SciPostPhys.3.1.005. URL: https://scipost.org/10.21468/SciPostPhys.3.1.005.

[68] O. A. Starykh and L. Balents. "Dimerized Phase and Transitions in a Spatially Anisotropic Square Lattice Antiferromagnet". In: *Phys. Rev. Lett.* 93 (12 2004), p. 127202. DOI: 10.1103/PhysRevLett.93.127202. URL: https://link.aps.org/doi/10.1103/PhysRevLett.93.127202.

[69] B. W. Ramakko and M. Azzouz. "Effect of temperature on quantum criticality in the frustrated two-leg Heisenberg ladder". In: *Phys. Rev. B* 76 (6 2007), p. 064419. DOI: 10.1103/PhysRevB.76.064419. URL: https://link.aps.org/doi/10.1103/PhysRevB.76.064419.

[70] G. H. Liu, H. L. Wang, and G. S. Tian. "Existence of dimerized phases in frustrated spin ladder models". In: *Phys. Rev. B* 77 (21 2008), p. 214418. DOI: 10.1103/PhysRevB.77.214418. URL: https://link.aps.org/doi/10.1103/PhysRevB.77.214418.

[71] W. Rui, L. Guang-Hua, and T. Guang-Shan. "Quantum Phase Transitions and Dimerized Phases in Frustrated Spin Ladder". In: *Communications in Theoretical Physics* 55.6 (2011), p. 1102. URL: http://stacks.iop.org/0253-6102/55/i=6/a=26.

[72] Y. C. Li and H. Q. Lin. "Quantum phase diagram of the frustrated spin ladder with next-nearest-neighbor interactions". In: *New Journal of Physics* 14.6 (2012), p. 063019. URL: http://stacks.iop.org/1367-2630/14/i=6/a=063019.

[73] B. Koteswararao et al. "Spin-gap behavior in the two-leg spin-ladder $BiCu_2PO_6$". In: *Phys. Rev. B* 76 (5 2007), p. 052402. DOI: 10.1103/PhysRevB.76.052402. URL: https://link.aps.org/doi/10.1103/PhysRevB.76.052402.

[74] O. Mentré et al. "Incommensurate spin correlation driven by frustration in $BiCu_2PO_6$". In: *Phys. Rev. B* 80 (18 2009), p. 180413. DOI: 10.1103/PhysRevB.80.180413. URL: https://link.aps.org/doi/10.1103/PhysRevB.80.180413.

[75] K. W. Plumb et al. "Incommensurate dynamic correlations in the quasi-two-dimensional spin liquid $BiCu_2PO_6$". In: *Phys. Rev. B* 88 (2 2013), p. 024402. DOI: 10.1103/PhysRevB.88.024402. URL: https://link.aps.org/doi/10.1103/PhysRevB.88.024402.

[76] K. W. Plumb et al. "Quasiparticle-continuum level repulsion in a quantum magnet". In: *Nat. Phys.* 12 (2016), pp. 224–229. DOI: 10.1038/nphys3566.

[77] E. K. U. Gross and R. M. Dreizler. *Density functional theory: an approach to the quantum many-body problem*. 1990.

[78] R. G. Parr and W. Yang. *Density-Functional Theory of Atoms and Molecules*. International Series of Monographs on Chemistry. Oxford University Press, USA, 1994. ISBN: 9780195092769. URL: https://books.google.fr/books?id=mxiOngEACAAJ.

[79] R. M. Martin. *Electronic Structure: Basic Theory and Practical Methods*. Cambridge University Press, 2004. DOI: 10.1017/CBO9780511805769.

[80] E. Engel and R. M. Dreizler. *Density functional theory: an advanced course*. Springer Science & Business Media, 2011.

[81] W. Yang and P. W. Ayers. "Density-functional theory". In: *Computational Medicinal Chemistry for Drug Discovery*. CRC Press, 2003, pp. 103–132.

[82] A. D. Becke. "A new mixing of Hartree–Fock and local density-functional theories". In: *The Journal of chemical physics* 98.2 (1993), pp. 1372–1377.

[83] E. Runge and E. K. U. Gross. "Density-Functional Theory for Time-Dependent Systems". In: *Phys. Rev. Lett.* 52 (12 1984), pp. 997–1000. DOI: 10.1103/PhysRevLett.52.997. URL: https://link.aps.org/doi/10.1103/PhysRevLett.52.997.

[84] R. Car and M. Parrinello. "Unified Approach for Molecular Dynamics and Density-Functional Theory". In: *Phys. Rev. Lett.* 55 (22 1985), pp. 2471–2474. DOI: 10.1103/PhysRevLett.55.2471. URL: https://link.aps.org/doi/10.1103/PhysRevLett.55.2471.

[85] P. Hohenberg and W. Kohn. "Inhomogeneous Electron Gas". In: *Phys. Rev.* 136 (3B 1964), B864–B871. DOI: 10.1103/PhysRev.136.B864. URL: https://link.aps.org/doi/10.1103/PhysRev.136.B864.

[86] W. Kohn and L. J. Sham. "Self-Consistent Equations Including Exchange and Correlation Effects". In: *Phys. Rev.* 140 (4A 1965), A1133–A1138. DOI: 10.1103/PhysRev.140.A1133. URL: https://link.aps.org/doi/10.1103/PhysRev.140.A1133.

[87] J. C. Slater. "A Simplification of the Hartree-Fock Method". In: *Phys. Rev.* 81 (3 1951), pp. 385–390. DOI: 10.1103/PhysRev.81.385. URL: https://link.aps.org/doi/10.1103/PhysRev.81.385.

[88] P. A. M. Dirac. "Note on Exchange Phenomena in the Thomas Atom". In: *Mathematical Proceedings of the Cambridge Philosophical Society* 26.3 (1930), 376–385. DOI: 10.1017/S0305004100016108.

[89] M. Gell-Mann and K. A. Brueckner. "Correlation Energy of an Electron Gas at High Density". In: *Phys. Rev.* 106 (2 1957), pp. 364–368. DOI: 10.1103/PhysRev.106.364. URL: https://link.aps.org/doi/10.1103/PhysRev.106.364.

[90] D. M. Ceperley and B. J. Alder. "Ground State of the Electron Gas by a Stochastic Method". In: *Phys. Rev. Lett.* 45 (7 1980), pp. 566–569. DOI: 10.1103/PhysRevLett.45.566. URL: https://link.aps.org/doi/10.1103/PhysRevLett.45.566.

[91] J. P. Perdew and A. Zunger. "Self-interaction correction to density-functional approximations for many-electron systems". In: *Phys. Rev. B* 23 (10 1981), pp. 5048–5079. DOI: 10.1103/PhysRevB.23.5048. URL: https://link.aps.org/doi/10.1103/PhysRevB.23.5048.

[92] J. P. Perdew. "Density-functional approximation for the correlation energy of the inhomogeneous electron gas". In: *Phys. Rev. B* 33 (12 1986), pp. 8822–8824. DOI: 10.1103/PhysRevB.33.8822. URL: https://link.aps.org/doi/10.1103/PhysRevB.33.8822.

[93] R. O. Jones and O. Gunnarsson. "The density functional formalism, its applications and prospects". In: *Rev. Mod. Phys.* 61 (3 1989), pp. 689–746. DOI: 10.1103/RevModPhys.61.689. URL: https://link.aps.org/doi/10.1103/RevModPhys.61.689.

[94] E. K. U. Gross and R. M. Dreizler. "Relativistic gradient expansion of the kinetic energy density". In: *Phys. Lett. A* 81.8 (1981), pp. 447–450. ISSN: 0375-9601. DOI: https://doi.org/10.1016/0375-9601(81)90408-4. URL: http://www.sciencedirect.com/science/article/pii/0375960181904084.

[95] J. P. Perdew. "Accurate Density Functional for the Energy: Real-Space Cutoff of the Gradient Expansion for the Exchange Hole". In: *Phys. Rev. Lett.* 55 (16 1985), pp. 1665–1668. DOI: 10.1103/PhysRevLett.55.1665. URL: https://link.aps.org/doi/10.1103/PhysRevLett.55.1665.

[96] J. P. Perdew and Y. Wang. "Accurate and simple analytic representation of the electron-gas correlation energy". In: *Phys. Rev. B* 45 (23 1992), pp. 13244–13249. DOI: 10.1103/PhysRevB.45.13244. URL: https://link.aps.org/doi/10.1103/PhysRevB.45.13244.

[97] J. P. Perdew, K. Burke, and M. Ernzerhof. "Generalized Gradient Approximation Made Simple". In: *Phys. Rev. Lett.* 77 (18 1996), pp. 3865–3868. DOI: 10.1103/PhysRevLett.77.3865. URL: https://link.aps.org/doi/10.1103/PhysRevLett.77.3865.

[98] V. I. Anisimov and O. Gunnarsson. "Density-functional calculation of effective Coulomb interactions in metals". In: *Phys. Rev. B* 43 (10 1991), pp. 7570–7574. DOI: 10.1103/PhysRevB.43.7570. URL: https://link.aps.org/doi/10.1103/PhysRevB.43.7570.

[99] V. I. Anisimov, J. Zaanen, and O. K. Andersen. "Band theory and Mott insulators: Hubbard U instead of Stoner I". In: *Phys. Rev. B* 44 (3 1991), pp. 943–954. DOI: 10.1103/PhysRevB.44.943. URL: https://link.aps.org/doi/10.1103/PhysRevB.44.943.

[100] A. I. Liechtenstein, V. I. Anisimov, and J. Zaanen. "Density-functional theory and strong interactions: Orbital ordering in Mott-Hubbard insulators". In: *Phys. Rev. B* 52 (8 1995), R5467–R5470. DOI: 10.1103/PhysRevB.52.R5467. URL: https://link.aps.org/doi/10.1103/PhysRevB.52.R5467.

[101] S. L. Dudarev et al. "Electron-energy-loss spectra and the structural stability of nickel oxide: An LSDA+U study". In: *Phys. Rev. B* 57 (3 1998), pp. 1505–1509. DOI: 10.1103/PhysRevB.57.1505. URL: https://link.aps.org/doi/10.1103/PhysRevB.57.1505.

[102] J. Hubbard. "Electron correlations in narrow energy bands". In: *Proceedings of the Royal Society of London A: Mathematical, Physical and Engineering Sciences* 276.1365 (1963), pp. 238–257. ISSN: 0080-4630. DOI: 10.1098/rspa.1963.0204. eprint: http://rspa.royalsocietypublishing.org/content/276/1365/238.full.pdf. URL: http://rspa.royalsocietypublishing.org/content/276/1365/238.

[103] J. Hubbard. "Electron correlations in narrow energy bands. II. The degenerate band case". In: *Proceedings of the Royal Society of London A: Mathematical, Physical and Engineering Sciences* 277.1369 (1964), pp. 237–259. ISSN: 0080-4630. DOI: 10.1098/rspa.1964.0019. eprint: http://rspa.royalsocietypublishing.org/content/277/1369/237.full.pdf. URL: http://rspa.royalsocietypublishing.org/content/277/1369/237.

[104] J. Hubbard. "Electron correlations in narrow energy bands III. An improved solution". In: *Proceedings of the Royal Society of London A: Mathematical, Physical and Engineering Sciences* 281.1386 (1964), pp. 401–419. ISSN: 0080-4630. DOI: 10.1098/rspa.1964.0190. eprint: http://rspa.royalsocietypublishing.org/content/281/1386/401.full.pdf. URL: http://rspa.royalsocietypublishing.org/content/281/1386/401.

[105] M. Cococcioni and S. de Gironcoli. "Linear response approach to the calculation of the effective interaction parameters in the LDA + U method". In: *Phys. Rev. B* 71 (3 2005), p. 035105. DOI: 10.1103/PhysRevB.71.035105. URL: https://link.aps.org/doi/10.1103/PhysRevB.71.035105.

[106] H. J. Kulik et al. "Density Functional Theory in Transition-Metal Chemistry: A Self-Consistent Hubbard U Approach". In: *Phys. Rev. Lett.* 97 (10 2006), p. 103001. DOI: 10.1103/PhysRevLett.97.103001. URL: https://link.aps.org/doi/10.1103/PhysRevLett.97.103001.

[107] F. Bloch. "Über die Quantenmechanik der Elektronen in Kristallgittern". In: *Zeitschrift für Physik* 52.7 (1929), pp. 555–600. ISSN: 0044-3328. DOI: 10.1007/BF01339455. URL: https://doi.org/10.1007/BF01339455.

[108] C. Herring. "A New Method for Calculating Wave Functions in Crystals". In: *Phys. Rev.* 57 (12 1940), pp. 1169–1177. DOI: 10.1103/PhysRev.57.1169. URL: https://link.aps.org/doi/10.1103/PhysRev.57.1169.

[109] G. Kresse and J. Furthmüller. "Efficient iterative schemes for ab initio total-energy calculations using a plane-wave basis set". In: *Phys. Rev. B* 54 (16 1996), pp. 11169–11186. DOI: 10.1103/PhysRevB.54.11169. URL: https://link.aps.org/doi/10.1103/PhysRevB.54.11169.

[110] D.J. Singh and L. Nordström. *Planewaves Pseudopotentials and the LAPW Method, Second Edition*. Springer, 2006.

[111] D. R. Hamann, M. Schlüter, and C. Chiang. "Norm-Conserving Pseudopotentials". In: *Phys. Rev. Lett.* 43 (20 1979), pp. 1494–1497. DOI: 10.1103/PhysRevLett.43.1494. URL: https://link.aps.org/doi/10.1103/PhysRevLett.43.1494.

[112] J. C. Slater and G. F. Koster. "Simplified LCAO Method for the Periodic Potential Problem". In: *Phys. Rev.* 94 (6 1954), pp. 1498–1524. DOI: 10.1103/PhysRev.94.1498. URL: https://link.aps.org/doi/10.1103/PhysRev.94.1498.

[113] G. H. Wannier. "The Structure of Electronic Excitation Levels in Insulating Crystals". In: *Phys. Rev.* 52 (3 1937), pp. 191–197. DOI: 10.1103/PhysRev.52.191. URL: https://link.aps.org/doi/10.1103/PhysRev.52.191.

[114] N. Marzari and D. Vanderbilt. "Maximally localized generalized Wannier functions for composite energy bands". In: *Phys. Rev. B* 56 (20 1997), pp. 12847–12865. DOI: 10.1103/PhysRevB.56.12847. URL: https://link.aps.org/doi/10.1103/PhysRevB.56.12847.

[115] A. A. Mostofi et al. "Wannier90: A tool for obtaining maximally-localised Wannier functions". In: *Computer Physics Communications* 178.9 (2008), pp. 685–699. ISSN: 0010-4655.

[116] L. Noodleman. "Valence bond description of antiferromagnetic coupling in transition metal dimers". In: *The Journal of Chemical Physics* 74.10 (1981), pp. 5737–5743. DOI: 10.1063/1.440939. eprint: https://doi.org/10.1063/1.440939. URL: https://doi.org/10.1063/1.440939.

[117] L. Noodleman and E. J. Baerends. "Electronic structure, magnetic properties, ESR, and optical spectra for 2-iron ferredoxin models by LCAO-X.alpha. valence bond theory". In: *Journal of the American Chemical Society* 106.8 (1984), pp. 2316–2327. DOI: 10.1021/ja00320a017. eprint: https://doi.org/10.1021/ja00320a017. URL: https://doi.org/10.1021/ja00320a017.

[118] A. Saúl and G. Radtke. "Magnetic Couplings in CsV_2O_5: A New Picture". In: *Phys. Rev. Lett.* 106 (17 2011), p. 177203. DOI: 10.1103/PhysRevLett.106.177203. URL: https://link.aps.org/doi/10.1103/PhysRevLett.106.177203.

[119] G. Radtke et al. "Magnetic nanopantograph in the $SrCu_2(BO_3)_2$ Shastry–Sutherland lattice". In: *Proceedings of the National Academy of Sciences* 112.7 (2015), pp. 1971–1976. ISSN: 0027-8424. DOI: 10.1073/pnas.1421414112. eprint: http://www.pnas.org/content/112/7/1971.full.pdf. URL: http://www.pnas.org/content/112/7/1971.

[120] M. Okada et al. "Quasi-two-dimensional Bose-Einstein condensation of spin triplets in the dimerized quantum magnet $Ba_2CuSi_2O_6Cl_2$". In: *Phys. Rev. B* 94 (9 2016), p. 094421. DOI: 10.1103/PhysRevB.94.094421. URL: https://link.aps.org/doi/10.1103/PhysRevB.94.094421.

[121] G. Radtke et al. "Interplay between Structural, Electronic, and Magnetic Degrees of Freedom in $Sr_3Cr_2\mathbf{O}_8$". In: *Phys. Rev. Lett.* 105 (3 2010), p. 036401. DOI: 10.1103/PhysRevLett.105.036401. URL: https://link.aps.org/doi/10.1103/PhysRevLett.105.036401.

[122] A. W. Sandvik. "Computational Studies of Quantum Spin Systems". In: *AIP Conference Proceedings* 1297.1 (2010), pp. 135–338. DOI: 10.1063/1.3518900. eprint: https://aip.scitation.org/doi/pdf/10.1063/1.3518900. URL: https://aip.scitation.org/doi/abs/10.1063/1.3518900.

[123] G. Baym. *Lectures on quantum mechanics*. CRC Press, 2018.

[124] B. D. Josephson. "Possible new effects in superconductive tunnelling". In: *Phys. Lett.* 1.7 (1962), pp. 251–253. ISSN: 0031-9163. DOI: https://doi.org/10.1016/0031-9163(62)91369-0. URL: http://www.sciencedirect.com/science/article/pii/0031916362913690.

[125] L. H. Lewis and K. M. Bussmann. "A sample holder design and calibration technique for the quantum design magnetic properties measurement system superconducting quantum interference device magnetometer". In: *Review of Scientific Instruments* 67.10 (1996), pp. 3537–3542. DOI: 10.1063/1.1147172. eprint: https://doi.org/10.1063/1.1147172. URL: https://doi.org/10.1063/1.1147172.

[126] S.W. Lovesey. *Theory of Neutron Scattering from Condensed Matter*. International Series of Monogr v. 2. Clarendon Press, 1986. ISBN: 9780198520290. URL: https://books.google.fr/books?id=JuupZxrsCTEC.

[127] G. L. Squires. *Introduction to the Theory of Thermal Neutron Scattering*. 3rd ed. Cambridge University Press, 2012. DOI: 10.1017/CBO9781139107808.

[128] G. Shirane, S. M. Shapiro, and J. M. Tranquada. *Neutron Scattering with a Triple-Axis Spectrometer: Basic Techniques*. Cambridge University Press, 2002. ISBN: 9781139431019. URL: https://books.google.fr/books?id=agc8GeLZ-joC.

[129] J. Weber. "Fluctuation Dissipation Theorem". In: *Phys. Rev.* 101 (6 1956), pp. 1620–1626. DOI: 10.1103/PhysRev.101.1620. URL: https://link.aps.org/doi/10.1103/PhysRev.101.1620.

[130] A. Furrer, J.Ã. Mesot, and T. StrÃssle. *Neutron Scattering in Condensed Matter Physics*. Series on Neutron Techniques and Applications. World Scientific, 2009. ISBN: 9789813102507. URL: https://books.google.fr/books?id=SPQ7DQAAQBAJ.

[131] Institut Laue-Langevin. *Thermal neutron time-of-flight spectrometer IN4C*. URL: https://www.ill.eu/instruments-support/instruments-groups/instruments/in4c/description/instrument-layout/.

[132] S. Baroni et al. "Phonons and related crystal properties from density-functional perturbation theory". In: *Rev. Mod. Phys.* 73 (2 2001), pp. 515–562. DOI: 10.1103/RevModPhys.73.515. URL: https://link.aps.org/doi/10.1103/RevModPhys.73.515.

[133] B. Szigeti. "The Infra-Red Spectra of Crystals". In: *Proceedings of the Royal Society of London. Series A, Mathematical and Physical Sciences* 258.1294 (1960), pp. 377–401. URL: http://www.jstor.org/stable/2413966.

[134] T. J. Shankland, U. Nitsan, and A. G. Duba. "Optical absorption and radiative heat transport in olivine at high temperature". In: *Journal of Geophysical Research: Solid Earth* 84.B4 (1979), pp. 1603–1610. ISSN: 2156-2202. DOI: 10.1029/JB084iB04p01603. URL: http://dx.doi.org/10.1029/JB084iB04p01603.

[135] S. Bhagavantam and T. Venkatarayudu. "Raman effect in relation to crystal structure". In: *Proceedings of the Indian Academy of Sciences - Section A* 9.3 (1939), pp. 224–258. ISSN: 0370-0089. DOI: 10.1007/BF03046465. URL: https://doi.org/10.1007/BF03046465.

[136] R. Newman and R. M. Chrenko. "Optical Properties of Nickel Oxide". In: *Phys. Rev.* 114 (6 1959), pp. 1507–1513. DOI: 10.1103/PhysRev.114.1507. URL: https://link.aps.org/doi/10.1103/PhysRev.114.1507.

[137] Y. Mizuno and S. Koide. "Vibrationally induced electronic transitions in crystals of magnetic compounds". In: *Physik der kondensierten Materie* 2.2 (1964), pp. 166–179.

[138] J. Lorenzana and G. A. Sawatzky. "Theory of phonon-assisted multimagnon optical absorption and bimagnon states in quantum antiferromagnets". In: *Phys. Rev. B* 52 (13 1995), pp. 9576–9589. DOI: 10.1103/PhysRevB.52.9576. URL: https://link.aps.org/doi/10.1103/PhysRevB.52.9576.

[139] J. D. Perkins et al. "Mid-infrared optical absorption in undoped lamellar copper oxides". In: *Phys. Rev. Lett.* 71 (10 1993), pp. 1621–1624. DOI: 10.1103/PhysRevLett.71.1621. URL: https://link.aps.org/doi/10.1103/PhysRevLett.71.1621.

[140] H. Suzuura et al. "Singularities in Optical Spectra of Quantum Spin Chains". In: *Phys. Rev. Lett.* 76 (14 1996), pp. 2579–2582. DOI: 10.1103/PhysRevLett.76.2579. URL: https://link.aps.org/doi/10.1103/PhysRevLett.76.2579.

[141] M. Grüninger et al. "Midinfrared absorption in $YBa_2Cu_3O_6$: Evidence for a failure of spin-wave theory for spin $\frac{1}{2}$ in two dimensions". In: *Phys. Rev. B* 62 (18 2000), pp. 12422–12426. DOI: 10.1103/PhysRevB.62.12422. URL: https://link.aps.org/doi/10.1103/PhysRevB.62.12422.

[142] I. Dzyaloshinsky. "A thermodynamic theory of weak ferromagnetism of antiferromagnetics". In: *Journal of Physics and Chemistry of Solids* 4.4 (1958), pp. 241–255. ISSN: 0022-3697. DOI: https://doi.org/10.1016/0022-3697(58)90076-3. URL: http://www.sciencedirect.com/science/article/pii/0022369758900763.

[143] T. Moriya. "Magnetism ed. G.T. Rado and H. Shul". In: 85 (1963).

[144] L. Shekhtman, O. Entin-Wohlman, and A. Aharony. "Moriya's anisotropic superexchange interaction, frustration, and Dzyaloshinsky's weak ferromagnetism". In: *Phys. Rev. Lett.* 69 (5 1992), pp. 836–839. DOI: 10.1103/PhysRevLett.69.836. URL: https://link.aps.org/doi/10.1103/PhysRevLett.69.836.

[145] L. Shekhtman, A. Aharony, and O. Entin-Wohlman. "Bond-dependent symmetric and antisymmetric superexchange interactions in La_2CuO_4". In: *Phys. Rev. B* 47 (1 1993), pp. 174–182. DOI: 10.1103/PhysRevB.47.174. URL: https://link.aps.org/doi/10.1103/PhysRevB.47.174.

[146] T. Rõõm et al. "Low-energy excitations and dynamic Dzyaloshinskii-Moriya interaction in $\alpha' - NaV_2O_5$ studied by far-infrared spectroscopy". In: *Phys. Rev. B* 69 (14 2004), p. 144410. DOI: 10.1103/PhysRevB.69.144410. URL: https://link.aps.org/doi/10.1103/PhysRevB.69.144410.

[147] O. Cépas et al. "Dzyaloshinski-Moriya Interaction in the 2D Spin Gap System $SrCu_2(BO_3)_2$". In: *Phys. Rev. Lett.* 87 (16 2001), p. 167205. DOI: 10.1103/PhysRevLett.87.167205. URL: https://link.aps.org/doi/10.1103/PhysRevLett.87.167205.

[148] O. Cépas, T. Sakai, and T. Ziman. "Dynamics, Selection Rules and Dzyaloshinsky-Moriya Interactions in Strongly Frustrated Magnets". In: *Progress of Theoretical Physics Supplement* 145 (2002), pp. 43–51. DOI: 10.1143/PTPS.145.43. eprint: /oup/backfile/content_public/journal/ptps/145/10.1143/ptps.145.43/2/145-43.pdf. URL: http://dx.doi.org/10.1143/PTPS.145.43.

[149] P. Giannozzi et al. "QUANTUM ESPRESSO: a modular and open-source software project for quantum simulations of materials". In: *Journal of Physics: Condensed Matter* 21.39 (2009), p. 395502.

[150] K. F. Garrity et al. "Pseudopotentials for high-throughput {DFT} calculations". In: *Computational Materials Science* 81 (2014), pp. 446 –452. ISSN: 0927-0256.

[151] L. Li et al. "An Unprecedented Asymmetric End-On Azido-Bridged Copper(II) Imino Nitroxide Complex: Structure, Magnetic Properties, and Density Functional Theory Analysis". In: *Inorganic Chemistry* 45.19 (2006), pp. 7665–7670.

[152] J.-M. Mouesca. "Quantitative harmonization of the three molecular orbital, valence bond, and broken symmetry approaches to the exchange coupling constant: Corrections and discussion". In: *The Journal of Chemical Physics* 113.23 (2000), pp. 10505–10511.

[153] L. D. Casto et al. "Strong spin-lattice coupling in $CrSiTe_3$". In: *APL Mater.* 3.4 (2015), p. 041515. DOI: 10.1063/1.4914134. URL: https://doi.org/10.1063/1.4914134.

[154] F. E. Mabbs and D. J. Machin. *Magnetism and transition metal complexes*. Courier Corporation, 2008.

[155] G.L. Squires. *Introduction to the Theory of Thermal Neutron Scattering*. Dover books on physics. Dover Publications, 1978. ISBN: 9780486694474. URL: https://books.google.fr/books?id=Lx4xcz3v9IMC.

[156] H. F. Fong et al. "Phonon and Magnetic Neutron Scattering at 41 meV in $YBa_2Cu_3O_7$". In: *Phys. Rev. Lett.* 75 (2 1995), pp. 316–319. DOI: 10.1103/PhysRevLett.75.316. URL: https://link.aps.org/doi/10.1103/PhysRevLett.75.316.

[157] J. P. Clancy et al. "Singlet-Triplet Excitations in the Unconventional Spin-Peierls TiOBr Compound". In: *Phys. Rev. Lett.* 106 (11 2011), p. 117401. DOI: 10.1103/PhysRevLett.106.117401. URL: https://link.aps.org/doi/10.1103/PhysRevLett.106.117401.

[158] V. C. Farmer. *The Infrared Spectra of Minerals*. Mineralogical Society of Great Britain and Ireland, 1974. DOI: 10.1180/mono-4. URL: https://doi.org/10.1180/mono-4.

[159] M. Tinkham. *Group theory and quantum mechanics*. International series in pure and applied physics. McGraw-Hill, 1964. URL: https://books.google.fr/books?id=n_9QAAAAMAAJ.

[160] W. G. Fateley, N. T. McDevitt, and F. F. Bentley. "Infrared and Raman Selection Rules for Lattice Vibrations: The Correlation Method". In: *Appl. Spectrosc.* 25.2 (1971), pp. 155–173. URL: http://as.osa.org/abstract.cfm?URI=as-25-2-155.

[161] T. Rõõm et al. "Far-infrared spectroscopy of spin excitations and Dzyaloshinskii-Moriya interactions in the Shastry-Sutherland compound $SrCu_2(BO_3)_2$". In: *Phys. Rev. B* 70 (14 2004), p. 144417. DOI: 10.1103/PhysRevB.70.144417. URL: https://link.aps.org/doi/10.1103/PhysRevB.70.144417.

[162] S. Trebst et al. "Strong-Coupling Expansions for Multiparticle Excitations: Continuum and Bound States". In: *Phys. Rev. Lett.* 85 (20 2000), pp. 4373–4376. DOI: 10.1103/PhysRevLett.85.4373. URL: https://link.aps.org/doi/10.1103/PhysRevLett.85.4373.

[163] M. Windt et al. "Observation of Two-Magnon Bound States in the Two-Leg Ladders of $(Ca,La)_{14}Cu_{24}O_{41}$". In: *Phys. Rev. Lett.* 87 (12 2001), p. 127002. DOI: 10.1103/PhysRevLett.87.127002. URL: https://link.aps.org/doi/10.1103/PhysRevLett.87.127002.

[164] R. L. Martin and F. Illas. "Antiferromagnetic Exchange Interactions from Hybrid Density Functional Theory". In: *Phys. Rev. Lett.* 79 (8 1997), pp. 1539–1542. DOI: 10.1103/PhysRevLett.79.1539. URL: https://link.aps.org/doi/10.1103/PhysRevLett.79.1539.

[165] A. Saúl and G. Radtke. "Density functional approach for the magnetism of β-$TeVO_4$". In: *Phys. Rev. B* 89 (10 2014), p. 104414. DOI: 10.1103/PhysRevB.89.104414. URL: https://link.aps.org/doi/10.1103/PhysRevB.89.104414.

[166] Harald Jeschke et al. "Multistep Approach to Microscopic Models for Frustrated Quantum Magnets: The Case of the Natural Mineral Azurite". In: *Phys. Rev. Lett.* 106 (21 2011), p. 217201. DOI: 10.1103/PhysRevLett.106.217201. URL: https://link.aps.org/doi/10.1103/PhysRevLett.106.217201.

[167] M. E. Zhitomirsky. "Decay of quasiparticles in quantum spin liquids". In: *Phys. Rev. B* 73 (10 2006), p. 100404. DOI: 10.1103/PhysRevB.73.100404. URL: https://link.aps.org/doi/10.1103/PhysRevB.73.100404.

[168] M. E. Zhitomirsky and A. L. Chernyshev. "Colloquium: Spontaneous magnon decays". In: *Rev. Mod. Phys.* 85 (1 2013), pp. 219–242. DOI: 10.1103/RevModPhys.85.219. URL: https://link.aps.org/doi/10.1103/RevModPhys.85.219.

[169] J. Lorenzana and G. A. Sawatzky. "Phonon Assisted Multimagnon Optical Absorption and Long Lived Two-Magnon States in Undoped Lamellar Copper Oxides". In: *Phys. Rev. Lett.* 74 (10 1995), pp. 1867–1870. DOI: 10.1103/PhysRevLett.74.1867. URL: https://link.aps.org/doi/10.1103/PhysRevLett.74.1867.

[170] J. Lorenzana and R. Eder. "Dynamics of the one-dimensional Heisenberg model and optical absorption of spinons in cuprate antiferromagnetic chains". In: *Phys. Rev. B* 55 (6 1997), R3358–R3361. DOI: 10.1103/PhysRevB.55.R3358. URL: https://link.aps.org/doi/10.1103/PhysRevB.55.R3358.

[171] H. Suzuura et al. "Singularities in Optical Spectra of Quantum Spin Chains". In: *Phys. Rev. Lett.* 76 (14 1996), pp. 2579–2582. DOI: 10.1103/PhysRevLett.76.2579. URL: https://link.aps.org/doi/10.1103/PhysRevLett.76.2579.

[172] T. Rõõm et al. "Low-energy excitations and dynamic Dzyaloshinskii-Moriya interaction in $\alpha'-NaV_2O_5$ studied by far-infrared spectroscopy". In: *Phys. Rev. B* 69 (14 2004), p. 144410. DOI: 10.1103/PhysRevB.69.144410. URL: https://link.aps.org/doi/10.1103/PhysRevB.69.144410.

[173] O. Cépas and T. Ziman. "Theory of phonon-assisted forbidden optical transitions in spin-gap systems". In: *Phys. Rev. B* 70 (2 2004), p. 024404. DOI: 10.1103/PhysRevB.70.024404. URL: https://link.aps.org/doi/10.1103/PhysRevB.70.024404.

[174] C. Knetter and G. S. Uhrig. "Perturbation theory by flow equations: dimerized and frustrated $S = 1/2$ chain". In: *The European Physical Journal B-Condensed Matter and Complex Systems* 13.2 (2000), pp. 209–225. ISSN: 1434-6036. DOI: 10.1007/s100510050026.

[175] T. Barnes, J. Riera, and D. A. Tennant. "$S = \frac{1}{2}$ alternating chain using multiprecision methods". In: *Phys. Rev. B* 59 (17 1999), pp. 11384–11397. DOI: 10.1103/PhysRevB.59.11384.